Metallic corrosion at the steel/bentonite interface under anoxic and water saturated conditions.

Zur Erlangung des akademischen Grades eines

DOKTORS DER NATURWISSENSCHAFTEN

(Dr. rer. nat.)

von der KIT-Fakultät für Chemie und Biowissenschaften

des Karlsruher Instituts für Technologie (KIT)

genehmigte

DISSERTATION

von

MEng. Ashutosh R. Singh

aus

Varanasi, India

1. Referent: Prof. Dr. Horst Geckeis

2. Referent: Priv. -Doz. Dr. Frank Heberling

Tag der mündlichen Prüfung: 14.07.2025

Statement of originality – Eidesstattliche Erklärung

Hiermit versichere ich, dass ich die vorliegende Arbeit selbstständig verfasst und keine anderen Quellen oder Hilfsmittel verwendet zu haben als die hier angegebenen. Außerdem versichere ich, dass alle Stellen der Arbeit, die aus anderen Quellen wörtlich oder sinngemäß übernommen wurden, als solche kenntlich gemacht worden sind und die schriftliche Version der Arbeit mit der digitalen übereinstimmt. Die Arbeit wurde in gleicher oder ähnlicher Form noch bei keiner anderen Prüfungsbehörde vorgelegt. Die Satzung des Karlsruher Instituts für Technologie zur Sicherung guter wissenschaftlicher Praxis wurde in der jeweils gültigen Fassung beachtet.

Ort, Datum : Karlsruhe, 11.09.2025

Acknowledgments

This PhD work was carried out at Institute for Nuclear Waste Disposal (INE), of the Karlsruhe Institute of Technology (KIT), Karlsruhe, Germany. I would like to express my gratitude to Prof. Horst Geckeis for giving me the opportunity to perform my PhD at INE and for offering his supervision and guidance. I have gathered a lot of valuable scientific experience and was given a chance to contribute to high-level scientific research. I would also like to thank Dr. Marcus Altmaier, head of the Radiochemistry Division at INE, which I was part of. I am grateful for his positive attitude, guidance and many fruitful scientific discussions.

I especially would like to express my gratitude to my direct supervisor, Dr. Nicolas Finck for always finding time for my questions, ideas and discussions, and for his endless support during my PhD journey. I feel very lucky and honoured to be supervised by such great scientist.

I would like to thank my colleagues, Dr. Dieter Schild for SEM-EDXS and XPS measurements, Dr. Natalie Muller for EBSD measurement, Mrs Eva Soballa for her assistance with metallic coupons surface preparation using grinding and polishing, Dr. Frank Heberling and Dr. Teba Gil for AFM measurements, Dr. Andrej Skerencak-Frech for ultracentrifuge, Mr. Frank Geyer for ICP-MS measurements, Mrs Stephanie Kraft for ICP-OES measurements, Mrs Stephanie Kuschel for IC measurements, Mrs Elke Bohnert for glove box training, Dr. Jorg Rothe and Dr. Kathy Dardenne for XAS measurements at the INE beamline at the KIT Light Source.

I am very grateful to the Radioprotection group at INE and workshop group for always managing to fulfil my demands for equipment construction and endless samples cutting. I would like to thank the ex-members of my Secondary Phases group, Dr. Tim Platte, Dr. Pelin Cakir-Wüttke for their support, knowledge sharing and optimism. I am very grateful to my friends, Dr. Vinay Kumar, Dr. Arun Jaiswal, Dr. Ramamohan Dumpala, Dr. Avnish Pal Singh, Dr. Pankaj Kumar, Dr. Mohit Singh, Dr. Anuja Hariharan, Balaji Venugopal, Manuel Schorer, Justice Nwade and all other KIT- INE colleagues for their never ending support whenever I needed it.

A huge thank you goes to my grandparents (Shyam Narayan Singh, Taradevi) and parents (Ravindra Narayan Singh, Manorama R Singh), and my brother (Shivam Singh), sister (Neha Singh) for their endless support and understanding during my PhD journey.

The biggest thank you goes to my amazing wife Pooja Singh and son Krishiv Ashutosh Singh for his limitless love and patience. They never stopped taking care of me, supported me and trusted in me when times were difficult, which kept me going.

This work has been performed within the framework of different international and national projects: IMKORB project, funded by the German Federal Ministry for the Environment, Nature Conservation, Nuclear Safety and Consumer Protection (BMUV) under grant agreement N°02E11981B and the EURAD- CONCORD project, funded by European Union's Horizon 2020 research and innovation program 2014-2018 under grant agreement N°847593.

Abstract

The international community considers deep geological disposal to be the most sustainable solution for managing high-level nuclear waste (HLW), involving its storage in underground facilities within stable geological formations. The solution relies on a series of barriers both natural and engineered to isolate the waste from the biosphere, with the geological barrier (host rock), a buffer material (bentonite), and a container all playing vital roles in ensuring safety. Corrosion rates are needed to evaluate the container lifetime, and information on corrosion mechanism can be obtained knowing the nature of formed products. Furthermore, anaerobic metallic corrosion at the steel/bentonite interface determines the performance of bentonite based high level radioactive waste barrier.

Iron-based and copper-based materials were mostly considered as candidate canister materials by many countries for deep geological repositories, where they serve as barriers to prevent radionuclide migration possibly for hundreds of thousands of years. **This dissertation investigates the corrosion behavior of candidate canister materials for HLW disposal, focusing on three iron-based materials like low carbon steel (CS), spheroidal graphite iron (SGI) and spring steel (SS) which has high silicon content compared to carbon steel, as well as a copper based material like cupronickel alloy, under widely anoxic, water saturated conditions in contact with bentonite, a potential buffer material for radioactive waste disposal**. **This study simulates the corrosion processes in the initial, transient phase and does not look to the long-term processes under really oxygen free (anoxic) and reducing conditions**. The SGI and CS are constituents of the reference POLLUX container for heat generating HLW in Germany developed for the previously considered repository at the Gorleben site. The cupronickel alloy and SS were selected as potential alternative or reference materials. The goal of this work was to fill the knowledge gap in the corrosion mechanisms and rates of these candidate canister materials, specifically focusing on the role of bentonite in the corrosion process, given the lack of studies on the potential bentonite based design for German radioactive waste repositories. A further aim is to identify secondary corrosion phases, which in case of container through corrosion may play a role for radionuclide retention.

Experiments have been performed either under static conditions in closed vessels or under dynamic conditions in vessels allowing imposing a low water flow rate. Setups have been developed and tested, then a series of controlled static and dynamic batch experiments were conducted over time periods of three, six, nine and maximum 12 months at room temperature (25°C) and elevated temperature (50°C) under anoxic and water saturated conditions, simulating repository environments in crystalline rock. Synthetic Grimsel groundwater and MX-80 bentonite were used to allow comparison with the in-situ MaCoTe experiment at the Grimsel Test Site (GTS), Switzerland. For cupronickel alloy, the effect of sulfide presence, mimicking the development of bacterial activity, was further investigated. For SGI, the effect of hematite presence, mimicking the presence of early oxic phase corrosion products, was also investigated.

For SS and CS, the effect of scratching the surface, as may possibly occur during canister handling, was investigated. Finally, for CS a series of experiments was performed with GMZ bentonite (from Gaomiaozi country in Inner Mongolia Autonomous Region, China) to identify a possible effect of bentonite composition on corrosion behavior. At the end of contact time, the systems were characterized. First pH and E_h of bentonite slurry/ground water were measured in

situ and at room temperature, and then the collected slurry/groundwater was ultracentrifuged. The composition of the collected supernatant was determined by ICP-OES/MS and IC.

The coupon/bentonite interface was characterized by using various microscopy and spectroscopy techniques like SEM-EDX, XRD, XPS, XAS and corrosion rates were determined using weight loss measurement method. The findings of the study aim to fill knowledge gaps especially related to corrosion behavior, secondary corrosion phase formation and possibly bentonite alteration, because these may play an important role in the retention in the nearfield of radionuclide that will be released following breach of the canister.

The results reveal that all candidate materials exhibit varying corrosion behavior under the different experimental conditions, including temperature, time, presence of sulfide, hematite and mechanical scratches. Cupronickel alloy, which showed the lowest corrosion rates lying after 6 months in a range of (0.08±0.05 µm/a to 0.44±0.12 µm/a at 25°C) with a tendency of a temporal higher rates at elevated temperature of 50°C. Conversely, carbon steel showed the highest corrosion rates from all iron based materials ranging (3.84±1.87 µm/a to 5.07±1.60 µm/a at 25°C and up to ~ 17±10 µm/a at 50°C after 6 months). Scratching, addition of sulfide or hematite has a limited effect on corrosion rates and also the impact of increased temperature appears to decrease over time. These corrosion rates align closely with those measured in in-situ MaCoTe experiments, where observed corrosion rates of carbon steel (1-2 µm/a) and copper (0.1-0.3 µm/a) over similar periods of exposure.

The pH in static experiments remained stable for all materials, with a slight decrease observed at elevated temperature, whereas in dynamic experiments, the pH increased with time, tending towards that in the inlet groundwater (pH 9.8), indicating moderately alkaline conditions. The redox potential for all iron-based materials remained negative, indicating reducing conditions which develop due to formation of Fe(II) bearing compounds. For cupronickel, on the other hand, positive E_h maintained in static experiment, which shifted to negative values in dynamic experiments but remained in a range that corresponds to the stable metallic state for Cu, with low corrosion rates observed at room temperature. Note that the experimental setup does not reflect the real situation in a repository, where compacted bentonite is emplaced and advective flow normally is not expected. However, in the case of bentonite erosion, a situation as simulated in the experiments presented here, can develop.

Secondary phase analysis for cupronickel indicated the formation of copper oxide (Cu_2O) in all static experiments and a mixture of nickel hydroxide $Ni(OH)_2$, copper oxide (Cu_2O), and copper sulfide (Cu_2S) in dynamic experiments. Overall, the corrosion products observed in dynamic experiments were more complex, with notable contributions from sulfide, these findings are partly consistent with those observed in in-situ corrosion studies, such as MaCoTe, where copper corrosion products were predominantly oxides, with only minor sulfide compounds detected.

Iron-based candidate materials exhibited a wide variety of corrosion products, including iron oxides, iron silicates, iron sulfides, and green rust. Secondary phases such as berthierine (iron silicate) and green rust were observed at extended exposure times, particularly at elevated temperature, indicating an evolving corrosion process. The formation of iron silicate layers at the metal/bentonite interface, particularly at longer time period, slowed corrosion by slowing down further metal dissolution. These protective layers were more prominent in static conditions and at

higher temperatures, in contrast to the MaCoTe in-situ experiments, where no such iron silicate layers were observed, likely due to differing environmental conditions (e.g., rock vs room temperature).

Surface characterization of corroded coupons confirmed the presence of the corrosion products, with significant differences in the composition and distribution of corrosion phases observed across the different materials and experimental conditions. The corrosion products detected on the iron-based materials in both static and dynamic conditions were influenced by temperature, exposure time, and the presence of added hematite. For example, in the presence of hematite (α-Fe_2O_3), the corrosion rate of SGI was elevated during the initial period, as hematite presumably acts as an oxidant and accelerates corrosion. Graphite inclusions in SGI also acted as cathodic sites, accelerating the anodic corrosion of ferrite, which ultimately led to the formation of mixed Fe(II)/Fe(III) corrosion products, such as magnetite. Spring steel exhibited similar corrosion behavior in both static and dynamic experiments, with the formation of iron (hydr)oxides and iron silicates observed at the metal/bentonite interface.

XPS and SEM-EDX results corroborated these findings, with iron silicate being identified as a major corrosion product. Carbon steel showed the formation of iron oxides, iron silicates, iron sulfides, and iron-rich carbonates (such as chukanovite evidenced by XANES) in the presence of MX-80 bentonite. In dynamic experiments, corrosion products formed more rapidly compared to static conditions, especially at elevated temperature, leading to more pronounced changes in corrosion behavior over time. For carbon steel, magnetite and iron silicate form predominantly in the presence of GMZ bentonite, and extended exposure periods (12 months) resulted in a more distinct morphology of corrosion products, including octahedral magnetite crystals.

The alteration of bentonite, as a result of the corrosion processes, was confirmed through XAS (XANES), and ICP-MS analysis following digestion of bentonite that was in contact with the metallic coupons which revealed changes in the elemental composition. For cupronickel, small amounts of copper and nickel were adsorbed onto the bentonite, with concentrations increasing at elevated temperatures in the presence of sulfide. The presence of secondary phases like berthierine (iron silicate), green rust, magnetite (iron oxide), and chukanovite (iron-rich carbonate) in altered bentonite was confirmed using XAS (XANES) analysis and these findings were corroborated by SEM-EDX analysis. These secondary phases could potentially act as a long-term sink for radionuclide retention, reducing the risk of their migration into the biosphere.

This study suggests that while the surface roughness caused by scratches during canister handling may not significantly affect the corrosion behavior of the candidate materials (carbon steel and spring steel), the formation of protective layers (such as iron silicates) and the alteration of bentonite play crucial roles in mitigating long-term corrosion. The short-term nature of this study does not fully capture the long-term corrosion behavior under real case geological conditions, where residual oxygen does not anymore play a role. Furthermore, microbially induced corrosion aspects are not investigated here. Future research should focus on predictive modeling of the long-term evolution of a repository nearfield taking corrosion processes and secondary phases forming in the short and long term into account.

Keywords: Cupronickel corrosion, Steel corrosion, Corrosion rate, Secondary Phases, XANES, SEM-EDX, XPS, Bentonite alteration, Nuclear Waste Disposal

Zusammenfassung

International wird die Endlagerung in tiefen geologischen Formationen als sicherste Entsorgungslösung betrachtet, bei der hochradioaktive Abfälle in einem Bergwerk in einer stabilen geologischen Formation eingelagert werden. Die Sicherheit eines tiefengeologischen Endlagers wird durch eine Reihe natürlicher und technischer und geotechnischer Barrieren gewährleistet, die die Aufgabe haben, die Abfälle von der Biosphäre zu isolieren. Dabei spielen die geologische Barriere (Wirtsgestein und Deckgebirge), ein Puffermaterial (z.B. Bentonit) und der Behälter eine entscheidende Rolle. Experimentell bestimmte Korrosionsraten werden benötigt, um die Behälterlebensdauer abzuschätzen. Informationen zu Korrosionsmechanismen erlauben es, die Art der gebildeten Korrosionsprodukte abzuleiten. Zusätzlich kann die anaerobe Metallkorrosion an der Stahl/Bentonit Grenzfläche die Eigenschaften der Bentonit Barriere verändern. Auch dies gilt es zu untersuchen.

Eisen und kupferbasierte Materialien wurden in vielen Ländern als mögliche Behältermaterialien für die tiefe geologische Endlager in Betracht gezogen, wo sie im Zusammenspiel mit anderen Barrieren die Migration von Radionukliden über hundertausende von Jahren mininieren oder gar verhindern sollen. **Diese Dissertation untersucht das Korrosionsverhalten von in Frage kommenden Behältermaterialien für ein HLW Endlager und konzentriert sich dabei auf drei eisenbasierte Materialien wie kohlenstoffarmem Stahl (CS), Gusseisen mit Kugelgraphit (SGI) und Federstahl (SS) der im Vergleich zum Kohlenstoffstahl einen hohen Siliziumgehalt aufweist. Weiterhin wurde eine Kupfernickel Legierung als Vertreter eines kupferbasierten Materials untersucht. In allen Fällen geschah dies unter weitgehend anoxischen, wassergesättigten Bedingungen in Kontakt mit Bentonit, einem potenziellen Puffermaterial für ein Endlager für radioaktive Abfälle**. **Diese Studie simuliert die Korrosionsprozesse in der initialen, transienten Phase nach Einlagerung der Abfälle, in der erhöhte Temperaturen auftreten und noch residuale Sauerstoffmengen im Einlagerungsbereich vorliegen. Die Arbeit befasst sich nicht mit den langfristigen Prozessen unter wirklich sauerstofffreien (anoxischen) und reduzierenden Bedingungen, die über lange Zeiträume wirksam bleiben, wenn Restsauerstoff durch Korrosionsprozesse verbraucht und sich wieder Umgebungstemperaturen eingestellt haben**. SGI und CS sind Bestandteile des POLLUX Behälters, des in Deutschland entwickelten Referenzbehälterkonzepts für die Endlagerung von wärmeentwickelndem HLW im früher vorgesehenen Endlager in Gorleben. Kupfernickel und SS wurden als mögliche Alternativwerkstoffe ausgewählt. Ziel dieser Arbeit war es, Wissenslücken in Bezug auf Korrosionsmechanismen und raten dieser in Frage kommenden Behältermaterialien zu schließen und sich dabei insbesondere auf die Rolle von Bentonit während des Korrosionsprozesses zu konzentrieren.

Experimente wurden entweder in geschlossene Gefäße unter statischen Bedingungen oder unter dynamischen Bedingungen in Gefäßen, welche es erlauben, eine niedrige Wasserdurchflussrate einzustellen, durchgeführt. Ein entsprechender Aufbau wurde entwickelt und getestet. Im Rahmen der hier beschriebenen Experimente erfolgte die Durchführung einer Reihe statischer und dynamischer Experimente über Zeiträume von drei, sechs, neun und maximal zwölf Monaten bei Raumtemperatur (25°C) und erhöhter Temperatur (50°C) unter anoxischen, wassergesättigten Bedingungen, die die Bedingungen in einem Endlager in Kristallgestein simulieren.

Synthetisches Grundwasser aus dem Grimsel Felslabor (Grimsel Test Site, GTS, Schweiz) und MX-80 Bentonit wurden ausgewählt, um einen Vergleich mit dem MaCoTe in-situ Experiment im GTS zu ermöglichen. Für Kupfernickel wurde der Effekt der Entwicklung bakterieller Aktivität durch Zugabe von Sulfid simuliert. In den Experimenten mit SGI wurde Hämatit zugegeben, um den Einfluss von Korrosionsprodukten aus einer frühen oxischen Phase im Einlagerungsbereich eines Endlagers zu untersuchen. Für SS und CS wurde zusätzlich die Anwesenheit von Oberflächenkratzern auf das Korrosionsverhalten untersucht, die durch eine Handhabung der Behälter bei der Einlagerung entstehen könnten. Letztlich wurde für CS ebenso eine experimentelle Serie mit GMZ Bentonit (ein in China untersuchtes Material, das für ein dortiges Endlager vorgesehen ist; GMZ Bentonit stammt aus Gaomiaozi in der Autonomen Region Innere Mongolei, China) angesetzt, um einen möglichen Effekt der Bentonit Zusammensetzung auf das Korrosionsverhalten zu identifizieren. Die Bestimmung von pH und E_h Werten in Bentonit Suspensionen bzw. im simulierten Grundwasser erfolgte in situ und bei Raumtemperatur. Danach wurden die Lösungen nach Ultrazentrifugation mittels ICP-OES/MS und IC analysiert. Die Grenzfläche zwischen Metallcoupons und Bentonit wurde mit Hilfe verschiedener mikroskopischer und spektroskopischer Techniken wie SEM-EDX, XRD, XPS, XAS charakterisiert. Die Bestimmung von Korrosionsraten erfolgte mit einer Gewichtsverlustmessverfahrensmethode. Die Studie zielt darauf ab, Wissenslücken in Bezug auf Korrosionsverhalten, Bildung sekundärer Korrosionsphasen und Bentonitalteration zu schließen, um deren Rolle für die Ausbreitung bzw. Rückhaltung von Radionukliden, die nach Behälterversagen freigesetzt werden können, bewerten zu können.

Experimentell bestimmte Korrosionsraten weisen teilweise große Streuwerte auf. Wie zu erwarten wies die Kupfernickellegierung in allen Experimenten die niedrigsten Korrosionsraten auf (0.08±0.05 µm/a zu 0.44±0.12 µm/a bei 25°C) mit einer Tendenz zu höheren Korrosionsraten bei der erhöhten Temperatur von 50ºC nach 6 Monaten. Von allen eisenbasierten Materialien zeigte Kohlenstoffstahl die höchste Korrosionsrate (3.84±1.87 µm/a zu 5.07±1.60 µm/a bei 25°C und bis zu ~ 17±10 µm/a bei 50°C nach 6 Monaten). Oberflächenrauhigkeit, Zugabe von Sulfid oder Hämatit hatten nur begrenzten und temporären Einfluss auf Korrosionsraten und auch der Einfluss der erhöhten Temperatur nimmt offenbar mit zunehmender Zeit ab. Die hier bestimmten Korrosionsraten stimmen gut mit den unter in-situ-Bedingungen im GTS Labor im Rahmen des MaCoTe (Material Corrosion Test) Experiments über ähnliche Expositionszeiträume gemessenen Raten überein (Kohlenstoffstahl: 1–2 µm/a; Kupfer: 0,1–0,3 µm/a).

Das Vorhandensein von Restsauerstoff und das Fehlen einer Passivierungsschicht führten in den Experimenten anfänglich zu erhöhten Korrosionsraten. pH-Werte blieben in statischen Experimenten mit allen Materialien konstant, wobei bei erhöhter Temperatur eine leichte Abnahme beobachtet wurde, während in dynamischen Experimenten der pH-Wert mit der Zeit anstieg und sich dem pH-Wert des einströmenden Grundwassersimulats (pH 9,8) annäherte. E_h-Werte in allen Experimenten mit eisenbasierten Materialien blieben negativ, zeigten damit reduzierende Bedingungen an, die auf die Bildung von Fe(II) in Lösung und Fe(II)-haltigen Sekundärphasen zurückzuführen sind. In Experimenten mit Kupfernickel hingegen stellten sich im statischen Experiment positive E_h Werte ein, während in dynamischen Experimenten negative Werte auftraten. Die Redox Bedingungen lagen alle im Stabilitätsfeld des stabilen metallischen Zustands für Cu. Folgerichtig wurden generell niedrige Korrosionsraten beobachtet.

Es ist zu beachten, dass der Versuchsaufbau des dynamischen Experiments nicht die reale Situation in einem Endlager widerspiegelt, wo verdichteter Bentonit vorliegt und advektiven Strömungen normalerweise nicht zu erwarten sind. Im Falle der Erosion der Bentonit Barriere können sich allerdings durchaus Bedingungen einstellen, wie sie in den hier vorgestellten Experimenten simuliert wurde.

Die Sekundärphasenanalyse von Kupfernickel ergab in allen statischen Experimenten die Bildung von Kupferoxid (Cu_2O) und in dynamischen Experimenten eine Mischung aus Nickelhydroxid ($Ni(OH)_2$), Kupferoxid (Cu_2O) und Kupfersulfid (Cu_2S). Insgesamt waren die in den dynamischen Experimenten beobachteten Korrosionsprodukte vielfältiger, mit bemerkenswerten Beiträgen von Sulfiden. Diese Ergebnisse stimmen teilweise mit denen überein, die in In-situ-Korrosionsstudien wie MaCoTe beobachtet wurden. Dort wurden überwiegend Kupferoxide als Kupferkorrosionsprodukte gefunden mit nur geringen Beiträgen an Sulfidverbindungen. Eisenbasierte Materialien wiesen eine große Vielfalt an Korrosionsprodukten auf, darunter Eisenoxide, Eisensilikate, Eisensulfide und Grünen Rost. Sekundärphasen wie Berthierin (Eisensilikat) und Grüner Rost wurden bei längeren Reaktionszeiten, insbesondere bei erhöhter Temperatur, beobachtet, was auf einen fortschreitenden Korrosionsprozess mit der Zeit hindeutet. Die mit der Zeit zunehmende Bildung von Eisenschichtsilikaten an der Metall/Bentonit Grenzfläche bildet eine Schutzschicht, die vermutlich für die mit der Zeit abnehmende Korrosionsrate verantwortlich ist, indem sie eine weitere Metallauflösung behindert. Diese Schutzschichten waren unter statischen Bedingungen und bei höherer Temperatur ausgeprägter, im Gegensatz zu den Ergebnissen von MaCoTe in-situ Experimenten, bei denen keine derartigen Eisenschichtsilikate beobachtet wurden. Dies ist wahrscheinlich auf die niedrigeren Gebirgstemperaturen im GTS-Labor zurückzuführen.

Die bei statischen und dynamischen Bedingungen auf den eisenbasierten Materialien nachgewiesenen Korrosionsprodukte wurden von Temperatur, Einwirkungsdauer und dem Vorhandensein von zugesetztem Hämatit beeinflusst. Beispielsweise war in Gegenwart von Hämatit (α-Fe_2O_3) die Korrosionsrate von SGI während der Anfangsphase erhöht, da Hämatit vermutlich als Oxidans wirkt und die Korrosion beschleunigt. Graphiteinschlüsse bildeten in SGI Lokalelemente aus und beschleunigten die anodische Korrosion von Eisen, was letztendlich zur Bildung gemischter Fe(II)/Fe(III)-Korrosionsprodukte wie Magnetit führte.

Federstahl zeigte in statischen und dynamischen Experimenten ein ähnliches Korrosionsverhalten, wobei an der Metall/Bentonit Grenzfläche mittels XPS und SEM-EDX die Bildung von Eisen(hydr)oxiden und Eisensilikaten beobachtet wurde, wobei Eisensilikat als Hauptkorrosionsprodukt identifiziert wurde. Kohlenstoffstahl zeigte in Gegenwart von MX80-Bentonit die Bildung von Eisenoxiden, Eisensilikaten, Eisensulfiden und eisenreichen Karbonaten (wie z.B. Chukanovit, das durch XANES Analyse nachgewiesen wurde). In Gegenwart von GMZ-Bentonit bildeten sich überwiegend Magnetit und Eisensilikat. Längere Expositionszeiträume (12Monate) führten zu einer höheren Kristallinität der Korrosionsprodukte, u.a. zur Bildung oktaedrischer Magnetitkristalle. In dynamischen Experimenten bildeten sich Korrosionsprodukte im Vergleich zu statischen Bedingungen schneller, insbesondere bei erhöhten Temperaturen.

Die Veränderung des Bentonits infolge der Korrosionsprozesse wurde durch XAS (XANES) Messungen und ICP-MS Analyse der Elementzusammensetzung untersucht. In den Experimenten mit Kupfernickel fanden sich geringe Mengen an Kupfer und Nickel, die offenbar auf dem Bentonit adsorbiert vorlagen, wobei die Konzentrationen bei erhöhten Temperaturen und in Gegenwart von Sulfid anstiegen. Das Vorhandensein von Sekundärphasen wie Berthierin (Eisensilikat), Grünrost, Magnetit (Eisenoxid) und Chukanovit (eisenreiches Karbonat) in verändertem Bentonit wurde durch XAS (XANES) und SEM-EDX Analyse nachgewiesen. Diese Sekundärphasen könnten möglicherweise langfristig für die Rückhaltung von Radionukliden sorgen und die Ausbreitung im Endlagernahfeld behindern.

Oberflächenrauheit, die möglicherweise durch Kratzer während der Handhabung der Behälter verursacht werden kann, beeinflusste unter den Bedingungen der hier beschriebenen Studie das Korrosionsverhalten von Kohlenstoffstahl und Federstahl nicht wesentlich. Dagegen führt die Bildung von Schutzschichten (wie Eisensilikaten) zur Reduktion der Korrosionsraten. Die vorliegende Studie erfasst das langfristige Korrosionsverhalten unter realen geologischen Bedingungen, bei denen Restsauerstoff keine Rolle mehr spielt, nicht vollständig. Darüber hinaus werden mikrobiell induzierte Korrosionsaspekte hier nicht im Detail untersucht. Zukünftige Forschung sollte sich auf die prädiktive Modellierung der langfristigen Entwicklung eines Endlagers im Nahfeld konzentrieren und dabei kurz und langfristig Korrosionsprozesse und die Bildung von Sekundärphasen berücksichtigen.

Schlüsselwörter: KupferNickel Korrosion, Stahlkorrosion, Korrosionsrate, Sekundärphasen, XANES, SEM-EDX, XPS, Bentonitveränderung, Entsorgung radioaktiver Abfälle

Table of Contents

Abbreviations

AFM	Atomic Force Microscopy
COx	Callovo-Oxfordian claystone
CS	Construction Steel
Cu-Ni	Copper- Nickel alloy
D	Dynamic Experiments
EBSD	Electron backscatter diffraction
EDX	Energy Dispersive X-Ray spectroscopy
ESEM	Environmental Scanning Electron Microscopy
Fe	Iron
GW	Ground Water
IC	Ion Chromatography
ICP-MS	Inductively coupled plasma mass spectrometry
ICP-OES	Inductively Coupled Plasma Optical Emission spectroscopy
INE-BL	Institute of Nuclear waste disposal -Beam line
LCF	Linear combination fitting
MACOTE	Material Corrosion Test
NWMO	Nuclear waste management organization
PTFE	Poly tetra fluoro ethylene
S	Static Experiments
SGI	Spheroidal Graphite Iron
SS	Spring Steel
T	Temperature
T1	Reference experiment at Room Temperature (25°C)
T2	Reference experiment at Elevated Temperature (50°C)
XANES	X-ray absorption near edge structure
XAS	X-ray absorption spectroscopy
XPS	X-ray photoelectron spectroscopy
XRD	X-ray Diffraction

1. Introduction

1.1 Research background & motivation

In the modern era, the energy consumption has been significantly increased due to various humankind activities. Energy is produced by different methods, which in turn generate significant amount of waste materials, which must be managed and disposed of safely to minimize its impact on biosphere. Nuclear energy plays avital role in various countries and is considered as an appropriate technology for generating electricity with low CO_2 emissions. It may contribute to cover the huge energy demand, however also produces radioactive wastes of partly high specific activity. These wastes also arise from other activities such as nuclear medicine, research, military operations and rare-earth mining. High-level radioactive waste generated by energy production mainly consists of spent nuclear fuel, which contains highly radioactive materials (actinides) like uranium, plutonium, and fission products such as cesium-137 and strontium-90. These wastes are highly radioactive, toxic and is heat generating. These High-level waste (HLW) needs to be disposed of properly in a safe way to protect future generations and the environment from its harmful effects. Deep geological repositories are the most acceptable international solution to the disposal of highly radioactive waste material since they isolate the waste from the biosphere for very long timeframes **(Féron et al., 2008)**. In a deep geological repository, the nuclear waste is emplaced in tight and stable rock formations at a depth of several hundreds of meters, thus ensuring long-term safety without the need for human intervention.

A multi-barrier system protects the waste from external impacts and retains radioactive substances in the repository. The repository can be hosted in either salt, crystalline (mostly granite) or sedimentary clay rock; the nuclear waste is foreseen to be encapsulated in metallic containers and surrounded by engineered barriers. Bentonite can be used as buffer materials surrounding the canister for nuclear waste disposal. It holds as a barrier with high swelling properties, low permeability, strong sorption capacity, **(García-Romero et al., 2019)**, and microorganisms may not be able to grow in the nanopores of compacted bentonite. Therefore, it is important to ensure that these properties are preserved under real repository conditions for hundreds of thousands of years. Bentonite is divided into Ca and Na type bentonite according to the species of exchangeable cations present between the layers, and volume expansion is achieved via swelling through interlayer hydration **(Muhammad & Siddiqua, 2022; Yoo et al., 2016)**. The swelling ability of bentonite acts as a seal of the space between the disposal canister and disposal hole and blocks the inflow of groundwater from the surrounding host rock **(Birgersson & Karnland, 2009)**. Upon closure of the repository, the surrounding bentonite is gradually saturated with the influx of natural pore water from the surrounding parent rock, while simultaneously experiencing a temperature rise owing to the radioactive decay of the waste. However, during the geological evolution of the repository system, groundwater may diffuse through the barriers and ultimately reach the near field. The presence of water at the canister/engineered barrier interface will result in alteration and corrosion processes, which depend on the characteristics of the canister material and of the backfill material as well as on the

prevailing geochemical conditions **(S. Kaufhold et al., 2020)**. For a robust nuclear waste disposal Safety Case, a detailed understanding of the underlying sub-processes is required. The choice of the material used to construct canisters is mainly governed by the nature of the host rock. Indeed, carbon steel is typically selected as over pack material when a deep repository is planned to be hosted in a sedimentary clay rock formation owing to the controlled, predictable nature of its corrosion behavior and because its use is based on industrially proven technologies **(Féron et al., 2008)**. In the context of nuclear waste disposal, a robust and reliable prediction of the corrosion behavior over much longer periods requires the development of semi-empirical models and scientific process understanding. Predictions should be based on known mechanisms of corrosion phenomena **(Féron et al., 2008)**.

For more permeable or fractured host rocks (e.g., crystalline rock) copper is an ideal canister material owing to its thermodynamic stability in anoxic ground water (in the absence of sulfides) and its tendency to uniform dissolution in the presence of chloride **(King & Padovani, 2011)**. Unfortunately, sulfide can be present naturally in the environment resulting in corrosion of copper driven by the formation of cuprous sulfide **(Chen et al., 2011; King & Padovani, 2011)**. However, sulfide induced corrosion can be inhibited by protecting the copper coating using bentonite buffer as a diffusion barrier for nuclear waste disposal **(Boyle & Meguid, 2015; Pedersen, 2010)**. Interestingly, studies also showed that alloying copper with nickel (e.g., 30 wt. % Ni) results in a material with good corrosion resistance in contact with bentonite **(Kursten et al., 2004)**. Such material has been under consideration as canister material for disposal in crystalline rock, but detailed knowledge on its corrosion behavior under repository relevant conditions is still insufficient for being able to predict its behavior over longer periods.

Some information about steel corrosion in conditions representative of disposal in clay-based repositories (e.g., under consideration in France, Switzerland and Belgium) has been reported **(El Mendili et al., 2014)**. However, a detailed knowledge of corrosion mechanisms and corrosion rates of cupronickel, spheroidal graphite iron, spring steel and carbon steel candidate canister materials in presence of bentonite as buffer possible for geologic formation in Germany is limited and particularly careful analysis of corrosion product formation is still lacking in such conditions. Some research has been conducted in the past **(King, 2008)** indicating the mechanism of corrosion in the presence of clay but clear idea about nature and fate of corrosion products is still lacking. This is crucial for optimization of canister materials, study long term material performance under geological conditions and ensuring safety of nuclear waste disposal. In a deep geological repository environment, the residual oxygen is expected to be consumed within a couple of tens to hundred years after closure of the emplacement cell, buffering the environment of the system to reducing (anoxic) conditions. Therefore, experimental effort should be dedicated for better understanding the effect of bentonite on steel/bentonite corrosion under anoxic and water saturated conditions. Here research is mainly focusing on MX-80 bentonite as engineering barrier surrounding the candidate canisters, which can be used for crystalline-based rock repository. In addition, attention is paid to identify long-term relevant corrosion products because they may act as sink and immobilize radionuclide in the near field. Data and scientific process understanding obtained in thesis will support to improve safety cases of geological repository.

1.2 Aim of present work

The thesis describes laboratory corrosion experiments which are performed with three iron-based materials like low carbon steel (CS), spheroidal graphite iron (SGI), and spring steel (SS), and one copper-based material like cupronickel alloy reference materials discussed as potentially relevant for nuclear waste containers under anoxic and water saturated conditions.

The main aims of the study are to:

- Identify corrosion products which may be present when radionuclides would be mobilized from the waste matrix and which may play a role for radionuclide retention in the near field.

- Investigate the effect of bentonite on iron and copper corrosion under anoxic and water saturated conditions. To obtain information on the potential alteration of bentonite.

- Obtain a detailed understanding of corrosion processes, i.e., mechanism and rate, under the applied conditions and to quantify the dependence of temperature, time, alloying elements, presence of different bentonite types (MX-80/GMZ) and secondary phases on corrosion rates.

- Investigate the effect of transient conditions (presence of early period oxic corrosion product (hematite) on SGI corrosion, elevated temperature, progressive increase of sulphide concentration due to development of bacterial activity on a Cu-Ni alloy), effect of surface roughness (CS and SS) on the corrosion behaviour of potential canister materials.

- Examine the potential impact of bentonite erosion in low ionic strength groundwater on corrosion by applying a dynamic experimental approach.

- Examine transferability of laboratory (KIT-INE) experimental data to field conditions of *in-situ* corrosion experiments at the Grimsel Test Site in Switzerland **(Reddy, Padovani, Rance, et al., 2021)**, the Material Corrosion Test (MaCoTe).

Overall, the idea is to obtain insights into the repository near-field environment after corrosion has taken place. The formation of secondary corrosion phases will have possible impact on the porosity of the geotechnical or geological barrier and will modify the mineralogy in this area. Both could influence radionuclide migration/retention in the repository near field. Note that the impact of bacteria (beside the influence of sulfide) and irradiation are not considered within the context of this thesis.

1.3 State of the art

1.3.1 Container corrosion in nuclear waste repositories

In the past, studies were carried out on metallic corrosion of SGI under anoxic, saline and elevated temperature conditions in the Korrosions und Sorptionsprozesse an Stahloberflächen bei hohen Temperaturen und Drücken im anaeroben salinaren Milieu (KORSO) project **(Finck et al., 2021)**. Limited information is available regarding corrosion behavior of spheroidal graphite iron as candidate canister materials for possible German repository design in contact with bentonite. Considering the concepts of final disposal of high-level radioactive waste in Switzerland, one candidate canister material over pack is made out of cast steel GS-40 which has good weld ability or a higher toughness and can withstand its property at elevated temperature. This material was chosen to minimize potential problems related to stress corrosion cracking which occur in repository because of tensile stress and corrosive environment **(Attinger et al., 1991)**.

The thesis also comprises Concord and Imkorb project work, which focuses on studying and understanding corrosion behavior of candidate canister materials in contact with bentonite under anoxic conditions for nuclear waste disposal. The systematic exploration of novel and traditional materials, which is one small part of EURAD (a HORIZON 2020 European Joint Programmed on Radioactive Waste Management), is covered under the work package Container Corrosion under Disposal conditions (Concord, https://www.ejp-eurad.eu/implementation/container-corrosion-under-disposal-conditions-concord) which will provide solid state-of-the-art for the pursuit of the container optimization according to the geological sites, disposal concepts and regulatory requirements **(Muñoz et al., 2024)**. A deep understanding of the corrosion process and underlying mechanism will help for development of assessment tools, which will ensure confidence and predictability of the long-term performance of containers under relevant conditions. The main goal of Concord is to optimize and evaluate the behavior of materials for disposal containers in view of their long-term barrier performance.

In the Concord project, a focus was laid on transient conditions (e.g., chemical, redox) of the early repository post closure phase. Those conditions are incorporated in the experimental part of this thesis either by using different concentrations of sulfide for investigations with Cu-Ni alloy coupons, or hematite powder for SGI coupon materials. For Cu-Ni alloy, in order to study the effect of bacterial activity some experiments involve investigations about the effect of sulfide on the corrosion behavior of cupronickel alloy. The development of bacterial activity may result in the formation of sulfide, which may initially increase with time as bacterial population grows and till sufficient substrates (sulfate) are available for sulfide production. However, over time depletion of available sulfate or other necessary nutrients, change in environmental conditions (may be pH) can lead to stabilization which could be expected in the long-term evolution of the repository. However, the amount of sulfide concentration reduces or limited at container surface due to diffusive layer of bentonite because of its extremely small pore sizes. Also, the bentonite buffer immediately surrounding the canisters maybe depleted microbially because of high levels

of radiation and desiccation. In this project, we have considered a sulfide concentration that is relevant to disposal sites **(Cloet et al., 2017)**. Here focus was to investigate on the effect of stepwise increasing sulfide content to compare with bacterial population growth with time (dynamic condition) and its effect on the corrosion behavior (e.g., corrosion products) compared to constant sulfide content (static condition) in the ground water. During the operation of the repository, canisters will experience a phase of oxic corrosion, resulting in the formation of ferric compounds at the surface in contact with bentonite. Here experiments were dedicated to investigate about the effect of the presence of ferric compounds (e.g., hematite), formed during the oxic phase, on the corrosion behavior of SGI. After repository closure, once all the residual oxygen has been consumed and steel corrosion started, ferric compounds present at the interface between steel and bentonite will be transformed and possibly affect the steel corrosion behavior due to change in chemical conditions (increased iron concentration) and further added hematite will be transformed into stable corrosion products (e.g., magnetite) which will act as protective layer. Information about the effect of the transient presence of such compounds e.g., in terms of nature of corrosion products will be provided by performing experiments in the presence and in the absence of such ferric corrosion product. Knowledge of corrosion products is of interest since it may alter chemical environment (pH, redox conditions and ionic compositions) around the canister. They may form stable protective layer and lower the corrosion rate of canister materials, also it can play a role for radionuclide retention in the near field. Thus, it has direct impact on safety and longevity of the repository for nuclear waste disposal.

The project Imkorb (Implementation of monitoring system to evaluate the corrosion processes on container materials in bentonite-based repository concepts) funded by the German Federal Ministry of Economic Affairs and Climate Action (BMWK), the German Federal Ministry for the Environment, Nature Conservation, Nuclear Safety and Consumer Protection (BMUV) focuses on obtaining detailed knowledge about corrosion processes affecting the mechanical and chemical stability of metallic canisters containing nuclear waste, which is important input for the Safety Case. The goal of this project is to significantly improve the understanding of metallic corrosion under conditions representative of clay-based disposal sites for heat generating waste. Partners involved in this project are Karlsruhe Institute of Technology (KIT), Gesellschaft für Anlagen und Reaktorsicherheit GmbH (GRS), Leibniz University Hannover, and the Federal Institute for Geosciences and Natural Resources (BGR). The ultimate goal is to quantify and evaluate the degradation processes based on a reliable description of the underlying corrosion mechanism.

In the Imkorb project the focus is on two iron-based candidate canister materials i.e., a spring steel having high tensile strength, resilience property, and a low-alloyed construction steel widely used in structural applications. Both materials are procured in similar dimensions and difference in (Si content) composition for a fair comparison as candidate materials for canisters. During operation of repository and handling of canisters, it might be possible that some scratches occur on the surface of canisters, which can change its surface roughness and have an effect on corrosion behavior of canisters. So, information about effect of change in surface roughness on

corrosion behavior of iron-based canister materials can be drawn by performing experiments with scratched and unscratched (polished) spring steel and construction steel coupons. This experimental approach will give valuable insights into how surface roughness, caused by scratches, affects the corrosion behavior of iron-based canister materials. The data will help assess the long-term durability and safety of canisters in real-world repository conditions and could guide the development of better handling protocols or surface treatments to minimize corrosion risks.

Iron based materials such as SGI and CS could be used in Pollux containers for nuclear waste in Germany (BGE Germany). The Pollux container system was developed by the Gesellschaft für Nuklear Service GmbH (GNS) for direct permanent storage of high-level radioactive waste in a deep geological repository in rock salt **(Bracke & Fischer-Appelt, 2015; Einfeld & Popp, 1988)**. However, it is not yet certain whether this cask will one day be used in this manner. This container for high-level radioactive waste, which consists of heat conducting material to dissipate generated heat due to radioactivity, can withstand lithostatic pressure as well as pressure, which potentially will build up over long period due to gas (hydrogen) evolution. These containers are made of GGG 40 nodular cast iron, which has similar ductility properties to that of carbon steel. Cu-Ni alloy material was selected as candidate material here to compare its corrosion behavior w.r.t pure Cu material in the presence of bentonite. Steel containers were used for coquilles in which the vitrified glass is delivered from reprocessing plant. Spring steel is also iron based candidate material selected here because it has comparable composition though it has high silicon content w.r.t carbon steel and to observe the effect of silicon content on corrosion behavior in presence of bentonite.

Container corrosion is a relevant process during storage and disposal of nuclear waste depending upon type of host rock in deep geological repositories. Various types of corrosion mechanisms can affect the integrity of waste containers. The materials used for nuclear waste containers must be carefully selected to fulfill their respective safety function in deep geological repositories, which varies for different repository concepts. Notably in disposal concepts in crystalline rock, the container in combination with geotechnical barriers is responsible for the containment of the radioactive waste over long time scales. Respective containers require corrosion resistant materials. In other host rocks, the container has to fulfill only a temporal protective function (e.g. in clay rock for about 10,000 years). In those concepts such type of materials is required which show a slow, uniform and thus reliably predictable corrosion behavior. Local pitting and crevice corrosion processes need to be avoided.

Geochemical conditions, temperature and varying levels of radiation have an impact on corrosion. Several studies emphasize the need to thoroughly understand the corrosion mechanisms that occur under these conditions. Factors such as galvanic corrosion between different materials, electrochemical interactions, and material degradation processes play key roles in determining the long-term performance of waste containment systems **(Mani Mathew & Krueger, 1989; Padovani et al., 2017; Shoesmith et al., 1997)**.

To ensure the safety of these systems, materials must exhibit high corrosion resistance, particularly against localized corrosion mechanisms like pitting and crevice corrosion, which may play a role in deep geological environments. **(Shoesmith et al., 1997)** applied electrochemical models to investigate the dissolution of nuclear fuel and the corrosion of container materials. Their work emphasized the importance of electrochemical stability in assessing the long-term safety of nuclear waste containers which may be play a role only when a container is placed in crystalline rock. In another study, **(Smailos & Kienzler, 2005)** investigated the potential effect of galvanic corrosion between copper-nickel alloys and carbon steel in salt brines, focusing on localized corrosion attacks. Galvanic corrosion will always play a role when using a corrosion resistant material, e.g. Cu as an outer shell and an iron-based pressure resistant material as an inner container material.

The environmental conditions in deep geological repositories, including groundwater composition and the presence of corrosive ions, significantly influence corrosion behavior. For instance, **(Nakayama et al., 1992)** studied how chloride, bromide, and thiosulfate ions affect crevice corrosion in stainless steel alloys used for disposal packages. These ions can create conditions that accelerate corrosion processes, particularly in confined spaces like crevices. **(Dunn et al., 2005)** focused on the corrosion resistance and mechanical properties of alloy 22, a Ni-based material used in waste disposal containers. Their work demonstrated how the material's fabrication process influences its corrosion resistance. Similarly, **(Hua et al., 2005)** in the U.S. High-Level Nuclear Waste Repository Study highlighted how groundwater composition drives the degradation of materials over time. The role of ions like HCO_3^- and SO_4^{2-} in pitting corrosion was explored by **(Zhang-Gang et al., 2012)**, showing the crucial impact of environmental chemistry on the longevity of containment materials. Different materials exhibit distinct corrosion behaviors under repository conditions. For example, **(Huttunen-Saarivirta et al., 2016)** conducted an electrochemical study on copper, commonly used in nuclear waste canisters for disposal concepts in crystalline rock, to assess its corrosion behavior in anoxic groundwater environments, with attention to both biotic and abiotic conditions. Their study revealed how copper reacts in oxygen-depleted environments, a condition typical in deep repositories. Research has offered valuable insights into the design and selection of materials for high-level nuclear waste canisters for nuclear waste disposal considering long-term repository safety. **(Cabrera et al., 2024)** used reactive transport models to predict the corrosion behavior of candidate canister materials in presence of bentonite, clay often used as a buffer material in repository designs. This research helps forecast long-term corrosion behavior, which is essential for repository design. Recent studies have used advanced techniques to deepen the understanding of corrosion processes in nuclear waste environments. **(Yun et al., 2024**) studied the corrosion of oxygen-free copper canisters in groundwater, identifying corrosion byproducts like copper chloride hydroxide and calcite. These byproducts provide a clearer picture of how copper react in repository conditions, contributing to the understanding of long-term corrosion in copper materials.

Iron-claystone interactions under hydrothermal conditions (90°C) by monitoring in situ pH and H_2 generation was carried out in literature **(Bourdelle et al., 2017)**. The study investigates the evolution of the Fe^0-CO_x system in a waste repository, focusing on how the Fe^0/claystone ratio and pH influence phase formation and iron corrosion. Two systems were considered: one near the steel container, where high pH and a high Fe^0/claystone ratio lead to the formation of magnetite and serpentine minerals; and another near unaltered claystone, where low pH and a low

Fe^0/claystone ratio result in poorly crystallized Fe-enriched phases (but not only ferrous). The experimental results, under abiotic conditions, show that hydrogen gas production, used to track the iron corrosion rate, reveals a competition between iron corrosion and claystone alteration. The rate of corrosion depends on the amount of claystone available to interact with the iron, with more claystone potentially slowing the corrosion process **(Bourdelle et al., 2017)**.

Corrosion in nuclear waste disposal is a complex issue influenced by material selection, environmental factors, and biological activity. Research has highlighted the importance of understanding electrochemical corrosion, environmental effects, and specific material behaviors to ensure long-term repository safety. By integrating these insights, researchers are developing strategies to mitigate corrosion and enhance the effectiveness of nuclear waste containment systems, ensuring that they remain robust over thousands of years.

1.3.1.1 Types of Corrosion

In nuclear waste disposal, various types of corrosion processes can affect the containment materials, each with distinct characteristics and implications. Different types of corrosion listed here are related to nuclear waste disposal but are not equally relevant for all host rocks (salt, clay or granite).

Uniform corrosion:

The most common form of corrosion is general or uniform corrosion **(Féron et al., 2008)**. In repository under long-term anoxic conditions, steel corrosion in bentonite is expected to occur as uniform **(Smart et al., 2003)**. As the name implies, uniform corrosion occurs across a broad front on the surface of the metal and the metal loss occurs at approximately the same rate over the whole surface, leading to a general thinning of the metal surface, possibly with some roughening due to statistical variation in the local rate of corrosion. Metals sometimes corrode uniformly throughout the surface in contact with a source of electron acceptors. Uniform corrosion in nuclear waste disposal occurs not only due to trapped oxygen or residual oxygen but also due to water reduction (iron and steel). Uniform corrosion rates can decrease in case a protective corrosion layer form. Uniform corrosion is a positive property of container material in a repository because it leads to a consistent, predictable degradation across the entire surface **(King et al., 2024)**. This helps ensure the material maintains structural integrity over time, preventing failure due to localized corrosion.

Pitting Corrosion

Pitting corrosion is relevant to nuclear waste disposal and its damage was studied **(Henshall, 1992)** using stochastic approach. In pitting corrosion small hemispherical depressions, or ‘pits’ develop in the surface of the metal, due to the formation of occluded cells under a covering of corrosion product, which allows the generation of acidic conditions by hydrolysis reactions and due to restrictions on the mass transport by electro-migration and diffusion of species into and out of the occluded cell. A necessary condition for pitting is that electric charge can be transported

not only in the metal but also in the corrosive medium. Stainless steel is relatively prone to pitting corrosion, as the passivation layer is very dense and stable. Pitting corrosion is not so much an issue for carbon steel, as the forming corrosion layer is usually porous and thus, does not favor the formation of pitting hole. A corrosion allowance of 10 mm has been estimated for pitting corrosion in the Swiss disposal concept **(Johnson & King, 2003)**.

Crevice corrosion

Crevice corrosion is also likely to happen in nuclear waste disposal. Enhanced crevice corrosion of stainless steel 316 as candidate canister material was studied for nuclear waste disposal **(Guo et al., 2022)**. Crevice corrosion occurs in regions where there is close contact between two metal surfaces e.g., in welding seams, which results in restricted mass transport into and out of the thin liquid film within the crevice. This can result in the formation of a liquid phase whose conditions are conducive to rapid rates of corrosion, for example by the development of a low pH, high Cl environment compared to the external bulk environment, in a similar manner to that experienced inside a pit. This form of corrosion needs to be considered in relation to the design of radioactive waste container materials particularly steel and alloys **(Guo et al., 2020; King, 2013)**. In the corrosive environment of disposal site (repository) crevice corrosion can occur in confined spaces where stagnant water or brine creates an oxygen-deprived environment. Its relevance lies in the risk it poses to the long term safety of nuclear waste isolation in geological repositories. Crevice corrosion behavior of Alloy 22 and Titanium grade 7 candidate materials in repository environment have been studied by few researchers **(Hua et al., 2001)**. Under bentonite porewater conditions, bicarbonate will promote passivation, whereas chloride will promote passive film breakdown. The fact that the re-passivation potential is close to the passivation potential suggests that crevice and pitting corrosion might occur during partially saturated phase.

Galvanic corrosion

Galvanic corrosion is relevant to nuclear waste disposal when using two dissimilar metals or alloys together. Galvanic corrosion for copper-nickel alloys and carbon steel in salt brines for nuclear waste disposal was studied **(Smailos & Kienzler, 2005)**. Galvanic corrosion occurs when metals with two different compositions are in electrical contact, within a conducting electrolyte medium. Where there is a difference in the equilibrium electrochemical potential of the two metals the metal which has the most negative electrochemical potential in the couple becomes the cathode and the other metal becomes the anode and it experiences an increase in the rate of corrosion due to the galvanic coupling. Studies have shown that galvanic corrosion, which occurs when different materials are in contact in a corrosive environment, is a concern in nuclear waste disposal. For example if copper shell is breached and ground water comes in contact with the cast iron insert, as a result galvanic corrosion may take place and this kind of research was investigated by **("Smart et al., 2004)**. In oxygen free water, the corrosion rate of cast iron galvanically coupled to copper were in the same range as those measured for cast iron in the absence of galvanic coupling to copper **("Smart et al., 2004)**.

Microbial Induced Corrosion

Microbial activity can be another significant factor influencing corrosion in nuclear waste disposal environments. Microbial corrosion, particularly hydrogen-induced corrosion, can occur in the early stages of disposal. Research by **(Zhang et al., 2023**) has shown that microorganisms can induce embrittlement, weakening the canisters over time. This highlights the need for further studies on the role of biological factors in corrosion, as they can significantly affect material integrity. The highly compacted bentonite buffer in a geological waste repository is expected to play an important role in precluding microbial activity due to its high swelling pressure and low water activity **(Pedersen et al., 2000; Stroes-Gascoyne, 2010)**. Hence bentonite at target dry density is of relevance and should be selected based on physical, chemical and biological (relevant) conditions.

From above information and details, it can be seen that a wide range of corrosion phenomena can occur, and it is clearly important to investigate and evaluate these various degradation mechanisms in relation to waste container materials and metals in waste, under all the possible environmental conditions that may arise during radioactive waste management. Some of these conditions are common to many industrial applications, and are not specific to the nuclear industry, but others are unique to the nuclear industry, particularly those that will be encountered in the long-term underground exposure in specially designed disposal facilities. The other main factor that distinguishes the problem of corrosion assessment of radioactive waste management facilities from conventional industrial problems is the much longer time scales under consideration and the need to be able to extrapolate results from relatively short-term experiments to cover periods of thousands or even millions of years. One approach to address this issue is the use of reactive transport models, such as the one developed for bentonites in COMSOL Multi-physics, to understand and predict corrosion behavior **(Cabrera et al., 2024)**. Other approach that can be followed to support such extrapolations is to consider how man-made and industrial analogues (e.g., ancient and more modern archaeological artifacts) have corroded over periods of many centuries' exposure to natural environments, together with assessment of geological deposits (e.g., native copper), which have been buried at depth for millions of years. Thus, Predictive modeling **(Briggs et al., 2021; Kiczka et al., 2024)** is a scientific approach to get information about corrosion behavior of materials and geological evolution for millions of years.

1.3.1.2 Corrosion Mechanism

Corrosion is an electrochemical reaction occurring between metals and its surrounding environment which leads to gradual deterioration of materials usually metals. In the presence of water, this process involves the establishment of equilibrium between the anodic oxidation of the metal, where it transitions from its elemental state (oxidation state zero) to a higher oxidation state, releasing electrons in the process, and a corresponding cathodic reaction, which consumes these electrons. In the presence of oxygen, typically sourced from the atmosphere, the cathodic reaction involves the reduction of oxygen. However, in environments lacking oxygen (anoxic conditions), the most common cathodic reaction for iron-based materials (iron and steel) is the

reduction of water to produce hydrogen gas. The overall outcome of these electrochemical reactions is the loss of metal from the surface, either in a uniform manner across the surface or at localized spots, leading to deterioration in the mechanical properties of the affected structure. The general corrosion process of carbon steel in clay environment was shown below in ***Figure1***.

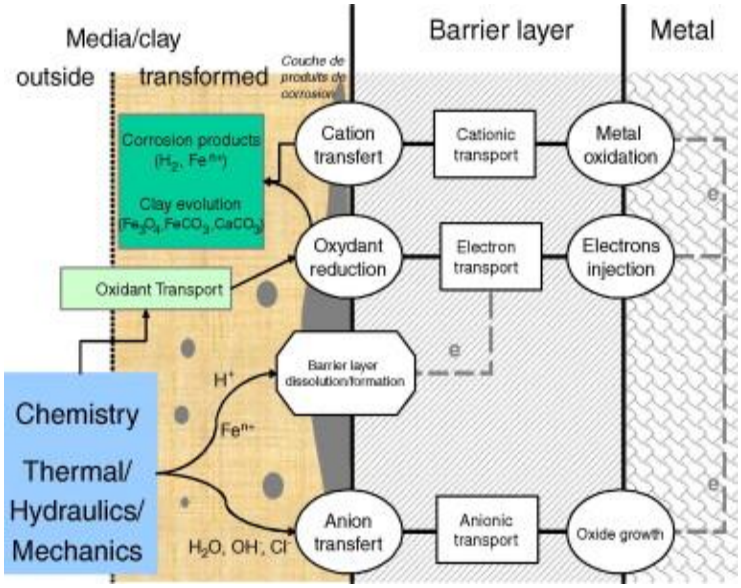

Figure 1 *General corrosion process of carbon steel in clay environment* ***(Féron et al., 2008).***

Corrosion mechanism of iron based materials

For iron, the following reactions are assumed to occur under oxygenated conditions:

- $4Fe + 6H_2O + 3O_2 \rightarrow 4Fe(OH)_3$ ……... (1)
- $4Fe + 3O_2 \rightarrow 2Fe_2O_3$ ……..... (2)

In anaerobic conditions, corrosion is believed to proceed through these reactions:

Water reduction and iron corrosion

- $Fe\ (0) \rightarrow Fe^{2+} + 2\ e^-$.....(iron oxidation) .....(3)
- $2\ H_2O + 2\ e^- \rightarrow H_2 + 2\ OH^-$ .....(water reduction) .....(4)
- $Fe^0 + 2H_2O \rightarrow Fe^{2+} + 2OH^- + H_2$……..(5)

This reaction represents the corrosion of metallic iron (Fe) in an aqueous, anoxic environment. In the absence of oxygen, water reduction is the primary mechanism for corrosion **(Smart et al., 2002a)**. Iron metal (Fe^0) reacts with water (H_2O) and electrons are transferred, leading to the formation of ferrous ions (Fe^{2+}) and hydroxide ions (OH^-). The reduction of water produces

hydrogen gas (H_2). The formation of Fe^{2+} indicates the initial stage of corrosion where iron is oxidized from a zero oxidation state to +2. The hydroxide ions (OH^-) formed in this reaction contribute to an increase in the pH around the iron surface, which can further influence the precipitation of corrosion products like iron hydroxides. In an anoxic environment, oxygen is absent, so the corrosion process shifts from typical oxygen-driven corrosion to water reduction process that occurs in case of anoxic conditions **(Kiczka et al., 2024)**. In such environments, hydrogen gas formation becomes prominent, and the corrosion rate may differ from that seen in the presence of oxygen.

Under anoxic and specific chemical conditions (dissolved species in solution), where oxygen is not available to further oxidize iron, the formation of magnetite is favored **(Smart et al., 2002b)**. This reaction is a key process in the formation of stable iron oxide phases under reducing conditions. The oxidation from Fe^{2+} (ferrous) to Fe^{3+} (ferric) is central to magnetite formation, and this transition helps stabilize the corrosion products. Ferrous hydroxide can be transformed to Fe_3O_4 (**Schikorr reaction**).

- $Fe + 2H_2O \rightarrow Fe(OH)_2 + H_2$ ……...(6)
- $3\ Fe(OH)_2 \rightarrow Fe_3O_4 + 2H_2O + H_2$……..(7)
- $3Fe + 4H_2O \rightarrow Fe_3O_4 + 4H_2$ ……....(8)

Ferrous hydroxide ($Fe(OH)_2$) forms as a primary corrosion product when iron is exposed to water under neutral pH or slightly alkaline conditions. Under anoxic conditions, $Fe(OH)_2$ can undergo a transformation to magnetite (Fe_3O_4), a mixed-valence iron oxide. The transformation involves the oxidation of Fe^{2+} to Fe^{3+} within the iron hydroxide matrix, leading to the formation of Fe_3O_4, which is a common corrosion product in anaerobic conditions. Additionally, hydrogen gas (H_2) is produced, a characteristic of the Schikorr reaction.

Bentonite alteration

$(Fe^{3+})_{clay} + Fe^{2+}{}_{aq} \rightarrow (Fe^{2+})_{clay} + Fe^{3+}{}_{sorbed}$…….(9)

Bentonite is an assemblage of various mineral phases and mostly made of montmorillonite, whereas amounts of iron, present in it usually in the form of octahedral Fe^{3+}. During corrosion, Fe^{2+} ions formed from the corrosion of metallic iron can interact with Fe^{3+} ions present in the bentonite clay **(Morelová et al., 2021)**. In this reaction, dissolved Fe^{2+} present in aqueous phase sorbs to clay mineral and exchanges an electron with octahedral Fe^{3+} ions that were originally present in the clay structure, leading to an exchange of electrons between the clay matrix and surface sorbed Fe(II) **(Ishidera et al., 2008)**. In anoxic conditions, Fe^{2+} is stable in the aqueous phase, and the clay acts as a sink for these ferrous ions. The sorption of Fe^{2+} ions onto the clay could potentially accelerate steel corrosion to some extent under certain conditions by removing Fe^{2+} ions from the solution and inducing some kind of a "pump effect" **(Savage et al., 2010)**. However, the reduced form of iron (Fe^{2+}) could still participate in secondary reactions such as the formation of green rust.

Green rust formation (sulfate based)

Green rust (GR) is a mixed-valence iron hydroxide, which typically forms under anoxic or reducing conditions **(Wang et al., 2023)**. Its structure is made of brucite like layers in which octahedral sites are filled by Fe^{2+} and Fe^{3+} ions, and the excess layer charge is balanced by anionic species (e.g., sulfate ions (SO_4^{2-})) located in the interlayer. In the present study, chloride and sulfate anions are present in the groundwater (or bentonite slurry). Green rust can precipitate from solution containing both Fe(II) and Fe(III) according to:

$$4Fe^{2+} + 2Fe^{3+} + 12OH^- + SO_4^{2-} \rightarrow [Fe_4^{2+}\ Fe_2^{3+}(OH^-)_{12}]^{2+}\ (SO_4)^{2-} \quad \text{.....(10)}$$

However, in the present study (pH ~8) the amount of dissolved Fe(III) available for this reaction is very limited, suggesting that this phase may form via another mechanism. **(Jones et al., 2017)** reported the formation of GR compounds upon interaction of Fe(II) with smectites at pH ~8. Under anoxic conditions, green rust formation is promoted in reducing environment, where Fe^{2+} is prevalent. GR compounds can serve as an intermediate corrosion product that may later transform into more stable phase (may be magnetite and iron sulfide).

Mechanism of iron silicate formation (Berthierine)

$$4Fe^{2+} + 4Si(OH)_4 + 2H_2O + x(Al^{3+},Mg^{2+}) + e^- \rightarrow 2(Fe^{2+},Fe^{3+},Al,Mg)_3Si_2O_5(OH)_4 + 12H^+ \quad \text{.....(11)}$$

In the presence of bentonite clay which has cations such as Al^{3+} and Mg^{2+}, Fe^{2+} ions from corrosion (due to dissolution) can react to form iron silicate minerals, such as berthierine. This iron-rich silicate mineral forms in anoxic conditions, particularly where the local pH is high **(Francisco et al., 2020)** (due to the presence of hydroxide ions). Berthierine is a silicate mineral belonging to the serpentine group **(Bailey, 1988; Brindley, 1982)** and is a mixed mineral containing iron and aluminum or magnesium, and it forms through a process where iron ions bind with silicate structures, producing a stable corrosion product. Under anoxic conditions, berthierine formation was typically seen in environments where both anoxic conditions and abundant silicate material are present. The formation of such corrosion products could contribute to the long-term stability of the corrosion process by protecting canister within silicate matrices.

In anoxic conditions, corrosion of iron-based materials occurs through a series of electrochemical reactions, predominantly driven by water reduction and results in formation of various corrosion products. These products include ferrous hydroxides, magnetite, green rust, and iron silicates, depending on the specific environmental conditions. The presence of bentonite, which contains clays and other minerals, facilitates the alteration of iron present in bentonite because of steel corrosion caused by water presence and results in the formation of mixed-oxide minerals and silicates **(Hofstetter et al., 2014)**. These corrosion processes are influenced by factors such as pH, ion concentration (e.g., sulfate, silicate), and the presence of reducing agents (hydrogen, ferrous ions and sulfides), making anoxic corrosion a complex interaction of electrochemical and mineralogical transformations.

Oxic corrosion of copper in water and chloride solutions

The corrosion of Cu in saline (Cl^-) solutions is known to be accelerated in aerated solution and have following general reactions

$Cu + xCl^- \rightarrow CuCl_X^{(1-x)-} + e^-$ (Anodic reaction) ……..(12)

$O_2 + 2H_2O + 4e^- \rightarrow 4OH^-$ (Cathodic reaction)…….....(13)

In absence of significant amounts of Cl^- the anodic reaction proceeds via a $(CuOH)_{ads}$ leads to form the stable corrosion product, Cu_2O **(Keech et al., 2021)**.

During initial stages of film formation involve competition between Cl^- and OH^- for exposed surface and Cu_2O formed.

$CuCl_{ads} + OH^- \rightarrow (CuOH)_{ads} + Cl^-$ …….....(14)

$2(CuOH)_{ads} \rightarrow Cu_2O + H_2O$ ..…….....(15)

The extent of Cu_2O formation will depend on the relative Cl^- and OH^- concentrations with higher pH favoring its formation.

According to the literature **(King et al., 2001)** islands of CuCl are formed in a surface film of Cu_2O. (Cu_2O is the main product at the presence of relatively low oxidant (oxygen) concentration as shown in Pourbaix diagram (**Figure 3**)).

$2CuCl_X^{(1-x)-} + 2OH^- \rightarrow Cu_2O + H_2O + 2xCl^-$ …….(16)

Anoxic corrosion of copper in presence of sulfide

Here in sulfide environment under anoxic conditions copper forms a layer of Cu_2S **(Zhang et al., 2021)**, which may accelerate the anoxic corrosion of copper by the reduction of sulfur in hydrosulfide as shown below **(Kong et al., 2017)**.

$2Cu + SH^- + H_2O \rightarrow Cu_2S + OH^- + H_2$ …….....(17)

Long-term corrosion can be evaluated by measuring the amount of hydrogen gas produced. Corrosion rate based on weight loss method is alternative. In addition, it can be evaluated using modeling based on experimental results under similar relevant conditions.

1.3.1.3 Thermodynamic and kinetics of corrosion

The electrochemical properties of every metal differ, leading to distinct free energies involved in anodic reactions. As a result, each type of metal experiences different corrosion behaviors. Moreover, the corrosion of each metal forms distinct dissolved corrosion products, with its own unique set of physicochemical properties. A useful method for depicting the domains of stability of these corrosion products is the Pourbaix diagram, named after Marcel Pourbaix, who developed it in the 1950s and 60s **(Pourbaix, 1974)**. These diagrams are also known as redox potential-pH or pH-E_h diagrams. Pourbaix diagrams display the regions of thermodynamic stability for metals and oxidized metal species as a function of pH and electrochemical potential (E_h) for over 70 different metals.

They are derived from thermodynamic calculations based on fundamental thermodynamic properties, such as the free energy of formation, and electrochemical relationships like the Nernst equation, which provides the equilibrium electrode potential for any given electrochemical reaction. Pourbaix diagrams provide a guide for assessing the corrosion behavior by showing the conditions under which a metal will be thermodynamically stable in water over a wide range of pH values (corrosion does not occur) and the conditions under which corrosion will occur.

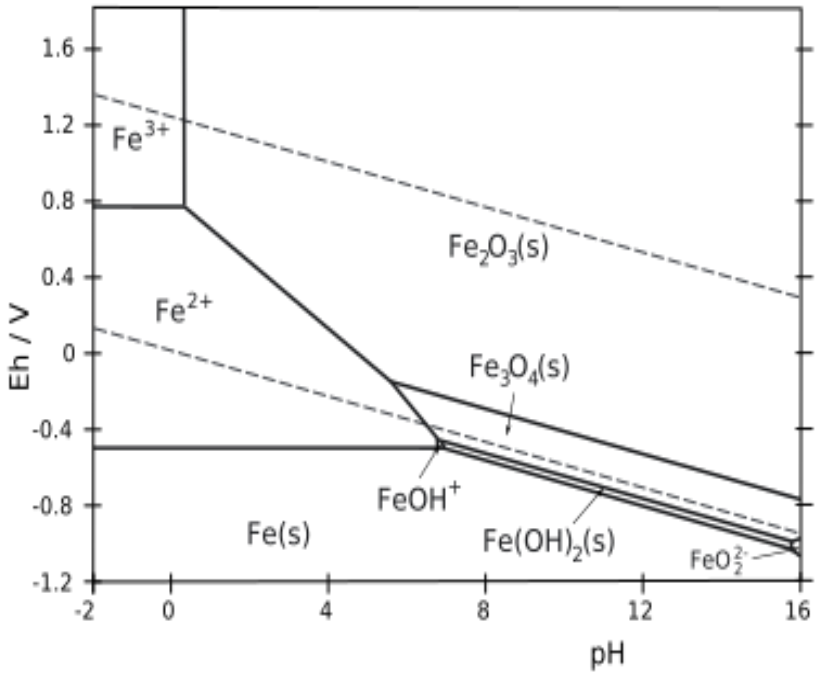

Figure 2 *Pourbaix diagram for iron at ionic concentration of 1.0 mM (oxygen presence not excluded). Lower dashed line in the above diagram is equilibrium line for H_2O/H_2, while upper dashed line is equilibrium line for H_2O/O_2 (CC BY-SA 3.0 Unported; Metallos via Wikipedia).*

However, Pourbaix diagrams have certain limitations. They only provide information on species, where data exist (not in case of many mixed corrosion phases). Another limitation is that only the thermodynamically most stable phases are considered.

However, metastable phases (e.g., less crystalline, amorphous phases) may play a role in the short term. Despite these limitations, Pourbaix diagrams are a useful starting point for assessing the potential corrosion behavior of a metal in an aqueous environment. In addition to the standard Pourbaix diagram for iron (***Figure 2***), other authors **(Drissi et al., 1995; King et al., 2010)** have developed similar thermodynamically based diagrams for specific environmental conditions, particularly relevant to the corrosion of metals in the context of geological disposal.

Pourbaix diagrams can also be used to study the dominant phases in more complex systems containing dissolved species such as carbonate, chloride, sulfate, and phosphate, which are similar to natural waters. For instance, **(Refait & Génin, 1993)** produced a Pourbaix diagram for iron in the presence of chloride, considering the green rust phases. Such phases are relatively unstable iron oxy-chloride, oxy-sulfate, or oxy-carbonate compounds with varying stoichiometries. Similarly, Pourbaix diagrams for copper at different chloride concentrations have been published **(King et al., 2010)**.

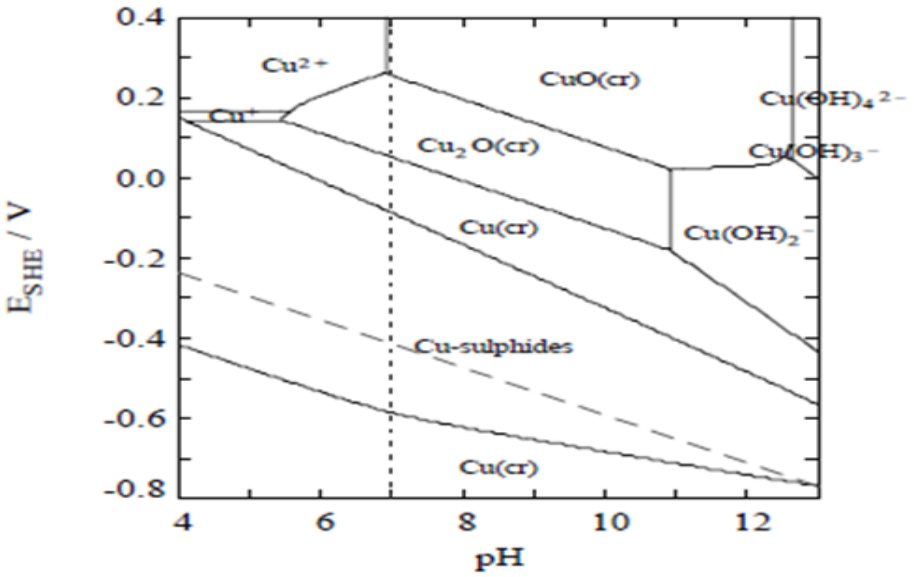

Figure 3 *Pourbaix diagram for copper at 25°C , [Cu]TOT = 1 µmol/kg* ***and*** *[HS−]TOT = 0.2 m mol/kg* ***(Puigdomenech & Taxén, 2000).***

The kinetics of the corrosion reactions or the overall corrosion rate is a key parameter in radioactive waste container materials, where long durability and specific lifetimes of canister material are crucial. The kinetics of corrosion depends on various factors such as the rates of the anodic and cathodic electrochemical reactions, properties of the corrosion product layer, changes in pH, the temperature of the system and radiation. The rates of the electrochemical reactions are described by fundamental electrochemical equations such as the Nernst equation, which defines the equilibrium electrochemical potential for any given redox reaction, and the Butler-Volmer equation, which defines the kinetics of any given electrochemical reaction **(Bard & Faulkner, 2012)**. The presence of a corrosion product layer will impede the progress of the electrochemical reactions occurring on the surface of the metal and thus reduce the overall corrosion rate. For some metals, such as stainless steel, the chromium-rich passive film forms very rapidly, within a

few seconds, due to reaction between the metal and oxygen, or with the water phase, whereas for carbon steel, the protective film develops over a much longer timescale, in which case the corrosion rate may continue to fall for many years after first exposure. This is of particular relevance in the case of radioactive waste container materials.

Most of the studies have focused on the corrosion behavior of materials such as copper and low carbon steel, with an emphasis on understanding the principles of chemical thermodynamics (stability of corrosion products) and kinetics **(Wei, Dong, & Ke, 2021)**. Research has shown that copper canisters is corrosion resistant under oxygen and sulfide free aqueous conditions. This is derived from existing thermodynamic data and supported by the observation that native copper can be found in certain locations in natural rock. Still, the actual corrosion behavior of Cu under different conditions is a topic of investigation **(Hedin et al., 2018; King et al., 2012)**. Computational models have been developed to study the interactions of corrosion products and materials like iron in specific geological environments, with a focus on thermodynamic and kinetic modeling **(Samper et al., 2008; Wersin et al., 1994)**.

1.3.2 Anaerobic copper corrosion in nuclear waste disposal

Copper based canister materials have been mainly preferred because of its excellent properties like corrosion resistance make it suitable for storage of nuclear waste for thousands of years **(King et al., 2010)**. It has a tendency to withstand both the geological environment and chemical environment (radiation induced damage) created by radioactive waste (presence of reactive radionuclides and their decay products), which is crucial for long-term storage of nuclear waste material. Its high thermal conductivity helps in dissipating the heat generated by the radioactive decay of radioactive waste materials thus preventing heating and ensuring the integrity of the canister. Copper based materials also have good mechanical strength which makes them strong and ductile metal providing strong integrity to the canister and ensuring it can withstand handling and potential geological stresses generated over a period **(King et al., 2013)**.

Copper based canister materials also provide effective shielding against radiation emitted by nuclear waste to some extent, enhancing the safety of the nuclear waste disposal. High-level radioactive nuclear waste expected to be disposed of in a deep geological repository. Its depth is about 500–1,000 m. This “multi-barrier system” is formed (Scandinavian disposal concept) as shown in (***Figure 4)***.

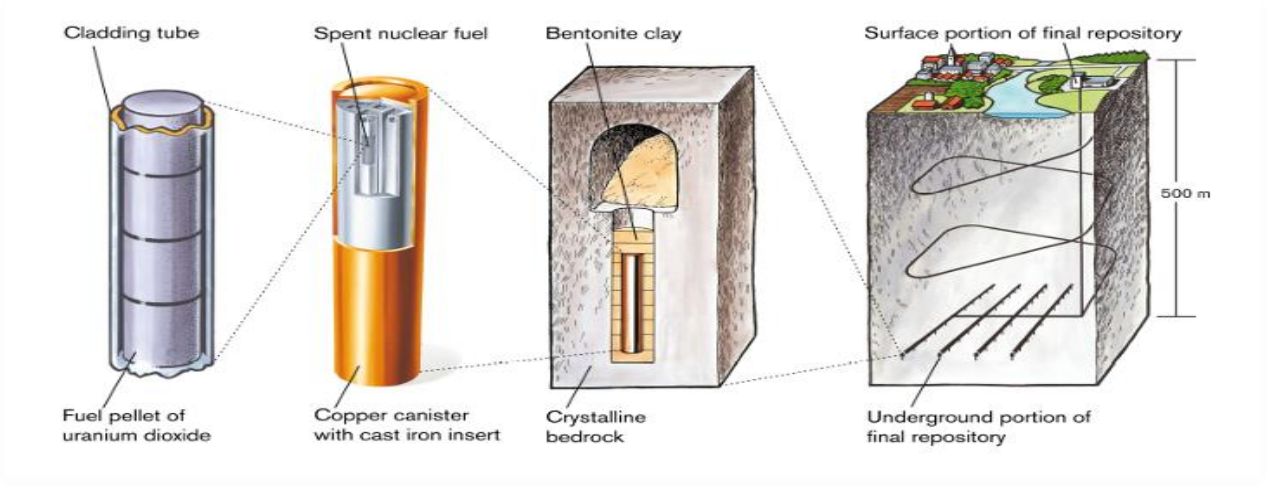

Figure 4 *Multi-barrier system of high-level nuclear waste illustrating in KBS-3 concept illustrator : Jan Rojmar* ***(Duquette et al., 2009).***

The nuclear waste container is the first barrier to ensure the sealing of solidified high-level nuclear waste, which is particularly important. Various factors affecting its service life and the selection of container materials should be considered. Finland, Sweden and Canada are proposing to use copper based canister materials for disposing of high level nuclear waste in a geological repository which is backfilled with compacted bentonite clay **(King et al., 2001)**.

1.3.2.1 Copper corrosion and evolution after deposition

The nature of the near-field environment will evolve with time and significantly influence the corrosion behavior of the containers. This evolution is the result of the repository excavation work on the geological host rock and the placement of heat-generating and radiation emitting nuclear waste. The repository environment gradually returns to its pre-excavation state as the heat dissipates, oxygen is consumed, and other redox processes take place **(King & Kolář, 2018)**. After being positioned, the container's outer surface temperature would be limited to a maximum value of 100^{o}C. When the canister cools down and the trapped atmospheric oxygen is used up, the repository atmosphere will change from being initially warm and aerobic to cool and anoxic. In terms of corrosion, the processes will change from rapid and possibly localized to slow and uniform corrosion. The consumption of trapped O_2 has been calculated to occur quite readily (10 to 100 of years) by reaction with the Cu container and microbes and minerals in the surrounding clay and backfill materials (**King et al., 2010)**.
King & Kolar divided the repository environment after final deposition into 6 periods from the initial oxic condition to the anaerobic state in long term, denoted from A to F (***Figure 5***) **(King & Kolář, 2018).** The prediction of time-dependent corrosion rate corresponding to the repository environment evolution was shown in the ***Figure 5***.

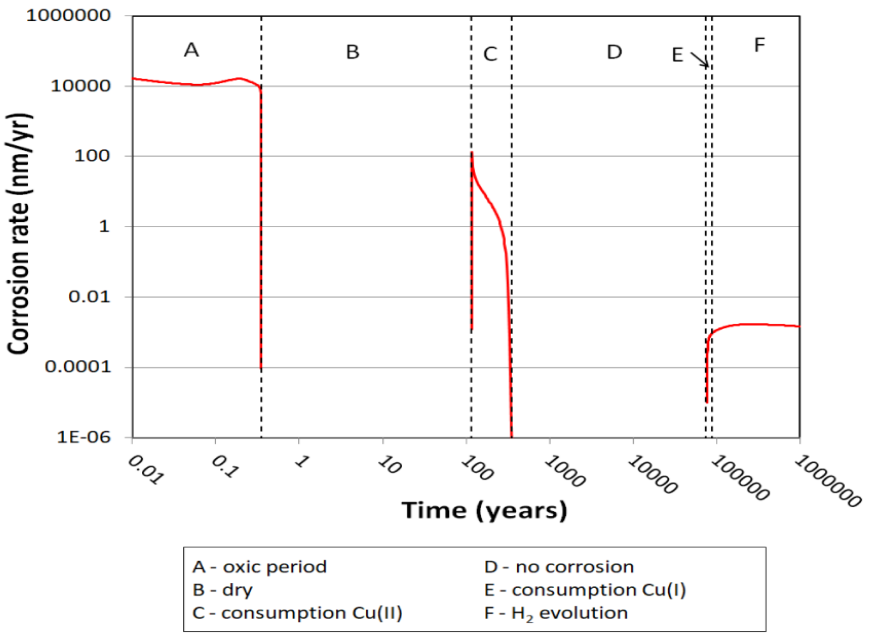

Figure 5 *Prediction of time-dependent corrosion rate corresponding to the repository environment evolution****(King & Kolář, 2018).***

The first period denoted as stage A is considered the most corrosive with highest corrosion rate of 10 μm/year recorded due to high temperatures and oxidizing conditions promoting moisture retention on the container surface, creating an environment conductive to corrosion. Cl^- and O_2 are the major contributors to copper corrosion at this stage **(King & Kolář, 2018)**. In contrast, during stage B, the temperature drops, and the environment (buffer) becomes drier, preventing moisture from accumulating on the container surface. As a result, corrosion slows down or ceases on the surface, but diffusion of species to other areas (apart of container surface) of the repository still continues. The cathodic reduction of oxygen has stopped by this point since all of the initial trapped oxygen has been consumed **(King & Kolář, 2018)**. **(Wersin et al., 1994)** estimated that anoxic conditions are established around a month after the backfill becomes saturated with water. Literature **(Lazo et al., 2011)** also concluded that the time to reach anoxic conditions would be short, especially if the calculations took into account the effects of microbial activities.

Once the container surface gets re-wet again (stage C), corrosion resumes with the dissolution of Cu supported by the cathodic reduction of Cu^{2+}, a period that lasts up to ~350 years. The initially trapped oxygen has been consumed by processes other than canister corrosion during stage B and it is the Cu^{2+} formed earlier by the homogeneous oxidation of Cu(I) by O_2 that acts as the oxidant. Redox conditions are still considered to be aerobic, as they remain relatively oxidizing and the corrosion potential is also relatively high during this period.

After the consumption of all Cu^{2+}, there follows stage D during which virtually no corrosion takes place. About 74000 years after closure, in the presence of sulfide, a chemical reaction transforms the previously precipitated Cu_2O into Cu_2S. Finally, copper oxide is oxidized to form copper sulfide in the presence of HS^- environment **(King & Kolář, 2018**).

The consumption of all initial oxidant results in the long cease of corrosion process (decrease corrosion rate), until HS^- reaches the canister surface at stage E and corrosion rate remains steady at 0.001 nm/year and continues during stage F **(King & Kolář, 2018)**. The initial inventory of O_2 trapped in the pores of the buffer and backfill materials limits the maximum depth of aerobic corrosion. After a million years, corrosion is expected to reach a maximum depth of 8 μm. Approximately 6.5 μm of total depth is attributable to initial aerobic corrosion, which is due to the cathodic reduction of O_2 and Cu^{2+}, however only 1.5 μm is on account of canister sulfidation **(King & Kolář, 2018)**. Whereas NWMO **(Binns et al., 2023)** considers a lifetime corrosion expectation of 270 μm and an extreme upper bound of corrosion of 1240 μm over one million years. So, different corrosion upper bounds will be considered based on type of canister material and surrounding environment.

Different studies have been done so far on the copper-based candidate canister materials under various environments which are suitable for nuclear waste disposal. Copper coated containers are currently primarily considered for granitic host rocks. For example, some countries plan to coat their canister with copper (e.g., Sweden) **(Shoesmith, 2006; Van Iseghem, 2012)**. *In situ* corrosion experiments yielded a Cu corrosion rate of 3 μm/a when exposed to bentonite, while high values between 30 to 50 μm/a have been reported for laboratory experiments when exposed to compacted bentonite/sand mixture saturated with synthetic groundwater during initial condition in repository in presence of residual oxygen **(Kursten et al., 2004)**. Much lower average corrosion rates were measured for the various types of copper ($0.13–0.32\ \mu m\ year^{-1}$) under anoxic conditions with low residual oxygen content **(Reddy, Padovani, Rance, et al., 2021)**. Variations in a range of 1 order of magnitude in corrosion rates of Cu are observed in in-situ experiments because of different experimental conditions like ground water composition, more residual oxygen content and transient conditions (presence of sulfide). Sulfide presence can also be considered as transient condition since it affects the corrosion behavior of copper based canister materials. Transient conditions refer to near field transitory environmental conditions which play an important role during early post-closure period and may affect container durability. These conditions do not remain constant over time but change due to varying temperature, radiation level, pore-water, chemical composition, redox conditions, mechanical stress, and process involving gas generation.

Corrosion rate of copper canister based on weight loss test were 5-8 μm/year in ground water and from less than one μm/year to 2 μm/year in bentonite clay pore water **(Aromaa, 2021)**. The concentration of dissolved oxygen and initial oxidized cupric species (oxidants) affects the corrosion rate. Dependence of the corrosion rate of copper in compacted clay on the salinity of ground water was studied by **(King et al., 2010)** who suggested that the corrosion rate decreases with increasing salinity which was based on Cu-transport rate-determining step. It refers to the rate at which copper ions are transported through the electrochemical interface between copper surface and bentonite (surrounding medium), often controlled by diffusion and migration process. This step governs the overall rate of copper dissolution in to the electrolyte (surrounding environment). Copper coupons obtained from Äspö Hard Rock Laboratory removed and examined, after ~1 yr. exposure, the surfaces of the coupons were found to be covered by a duplex $Cu_2O/Cu_2CO_3(OH)_2$ (malachite) corrosion products, with significant diffusion of copper into the surrounding bentonite.

The estimated corrosion rate was 3 µm/yr **(Karnland O & Motamedi M, 2000)**. These results are similar to those observed by King and co-workers **(King, 1995; King & Kolar, 1997)** in long-term laboratory tests of copper corrosion in compacted clay. Much lower corrosion rates were obtained for copper (0.13-0.32 µm/yr) after 394 days in presence of saturated bentonite from in-situ Grimsel Test Site experiment (MaCoTe) **(Reddy, Padovani, Rance, et al., 2021)**. Some copper oxides have been detected on the exposed surface and the bentonite surrounding copper coupons (interface) has very less discoloration. Copper corrosion has been studied in simulated ground water with and without bentonite clay and found that under aerated conditions an initially formed Cu_2S film is rapidly converted to a non-protective layer of cuprite **(Kosec et al., 2015)**.

There are various factors affecting long term corrosion behavior of copper based canister materials under repository conditions like ground water compositions, temperature, pressure, effect of Cu-iron galvanic couples, the surface discontinuity effect (defects arising due to fabrication practices or service damage), presence of gas, presence of residual oxygen and presence of micro-organisms on the corrosion of copper based canisters. The canister will be surrounded by bentonite based buffer material, which is further covered with natural rock barrier. Long-term corrosion is evaluated by measuring the amount of hydrogen gas produced and by assuming it is generated by corrosion. In addition, it can be evaluated using modeling based on experimental results under similar relevant conditions.

The study for Cu-Ni alloy is also relevant to this thesis, as it is one of the candidate materials chosen in this research due to its superior corrosion resistance compared to pure copper. Syrett investigated the corrosion rates and characterized the corrosion products on Cu-Ni alloys in sulfide-polluted seawaters. In this study **(Syrett, 1981)**, polarization resistance was monitored on a 90:10 Cu:Ni alloy as a function of time for various exposure conditions, and showed that deaerated, sulfide-polluted seawater did not cause accelerated corrosion of the Cu alloy. An increase in corrosion rate was observed only when the sulfide containing environment was replaced by aerated, sulfide free seawater. It was suggested that sulfide could precondition the alloy surface, thereby inhibiting the growth of a protective oxide film **(Syrett, 1981)**. Pre-exposure (up to 2 days) to deaerated sulfide polluted seawater was found to accelerate the corrosion of Cu alloys. Exposure to another 5 days in aerated, unpolluted seawater **(Drake et al., 2013)**, suggest the destabilization of Cu in the presence of sulfide. This shows the effect of sulfide containing water on corrosion behavior of CuNi alloy which may be used as reference for studying the corrosion behavior of cupronickel alloy in groundwater containing sulfide environment.

The growth of a thin Cu_2O film was observed when the alloy was pre-exposed to the sulfide-polluted seawater. XRD analyses also confirmed the growth of a thin Cu_2O film during the short-term experiments in deaerated sulfide solutions and the presence of both stoichiometric (Cu_2S) and non-stoichiometric copper sulfide ($Cu_{1.8}S$) at the outer layer of films after longer exposure durations. Syrett also proposed that the corrosion reaction was limited by the diffusion of protons to cathodic sites located at the Cu_2O/Cu_xS interface, and the thickening of the film was due to the migration of Cu^+ through the Cu_xS layer **(Syrett, 1981)**. The corrosion rate was observed to accelerate after the introduction of aerated solution. It was proposed that the reduction of oxygen occurred at a much faster rate than proton reduction, thereby accelerating the corrosion.

Corrosion of copper-based canister materials can be affected by different types of transient conditions such as change in temperature, redox potential, pressure, chemical environment and mechanical transients, which can change the integrity of the canister. It is necessary to design canisters to withstand such transient conditions to ensure the safety and containment of radioactive materials over the long term. There are limited studies on Cu corrosion under transient conditions reported in literature for long-term disposal of high-level nuclear waste in the repository.

(Smith et al., 2007) have reported electrochemical experiments on the effect of pre-oxidation on the surface attack of Cu by sulfides in 0.1 mol/L NaCl under anoxic conditions. Cu was pre-oxidized to mimic the formation of corrosion products during the warm oxic period. Depending on the extent of pre-oxidation, the surface was covered either with a thin film made of Cu_2O or Cu_2O covered by $CuO/Cu(OH)_2$ for longer reaction times. Samples were subsequently immersed in a sulfide-containing solution (30 $\mu molL^{-1}$) and the evolution of the corrosion potential (E_{corr}) was recorded. For all samples, E_{corr} stabilized at a value slightly more negative than observed in the absence of sulfide, then decreased to a value between -0.456V and -0.556V (SHE) before a sudden decrease to the equilibrium potential for the Cu/Cu_2S redox reaction. The time needed during the first decrease in E_{corr} increased with the extent of pre-oxidation and probably reflects the penetration of SH^- (the predominant species) to the Cu metal surface. The second drop was comparable for all samples and indicates that the redox conditions are dominated by the Cu/Cu_2S redox couple. Overall, outcomes pointed out a beneficial effect of Cu pre-oxidation, indicating that deposits could impede the reaction of Cu with aqueous sulfide.

More recently, **(Senior et al., 2019)** reported corrosion rates of copper in anoxic NaCl solutions at various temperatures by measuring the rate of hydrogen release. Copper exposed to 0.25 mol kg^{-1} NaCl at 30°C or 50°C produced negligible amounts of H_2 below the detection limit. At 75°C, the H_2 release was in agreement with a corrosion rate of about 10 nm yr^{-1}. When the temperature was returned to 50°C, the H_2 production immediately returned below the detection limit. Comparable findings were obtained for experiments performed in solutions containing up to 5 mol kg^{-1} NaCl. These results may suggest that the corrosion rate of copper in NaCl solutions up to 5 mol kg^{-1} is very low and decreases with temperature.

In this thesis, a focus was laid on transient conditions (e.g., chemical, redox) of the early repository post-closure phase. Those conditions are incorporated in the experimental part of the thesis by using different concentration of sulfide for investigations with Cu-Ni alloy coupons. Here, experiments involve investigations about the effect of production of sulfide (increase of sulfide content due to development of bacterial activity) on the corrosion behavior of cupronickel alloy. Initially sulfide content increases stepwise and later becomes constant which could be expected in the long-term-evolution of the repository excluding the reduction in amount of sulfide concentration at container surface due to diffusive layer of bentonite. In this work, we have considered sulfide concentration that is relevant to disposal sites **(Cloet et al., 2017)**. The aim here is the investigation about the stepwise increase of sulfide content in the groundwater on the corrosion behavior (e.g., corrosion products) compared to constant sulfide content in the ground water.

1.3.2.2 Effect of bentonite on copper corrosion

There were few studies **(Kong et al., 2023; Tully et al., 2020)** carried out to know the effect of bentonite on corrosion behavior of copper based canister materials under different experimental conditions. Studies were carried out for two different types of copper that is wrought copper and cold sprayed copper, which is considered as suitable candidate canister materials by few countries. Experiments were performed in contact with bentonite **(Tully et al., 2020**) and it was found that an increase in bentonite dry density resulted in a decrease in copper corrosion rates (due to high oxygen concentration), with the cold sprayed Cu corrosion rate being decreased more significantly than that of wrought Cu (wrought copper has higher amount of Cu_2O and lower amount of Cu_2S). Profilometry measurements of the surface, performed after removal of the corrosion products, showed a decrease in surface roughness on cold sprayed Cu as the dry density was increased, but the surface roughness of wrought Cu was not significantly affected.

One of the study (**Kong et al., 2023)** was carried out to understand change in d spacing of the montmorillonite due to interaction of cations from bentonite and canister materials, which can affect the corrosion resistance of copper-based canister materials. In the study, it was found that the increase in the d spacing of Ca and Na bentonite is caused by the replacement of Na ions with Ca ions in the interlayer, as well as changes in the hydration state of the first layer without ion exchange. It is mainly caused due to difference in size and hydration energy of Na^+ and $Ca2^+$ ions **(Liu et al., 2010**). The temperature had no significant effect during anaerobic conditions for number of years but if the concentration of dissolved Cu cations increases as the temperature increases, Cu cations will tend to exchange ions with interlayer cations; therefore, the interlayer spacing of bentonite will change, result in affecting the properties of the buffer material (bentonite alteration).The presence of either green Cu corrosion products or cuprite on the bentonite did not notably affect the pore water chemistry. At low corrosion, bentonite has tendency to suppress copper corrosion through anion-exclusion effect **(Ning, 2024)**. The anion-exclusion effect in bentonite prevents aggressive anions like chloride, from reaching the copper surface by repelling them. This reduces the formation of corrosion cells and minimizes the breakdown of protective oxide layers. As a result, copper corrosion is suppressed, preserving the metal's integrity. Bentonite hydrolysis has tendency to produce silicate ions which accelerates pitting corrosion by culminating in passive film breakdown in certain conditions (presence of phosphorous in Cu alloy may influence the acceleration of IGC following passivity breakdown) **(Macdonald & Lei, 2016; Ning, 2024)**.

1.3.3 Anaerobic iron corrosion in nuclear waste disposal

Iron based canister materials such as carbon steel, SGI and alloy steel have been considered as candidate materials due to their excellent properties like strength, ease of fabrication and economical. Iron-based alloys (carbon steel) are foreseen as the canister materials of choice in number of countries like France, Switzerland, Czech Republic, Belgium, Slovakia and Hungary **(Muñoz et al., 2024)**. There is wide range of experiments on the corrosion of carbon steel in various environments relevant to nuclear waste disposal **(Martin et al., 2008; Schlegel et al., 2016; Schlegel et al., 2021; Schlegel et al., 2018; Smart et al., 2001)**.

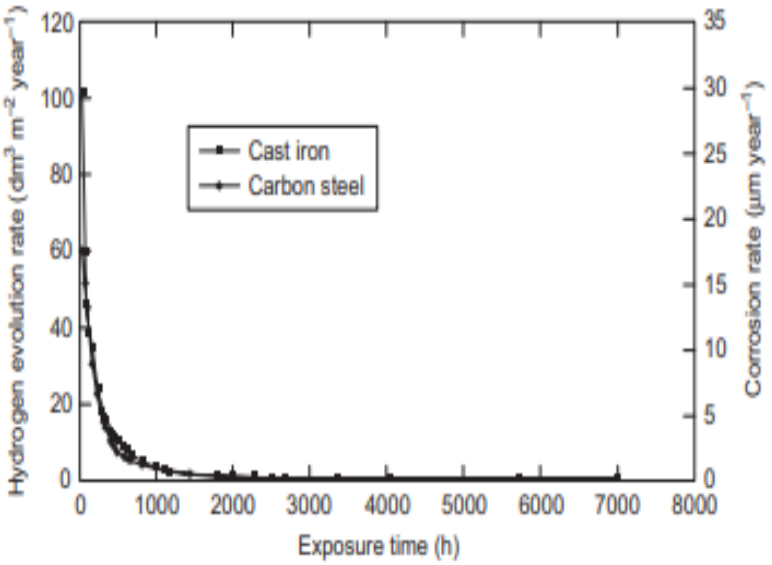

Figure 6 *Time dependence of the anaerobic corrosion rate of carbon steel and cast iron in a simulated ground water* ***(Smart et al., 2001).***

The corrosion of carbon steel in anoxic environments, such as those found in bentonite-backfilled geological repositories, is influenced by a range of factors, such as redox conditions, pH, temperature, and the composition of the surrounding aqueous phase. The presence of compacted bentonite plays a critical role in modulating the corrosion behavior by acting as a buffer and physical barrier. Bentonite's ability to control pH, ion concentrations, and redox conditions helps maintain the anoxic conditions necessary for uniform corrosion, while its low permeability limits the water access to the container and migration of corrosive species and ferrous ions.

Under anaerobic conditions, the corrosion rate decreases with time due to the buildup of a protective corrosion product film **(Smart et al., 2001)** , eventually attaining a steady-state rate that is a function of pH and of whether the test is done in bulk solution or in the presence of compacted bentonite **(Johnson & King, 2008)**. Steady-state corrosion rates of the order of a (few) 0.1-1 µm/year are expected in bentonite backfilled repositories. The corrosion rate of cast iron is similar to that of carbon steel as shown in (***Figure 6***) **(Smart et al., 2001)**. In cement or in

alkaline solutions simulating cement pore water, the steady-state corrosion rate of C-steel is <0.1 µm/year **(Smart et al., 2004)**. In bentonite-backfilled repositories, research suggests that carbon steel is not passive in moderately alkaline pore water. This implies that localized corrosion due to passive film breakdown should not occur. However, carbon steel will remain passive in cementitious environments as long as the cement pore water stays alkaline. As the cement degrades and the pore-water pH decreases, localized corrosion may become a concern, depending on the chloride concentration. In non-alkaline environments, localized attack manifests as surface roughening rather than discrete pitting.

Corrosion behavior of various materials under geological conditions of a disposal site in crystalline rock has been investigated by some researchers **(Hung et al., 2017; Kursten et al., 2004; Marsh et al., 1986)**. Among them low alloyed carbon steels have low corrosion rates ($\leq 2\ \mu m\ year^{-1}$), iron silicates and magnetite form as corrosion products. Weight loss measurements show that carbon steel had a relatively low average corrosion rate ($\sim 2\ \mu m\ year^{-1}$). Some people **(Kiczka et al., 2024)** put valuable efforts to model the behavior so that more sophisticated extrapolations made for the long-term, rather than relying on simple, empirical linear extrapolation. Effect of dissolved Si on the corrosion of iron in de-aerated and slightly solutions have been studied for approximately 30 days and found that iron corrosion led to the formation of layer consisting mixture of Fe oxides and Fe silicates on the metal surface **(Galai et al., 2023)**.

The anaerobic corrosion rate of carbon steel in clay systems is 1-2 µm/yr. The effect of temperature on corrosion rate for carbon steel was studied in literature **(Kursten et al., 2004)** indicating average corrosion rate of carbon steel in Boom clay formation of 1.81 µm/a at 16°C, while the rate reached 8.59 µm/a at 170°C. These studies also demonstrated the susceptibility of the carbon steel to pitting with pit depths of 100-200 µm after 5 years exposure period at 16°C. Spheroidal graphite iron corrosion under mildly saline conditions were studied by **(Hsu & Chen, 2010)**, confirming the presence of graphitic corrosion and the formation of $FeCl_2$.

Different types of corrosion products were formed depending on surrounding environmental conditions. Secondary Phases (corrosion products) such as magnetite, hematite, siderite, iron hydroxyl chloride and various silicate phases such as greenalite ($Fe_{2-3}Si_2O_5(OH)_4$), cronstedtite ($Fe_3(Si,Fe)O_5(OH)_4$) or berthierine ($(Fe,Al)_3(Si,Al)_2O_5(OH)_4$) formed due to presence of silicate (bentonite) and carbonate in the groundwater. A good summary of numerous experimental studies with various bentonite types was reported in literature **(Kaufhold et al., 2015)**.

1.3.3.1 Steel corrosion in bentonite environment

The corrosion of steel in the presence of bentonite, particularly in the context of geological disposal environments, has been the subject of numerous studies **(Stephan Kaufhold et al., 2020; Leupin et al., 2021; Reddy, Padovani, Rance, et al., 2021; Reddy, Padovani, Smart, et al., 2021)** aimed at understanding the long-term durability of steel canisters in underground repositories. A variety of research efforts have explored how bentonite interacts with steel, both to influence the corrosion processes and to potentially mitigate or accelerate corrosion under various environmental conditions.

The corrosion behavior of low-carbon steel in the presence of bentonite has also been investigated by literature **(Wei, Dong, Chen, et al., 2021)**. They studied the effects of bentonite content on corrosion evolution in simulated geological disposal environments and discovered that the presence of deteriorated bentonite sediments had a mitigating effect on the localized corrosion tendencies of steel. This finding highlights the potential for bentonite to reduce corrosion rates under certain conditions, which is critical for evaluating its effectiveness as a long-term corrosion barrier. Additionally some researcher **(Stoulil et al., 2021)** examined the localized corrosion of stainless steels in synthetic bentonite pore water and bentonite slurry, emphasizing the need to understand the complex corrosion mechanisms in different bentonite environments. Their research underscored the significance of pore water chemistry and the physical state of bentonite in influencing steel degradation processes. Reactive transport modeling has also played a key role in advancing understanding of steel-bentonite interactions, as demonstrated by researcher **(Chaparro et al., 2021)**. Their study used reactive transport models to simulate the long-term interaction between carbon steel and bentonite, offering insights into the diffusion processes and chemical reactions that drive corrosion over extended periods. This approach has proven valuable for predicting the behavior of steel canisters in geological disposal environments, providing a more comprehensive understanding of how corrosion evolves under both static and dynamic conditions.

Literature, **(Leupin et al., 2021)** further investigated the evolving interface between carbon steel and bentonite during anaerobic corrosion processes. Their research focused on the chemical changes and microstructural evolution at the steel-bentonite boundary, which is critical for understanding how corrosion processes are affected by the interface between steel and bentonite over time. This study adds to the body of knowledge regarding the dynamic nature of the corrosion process and the evolving role of bentonite as a buffer material. The mechanism of scaling of the calcite **(Zhu et al., 2019)** near corroding surfaces is not clear and this could be the subject of thermodynamic based modelling calculations; an initial consideration of calcite stability in bentonite containing corroding steel is described by **(Hunter, 2007)**. A recent study on samples of bentonite removed from other in situ corrosion experiments **(Kiczka et al., 2024)** (Febex) using a range of analytical techniques. It showed that although iron corrosion products were released into the bentonite, the change in bentonite properties was primarily due to precipitation of iron minerals/hydroxides, including magnetite and goethite, rather than any mineralogical changes to the clay.

In more recent research, **(Wersin et al., 2023)** conducted in situ microscopic and spectroscopic analyses on steel-bentonite interface samples, providing detailed insights into the corrosion processes occurring under real-world conditions. Their findings contribute to a deeper

understanding of how steel and bentonite interact in the complex environment of geological repositories. Similarly, **(Hesketh et al., 2023)** compared carbon steel corrosion rates in bentonite buffers under both in situ and ex situ exposure methods. Their results showed that the corrosion rate was not significantly affected by varying the density of compacted bentonite blocks, whereas granular bentonite led to a higher corrosion rate. This finding is important for optimizing the design of bentonite buffers in disposal environments, as it suggests that the physical form of bentonite can influence the extent of corrosion.

Together, these studies provide a comprehensive view of the corrosion behavior of steel in the presence of bentonite, highlighting the importance of environmental factors such as microbial activity, pore water chemistry, and the physical properties of bentonite. The research underscores the need for a detailed understanding of how bentonite behaves in contact with steel over time and how it can influence the long-term integrity of steel canisters in geological disposal environments. This knowledge is essential for improving the design and safety of nuclear waste disposal systems, ensuring that they remain secure for the thousands of years required to contain radioactive waste.

1.3.3.2 Bentonite alteration due to iron corrosion

All the experiments on the corrosion of carbon steel in bentonite have demonstrated that there is an interaction between the corroding carbon steel and the surrounding bentonite, with iron ions moving into the surrounding bentonite. The corrosion of carbon steel canisters in anoxic conditions in bentonite is a complex process that involves the formation of corrosion products, such as iron sulfides and silicates, which have both detrimental and beneficial impacts on the long-term performance of high-level radioactive waste repositories. While the corrosion of the canister may degrade its structural integrity, the iron corrosion products may act to enhance the barrier function of the bentonite by creating additional physical and chemical barriers to radionuclide migration. Furthermore, the migration of ferrous ions into the bentonite can lead to mineralogical changes that affect the ion-exchange capacity and swelling behavior of the clay, influencing the pore structure and thus the impact on ion diffusion. Understanding these interactions is crucial for the accurate prediction of the long-term safety of geological disposal systems for radioactive waste. Further research into the specific geochemical interactions between corrosion products and bentonite is needed to refine safety models.

Some studies focused on chemical interaction between carbon steel and bentonite at different experimental conditions. **(Wersin et al., 2021a)** explain interaction of iron with bentonite affect it's swelling and sealing properties due to redox reaction and alteration. Samples were analyzed by different analytical methods and it was found that corrosion induced an iron front of 5–20 mm into the bentonite, except for the high-Fe bentonite where no Fe increase was detected. The Fe fronts consisted mainly of ferric (oxyhydr) oxides in addition to the structural Fe in the smectite fraction, which had been partially reduced by the interaction process. Additional Fe (II) extended further into the clay, but its nature is still an open question for investigation. Here mostly the bentonite alteration is because of the reduction of structural iron. Such behavior can be explained

by redox evolution, which shifts from oxidizing to reducing conditions during exposure. Fe(II) sorption edges and isotherms have been measured on natural montmorillonites having low and high Fe content under anoxic and reducing conditions. Under anoxic conditions Fe(II) sorption on high structural Fe-content montmorillonites was significantly higher than on low structural Fe-content montmorillonites , whereas the sorption under reducing conditions was essentially the same **(Soltermann et al., 2014)**.

Early work from **(Alzamel et al., 2022)** showed chemical and micro structural changes of the materials can change important operational properties of the surrounding bentonite, such as hydraulic conductivity and swelling capacity. Since these properties are integral to the performance of the bentonite, it would be desirable to understand these factors in more detail. This could be achieved by applying analytical techniques to experiments that have been running for many years, together with setting up new cells to generate material in the presence of high concentrations of iron ions, then applying standard techniques to measure the relevant physico-mechanical processes. This should be coupled with continued mineralogical analysis to examine the extent of any changes in the composition and microstructure of the surrounding bentonite. This approach applies equally to laboratory experiments and material removed from in situ experiments. It has been shown that iron ions released by corrosion penetrate into the surrounding bentonite, but the chemical state of the iron is still not fully characterized. One technique that has great potential for investigating this phenomenon is the use of synchrotron-based techniques **(Finck et al., 2023)**, such a XANES and XRF to map the distribution of metals near the surfaces of the corroding surfaces. This would apply to both iron and copper. Ideally, this analysis should proceed by analyzing samples that are removed after certain increasing time intervals to enable the evolution of the interface to be characterized. The alteration induced by bentonite metal interactions did not alter the di octahedral structure of the montmorillonite nor introduced mineralogical changes. Bentonite was stained a red-brown color extending ~1 mm from the carbon steel surface, which is coincide with an increased iron concentration observed in Grimsel in-situ experiment bentonite samples after 394 days exposure **(Reddy, Padovani, Rance, et al., 2021)**.

1.3.3.3 In situ iron corrosion experiments

In order to validate laboratory experiments about corrosion behavior of canister materials in geological based environment it is necessary to carry out experiments (In-situ) under conditions that simulate those expected in reality with similar as possible. There are two different in-situ underground on-going laboratory experiments operated in Switzerland by Nagra. One of them is carried out at Mont Terri and other is at Grimsel underground research laboratories. A significant contribution regarding in-situ experiment was made by literature **(Diomidis & Reddy, 2021)**, based on the IC-A experiment at the Mont Terri Underground Research Laboratory to study the long-term anaerobic corrosion rate of carbon steel in compacted bentonite. This study provided crucial data for predicting the lifetime of steel canisters and explored the impact of bentonite on microbial activity, including microbial influenced corrosion (MIC), a key factor that can accelerate steel degradation in geological environments.

Here in Mont Terri underground research laboratory experiment after 20 months of exposure, corrosion coupons and bentonite were analyzed. The corrosion rate measured by weight loss, was in the range 1.5-3.5 μm/yr and affected by the density and initial form of the bentonite, with the lowest corrosion rates observed in the highest density, fully compacted bentonite. The grade of carbon steel and the presence of welds had a minor effect on corrosion rate. The smallest effect on the corrosion rate of the weld material occurred in the highest density bentonite, and the greatest effect occurred in the pellet-based bentonite, with the base metal showing the lowest corrosion rates and the deep weld metal showing the highest corrosion rate. Here, corrosion product mainly consists of magnetite. The bentonite adjacent to the metal was finer grained, more dispersed and enriched in iron. Aerobic, anaerobic and sulphate reducing bacteria were identified both in the pore-water surrounding the modules **(Smart et al., 2017)**.

The anaerobic corrosion behavior of candidate disposal canister materials in compacted bentonite exposed to natural granitic porewater containing native microbial populations was studied at Grimsel test site in the materials corrosion test long term experiments **(Reddy, Padovani, Rance, et al., 2021)**. The approach taken for design and operation of the experiments was similar to that of Mont Terri experiments, the main difference is that Grimsel experiment was in granitic geology rather than opalinus clay environment (Mont Terri). In this experiment after 394 days exposure, some coupons were characterized, each with different bentonite density. The corrosion rate of carbon steel was around ~2 μm/yr and was not much affected by the bentonite density (1250 kg/m^3 or 1500 kg/m^3). The carbon steel/bentonite interface was a mixture of corrosion products consisting of magnetite, hematite and traces of Fe-S compounds. The corrosion rate obtained in this in-situ experiment is similar to that of Mont Terri experiments.

Overall, these two in situ experiments have provided valuable information about behavior of candidate canister materials in a bentonite buffer material under conditions very close to this expected in a real geological disposal repository.

2. Experimental

2.1 Materials and Chemicals

2.1.1 Chemicals

All sample preparation and handling was performed in an Ar-filled glovebox with O_2 and H_2O content below 10 ppm at 22 ± 3°C. Ultrapure water (MilliQ system, 18.2 MΩ/cm at 25°C) was used to prepare synthetic Grimsel ground water (***Table 1***), which was further purged with Ar for 5 hours to remove traces of CO_2 and O_2 prior storage in the Ar-filled glovebox. All other chemical used in the work are mentioned in Appendices section.

Table 1 *Recipe of synthetic ground water* ***("Alexander et al., 2009")***.

Ground water content	Values
$CaCl_2.2H_2O$	11.760 mg
NaF	1.43 mg
Na_2SO_4	8.52 mg
$NaHCO_3$	2.45 mg
Si standard sol with 0.5M NaOH	20.2 mL volume
HCl	9.9 mL volume
MQ water	Rest to make 1 liter volume

All experiments were performed with MX-80 bentonite and synthetic Grimsel groundwater (composition in ***Table 2***) to allow comparison with results from the *in situ* MaCoTe experiment at the Grimsel Test Site. Corrosion experiments were performed in 100 g/L bentonite suspension to allow *in situ* pH and E_h measurements at the end of the experiments. Metallic coupons were used in all experiments and the ratio exposed metallic surface area to volume of suspension was kept constant.

Table 2 *Composition of the synthetic Grimsel groundwater (in mg/L) used in all experiments (*calculated from the amount of added salt). pH = 9.80 ± 0.10 and Eh = 115 ± 50 mV (vs S.H.E.).*

Ion	Na	Ca	Si	F	Cl	SO_4	CO_3
mg/L	242.0	2.9	17.3	0.6	309.5	5.7	1.8*

Table 3 Results from the XRD analyses of the Wyoming MX-80 material (±x is uncertainty) ("Karnland, 2010").

MX-80 Bentonite	% of total mass (average)
Montmorillonite	81.4(+2.5 or -1.9)
Illite	0.8(+0.1 or -0.1)
Calcite	0.2(1.1 or -0.2)
Cristobalite	0.9(+1.6 or -0.9)
Gypsum	0.9(+0.5 or -0.2)
Muscovite	3.4(+1.7 or -1)
Plagioclase	3.5(+1.2 or -1.2)
Pyrite	0.6(+0.3 or -0.3)
Quartz	3.0(+0.8 or -0.5)
Tridymite	3.8(+1.3 or -2.1)

Table 4 Results from the XRD analyses of the GMZ bentonite material (±x is uncertainty) (Shao et al., 2024).

GMZ Bentonite	% of total mass
Montmorillonite	75(±2)
Quartz	12(±1)
Cristobalite	7(±1)
Feldspar	4(±1)
Calcite	1(±1)
Kaolinite	1(±1)

2.1.2 Bentonite slurry Equilibration

Experimental design is carried out for four different candidate materials at two temperatures i.e. room temperature (25°C) and elevated temperature (50°C) using 100 g/L equilibrated MX-80 bentonite slurry for 3, 6 and 9 months at room temperature and 3 and 6 months at 50°C under static conditions, and 3 and 6 months at 25°C and 50°C for dynamic conditions.

Table 5 MX-80 Bentonite slurry equilibrium indicating pH, Eh and ions concentration (±x is uncertainty) during 4 weeks.

Sample	Time (weeks)	pH	E_h w.r.t SHE (mV)	Ions concentration (mg/L)					
				Na	Si	Ca	Cl	SO4	F
Slurry-A	1	7.9 *(±0.5)*	214 *(±50)*	434.2 *(3.6)*	13.0 *(0.6)*	6.4 *(1.2)*	434.5 *(21.7)*	400.3 *(20.0)*	1.1 *(0.1)*
Slurry-B	2	8.0 *(±0.5)*	207 *(±50)*	479.8 *(2.0)*	12.9 *(0.7)*	8.4 *(0.6)*	416.1 *(20.8)*	552.5 *(27.6)*	1.2 *(0.1)*
Slurry-C	3	8.1 (±0.5)	242 *(±50)*	507.9 *(1.6)*	12.8 *(0.7)*	9.0 *(1.1)*	440.1 *(22.0)*	547.8 *(27.4)*	1.2 *(0.1)*
Slurry-D	4	8.2 *(±0.5)*	244 *(±50)*	520.0 *(1.2)*	12.8 *(1.6)*	9.1 *(0.9)*	460.5 *(23.0)*	595.6 *(29.7)*	1.4 *(0.1)*

Equilibration of bentonite slurry was almost achieved around 30 days (after 4 weeks). Every week sampling was done (phase was separated using ultracentrifugation at 50000 rpm), *in situ* pH and E_h measured and the concentration of cations and anions determined by ICP-OES and IC up to 30 days. All experiments were performed under anoxic conditions in glove box (Ar atmosphere).

2.1.3 Metallic coupons

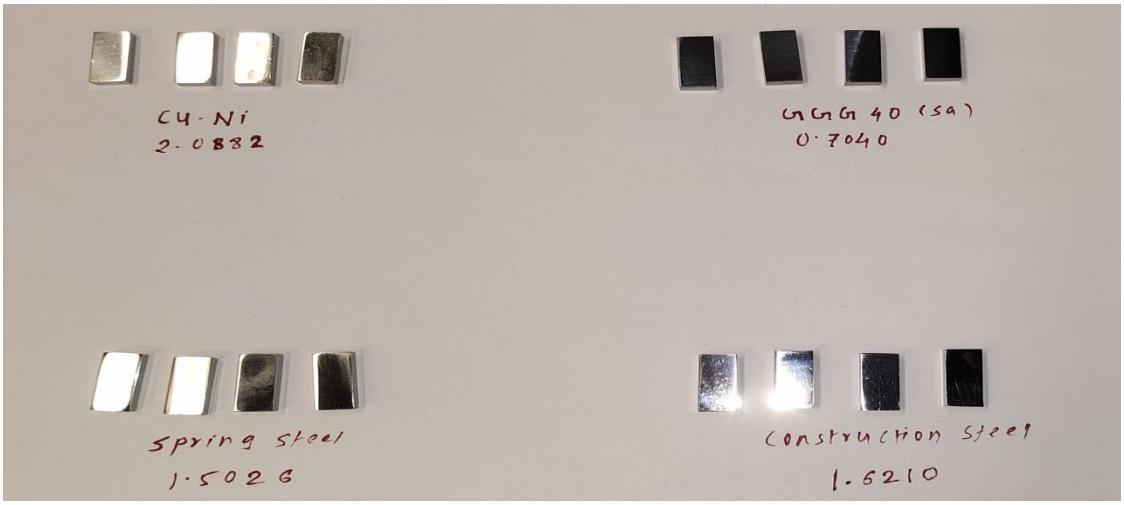

Figure 7 *Polished metallic coupons of all four investigated materials.*

Four types of metallic coupons were used in these corrosion experiments, which were obtained from different commercial suppliers. The steel specimens (coupons) were cut from a block of steel to obtain dimensions of 4 mm x 20 mm x 8 mm for static experiments and of dimension 4 mm x 8 mm x 8 mm for dynamic experiments. In order to reach defined and low initial roughness, all sides of each coupon were grinded on 500, 800 and 1200 SiC papers (Struers, Knuth-Rotor 3) and polished with diamond containing paste up to ¼ µm (Buehler, Ecomet 1 Polisher). Two sets of each metallic coupon were prepared for the experiments.

Considering wearing action during handling of canisters for disposal, one set of SS and CS metallic coupons were subjected to scratch on their surface using cylindrical block of concrete (composite material) having high surface roughness. There are 5 to 10 scratches applied on the polished SS and CS coupons surface that lead to increase surface roughness in that region as evidenced by AFM. After polishing, ultrasound with ethanol was used to remove impurities; the samples were dried, weighted and put into an Ar glove box to avoid oxidation. The initial state of the coupons was examined by various analytical techniques like AFM, SEM-EDX and XRD to obtain an overview of the initial surface. The chemical composition of the steels according to the certificates provided by the manufacturers is shown in (***Table 6).***

Table 6 *Elemental composition in wt. %, as indicated on the inspection certificate DIN EN 10204/3.1, of SGI, Cu-Ni alloy, SS and CS used in the corrosion experiments.*

Material	C	Si	Mn	P	Mg	Cr	Mo	Cu	Ni	Fe
Cu-Ni	<0.01	-	0.95	<0.01	-	-	-	Bal.	30.43	0.68
SGI	3.46	3.39	0.29	0.04	0.05	0.04	-	0.04	-	Bal.
SS	0.53	1.60	0.74	<0.01	-	0.18	-	-	0.22	Bal.
CS	0.17	0.29	1.59	<0.01	-	0.06	0.02	0.05	0.75	Bal.

2.2 Autoclave static experiments

Corrosion experiments were performed using two different setups. In the first more traditional approach (autoclave experiments), coupons were in contact with the bentonite suspension in a closed vessel and left to react. These experiments are referred to as under static conditions. The static corrosion experiments were performed in autoclaves, which are tightly closed vessels. The autoclaves are small reactors consisting of a stainless steel body, a Teflon and tantalum internal liner (tantalum is a highly corrosion resistant metal), fluorocarbon rubber Viton O-ring, underlid steel plate and a stainless steel lid **(Finck et al., 2023)**. The tight closing is ensured via six screws. For experiments at elevated temperature, in order to avoid the overpressure during the corrosion process, some of the autoclaves were modified and the lid was fitted with a manometer and an overpressure relief valve. The coupons were placed on a PTFE (Teflon) stand and put inside the autoclaves.

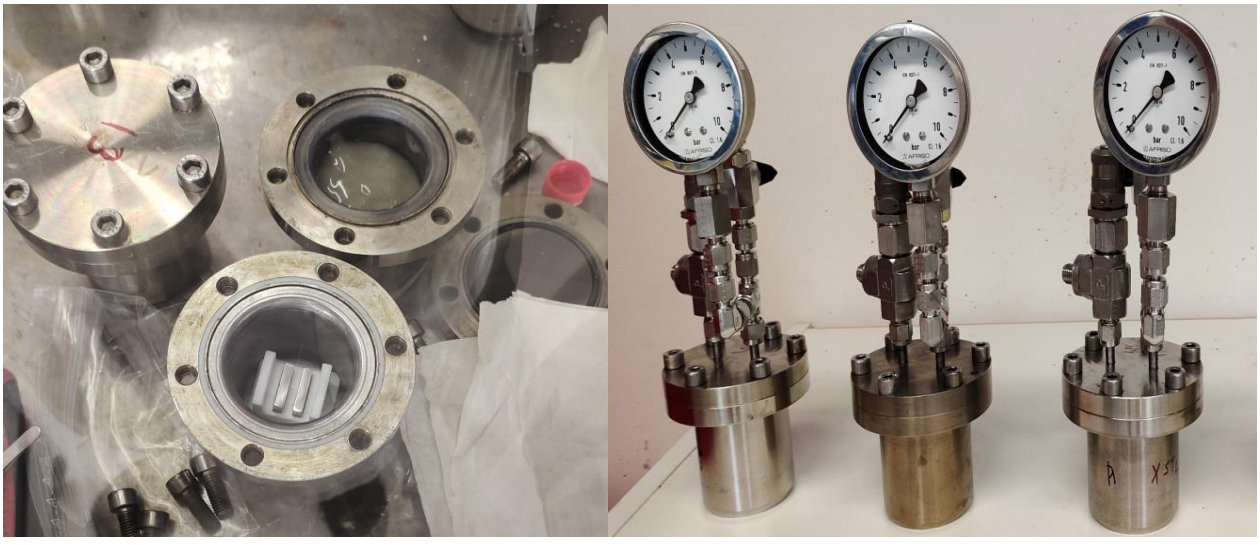

Figure 8 *The autoclaves setup with fittings (left) for 25°C and (right) side for 50 °C for static experiments.*

Two polished coupons were placed onto each PTFE stand and fully submerged in the 50 mL MX-80 bentonite slurry, not touching the bottom and not touching each other to avoid galvanic corrosion. The total volume of the autoclave was 90 mL and suspension filled up to 50 mL, so there is additional free space left above the suspension in which gas phase may be formed. The pH and E_h were measured in-situ and the autoclaves were closed inside the Ar glovebox. Prior to use in corrosion experiments, the PTFE stand for the coupons was washed with 0.1 M NaCl at 70°C for one week in oven to wash out fluorine from PTFE. Before the experiments, all autoclaves were thoroughly cleaned with iso-propanol. Prior the filling of the autoclaves, the polished coupons were weighted. Static corrosion experiments were performed at room temperature (25°C) and elevated temperature (50°C). At room temperature, vessels were standing

Figure 9 *Static experiments on the left at25°C and right side at50 °C for 3 and 6months.*

in the Ar-box. For the experiments performed at elevated temperature, a different setup was used.

Two aluminium blocks with four holes each to fit the autoclaves was manufactured and set onto heating plates with dimensions of 215 x 215 mm^2. Total 8 autoclaves could therefore be heated simultaneously on two heating plates. The whole setup was carefully isolated by an additional block of Teflon leaving the bottom free for cooling of the heating plate. A hole was made in the aluminium and Teflon to accommodate the heating element for the temperature control. The uncertainty for the temperature in the autoclave was determined as 50 ± 2°C.

The set of 9 autoclaves without manometer at room temperature and 8 autoclaves mounted with manometer at elevated temperature on heating plate were used, in which the static experiments were run batch wise in various configurations of metal coupons, temperatures and exposure as summarized in Appendices. Experiments at different temperatures allow the observation of the temperature effect on the corrosion rate, while the different exposure times aid observation of the corrosion front progress (dissolution enhanced) and possible corrosion phases transformation as well as determination of the corrosion rate. At room temperatures, contact times were 3, 6 and 9 months, and at elevated temperature contact time was 3 and 6 months. In CuNi corrosion experiments using this setup, the sulfide content could not be changed over time so that a defined starting concentration of 3 µM was used. In SGI corrosion experiments, hematite was added as

0.5 wt. %. At the end of the static experiments at elevated temperature, the heated autoclaves were first cooled down to room temperature inside the argon or nitrogen filled glove box. Once all autoclaves are opened, E_h and pH measurements were carried out in in-situ conditions prior to the removal of the coupons at room temperature for all the samples. In order to study effect of type of bentonite on corrosion behavior of carbon steel, a different series of static batch experiments were performed using GMZ bentonite at room temperature for 3, 6, 9 and 12 months and at elevated temperature for 3 and 6 months. All experimental setup was similar like MX-80 bentonite static experiments instead here GMZ bentonite was used.

2.3 Diffusion cells dynamic experiments

In the second approach, experiments were performed using a reactor having one inlet and one outlet and will be referred to as under dynamic conditions. Dynamic experiments setup testing was carried out outside the glove box at room temperature to check how it works under given conditions and to calibrate pump and monitor the flow rate. After checking, dynamic experiments were performed inside glove box under anoxic conditions at room temperature and elevated temperature (***Figure 11***) for three and six months. Due to some technical reasons there is little change in the design of experiment in terms of amount of bentonite (initially planned were 35 cm^3 at a dry density of 1.25 g/cm^3) but selected 100 g/L bentonite slurry was used in static experiments, for better comparison between two experiments (static and dynamic) under similar conditions. Dynamic experiments was carried out to investigate the corrosion behavior of candidate materials under flowing conditions. All metallic coupons, ground water and MX-80 bentonite slurry are the same as used in static experiments.

Figure 10 *Peristaltic pump on (left side) and reactor set up on (right side) for dynamic experiments.*

Figure 11 *Dynamic experiments on the left side at elevated temperature (50°C) and right side at room temperature (25°C).*

For 3 and 6 months Here one coupon per reactor (made of stainless steel body) having PTFE inner liner was used and metallic coupons having 8 mm x 8 mm x 4 mm dimension. As shown in the above (***Figure 10)*** equipment like tubing, connectors, peristaltic pump, reactor vessels, filters and O-rings were used in dynamic experiments. Volume of vessel is 3.36±0.04 mL vessels were filled with 3.10 ± 0.05 mL MX-80 bentonite slurry having 100 g/L concentration. Metallic filters of 316L stainless steel (Tridelta-Siperm GmbH, Germany) having a mean pore size of ~7 µm were placed at both ends of reactor to avoid clogging and coming out of bentonite slurry during experiment. At inlet and at outlet, reactors were connected to tubing made of PEEK (polyether ether ketone). The peristaltic pump (Minipuls 3, Gilson) pumps water from reservoir to vessel and is collected at outlet.

Here flow rate measured was in the range from 2±0.5 to 3±0.5 µL/min at 0.05±0.02 rpm pump speed. The water was collected at specific time intervals at the outlet and weighed to determine the precise flow rate. Dynamic experiment was carried out for 3 and 6 months contact time with all similar material coupons and similar experimental conditions. During the experiments ground water was collected (sampling) after every two weeks for three months experiments and after 4 weeks for six months dynamic experiments. Ground water analysis carried out for inlet ground water and collected outlet groundwater from the reactor (diffusion cell). Two series of dynamic experiments were performed with different reaction time (3 and 6 months). In dynamic experiments for cupronickel coupons an addition of sulphide in groundwater was carried out (stepwise increase) compared to static experiments. For reaction time of 3 months, sampling was carried out after 4, 5, 6, 8, 10 and 12 weeks. In CuNi corrosion experiments using this setup, the porewater initially contained no sulfide until week 6, then 1 µmol/L until week 8, subsequently 2 µmol/L until week 10 and finally 3 µmol/L until week 12. In SGI corrosion experiments, hematite was added as 0.5 wt.%. Second series was performed for six months reaction time where sampling was carried out after 6, 10, 14, 18, 22 and 26 weeks. Here in CuNi corrosion experiments, the pore water initially contained no sulfide until week 10, then 1 µmol/L until week 18, subsequently 2 µmol/L until week 22 and finally 3 µmol/L until week 26. In case of

SGI corrosion experiments, hematite was added as 0.5 wt. % in the beginning of the experiment. Applied transient condition evidenced the effect of sulphide on copper corrosion and addition of α-hematite on SGI corrosion was also verified by performing parallel experiment without sulfide addition for CuNi and without hematite addition for SGI coupons. pH and E_h measurements were carried out in in-situ conditions for out coming groundwater for fixed time interval (3 and 6 months). During measurement ground water was not in contact with metal coupons and all measurements were carried out at room temperature inside Ar box.

At the end of static experiments, coupons were subsequently taken out, the excess bentonite suspension and out coming ground water from in-situ dynamic experiments was collected in 10 mL vials and underwent ultracentrifugation at 50,000 rpm for one-hour using ultracentrifuge. After that, the supernatant was collected and examined for concentration of dissolved metal cations and anions by using the ICP-OES/MS and IC techniques. From all batch experiments the corroded coupons were quickly blown dry inside glove box and then all coupons were taken for XRD, XPS followed by SEM/EDX measurements. For six months dynamic experiments on few (six) bentonite samples XAS analysis was also carried out, which gave information about alteration of bentonite due to corrosion and presence of secondary phases in the altered bentonite. Bentonite digestion with HF and then concentration determination using ICP-MS was also carried out to know concentration of elements in altered bentonite due to corrosion experiments.

2.4 Analytical methods for liquid phase analysis

2.4.1 pH Measurements

Thermo Scientific Orion dual star pH/ISE meter is used to measure in-situ pH of the bentonite slurry in static batch experiments and in-situ pH of the out coming ground water in dynamic batch experiments. The pH/ISE meter is connected with Metrohm solitrode pH electrode with reference electrolyte 3M KCl. All the steps regarding pH measurements like its calibration and in-situ measurements were performed in Ar gloveboxes at room temperature. The pH electrode was conditioned in 0.5 M HCl solution for 10 minutes, stored in 3 M KCl solution and rinsed with deionized water prior every use. The pH electrode was calibrated using reference buffer solutions at pH 4.01, 7 and 10.01 (Orion Application Solution) prior pH measurement. No buffer additions or pH adjustments were performed in the corrosion studies for static and dynamic experiments at elevated temperature. Orion application buffer solutions were used for calibration throughout all in-situ pH measurement; the three buffer solutions selected for calibration purposes are shown in ***Appendices***.

The pH was measured about 30 to 60 minutes for each sample in static and dynamic experiments to allow stabilization. As the pH electrodes were not mounted on the autoclaves, it was not

possible to measure the in-situ pH at 50 °C, but only after cooling down at room temperature. The pH uncertainty at room temperature was determined as ±0.05 unit after repeated measurements and calibrations at various times. The value for the maximum uncertainty for the recalculated pH was estimated as ±0.5 unit. Corrections were not applied apart of uncertainty in any pH measurements.

2.4.2 E_h Measurements

Thermo Scientific Orion dual star ISE/pH meter is used to measure the redox potential (E_h) of bentonite slurry and groundwater in both static and dynamic batch experiments. The redox potential is an indicator of the solution's oxidizing or reducing conditions. Measurements are made using two different electrodes: a silver/silver chloride (Ag/AgCl) electrode combined with a platinum or gold electrode, both of which have a 3 M potassium chloride (KCl) reference electrolyte. To convert the measured E_h values to standard hydrogen electrode (SHE) potential, a standard offset of approximately +210 mV is added to the readings, based on established literature guidelines. This allows the results to be consistent and comparable with SHE based measurements. Before each measurement, the electrodes are calibrated and tested using a standard buffer solution with a known potential of +220 mV against E_h electrode. Any deviations from this standard (typically below 10 mV) are corrected in the final E_h values. Measurements are taken without stirring for up to an hour, allowing the potential to stabilize with a drift rate below 0.5 mV/min to ensure accuracy.

While all E_h values are reported relative to the SHE, temperature adjustments to E_h are not straight forward because the exact influence of dissolved ions and species on the redox potential isn't fully characterized in this system. Additionally, the study takes into account possible liquid junction potential differences, which should not exceed 50 mV, as suggested **(Barry, 1994; Yalçıntaş et al., 2015)**. Here care should be taken about potential sources of measurement variability, such as calibration offsets, temperature effects, and liquid junction potentials, to ensure reliable E_h measurements in the experimental setup.

2.4.3 ICP-OES Measurements

In all batch experiments, composition of the pore water basically cations was determined by Inductively coupled plasma optical emission spectroscopy (Optima8300DV, Perkin Elmer) which is a powerful tool to quantify dissolved elements at low concentrations in particular. ICP-OES measurement were carried out after ultracentrifugation for 1 hour at 50,000 rpm of bentonite slurry in static experiment and pore water in dynamic batch experiment using a Beckman Coulter XL-90 K ultracentrifuge. Sample preparation is done inside the Ar box under anoxic conditions at room temperature where 0.5 ml of groundwater is mixed with 4.5 ml of 2% HNO_3 with dilution

factor of 10, so the total volume of ground water is 5ml. ICP-OES shows the advantage to be able to handle moderately high ion (salt) concentrations in solution.

It is a robust method, and is mostly used for ground or wastewater analysis **(Olesik, 1991; Scientific, 2020)**. This technique enables the detection of multiple elements simultaneously with high sensitivity and precision, making it suitable for analyzing trace metals and other ions present in environmental samples like bentonite slurry and groundwater. More detailed information about working principle and other details about ICP-OES can be found in the literature **(Gey, 2008; Ritgen, 2023)**. Obtained results have some uncertainty in the measurements, which depends on the sensitivity of the instrument for each element.

2.4.4 ICP-MS Measurements

In all batch static and dynamic experiments, ICP-MS (NexION 5000 multi quadrupole) technique was used to measure the composition of pore water for the elements like Cu, Ni and Fe (few samples) which are below detection limit for ICP-OES measurements. Sample preparation adopted here was same as like for ICP-OES measurements after ultracentrifugation of pore water. The amount of Cu, Ni and other elements sorbed on the bentonite during exposure for 6 months dynamic experiment was also determined using ICP-MS method. Here sample preparation was done by digesting a low amount (few milligrams) of dry bentonite into hydrofluoric acid (HF) and then acidified using nitric acid prior to measurements. There are always some uncertainties associated with measurements, which is under acceptable limits.

The Inductively Coupled Plasma (ICP) is an ionization source that fully decomposes a sample into its constituent elements and transforms those elements into ions. It is typically composed of argon gas, and energy is "coupled" to it using an induction coil to form the plasma. Inductively coupled plasma mass spectrometry (ICP-MS) is an elemental analysis technology capable of detecting most of the periodic table of elements at milligram to nanogram levels per liter. ICP-MS provides highly sensitive, accurate, and reliable quantification of trace elements in corrosion samples, essential for understanding elemental interactions within the bentonite slurry and groundwater systems in batch experiments. This data is crucial for evaluating potential contaminant (ground water) mobility and understanding geochemical behavior in these experiments.

2.4.5 IC Measurements

Ion chromatography (IC) is a process that allows the separation of ions and polar molecules based on their charge. It can be used for almost any kind of charged molecule. Here it is used to measure the amounts of dissolved anions in the pore water in static and dynamic experiments. IC measurements was carried out using (ICS-3000, Thermo Scientific) instrument which comprises an auto sampler, gradient pump and chromatography detector module with an electrochemical detector. IC measurements were carried out after ultracentrifugation of bentonite slurry in static experiment and pore-water in dynamic batch experiment using (Beckman Coulter XL-90 K) ultra

centrifuged for 1 hour at 50,000 rpm. Sample preparation is done inside the Ar box under anoxic conditions at room temperature.

Two types of samples were prepared for each supernatant, where first sample is without dilution having a volume of 1mL of supernatant (ground water) for fluoride determination, and the second sample was (diluted) 10µL ground water mixed with 990 µL of MilliQ water, so the total volume of sample is 1mL for chloride and sulfate contents determination in the pore water. IC measurements provide a detailed profile of dissolved ions in the experimental solutions, essential for monitoring the ionic composition and understanding chemical changes during interactions between bentonite slurry and metal ions. These insights help assess the geochemical stability and behavior of the ions involved in the study.

2.5 Analytical methods for solid phase analysis

2.5.1 AFM

Atomic Force Microscopy (AFM) is a powerful technique to measure the topography of a sample surface at the nanoscale. The advantageous aspect of AFM is the use of a physical probe to determine the surface features of samples in contrast to light based microscopes, which are restricted to micro scale resolution levels, due to wavelength constraints. It operates by scanning a sharp nano tip attached to a small cantilever over a sample surface. As the tip approaches the surface by contact or tapping mode, various forces (like van der Waals forces, electrostatic forces, and chemical bonds) cause the cantilever to deflect. This deflection is measured to create a detailed topographic map of the surface. Atomic force microscopy (Cypher VRS1250, Oxford instruments) determines an average surface roughness; it was applied on the initial coupon surfaces. The RMS (root mean square) roughness was evaluated for all four polished unscratched and two surface scratched (carbon steel and spring steel) coupons. Here only one initial batch of coupons was analyzed exemplarily.

2.5.2 SEM, SEM-EDX and EBSD

Scanning electron microscopy (SEM) is an electron based analytical technique, where electrons are emitted as a beam from a so-called electron gun and then narrowed to a dimeter of about 0.4-5 nm, defining the maximum resolution of the images. All corrosion coupons were prepared in Ar box under anoxic conditions and then they were transferred to SEM. For a short time during transferring from anoxic sample holder to SEM instrument, samples were exposed to the

atmosphere. Information on morphology and chemical composition of corroded coupons and secondary phases was provided by scanning electron microscopy (SEM, Quanta 650 FEG, FEI) and energy dispersive X-ray spectroscopy (EDXS, Thermo Scientific NORAN System 7 equipped with UltraDry^{TM} silicon drift X-ray detector, Pathfinder X-ray microanalysis software v2.8).

The resolution is 1.2 nm at 30 kV, and 0.9 nm at 20 kV for mentioned microscopes, respectively. Electron micrographs were recorded either in backscattered electrons (BSE) or in secondary electrons (SE) mode. For selected corroded CuNi specimens, complementary electron backscatter diffraction (EBSD) analyses were carried out using a Crossbeam 350 KMAT (Zeiss) microscope equipped with an Oxford Instrument AZtec EDX/EBSD system.

Formed secondary phases having sizes ranging from 100 nm to 250 nm, no further specimen preparation method (e.g., surface coating) was used. EBSD patterns (Kikuchi patterns) were acquired by Symmetry, S2 detector at a resolution of 622 x 512 pixels to ensure a good compromise between angular resolution and acquisition time. The EBSD scans were optimized in areas of 500 nm × 750 nm. Optimizing indexing parameters, including the Hough transform parameters and number of reflections, a mean angular deviation (MAD) of 0.29° has been achieved, enabling to index 10 out of 11 bands. The angle between surface sample and electron beam was set to 20°, and the working distance to 13 mm. An acceleration voltage of 15 kV was selected. Monte Carlo simulations (Casino 2.4.8 software **(Demers et al., 2011)**) using 15 keV primary electrons showed that backscattered electrons are generated from a depth up to 150 nm at perpendicular incidence of electrons, which results in around 51 nm for the tilt angle of 20°, ensuring negligible contribution from the CuNi substrate. EBSD patterns were recorded and analyzed using the AZtec 6.1 (HF1) software (Oxford Instruments).

2.5.3 XPS

XPS measurements were performed to get information on chemical composition and element speciation of all corrosion coupons by using a PHI 5000 Versa Probe II (ULVAC-PHI Inc.) spectrometer equipped with a scanning microprobe X-ray source (monochromatic Al Kα (1486.7 eV) X-rays) in combination with an electron flood gun and a floating ion gun generating low energy electrons (1.0 eV) and low energy argon ions (6 eV) for charge compensation at isolating samples (dual beam technique), respectively. All samples from corrosion experiments were mounted inside an Ar glovebox on a sample holder using isolating tape (floating ground of the sample). The sample holder was placed inside a gas-tight transfer vessel and moved into the XPS without air contact.

Survey scans were recorded with an X-ray source power of 25 W and pass energy of 187.85 eV. Narrow scans of the elemental lines were recorded at 23.5 eV pass energy which yields an energy resolution of 0.69 eV FWHM at the Ag $3d_{5/2}$ elemental line of pure silver. Calibration of the binding energy scale of the spectrometer was performed using well-established binding energies of elemental lines of pure metals (monochromatic Al Kα:Cu $2p_{3/2}$ at 932.62 eV, Au $4f_{7/2}$ at 83.96

eV). The C 1s elemental line of adventitious hydrocarbon at 284.8 eV was used for charge referencing, which corresponds to a binding energy of Si 2p of bentonite at 102.9 eV. Atomic concentrations are calculated from the areas of elemental lines (after Shirley background subtraction) of survey spectra using sensitivity factors of the elemental lines, asymmetry parameters, and transmission function of the analyzer. Relative error of atomic concentrations is within ± (10-20) %. Narrow scans of elemental lines were recorded for determination of chemical shifts and spectral features. Data analysis was performed using ULVAC-PHI MultiPak Version 9.9.3.

2.5.4 XRD

X-ray diffraction (XRD) is a primary technique for determining the composition and crystalline structure of mineral samples. In XRD, a sample is illuminated by an X-ray beam. The scattering of the X-ray beam by the sample is influenced by the spacing between the atoms in the crystal lattice, which is similar to the wavelength of the X-rays.

X-ray diffactograms were recorded on a D8 ADVANCE (Bruker AXS, Germany) diffractometer equipped with a Cu Ka source and a Lynx Eye XE-T detector. Here X-ray diffraction was used to characterize the crystalline secondary phases on the corroded steels. The redox sensitive compounds and all corrosion samples were measured encapsulated in a special anoxic holder, which was closed in an argon atmosphere. The measurement was performed in angles of 2θ ranging from 2 to 80° with an incremental step of 0.015° and a measurement time of 0.700s per step. This duration avoided the diffusion of oxygen and ensured anoxic conditions throughout the measurement. Crystalline phases were identified by comparison with the PDF-2 database using the DIFFRAC.EVA v5.0 software (Bruker AXS, Germany).

2.5.5 XAS (XANES) measurements

2.5.5.1 KIT Light Source, INE-beamline

X-ray absorption spectroscopy (XAS) comprise of irradiation and absorption of intense, monochromatic X-Rays by the sample as a function of X-ray energy in the range of 0.1-100 KeV. X-ray absorption near-edge structure (XANES) spectroscopy is a powerful well-established technique which uses synchrotron radiation and provides information about electronic, structural and magnetic properties of the materials. In XANES, an X-ray photon is absorbed, causing an electron to be excited from a core level to an empty state. The photon energy must be similar or exceed the binding energy of the core electron to induce this transition, opening a new absorption channel as the photon energy is scanned. The resulting absorption edge, which corresponds to the core-level energy, is unique to each element, making XANES an element-selective technique. Thus XANES is an important tool for studying the mineral surfaces and adsorbents on the mineral surfaces. Altered bentonite samples in contact with iron based (steels) coupons from six

months dynamic experiments were characterized by application of synchrotron-based techniques at the INE beamline (INE-BL) **(Rothe et al., 2012)** of the KIT (Karlsruhe, Germany) light source. The measurements were completed in cooperation with the respective beamline scientists. Corrosion of steel results in the production of ferrous ions that can either remain dissolved in the porewater, sorbed at the surface of bentonite or precipitate as secondary corrosion products. Preliminary results showed that under the prevailing weakly alkaline conditions the dissolved amounts of Fe ions in the porewater are very low and comparable to that in the experiments performed in the absence of coupon (i.e., bentonite suspension alone), suggesting that the majority of Fe ions accumulate at or near to the coupon/bentonite interface. Information about nature of neoformed corrosion product presence in altered bentonite was obtained by probing the Fe *K*-edge by X-ray absorption spectroscopy **(Finck et al., 2023)**. Linear combination fits (LCF) to the experimental spectra using reference compounds can provide information about the nature and proportions of Fe species. Such information is required to elucidate processes occurring at the coupon/bentonite interface.

2.5.5.2 Sample preparation

Here few samples (six) were measured where one sample consist of bentonite without contact of metal coupon (MX-80 bentonite) and other five samples consist of bentonite scrapped off the coupon surface after 6 months exposure time from the dynamic experiments namely polished SGI corroded at 25°C, polished SGI corroded in the presence of hematite at 25°C, polished and subsequently scratched CS corroded at 25°C and at 50°C, and polished and subsequently scratched SS corroded at 50°C. Most of the reference compounds needed for LCF are already available from earlier investigations **(Finck et al., 2023)**.

Samples were prepared by placing the altered bentonite as shown in ***Figure 12*** in airtight holders equipped with Kapton® windows, which are subsequently inserted in cells allowing to flush with N_2 gas to ensure anoxic conditions during the measurements (available at the Institute). The sample preparation and encapsulation took place inside an argon glovebox. This setup (six samples in one cell) was transported to the INE beamline **(Rothe et al., 2012)** where the measurements were done under continuous nitrogen flow.

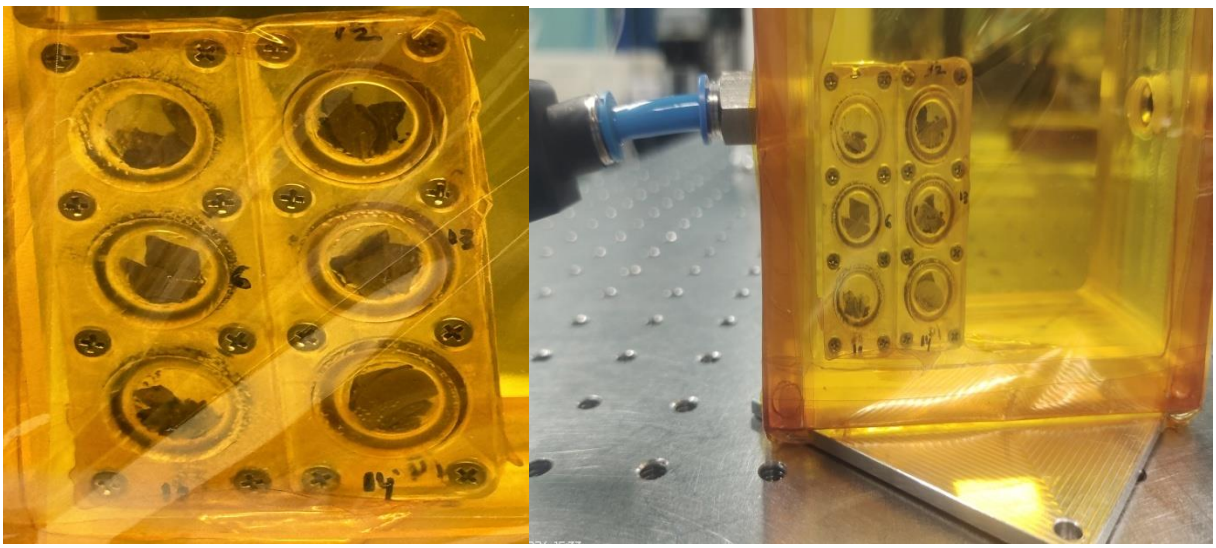

Figure 12 *Altered bentonite sample encapsulated in an anoxic cell built for XAS measurements.*

2.5.5.3 XANES measurements

Fe *K*-edge ($E_{Fe\ 1s}$ = 7112 eV) XANES spectra (2-4 scans to achieve adequate signal-to-noise ratio) were recorded on the solid phase at the INE-BL with the DCM equipped with a pair of Si(111) crystals, and with an X-ray beam of standard size. The energy was calibrated against a metallic Fe foil and spectra were recorded in fluorescence yield detection mode using the available solid-state detector.

2.5.5.4 Data evaluation

Data evaluation gives information about the nature of Fe-bearing phases present at the coupon/bentonite interface, and thus allowed determining the nature of the reactions associated with metallic corrosion upon exposure to bentonite. The collected data were analyzed following standard procedures using Athena (Demeter version 0.9.26) software **(Ravel & Newville, 2005)**. Structural information was obtained by applying the LCF for the data fitting. For data fitting using Athena software, the raw MX-80 bentonite scan (reference material) and other possible iron based secondary phases which were selected as referenced compound based on sample pre-characterization in the laboratory used for steel corrosion under similar conditions. Thus, Fe K-edge XAS analysis give information about alteration of bentonite which was in contact with metallic coupons during exposure and also helps in identification of secondary phases present in the altered bentonite.

2.5.6 Corrosion rate measurements

At last, in order to estimate corrosion rate of the corroded coupons, weight loss measurement is carried out using ASTM G1-03 standard practice **(International, 2003)**. The iron material based coupons were dipped several times in a solution of 50 wt. % de-ionized water and 50 wt. % HCl containing 3.5 g/L hexamethylenetetramine, which hinders dissolution of non-corroded steel surface and only allows dissolution of the hydro (oxides) under acidic conditions **(Bayol et al., 2007)**. Cu-Ni alloy based coupons were dipped several times in the solution of 10 wt. % H_2SO_4 (specific gravity 1.84) and 90 wt. % de-ionized water. The mass of the coupons after cleaning is compared to the initial mass and the difference represents the loss of material to corrosion. A minimum of six cleaning cycles were performed for each coupon. The mass loss can then be used to calculate a corrosion rate (CR) in m/a using below formula.

$$CR = \frac{\Delta m}{S \times \rho_S \times t} \quad \text{.....(18)}$$

Where Δm is the weight loss in kg, S is the surface area of the steel coupon in m^2, ρ_S is the steel density and t is the exposure time in years. Weight loss measurement was carried out for all coupons obtained from the static/dynamic experiments in fume-hood at room temperature. In this study corrosion rate measurement was done using a procedure of graphical analysis based on multiple cleaning cycles in order to extrapolate the actual weight loss due to corrosion from the total measured weight loss. The graphical analysis method is outlined in ISO 8407: 1991. The values for corrosion rates derived by applying the graphical method described in ASTM G1-03 and ISO 8407: 1991 and using the above mentioned equation (18) were then compared with the mean value of corrosion rates calculated for individual etching cycles. The difference of both values was taken as a measure to estimate experimental uncertainties.

In this study the surface area of a coupon is well defined and consistent for each test. The uncertainties, assuming errors obey a normal distribution, caused by the measurement of time, mass, and surface area of the coupon. For samples corroded during 3 months in static experiments, bentonite particles could not all be removed quantitatively from the coupons before determining the weight loss, implying that in some cases corrosion rates overestimate the actual value. For samples obtained from 6 and 9 months static, as well as 3 and 6 months of dynamic experiments, care was taken to clean off all bentonite particles using isopropanol before determining the weight loss.

3. Results and Discussion

3.1 Corrosion of Cu-Ni alloy in MX-80 bentonite

3.1.1 Initial characterization

The examination of the initial sample surface was an important first step to allow observation of the morphological changes as corrosion progresses. ***Figure 13*** shows the SEM (SE mode) images of polished non-corroded initial cupronickel coupon. SEM-EDX results show the chemical composition of the selected point which focussed on the average surface area of coupon and their results were shown in the (***Table 7 & Table 8)***. Only one point was focused on the coupon surface and the obtained composition of coupon had good match with the composition compared to the certificate when looking at the composition of the bulk cupronickel alloy. Finally, the surface roughness of the starting material was assessed by AFM. A value for the root mean square (RMS) roughness of 15± 2 nm was obtained for a scanned area of 20 x 20 μm^2.

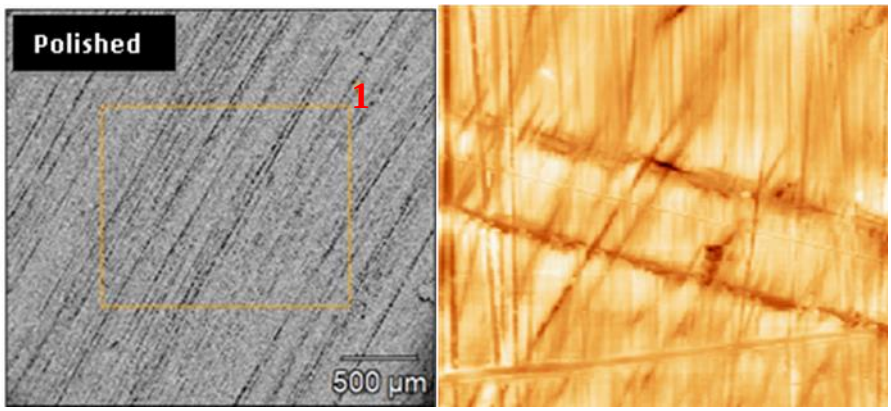

Figure 13 *SEM image on left side and surface roughness using AFM on right side of the initial Cu-Ni coupon.*

Table 7 *Composition of initial Cu-Ni coupon obtained by SEM-EDX before experiment with (+/- 3 Sigma) uncertainty.*

Material /Atom %	C	O	Al	Mn	Fe	Ni	Cu
Cu-Ni_point 1	7.5±0.6	2.1±0.6	0.5±0.2	0.9±0.4	0.9±0.4	28.7±1.0	59.5±1.6

Table 8 *Chemical composition of the initial copper-nickel alloy with (+/- 3 Sigma) uncertainty.*

Element / wt. %	C	O	Al	Mn	Fe	Ni	Cu
Certificate	0.0	-	-	0.9	0.7	30.4	67.9
EDX of overall surface point 1	1.6±0.1	0.6±0.2	0.2±0.1	0.8±0.3	0.9±0.3	29.6±1.1	66.3±1.8

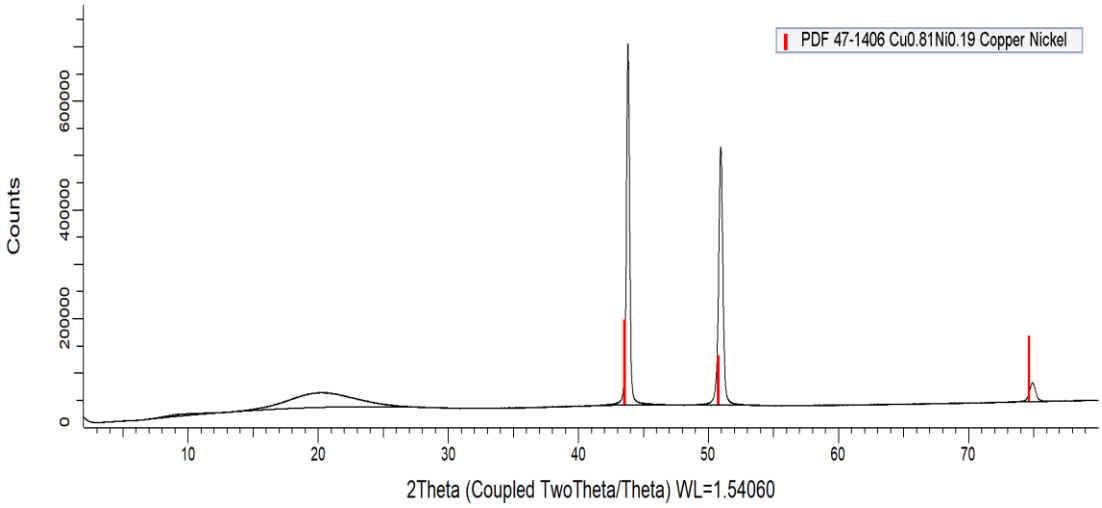

Figure 14 *X-ray diffractogram of the initial Cu-Ni coupon before experiment (with air scattering effect).*

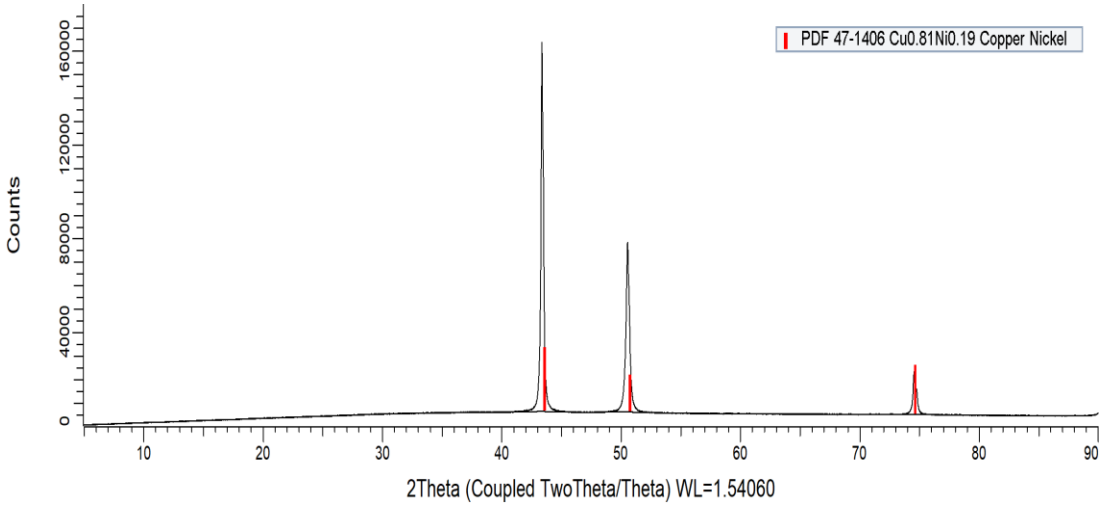

Figure 15 *X-ray diffractogram of the initial Cu-Ni coupon before experiment (without air scattering effect).*

The X-ray diffractogram of initial cupronickel coupon was shown in the (***Figure 14 & 15).*** The broadband in the (***figure 14***) around 20^{o} two theta is due to absence of anti-scatter blade inside the cap of anoxic holder. In ***(Figure 15)*** measurement was done in oxic conditions without anoxic holder and air scattering effect was minimized by using an external motorized anti-scatter blade. XRD analysis corroborates the presence of cupronickel alloy (PDF 47-1406) as primary phase.

3.1.2 Dissolved metal ions evolution

The quantification of the dissolved ions in the solution after ultracentrifugation at the end of the static and dynamic experiments was done using ICP-OES, Ion chromatography and ICP-MS following the procedure for sample preparation described in methods section ***2.4.3, 2.4.4 and 2.4.5.*** In case of cupronickel alloy, copper, nickel evolution is mainly due to cupronickel corrosion whereas iron, silicon and aluminium evolution is due to clay dissolution. In addition, silicon and aluminium are also the components of the pore water and simulated groundwater. Dissolved amounts of copper, nickel, iron, silicon and aluminium during 3, 6 and 9 months static experiments in presence of cupronickel coupons were shown in ***Table 9*** and without coupons as reference were shown in ***Table 10.*** For dynamic experiments dissolved amount of copper, nickel, iron, silicon and aluminium during 3 and 6 months were shown below in ***Table 11*** and ***Table 12***. For reference dissolved ions without metallic coupon for dynamic experiments was shown in ***Table 13.*** Concentrations of other dissolved cations and anions are tabulated in ***appendices section*** since such ions do not have significant effects and their variations lie within experimental uncertainties.

Table 9 *Dissolved amounts of Cu, Ni, Fe, Si and Al ions in the pore water solutions in contact with Cu-Ni coupons after 3, 6 and 9 months static experiments. Numbers in parentheses correspond to the relative standard deviation in percentage.*

System/ Amounts in µg/L	Cu	Ni	Fe	Si	Al
3months 25°C w/o sulfide	7 (6.5)	5(6.7)	38(5.4)	14900(1.0)	500(1.6)
3months 25°C with 3µM sulfide	21(7.3)	5(7.9)	71(5.6)	14800(0.8)	300(15)
3months 50°C w/o sulfide	9(7.1)	5(6.3)	32(5.5)	22100(1.3)	500(2.8)
3months 50°C with 3µM sulfide	8(7.1)	50(7.1)	289(4.8)	10400(1.5)	3940(1.6)
6months 25°C w/o sulfide	21(6.3)	9(8.3)	37(4.1)	15600(1.0)	700(4.5)
6months 25°C with 3µM sulfide	25(6.4)	11(6.2)	41(4.8)	15200(0.8)	1500(2.4)
6months 50°C w/o sulfide	36(5.8)	43(5.6)	52(5.3)	24500(0.6)	<100
6months 50°C with 3µM sulfide	37(5.8)	103(5.9)	526(4.3)	21900(1.5)	1900(11)
9months 25°C w/o sulfide	19(5.5)	10(5.2)	407(3.8)	18500(0.2)	600(4.9)
9months 25°C with 3µM sulfide	23(6.0)	10(5.2)	156(3.8)	17900(1.5)	800(2.6)

Table 10 *Dissolved amounts of Cu, Ni, Fe, Si and Al ions in the pore water solutions without coupon after 3, 6 and 9 months static experiments. Numbers in parentheses correspond to the relative standard deviation in percentage.*

System/ Amounts in µg/L	Cu	Ni	Fe	Si	Al
3months 25°C w/o coupon	<10	-	<10	14100(1.2)	2600(7.2)
3months 50°C w/o coupon	<10	-	3900(1.9)	28000(0.6)	18500(0.6)
6months 25°C w/o coupon	<10	-	600(1.9)	15600(1.2)	600(4.9)
6months 50°C w/o coupon	<10	-	<10	24800(0.2)	<100
9months 25°C w/o coupon	38(7.0)	7(5.9)	64(7.3)	18500(0.1)	500(8.0)

Table 11 *Dissolved amounts of Cu, Ni, Fe, Si and Al ions in the ground water (solution) in contact with Cu-Ni coupons during 3 months-dynamic experiment. Numbers in parentheses correspond to the relative standard deviation in percentage.*

25°C w/o sulfide (System)/ Amounts in µg/L	**Cu**	**Ni**	**Fe**	**Si**	**Al**
A (4 weeks)	15(6.7)	20(6.8)	516(4.5)	17600(0.8)	1200(5.7)
B (5 weeks)	5(7.5)	5(6.2)	332(5.3)	18600(1.8)	900(4.2)
C (6 weeks)	3(6.8)	3(7.7)	54(5.9)	18800(1.1)	1000(3.1)
D (8 weeks)	4(7.0)	2(12.1)	63(14.5)	17200(1.0)	300(6.2)
E (10 weeks)	10(6.7)	2(7.9)	167(5.2)	21500(0.4)	300(4.9)
F (12 weeks)	7(7.2)	1(10.9)	13(4.7)	21100(0.6)	200(4.1)

50°C w/o sulfide (System)/ Amounts in µg/L	**Cu**	**Ni**	**Fe**	**Si**	**Al**
A (4 weeks)	24(7.1)	43(7.9)	513(5.9)	18400(0.3)	1200(3.1)
B (5 weeks)	4(6.9)	6(8.6)	238(4.6)	21100(0.4)	1200(3.2)
C (6 weeks)	3(6.3)	3(6.3)	52(4.9)	20900(0.6)	1300(0.6)
D (8 weeks)	4(6.5)	2(9.2)	88(1.9)	20900(1.1)	800(2.1)
E (10 weeks)	3(6.9)	3(8.8)	86(4.7)	21000(1.5)	800(1.6)
F (12 weeks)	19(7.5)	2(9.2)	58(6.5)	21300(0.9)	800(3.4)

25°C with 1-2-3µM sulfide (System)/Amounts in µg/L	**Cu**	**Ni**	**Fe**	**Si**	**Al**
A (4 weeks)	5(7.9)	27(6.9)	358(5.2)	19800(0.9)	1100(3.8)
B (5 weeks)	7(7.0)	3(8.9)	37(5.2)	18700(1.0)	1000(3.5)
C (6 weeks)	8(7.8)	5(7.5)	76(5.6)	18200(0.9)	800(4.1)
D (8 weeks)	5(6.3)	2(5.2)	16(3.6)	17900(1.2)	300(3.4)
E (10 weeks)	8(6.3)	2(6.8)	41(4.3)	20100(1.1)	300(4.8)
F (12 weeks)	4(7.4)	2(8.7)	95(5.4)	21500(0.4)	400(2.8)

50°C with 1-2-3µM sulfide (System)/ Amounts in µg/L	**Cu**	**Ni**	**Fe**	**Si**	**Al**
A (4 weeks)	15(7.2)	55(6.9)	3101(10.1)	20900(0.5)	1100(6.1)
B (5 weeks)	4(6.6)	7(6.3)	83(9.6)	21700(1.4)	6200(1.7)
C (6 weeks)	4(7.3)	14(7.2)	580(4.7)	21400(0.8)	1400(3.4)
D (8 weeks)	8(7.3)	5(5.9)	70(6.9)	20600(0.4)	500(2.1)
E (10 weeks)	6(7.6)	11(6.2)	90(4.5)	23300(1.2)	400(25)
F (12 weeks)	4(6.6)	6(6.6)	34(9.4)	25400(0.3)	400(0.2)

Table 12 *Dissolved amounts of Cu, Ni, Fe, Si and Al ions in the ground water (solution) in contact with Cu-Ni coupons during 6 months-dynamic experiments. Numbers in parentheses correspond to the relative standard deviation in percentage.*

25°C w/o sulfide (System)/ Amounts in µg/L	**Cu**	**Ni**	**Fe**	**Si**	**Al**
A (6 weeks)	13(3.3)	6(4.6)	397(4.8)	19100(1.2)	100(2.8)
B (10 weeks)	7(3.4)	3(3.7)	66(5.9)	19800(1.0)	200(2.7)
C (14 weeks)	7(3.8)	2(4.8)	74(5.4)	25000(1.4)	200(1.1)
D (18 weeks)	13(3.1)	2(6.3)	62(6.7)	18300(1.0)	100(10)
E (22 weeks)	10(3.6)	2(2.7)	46(4.6)	20000(1.4)	1100(2.0)
F (26 weeks)	7(3.1)	2(4.4)	44(6.0)	19500(1.0)	100(6.8)

50°C w/o sulfide (System)/ Amounts in µg/L	**Cu**	**Ni**	**Fe**	**Si**	**Al**
A (6 weeks)	6(4.1)	3(2.7)	81(5.1)	20700(0.7)	400(1.1)
B (10 weeks)	8(3.6)	3(4.9)	187(5.3)	23500(0.3)	1200(2.4)
C (14 weeks)	7(4.0)	3(5.3)	57(5.9)	23200(0.7)	600(0.6)
D (18 weeks)	7(3.4)	7(7.1)	51(5.6)	21300(0.9)	500(1.6)
E (22 weeks)	7(4.6)	2(5.7)	50(5.4)	21300(0.5)	500(4.3)
F (26 weeks)	7(4.9)	2(5.2)	47(5.9)	21300(1.4)	500(4.1)

25°C with 1-2-3µM sulfide (System)/ Amounts in µg/L	**Cu**	**Ni**	**Fe**	**Si**	**Al**
A (6 weeks)	7(3.6)	5(5.6)	154(5.7)	20200(0.5)	100(4.3)
B (10 weeks)	10(2.8)	3(4.1)	83(5.7)	20000(1.3)	100(4.1)
C (14 weeks)	8(2.9)	2(6.1)	56(5.6)	21700(0.9)	200(3.0)
D (18 weeks)	7(3.2)	3(6.9)	58(6.3)	19600(2.2)	100(1.1)
E (22 weeks)	7(3.7)	2(6.2)	50(5.6)	19900(1.1)	100(13)
F (26 weeks)	7(3.5)	2(6.5)	51(5.7)	20400(1.7)	100(13)

50°C with 1-2-3µM sulfide (System)/ Amounts in µg/L	**Cu**	**Ni**	**Fe**	**Si**	**Al**
A (6 weeks)	6(3.9)	6(5.0)	126(6.0)	22400(0.7)	400(0.8)
B (10 weeks)	7(3.3)	3(4.9)	77(6.1)	22300(0.4)	400(0.4)
C (14 weeks)	7(3.6)	2(3.2)	60(5.6)	25100(0.1)	500(2.4)
D (18 weeks)	7(3.5)	2(6.9)	46(5.6)	22500(0.4)	500(2.8)
E (22 weeks)	8(3.7)	2(6.2)	52(5.5)	22800(0.5)	500(2.1)
F (26 weeks)	7(3.9)	2(4.9)	58(5.4)	22200(0.5)	400(2.4)

Table 13 *Dissolved amounts of Cu, Ni, Fe, Si and Al ions in the ground water (solution) without coupon during 3 & 6 months dynamic experiments. Numbers in parentheses correspond to the relative standard deviation in percentage.*

3months 25°C w/o coupon (System)/ Amounts in µg/L	**Cu**	**Fe**	**Si**	**Al**
A (4 weeks)	900(4.3)	<10	18100(0.3)	1000(2.6)
B (5 weeks)	<10	<10	18100(0.2)	900(4.4)
C (6 weeks)	<10	<10	17500(0.8)	800(4.8)
D (8 weeks)	300(2.7)	<10	17800(0.5)	300(5.6)
E (10 weeks)	<10	<10	19000(0.3)	200(3.4)
F (12 weeks)	<10	<10	20500(0.4)	200(3.2)

3months 50°C w/o coupon (System)/ Amounts in µg/L	**Cu**	**Fe**	**Si**	**Al**
A (4 weeks)	100(2.7)	800(1.2)	23000(0.7)	1100(7.4)
B (5 weeks)	<10	2400(0.5)	25100(1.1)	900(6.6)
C (6 weeks)	<10	<10	23900(0.8)	1000(10)
D (8 weeks)	<10	<10	22600(0.5)	200(6.2)
E (10 weeks)	<10	<10	23400(0.8)	200(4.4)
F (12 weeks)	<10	<10	24800(1.4)	200(4.2)

6months 25°C w/o coupon (System)/ Amounts in µg/L	**Cu**	**Fe**	**Si**	**Al**
A (6 weeks)	8(4.2)	53(5.8)	19200(0.5)	200(7.2)
B (10 weeks)	11(4.4)	63(12.7)	20400(0.4)	100(3.5)
C (14 weeks)	11(4.0)	107(6.1)	21800(1.5)	200(0.8)
D (18 weeks)	8(3.4)	133(5.7)	20300(0.7)	300(1.9)
E (22 weeks)	7(4.2)	54(5.8)	19800(0.3)	100(13)
F (26 weeks)	10(3.9)	69(5.7)	19000(1.5)	100(15)

6months 50°C w/o coupon (System)/ Amounts in µg/L	**Cu**	**Fe**	**Si**	**Al**
A (6 weeks)	<10	200(29)	21100(0.7)	400(3.3)
B (10 weeks)	<10	<20	22900(0.6)	500(0.9)
C (14 weeks)	<10	<20	26200(0.5)	500(1.7)
D (18 weeks)	200(19)	<10	25100(2.0)	700(19)
E (22 weeks)	<10	<10	23000(2.0)	400(2.0)
F (26 weeks)	<10	<10	19800(0.3)	200(2.3)

Here for static experiments, Cu, Ni, and Fe concentrations generally are not affected much by time, temperature or sulfide presence. Copper (Cu) concentrations remain consistently low across

all time points, with slight change observed at 50°C for 6 months with sulfide (37 µg/L) (***Table 9***). Nickel (Ni) concentrations tend to be more stable but show an increase in one system (103 µg/L) at 50°C particularly at 6 months with presence of sulfide. Iron (Fe) concentrations demonstrate significant fluctuations, highest dissolution was observed in the presence of sulfide at 50°C (526 µg/L) after 6 months (***Table9***). A silicon (Si) concentration seems to be increased at elevated temperature compared to room temperature ***(Table10***).

Overall, Cu, Ni, and Fe concentrations suggest minimal dissolution. The measured concentration of silicon, aluminium and iron is quite similar to the concentration of equilibrium bentonite slurry where Si concentration is ~13000 µg/L, Al concentration is ~500 µg/L and Fe concentration is ~400 µg/L. Without coupons there is only dissolution of iron, silicon and aluminium compared to copper and nickel (***Table10***). The dissolution of iron, silicon and aluminium was mainly due to bentonite. For dynamic experiments, the concentration of Si variesis quite in agreement with concentration of simulated groundwater where Si concentration is ~17000 µg/L (***Table2***). Results of concentrations of dissolved ions in dynamic experiments (***Table 11 & Table12***) were comparable with that of static experiments. Overall, temperature, time and the presence of sulfide does not have significant effect on the concentrations of Cu, Ni, Fe and Al. The uncertainties suggest that variations in ions concentration lie within the scatter of the data. Here, Cu, Ni dissolution is mainly due to cupronickel corrosion whereas Fe, Si, Al concentrations indicate clay dissolution not metal corrosion. The observed differences in most cases may rather be attributed to experimental uncertainties.

Cu and Ni concentration observed in the static experiments and dynamic experiments lie in lower range (below 1. E-6 mol/L). Under the experimental pH conditions, solubility concentration for $Ni(OH)_2$ is around 1. E-4 mol/L at pH 8 **(González-Siso et al., 2018)**. This can be taken as a first indication that Ni(II) released due to cupronickel corrosion is bound to clay minerals and cannot be found as dissolved species in solution. A similar trend was observed for copper corrosion products.

Table 14 *Determination of Cu, Ni, Fe, Si and Al concentrations for a bentonite that was in contact with CuNi coupons has been digested in acid and the resulting liquid phase has been quantified by using ICP-MS for 6 months dynamic experiment and using reference.*

(Dynamic) System/ Amounts in µg/g	**Cu**	**Ni**	**Fe**	**Si**	**Al**
6months 25°C Cu-Ni w/o sulfide	51(1.7)	275(1.9)	16550(1.3)	248800(1.4)	34220(1.9)
6months 25°C Cu-Ni with 1-2-3 µm sulfide	194(3.5)	313(3.2)	15420(1.0)	229300(1.7)	34040(1.8)
6months 50°C Cu-Ni w/o sulfide	177(1.3)	197(1.1)	17080(0.7)	248600(0.4)	46280(0.8)
6months 50°C Cu-Ni with 1-2-3 µm sulfide	221(1.0)	496(1.0)	16840(0.7)	241400(1.1)	38550(0.9)
Raw MX-80 bentonite	4(1.2)	4(1.7)	16450(0.8)	249300(1.0)	38900(3.9)

Determination of Cu, Ni, Fe, Si and Al concentration for a bentonite that was in contact with CuNi coupons and raw MX-80 bentonite without coupon has been digested in acid and the resulting liquid phase has been quantified by using ICP-MS for 6 months dynamic experiment. The variation in concentration of Cu and Ni which was interest for CuNi alloy was shown in ***(Table 14)***. The concentration of mainly Cu, Ni increases in presence of CuNi coupon indicating that Cu and Ni ions release due to cupronickel corrosion are mainly sorbed on the clay surface rather than remaining dissolved into the solution. Copper and nickel concentrations are notably low in raw MX-80 bentonite (4 µg/g) which is quite low compared to found in literature **(Zhao et al., 2010)** suggesting minimal mobilization in these environments.

For Cu-Ni systems, Cu concentrations increase with temperature and with the addition of sulfides. For instance, the Cu concentration increases from 51 µg/g at 25°C to 177 µg/g at 50°C without sulfides, and further rises to 221 µg/g with sulfide addition at 50°C, indicating the role of temperature and sulfide presence in enhancing Cu solubility or mobilization. Nickel shows consistently high concentrations in Cu-Ni systems, particularly without sulfides at 25°C (275 µg/g). The concentration remains relatively high even with sulfides and at elevated temperatures. For example, at 50°C without sulfides, Ni reaches 197 µg/g, and with sulfides, it increases to 496 µg/g. The association of Ni with bentonite demonstrates its limited mobility in the solution although system tries to achieve equilibrium. Concentration of Fe, Si and Al are lying within experimental uncertainty. The analyses of bentonite show that Cu and Ni being released via corrosion processes are retained due to interaction with bentonite either by surface adsorption or formation of secondary alteration phases. There is more Ni retained at the bentonite surface than Cu although CuNi alloy contains much more Cu than Ni. So, the analysis of corrosion layer suggests that, it has different behaviors.

3.1.3 pH / E_h evolution

The pH and E_h values of a system, along with dissolved metals amounts, play a significant role and allow identification of thermodynamically stable corrosion phases in *Pourbaix* diagram (***Figure 3***) under those conditions.

Table 15 *pH / Eh evolution of Cu-Ni alloy in contact with MX-80 bentonite slurry after 3, 6 and 9 months static experiments.*

System	pH	E_h w.r.t SHE(mV)
3months 25°C w/o sulfide	8.17±0.05	225±50
3months 25°C with 3µM sulfide	8.09±0.05	271±50
3months 50°C w/o sulfide	8.04±0.05	283±50
3months 50°C with 3µM sulfide	7.58±0.05	167±50
6months 25°C w/o sulfide	8.09±0.10	287±50
6months 25°C with 3µM sulfide	7.94±0.10	245±50
6months 50°C w/o sulfide	8.34±0.10	297±50
6months 50°C with 3µM sulfide	8.09±0.10	263±50
9months 25°C w/o sulfide	8.01±0.10	330±50
9months 25°C with 3µM sulfide	7.98±0.10	329±50

Table 16 pH / Eh evolution without coupon in MX-80 bentonite slurry after 3, 6 and 9 months static experiments.

System	pH	E_h w.r.t SHE (mV)
3months 25°C w/o coupon	8.55±0.05	-7±50
3months 50°C w/o coupon	8.03±0.05	-55±50
6months 25°C w/o coupon	8.19±0.10	115±50
6months 50°C w/o coupon	8.09±0.10	129±50
9months 25°C w/o coupon	8.06±0.10	167±50

The pH and E_h values for Cu-Ni alloy for static experiments were shown in (***Table 15***) and without coupons were shown in (***Table 16***) for different systems. The in-situ measured pH and Eh values for most of the Cu-Ni systems either remain stable or change slightly. During the entire reaction time under static conditions, the measured *in situ* pH and E_h did not evolve much from the values of the starting pre-equilibrated bentonite (pH = 8.15; E_h = 245 mV) suspension. pH values were ranging from 7.98 to 8.01 and Eh values ranging from 167 mV to 330 mV. Results suggest that neither the presence of sulfide nor temperature had any significant effect on pH and E_h evolutions. It is interesting to note that E_h values are clearly positive, in contrast to experiments with the iron based materials, suggesting that conditions did not become reducing even in the presence of added sulfide. Without coupons pH values decreases and Eh values increase in most of the cases.

Upon removal of the coupons from the suspension, the interface was brownish (***appendices section***) in some experiments performed at 50°C, and rather pale brown for experiments at 25°C, suggesting that reactions occurred at the coupon/suspension interface despite the absence of limited change for pH and E_h evolutions. Since, the color of bentonite suspension does not change, hence the redox state change of structural iron of bentonite **(Ishidera et al., 2008)** may be excluded, also supported by the measured positive *in situ* E_h values (***Table 15***). Instead, observations suggest the formation of secondary copper and/or nickel compounds accumulating at the coupon surface.

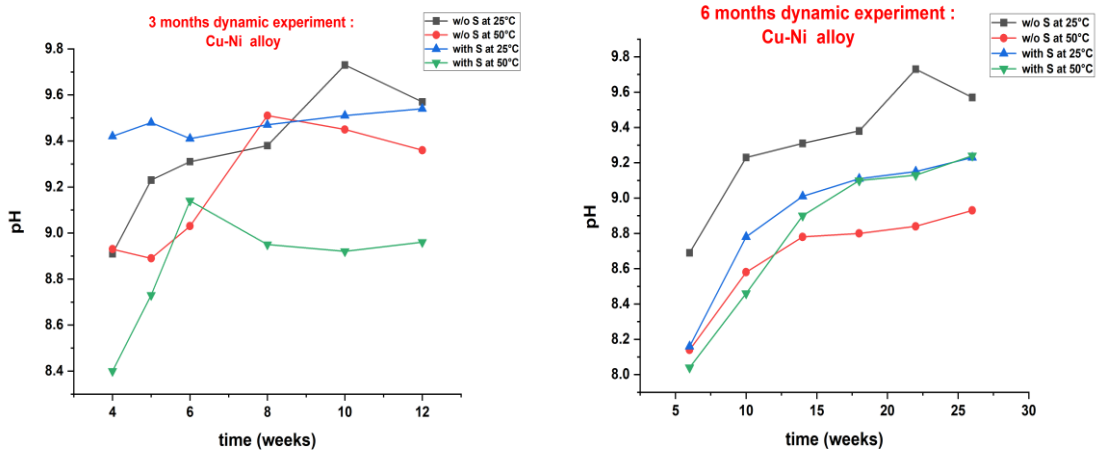

Figure 16 The pH evolution of the Cu-Ni coupons in ground water (solution) during 3 (left side) and 6 months (right side) dynamic experiments (±0.1 is uncertainty).

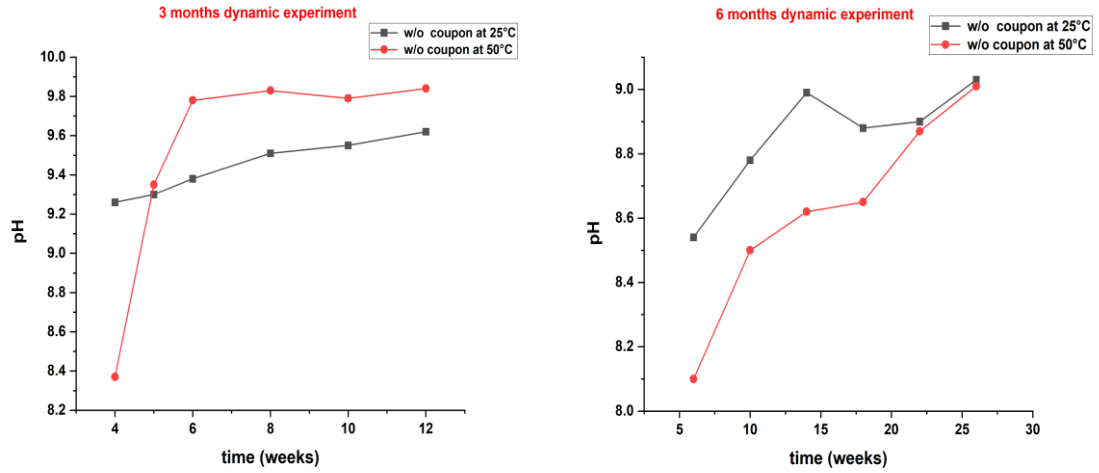

Figure 17 *The pH evolution without coupon in ground water (solution) during 3 (left side) and 6 months (right side) dynamic experiments (±0.1 is uncertainty).*

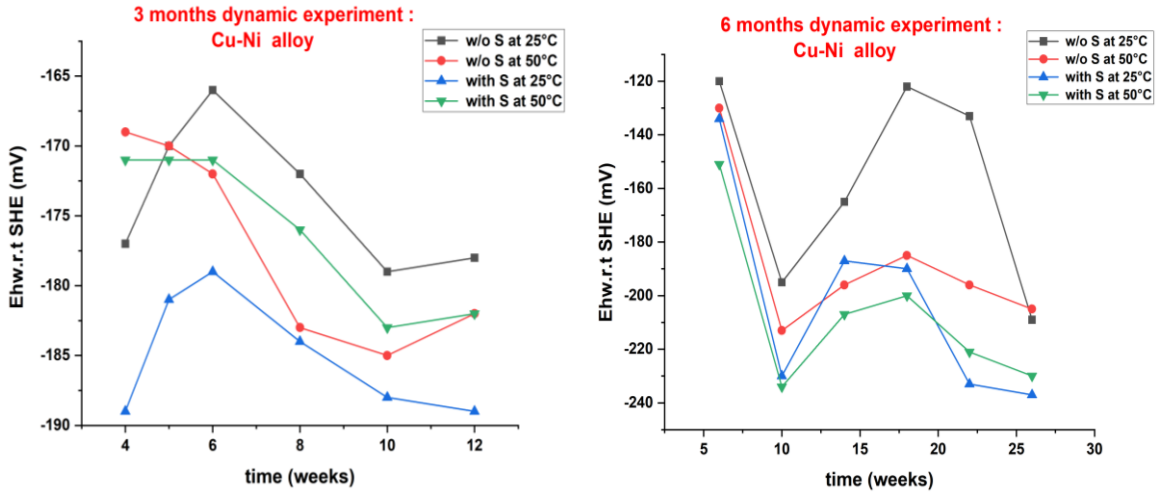

Figure 18 *The Eh evolution of the Cu-Ni coupons in ground water (solution) during 3 (left side) and 6 months (right side) dynamic experiments (±50mV is uncertainty).*

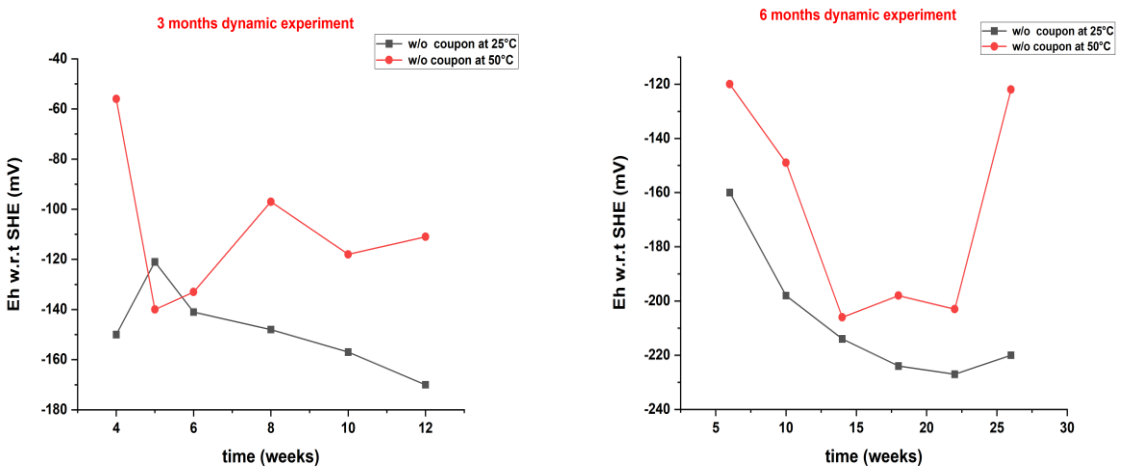

Figure 19 *The Eh evolution without coupon in ground water (solution) during 3 (left side) and 6 months (right side) dynamic experiments (±50mV is uncertainty).*

The pH and E_h values for Cu-Ni alloy for dynamic experiments were shown in (***Figure 16 & Figure 18***) and without coupons was shown in (***Figure 17 & Figure 19***) for different systems. The pH measured at reactor outlet increased with time to values around 9 and moving towards pH of inlet ground water (pH 9.8) in most of the experiments (***Figure 16***), the lowest increase being observed for the experiment at 50°C without sulfide for 6 months reaction time. Compared to experiments under static conditions, measured pH values are significantly higher. Measured E_h values are all very comparable and clearly negative, ranging from -120 mV to -230 mV, and do not exhibit any significant variation with time, temperature of sulfide presence. These outcomes suggest that given pH and Eh values lie in the stability range of metallic copper with respect to the Pourbaix diagram of copper **(Puigdomenech & Taxén, 2000)**. Also, values obtained here suggest the development of reducing conditions, which contrasts with results from experiments under static conditions. As in most of the experiments with other iron materials, reactors have a PTFE inner liner and metallic filters made of stainless steel at inlet and outlet, and these components are not expected to have any effect on pH and E_h values.

Interestingly, the observed pH and E_h values and their evolution with time compare well with those obtained in experiments under dynamic conditions without coupons. Obtained pH and Eh values are in same range with and without presence of metallic coupons in most of the system. Though pH variations can be interpreted as dilution of the suspension by the inlet water, this may hardly explain observed E_h evolutions because the redox potential of the inlet water is positive (115 mV), suggesting that either the protocol used to measure E_h (i.e., in water at outlet) or the used setup may have an effect on these values. Results from the analysis of the corroded specimens will provide complementary information as the nature of formed corrosion products will allow drawing some conclusions.

3.1.4 Corrosion rate

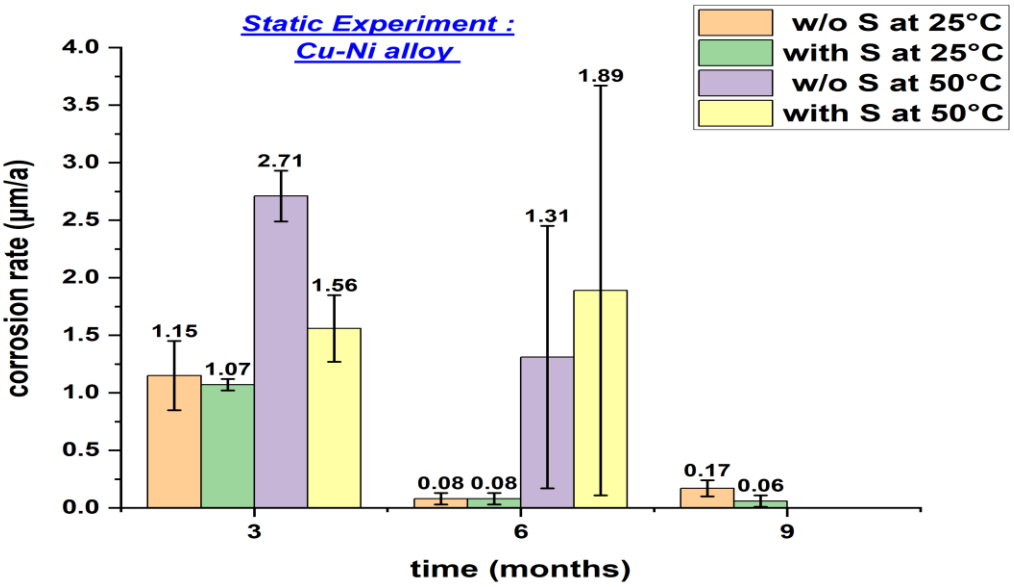

Figure 20 *Corrosion rates of all Cu-Ni coupons obtained after 3, 6 and 9 months static experiments.*

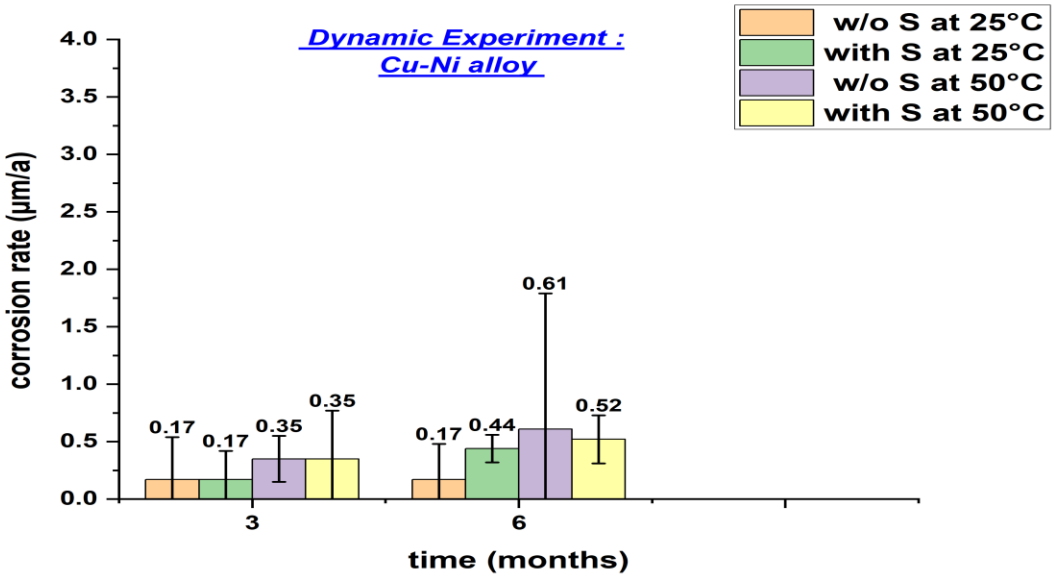

Figure 21 *Corrosion rates of all Cu-Ni coupons obtained after 3 and 6 months dynamic experiments.*

The corrosion rates of copper nickel alloy for static and dynamic experiments were calculated using the weight loss method and are shown in (***Figure 20***) for 3, 6 and 9 months of static experiments and in (***Figure 21***) for 3 and 6 months dynamic experiments. The procedure for post-corrosion sample cleaning was described in ***section2.5.6.***

After 3 months of static experiment without sulfide at 25°C in contact with the bentonite suspension, the corrosion rate obtained was 1.15±0.30 µm/a (***Figure 20***) is comparable with reported average corrosion rate of (~0.17 µm/a) for cold-sprayed copper and average corrosion rate of wrought copper (~0.24 µm/a) embedded within compacted MX-80 and exposed to natural granitic porewater for 394 days in the MaCoTe experiment **(Reddy, Padovani, Rance, et al., 2021)**. However, note that corrosion rate of copper nickel alloy for 3 months static experiments was overestimated due to adhering of bentonite. Apart of this, the difference in reaction time (90 days vs 394 days) and the difference in temperature (25°C vs rock temperature) can also account for the different rates. In addition, the use of a suspension instead of compacted bentonite also plays a role because of the larger amount of water available. Increasing the temperature to 50°C significantly increased the corrosion rate in the present study, in agreement with reported findings **(Hesketh et al., 2023)**. Corrosion rates increase with temperature because of decreased activation energy for e.g., chemical and electrochemical reactions; however measured corrosion rate have high uncertainties in most data. Corrosion rates changes systematically with increasing reaction time, for instance at 25°C from 1.15±0.30 µm/a after 3 months to 0.17±0.07 µm/a after 9 months. This result also agrees with reported corrosion rate evolutions in general and hints at the formation of a protective passivation layer at the coupon surface. The same trends were observed in experiments performed in the presence of sulfide, and the rates were in similar range compared to experiments in the absence of added sulfide in static experiment systems. Initially the corrosion rate is high due to presence of residual oxygen, once all residual oxygen is consumed the corrosion rate decreases for most of the samples. Addition of sulphide has not much affect for the static experiments

It was observed from the dynamic experiment results of corrosion rate measurements that values for Cu-Ni alloy are in range from 0.17±0.31-0.44±0.12 µm/a at room temperature and increased to 0.35±0.20-0.52±0.21 µm/a at elevated temperature due to increase in reaction kinetics. Corrosion rates at room temperature without added sulphide do not change over time observed even after six months of dynamic experiments. Most of the Cu and Ni adsorbed in bentonite and some of them may be present at metal/bentonite interface in the form of secondary phase. Higher corrosion rate was observed at elevated temperature compared to room temperature for dynamic experiment. Results of corrosion rates for dynamic experiments are comparable with long term static experiments (9 months) and also has good match with the literature results for the in situ MaCoTe experiments **(Reddy, Padovani, Rance, et al., 2021)**.

3.1.5 Secondary phase characterization

3.1.5.1 Static condition systems (3, 6 & 9 months)

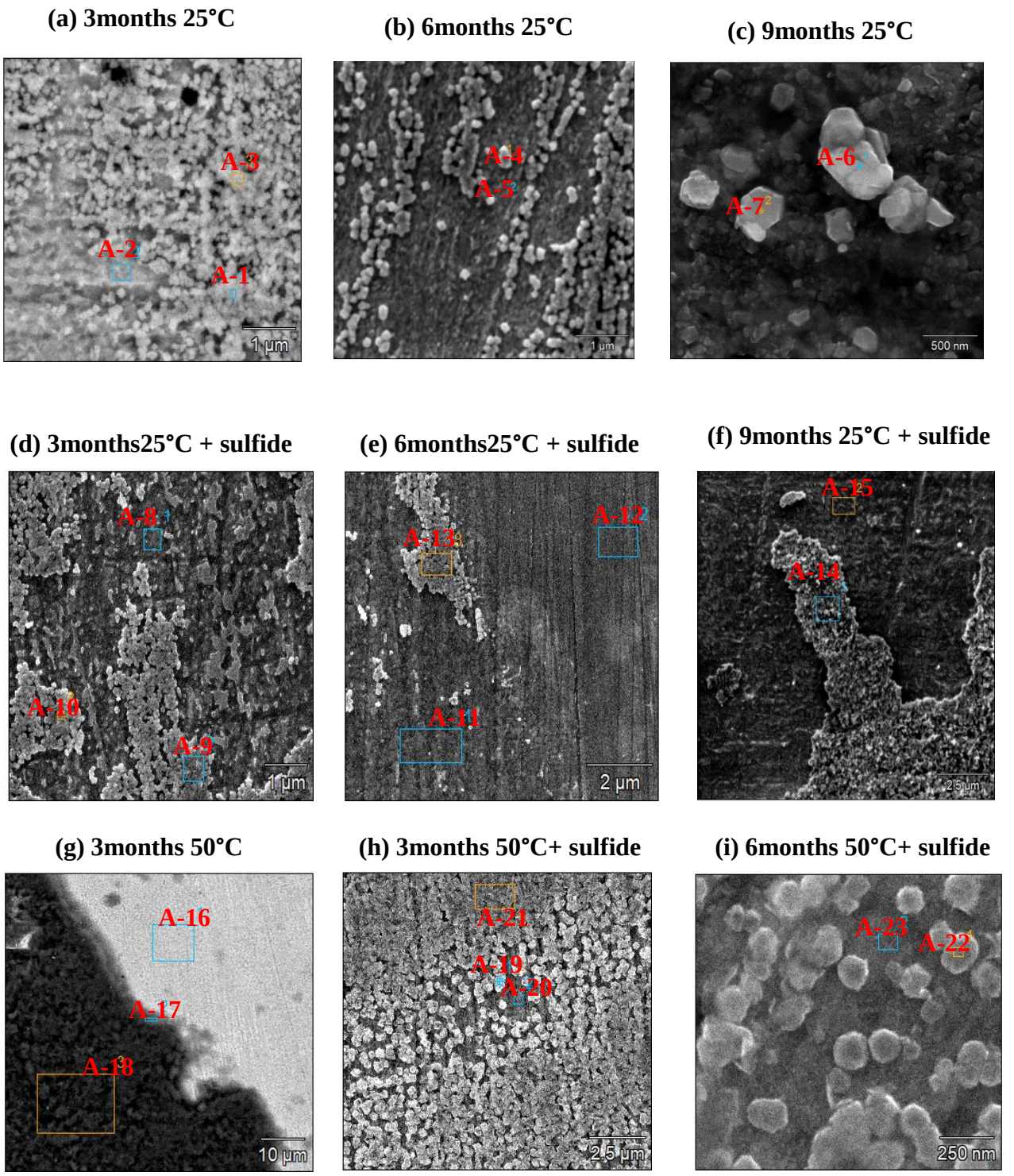

Figure 22 *Scanning electron micrographs (in SE mode) of all Cu-Ni coupons corroded for 3, 6 and 9 months under static conditions at different temperature (exact conditions are indicated above the micrographs). Marked alpha-numeric areas were selected for EDXS analysis, quantitative results are provided in* ***Table 17****.*

Table 17 *Relative atomic concentrations by EDXS analyses at selected areas shown in above* ***Figure22****. Relative errors are estimated to be within ± 10%.*

Area	C	O	S	Al	Si	Mn	Fe	Ni	Cu
A-1	3.6	13.5	/	/	0.5	0.7	/	16.5	65.2
A-2	3.0	1.6	/	/	0.3	1.1	0.6	26.7	66.8
A-3	3.7	12.8	/	/	0.6	0.7	0.4	17.4	64.2
A-4	2.2	23.3	/	/	/	/	/	0.0	74.5
A-5	2.3	3.0	/	/	/	/	/	21.8	72.9
A-6	12.3	16.5	/	/	0.9	0.5	0.7	15.5	53.0
A-7	13.3	22.5	/	/	/	0.8	0.6	18.1	44.1
A-8	7.5	/	/	/	/	1.1	0.6	31.5	59.2
A-9	3.9	4.6	/	/	0.2	1.0	0.7	28.2	61.4
A-10	3.9	7.2	/	0.2	0.3	1.0	0.5	26.1	60.6
A-11	2.7	1.4	/	/	/	1.3	0.9	37.1	56.6
A-12	3.3	1.6	/	0.3	0.3	0.8	1.5	37.9	54.3
A-13	3.3	10.5	/	/	0.4	0.9	0.6	29.3	55.0
A-14	2.3	21.5	/	/	/	/	/	/	76.3
A-15	3.3	/	/	/	/	/	/	19.5	77.1
A-16	5.1	17.3	5.0	/	0.5	/		15.9	56.3
A-17	5.6	53.9	1.2	6.6	13.9	/	0.7	2.6	14.3
A-18	4.5	60.4	0.2	8.1	21.7	/	1.0	0.6	/
A-19	7.6	9.1	10.1	/	/	/	/	16.9	56.2
A-20	5.8	/	6.2	/	/	1.5	0.9	28.1	58.4
A-21	5.2	5.7	9.6	/	/	/	/	16.6	62.4
A-22	5.2	3.7	4.5	/	/	/	0.9	23.9	61.8
A-23	4.3	1.0	2.7	/	/	1.2	/	28.6	62.1

Scanning electron microscopy was subsequently applied to analyze the corroded CuNi coupons. SEM-EDXS analysis micrographs for various selected areas were shown in (***Figure 22***) and their atomic concentration results were tabulated in (***Table 17***). EDXS analyses results of selected areas shown in (***Figure 22***) show the presence of Cu-rich oxide particles in most of the samples, sometimes with low amounts of associated sulfur (A-16 to A-23, ***Table 17***) for elevated temperature for three and six months in presence of added sulfide. Here, EDXS spectra recorded on well separated particles allow concluding the absence of Fe and Ni associations with the particles of corrosion products, which may be adsorbed on adjacent bentonite or dissolved in pore water. Sulfur is only detected in some samples, ruling out the compelling formation of Cu sulfide as corrosion products. Although minor amount of iron is present in CuNi system the formation of iron silicate is not observed in any system in presence of bentonite.

SEM-EDXS results shown above, and obtained using the FEI Quanta 650 FEG microscope, were complemented by electron backscatter diffraction (EBSD) using the sample corroded for 6 months at 25°C without added sulfide with the Zeiss Crossbeam 350 KMAT microscope. The acceleration voltage was set to 2.5 kV (compared to 15 kV using the FEI microscope) to record EDXS spectra, which will prevent picking up signal from the substrate. This allowed revealing a Cu:O atomic ratio of 2:1, thus suggesting the presence of Cu_2O (cuprite) particles. For EBSD analysis, the acceleration voltage was subsequently increased to 15 kV, and EBSD scans were

optimized in areas of 500 nm x 750 nm. By optimizing the indexing parameters, including the Hough transform parameters (feature used in image analysis) and number of reflections, a mean angular deviation of 0.29° was achieved, enabling to index 10 out of 11 bands (***Figure 23***). The bands indexing was consistent with a cubic crystal structure. Using this information, secondary phases could be identified as Cu_2O **(Kirfel & Eichhorn, 1990)**, which is consistent with the EDXS quantitative analysis at 2.5 kV. Based on electron micrographs and EDXS results (***Figures 22C***), also based on obtained pH and Eh results (Pourbaix diagram, ***Figure 3***) **(Puigdomenech & Taxén, 2000)** formation of cuprite takes place at the exposed surface of CuNi coupons in most of the static experiments.

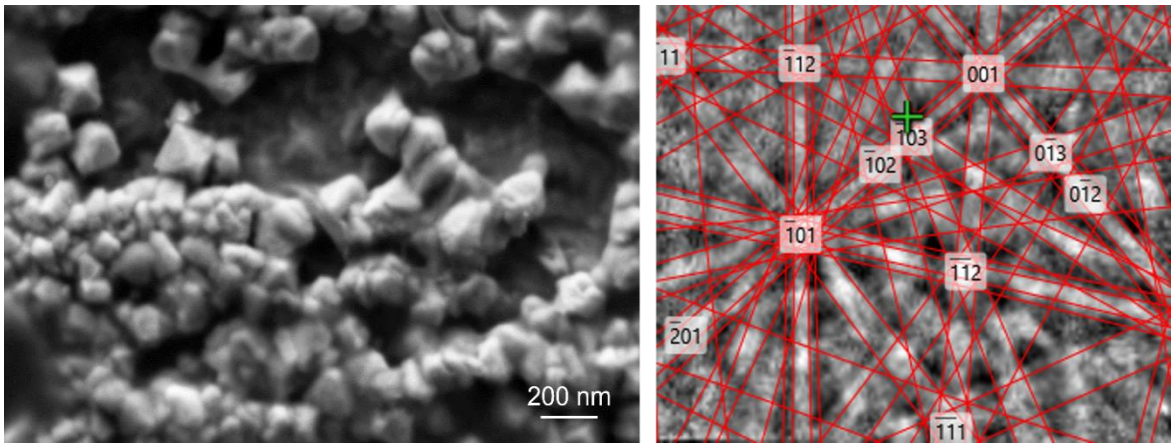

Figure 23 *Scanning electron micrograph recorded at 2.5 kV acceleration voltage (left), and Kikuchi pattern and indexing with Cu2O (red) (right).*

Overall similar corrosion products were obtained for all coupons of static experiments under different experimental conditions. Corrosion products mainly consist of cuprite for most of the samples, however minor amount of Cu_xS_y was also observed in some sample (with added sulfide) at elevated temperature for 3 months of static experiment (***Figure 22h***).

The XRD analysis of corroded CuNi coupons obtained after three, six and nine months of static experiments was carried out and its diffractograms were shown in (***Figure 24***). The primary peak in the XRD spectrum for three, six and nine months of static experiments correspond to the metallic cupronickel phase which is starting material. Apart of this, other reflections like Illite which can be observed on the exposed surface in (***Figure 24***) specially for three and six months come from the adhered bentonite and remaining peaks correspond to corrosion products or secondary phase cuprite that was detected in most of the samples of three, six and nine months of static experiments as shown in (***Figure 24***). Observed secondary phase (Cu_2O) was also confirmed by SEM-EDXS analysis which was already discussed in previous section of SEM analysis.

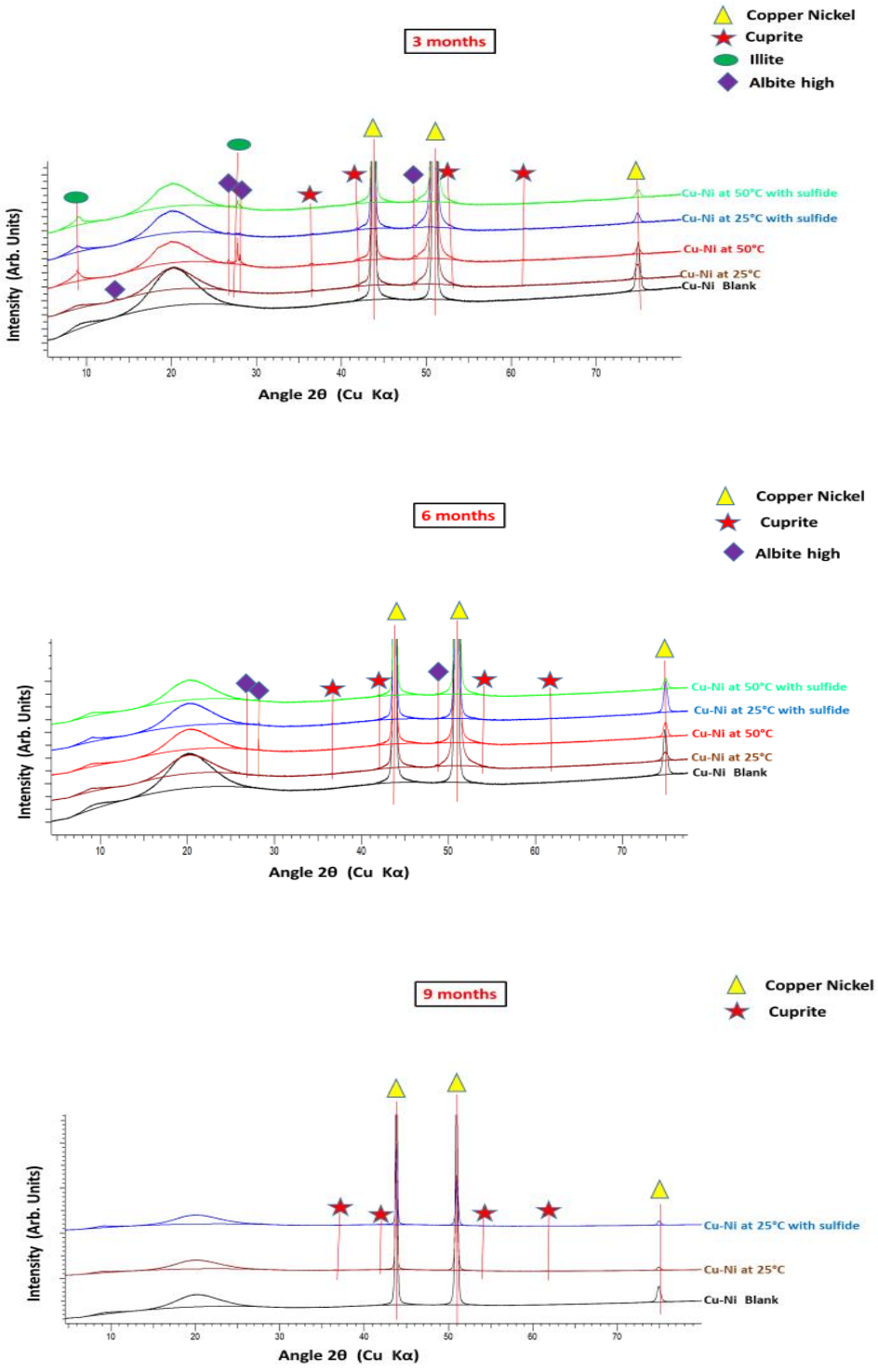

Figure 24 *X-ray diffractograms recorded on the corroded CuNi coupons after 3 months (top), 6 months (middle) and 9 months (bottom) reaction time under static conditions (exact conditions are indicated on individual XRD plot).*

There is not much difference observed in 9 months coupons compared to three and six months in terms of secondary phase (corrosion products) from XRD analysis. The broad reflection around 10 and 20 two theta is due to air scattering effect (***Figure 24***) which was common for all coupons tested under anoxic conditions using anoxic holder. Findings suggest that secondary phases like Cu_2O (PDF74-1230) formed in too low amounts and are weakly crystalline while in some coupons covered by bentonite. Although sulfide was added in some experiments it does not form any secondary products because the amount added may be too low to be effective. Overall XRD analysis provides insights into the phases present in CuNi coupons after corrosion, which is critical for understanding the extent of corrosion and deriving a corrosion mechanism.

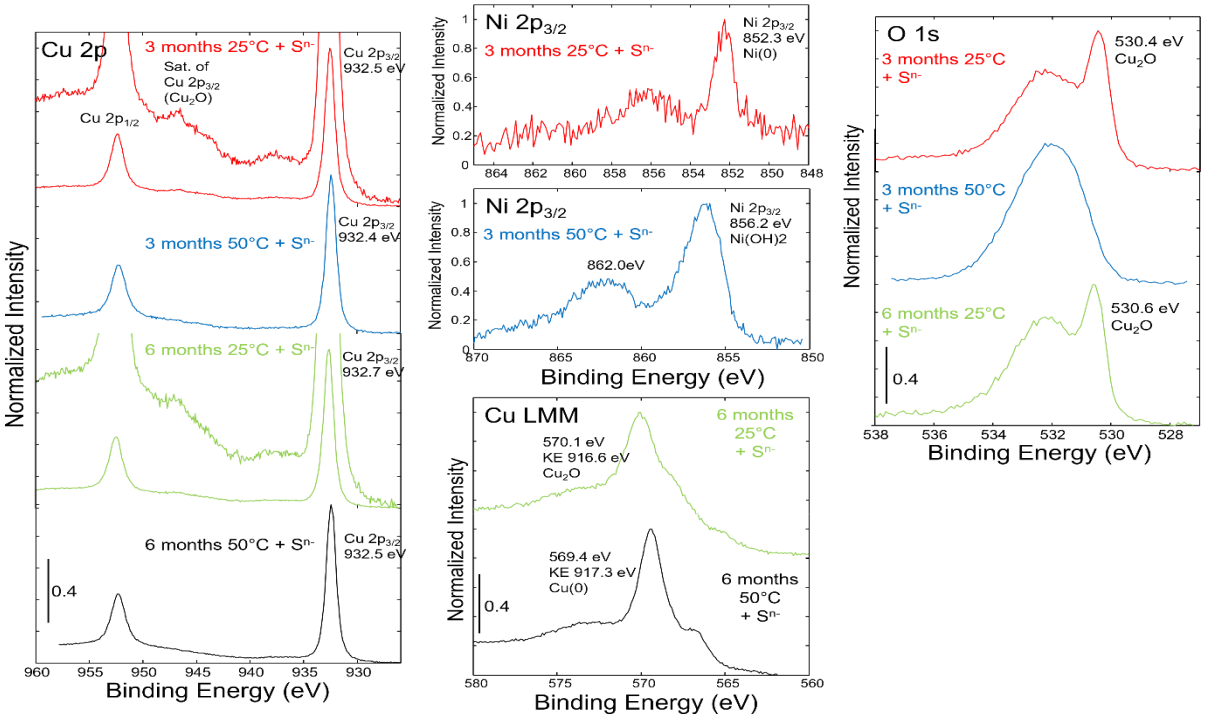

Figure 25 *X-ray photoelectron spectra recorded on Cu-Ni coupons corroded under static conditions (exact conditions are indicated on the individual graphs).*

Complementary X-ray Photoelectron Spectroscopy measurements provided additional speciation information. XPS spectra recorded for selected Cu-Ni coupons under static conditions were shown above in (***Figure 25***). The spectral lines here gave information about oxidation state and speciation of copper, nickel and oxygen. Measurements were challenging especially for Cu because 2p narrow lines of metallic Cu and Cu_2O are very close. Recording Cu LMM and complementary O 1s narrow lines proved to be very helpful in the identification of the Cu speciation. After 3 months at 25°C, the presence of Cu_2O was detected at the coupon surface together with Ni **(Karnland O & Motamedi M)**, while Cu **(Karnland O & Motamedi M)** and $Ni(OH)_2$ were detected in the parallel experiment at 50°C. The Cu speciation did not evolve between 3 and 6 months with the presence of Cu_2O at 25°C and Cu **(Karnland O & Motamedi**

M) at 50°C, but no Ni could be detected in samples after 6 months certainly because of its too low concentration at the surface. These findings show that at 25°C Cu is oxidized to Cu (I), only at 50°C Ni oxidation to Ni(II) becomes visible. The presence of added sulfide had no significant impact on the Cu and Ni speciation (except sample for 6 months at 50°C with added sulfide) at both temperatures and both exposure times, with comparable speciation found in all experiments (***Figure 25***)**.** Sulfides could be detected at the surface of some coupons (with added sulfide), with larger amounts detected in experiments at 50°C (***Table 18***, point 18-19) and also confirmed by S speciation as shown in appendices (***Figure A11***).

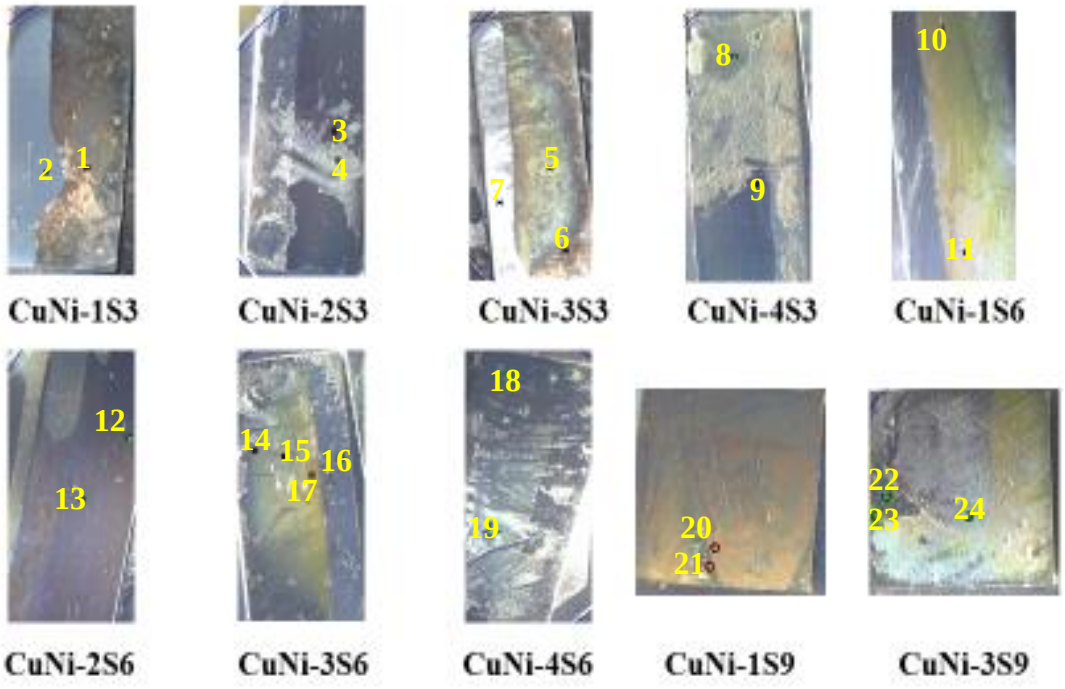

Figure 26 *X-ray photoelectron images of Cu-Ni coupons corroded under static conditions (exact conditions are indicated on the individual sample, details of conditions are available in appendix). Marked points were selected for atomic concentration analysis, quantitative results are provided in* ***Table 18****.*

Table 18 *Relative atomic concentrations by XPS analyses at selected points of Cu-Ni coupons for static experiments shown in above* ***Figure 26****. Relative errors are estimated to be within ± 10% (Here each measurement has two type of atomic concentration: one with presence of carbon and one without carbon presence).*

Point	C	N	O	Na	Mg	Al	Si	S	Cl	Ca	Fe	Ni	Cu
1S3-1	27.5	1.7	40.0	/	1.7	/	6.4	1.6	1.7	0.5	/	1.1	17.9
	/	2.4	55.1	/	2.4	/	8.8	2.2	2.3	0.7	/	1.6	24.7
1S3-2	64.3	/	17.3	/	/	/	/	/	/	/	/	6.2	12.3
	/	/	48.3	/	/	/	/	/	/	/	/	17.4	34.3
2S3-3	27.3	1.1	36.7	0.6	1.1	/	3.4	6.8	0.9	/	/	2.3	19.9
	/	1.5	50.5	0.8	1.5	/	4.7	9.4	1.2	/	/	3.1	27.3

2S3-4	9.4	/	61.4	1.5	1.1	5.8	19.7	/	0.1	/	1.0	/	/
	/	/	67.8	1.6	1.3	6.4	21.7	/	0.2	/	1.1	/	/
3S3-5	25.8	1.8	29.6	1.0	1.0	/	2.4	2.4	1.5	0.6	/	1.2	32.9
	/	2.4	39.9	1.4	1.4	/	3.3	3.2	2.0	0.8	/	1.6	44.3
3S3-6	29.7	2.0	29.0	/	1.7	/	3.4	2.9	1.4	/	/	0.9	29.0
	/	2.8	41.2	/	2.4	/	4.8	4.1	2.0	/	/	1.3	41.3
3S3-7	51.0	/	31.4	/	0.4	/	2.6	/	0.5	/	/	7.2	7.1
	/	/	64.0	/	0.8	/	5.2	/	0.9	/	/	14.6	14.5
4S3-8	10.6	0.3	61.8	1.3	0.9	5.6	18.2	/	0.2	0.2	0.9	/	/
	/	0.4	69.1	1.4	1.0	6.3	20.4	/	0.3	0.2	1.0	/	/
4S3-9	19.6	1.5	42.5	/	1.4	/	4.7	6.2	2.0	0.6	/	7.2	14.4
	/	1.8	52.9	/	1.7	/	5.8	7.8	2.5	0.7	/	9.0	17.9
1S6-10	21.0	1.4	45.1	0.8	1.3	/	9.0	1.1	2.0	0.5	/	/	18.0
	/	1.7	57.1	1.0	1.6	/	11.3	1.4	2.6	0.6	/	/	22.7
1S6-11	6.6	/	61.3	1.3	1.1	6.6	21.2	/	0.3	0.2	0.9	/	/
	/	/	65.7	1.4	1.2	7.1	22.7	/	0.3	0.3	1.0	/	/
2S6-12	15.7	/	58.0	1.2	0.9	/	14.5	2.8	/	/	/	/	6.9
	/	/	68.8	1.4	1.1	/	17.2	3.3	/	/	/	/	8.2
2S6-13	18.6	/	50.2	0.9	0.6	/	11.2	5.4	/	/	/	/	13.1
	/	/	61.6	1.1	0.8	/	13.8	6.6	/	/	/	/	16.0
3S6-14	27.0	3.2	26.2	/	/	/	/	4.9	3.7	0.6	/	/	34.5
	/	4.4	35.9	/	/	/	/	6.7	5.1	0.8	/	/	47.2
3S6-15	4.3	/	63.3	1.4	1.4	7.0	20.8	/	0.2	0.3	1.2	/	0.2
	/	/	66.1	1.5	1.4	7.3	21.7	/	0.2	0.3	1.2	/	0.2
3S6-16	58.8	/	22.6	/	/	/	/	/	/	/	/	8.0	10.6
	/	/	54.8	/	/	/	/	/	/	/	/	19.5	25.7
3S6-17	22.6	1.4	34.6	/	/	/	2.7	2.0	2.5	/	/	1.0	33.3
	/	1.8	44.7	/	/	/	3.5	2.6	3.2	/	/	1.3	43.0
4S6-18	24.8	1.4	13.9	/	/	/	/	16.8	/	/	/	/	43.1
	/	1.8	18.5	/	/	/	/	22.4	/	/	/	/	57.3
4S6-19	26.8	1.8	25.1	/	0.6	/	/	14.0	0.8	/	/	/	30.9
	/	2.4	34.4	/	0.8	/	/	19.1	1.1	/	/	/	42.2
1S9-20	24.5	/	41.9	/	/	/	7.4	/	2.8	/	/	4.5	18.8
	/	/	55.6	/	/	/	9.8	/	3.8	/	/	5.9	25.0
1S9-21	30.7	/	38.5	/	/	/	5.9	0.4	2.9	/	/	3.6	18.0
	/	/	55.6	/	/	/	8.5	0.6	4.2	/	/	5.1	26.0
3S9-22	47.4	3.6	9.2	/	/	/	/	8.9	/	0.8	/	3.7	26.3
	/	6.9	17.5	/	/	/	/	17.0	/	1.6	/	7.0	50.0
3S9-23	26.0	2.3	38.6	0.2	/	/	5.8	3.3	2.1	/	/	1.6	20.2
	/	3.1	52.1	0.2	/	/	7.9	4.5	2.8	/	/	2.1	27.3
3S9-24	5.6	/	61.6	1.1	1.6	7.6	22.1	/	/	/	0.5	/	/
	/	/	65.2	1.1	1.7	8.0	23.4	/	/	/	0.5	/	/

The Cu-Ni coupons selected for XPS analysis were shown in (***Figure 26***) for static experiments under different experimental conditions. Relative atomic concentration using XPS for selected points on exposed surface of CuNi coupons were tabulated in (***Table 18***). A color change like golden green, blue-green, brownish and blackish was observed on the exposed coupon surface indicating the formation of different corrosion products (secondary phases). From atomic concentrations (***Table 18***) it is clear most of exposed surface consists of copper, oxygen and sulfur as chief elements which form corrosion products.

Here for coupon at 25°C with sulfide (CuNi-3S3) (***Figure 26***), atomic ratio (***Table 18***, *point 5, 6*) show possibility of CuO (brownish, ***Figure 26***) formation, whereas in most of the cases the copper to oxygen ratio is 2:1 and indicates formation of cuprite (Cu_2O). In some cases there is a possibility of presence of Cu_2O + Cu_2S (***Table 18***, *points 18, 19*). Thus, exposed corroded surface consist of inhomogeneous distribution of secondary phase on the surface of CuNi coupons for the static experiments. A dense layer of corrosion products like cuprite form for longer time period (9 months) in static experiments that results in a decrease of the corrosion rate with increasing time as discussed in corrosion rate measurement (***Figure 20***).

The position of the Cu $2p_{3/2}$ line (932.4-932.7 eV) would also agree with the presence of Cu_2S **(Biesinger, 2017)**, suggesting that the presence of this compound in low amounts cannot be excluded. However, bentonite contains low amounts of pyrite that may account for the detected low amounts of sulfides, at least for experiments performed in absence of added sulfide. The presence of NiS is excluded based on the position of Ni $2p_{3/2}$ line **(Legrand et al., 1998)**. Finally, only little Cu or Ni could be found associated with the clay surface, meaning that CuNi corrosion resulted in the formation of low soluble secondary phases at the coupon/suspension interface where the alloy is exposed.

3.1.5.2 Dynamic condition systems (3 & 6 months)

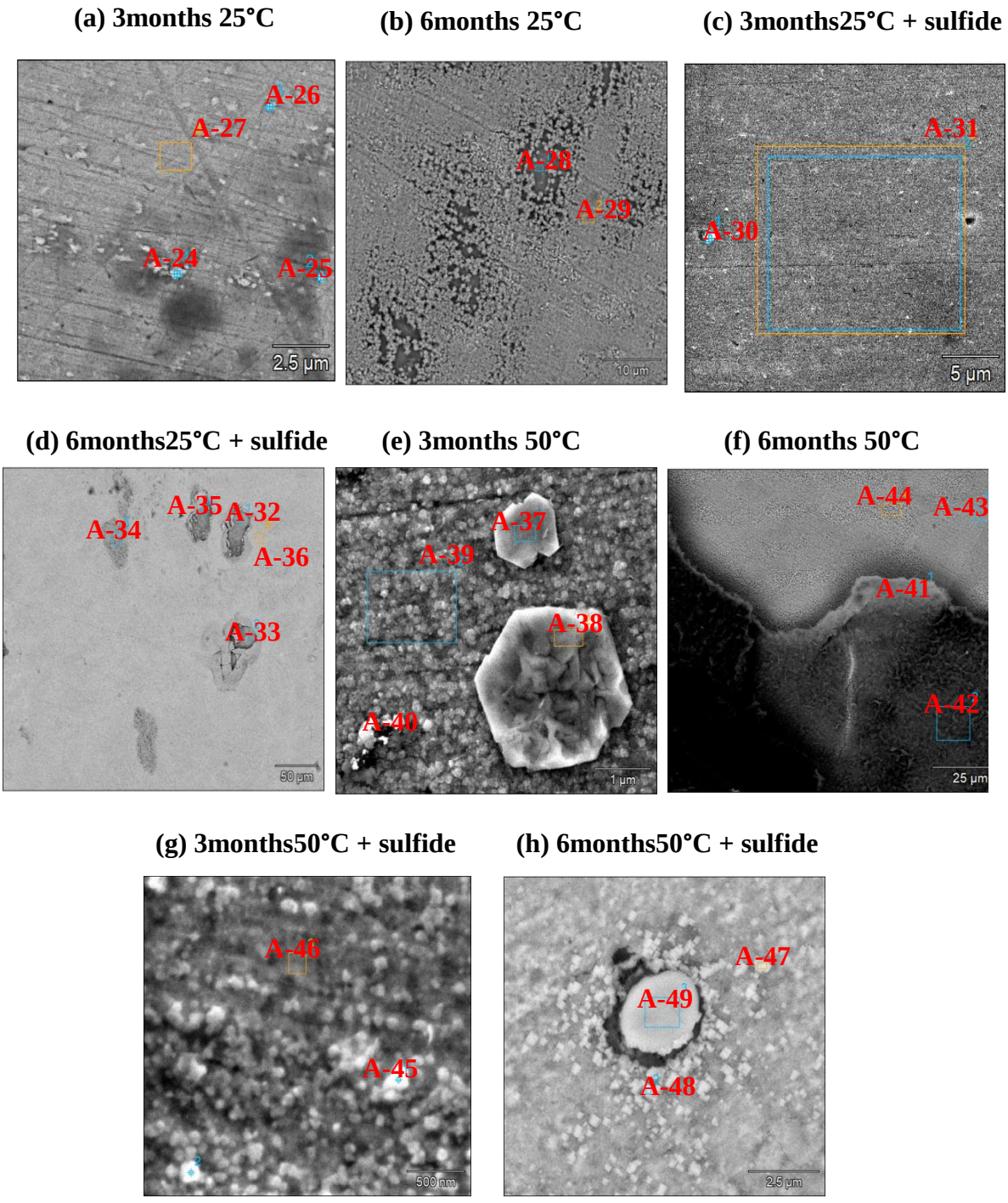

Figure 27 *Scanning electron micrographs (in SE mode) of all Cu-Ni coupons corroded for 3 and 6 months under dynamic conditions at different temperature (exact conditions are indicated above the micrographs). Marked areas were selected for EDXS analysis, quantitative results are provided in* ***Table 19****.*

__Table 19__ Relative atomic concentrations by EDXS analyses at selected areas shown in above __Figure27__. Relative errors are estimated to be within ± 10%.

Area	C	O	S	Al	Si	Mn	Fe	Ni	Cu
A-24	7.3	18.3	0.2	2.5	5.4	0.5	0.4	12.5	52.4
A-25	6.5	18.6	0.2	2.6	5.1	0.4	0.5	13.2	52.2
A-26	4.7	5.5	/	1.0	1.8	0.9	0.4	19.5	66.1
A-27	5.6	3.9	0.2	0.8	1.3	1.1	/	30.5	56.7
A-28	5.5	28.7	1.4	0.5	2.8	0.6	1.8	26.2	29.2
A-29	3.8	18.0	/	0.5	/	/	/	12.9	64.8
A-30	6.9	9.1	0.1	1.6	3.2	0.2	0.2	4.8	9.0
A-31	6.6	0.9	0.4	/	/	1.1	0.6	28.1	62.4
A-32	4.1	40.9	/	/	4.7	0.5	1.0	10.0	35.7
A-33	5.7	35.8	/	/	5.6	0.6	1.2	21.2	27.0
A-34	17.1	24.5	1.5	/	1.2	/	0.5	4.7	48.7
A-35	5.6	36.9	/	/	6.1	0.6	1.1	21.1	25.8
A-36	3.7	16.6	0.6	/	0.8	/	/	16.0	61.7
A-37	3.8	18.4	6.1	0.5	1.0	/	/	3.8	65.7
A-38	2.6	21.9	4.9	0.8	1.4	/	/	1.7	66.3
A-39	6.7	6.2	7.5	0.5	0.9	/	/	9.3	68.3
A-40	7.7	27.5	3.7	4.5	10.8	/	1.1	14.0	28.3
A-41	3.2	44.0	3.7	5.5	12.6	0.3	0.8	6.2	21.1
A-42	3.7	1.2	/	0.5	0.5	1.1	/	30.7	62.3
A-43	4.4	1.6	/	0.4	/	0.9	/	18.8	74.0
A-44	9.7	10.7	14.3	0.6	1.3	/	/	/	63.5
A-45	9.7	9.6	15.3	/	/	/	/	/	65.3
A-46	7.8	10.7	12.4	/	0.9	/	/	/	68.2
A-47	7.4	20.0	3.6	/	1.7	/	/	5.2	62.2
A-48	/	21.5	5.1	/	1.7	/	/	6.1	65.6
A-49	4.6	/	29.6	/	/	/	/	1.8	62.4

SEM-EDXS analysis for 3 and 6 months of dynamic experiments of various selected areas were shown in (***Figure 27***) and their atomic concentration results were tabulated in (***Table 19***). EDXS analysis at 5 kV acceleration voltage of this fine-grained material allowed the detection of copper, nickel and oxygen, with only minor proportions of Fe, Al, Si and S, suggesting significant contribution from the underlying substrate. At 50°C, secondary phases exhibit a different morphology having several µm sizes across, suggesting that temperature played a role in the morphology of the formed secondary phases. SEM- EDXS results of areas (A-34, A-38) shown in (***Figure 27***) and results of areas (A-30, A-32, A-35, A-40) shown in (***Table19***) indicates formation of copper oxide (Cu_xO_y) as a secondary phase on the exposed surface. Compared to static experiments, SEM-EDXS results of coupons with added sulfide for areas (A-44, A-45, and A-46) shows enrichment of sulphur and presence of mixture of copper sulfides and copper oxides on the exposed surface of corroded CuNi coupons. For example, the sample corroded for 6 months at 50°C with added sulfide (***Figure 27h***) shows distribution of different corrosion products like (Cu_2S) was present in the area A-49 where copper oxide film breaks and is no more protective whereas areas like (A-47, A-48) form copper oxides still act as protective although sulfur is present in low amount (***Table 19***). The sample corroded for 6 months at 50°C shown in

(***Figure 27h***) shows different concentrations of elements at different areas. For example, areas (A-42, A-43) shows presence Cu and Ni alloy mainly and seems to be non-corroded region, area A-40 was CuNi/bentonite interface enriched with bentonite elements like Si, Al ,Fe, and relatively low amounts of Cu, Ni presence along with oxygen and sulfur. Whereas area A-44 was the region on the coupon surface which was covered with bentonite enriched with oxygen and bentonite elements along with Cu, Ni in low amount. Thus, there is inhomogeneous distribution of elements on the exposed surface of same coupon with different areas. Based on the formed corrosion products, findings suggest comparable degradation mechanisms occurred under static and under dynamic conditions.

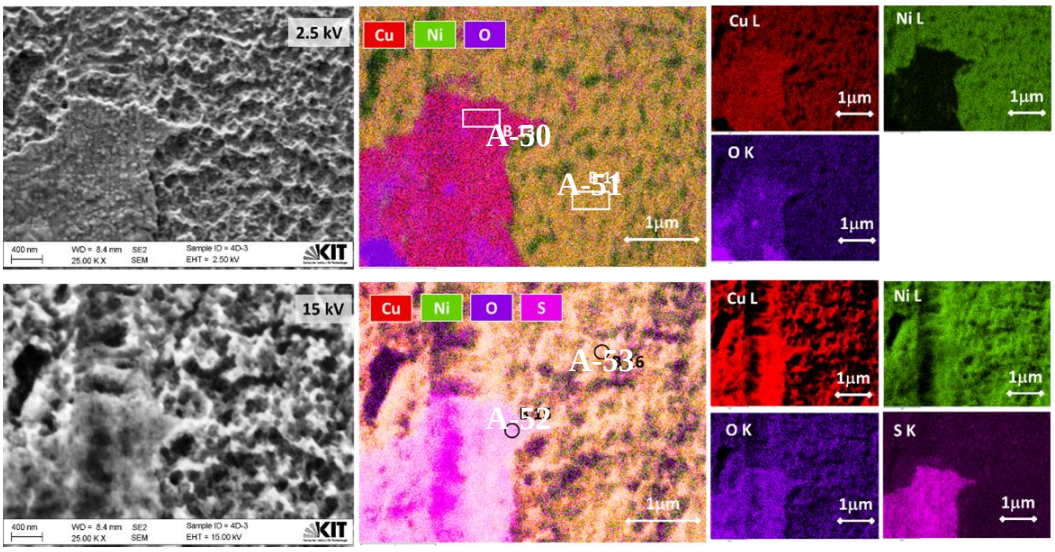

Figure 28 *Electron micrographs recorded at an acceleration voltage of either 2.5 kV (top) or 15 kV (bottom) of the Cu-Ni coupon corroded for 3 months under dynamic conditions with added sulfide present at 50°C together with elemental distribution maps. Marked areas were selected for local EDXS analysis, quantitative results are provided in* ***Table 20****.*

Table 20 *Relative atomic concentrations by EDXS analyses at an acceleration voltage of either 2.5 kV (A-50, A-51) or 15 kV (A-52, A-53) selected areas shown in* ***Figure 28****. Relative errors are estimated to be within ± 10%.*

Area	O	Mg	Al	Si	S	Ca	Mn	Fe	Ni	Cu
A-50	19.1	/	/	/	/	/	/	/	/	80.9
A-51	5.0	/	/	/	/	/	/	/	37.0	58.0
A-52	1.3	/	0.1	0.1	0.5	/	1.0	1.1	37.6	58.3
A-53	2.9	/	0.1	0.1	3.4	0.2	0.9	0.9	31.2	60.3

The sample corroded for 3 months at 50°C in the presence of added sulfide was also selected for further EDXS mapping using the Zeiss Crossbeam 350 KMAT microscope (***Figure 28***). Since the surface coverage was low, two acceleration voltages were selected to provide information originating from different depths, i.e., near surface at low acceleration voltage and including substrate at higher acceleration voltage. At 15 kV Cu and Ni appear homogeneously distributed because at this acceleration voltage the elemental distribution is dominated by the substrate. Setting the acceleration voltage to 2.5 kV enabled to separate the surface signal from the CuNi substrate signal because of the decrease of the information depth from 400 nm at 15 kV to 25 nm at 2.5 kV. EDXS mapping at 2.5 kV suggests the formation of a Cu-rich interface, e.g., coexistence of Cu oxides along with Cu **(Karnland O & Motamedi M)**, on top of a Ni-rich interface, with the pristine coupon underneath. EDXS data further indicate that the Cu-rich layer contains O and minor S, suggesting the presence of Cu oxide (***Table 20***). The Ni-rich layer seems to be made of (hydr)oxide and contains only marginal amounts of S.

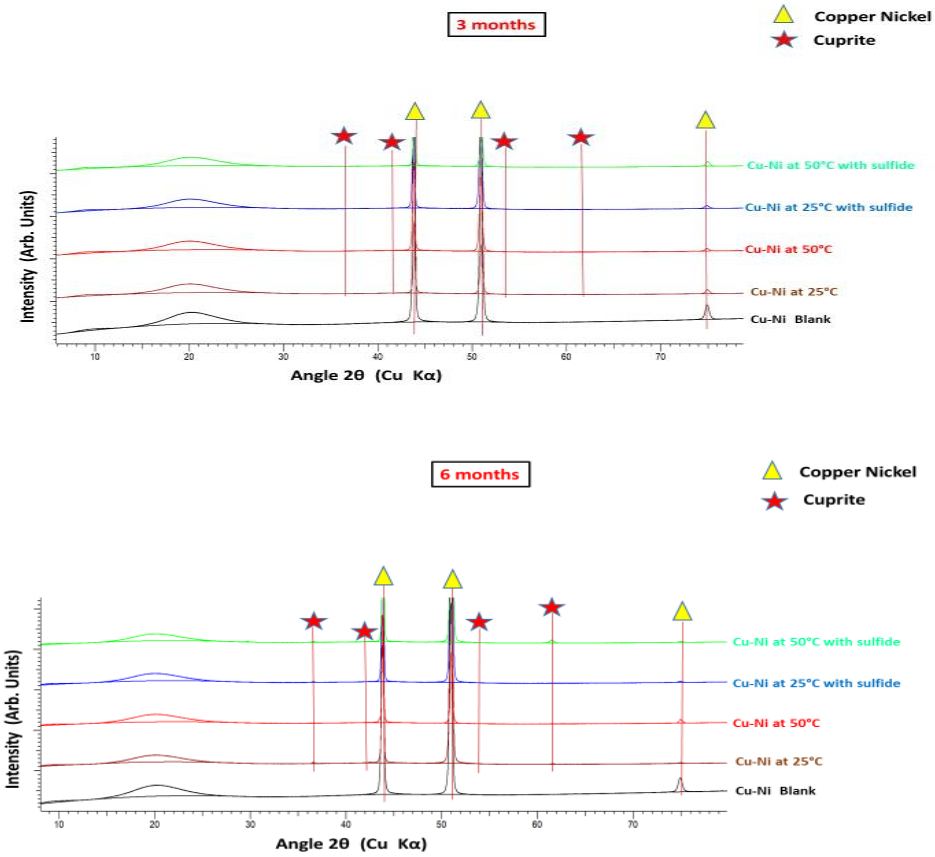

Figure 29 *X-ray diffractograms recorded on the corroded Cu-Ni coupons after 3 months (top) and 6 months (down) reaction time under dynamic conditions (exact conditions are indicated on individual XRD plot).*

The XRD analysis of corroded CuNi coupons obtained after three and six months of dynamic experiments was carried out and diffractograms were shown in (***figure 29***). The primary peaks in

the XRD spectrum for three and six months of dynamic experiments correspond to the metallic cupronickel phase (PDF 47-1406) which is starting material. Apart of this, other peaks correspond to corrosion products (Cu_2O) cuprite (PDF 74-1230) which was detected in most of the samples after three and six months of static experiments as shown in (***Figure 29***) and thus confirmed SEM-EDX data. Dynamic XRD analysis results are comparable with that of static experiments for CuNi coupons.

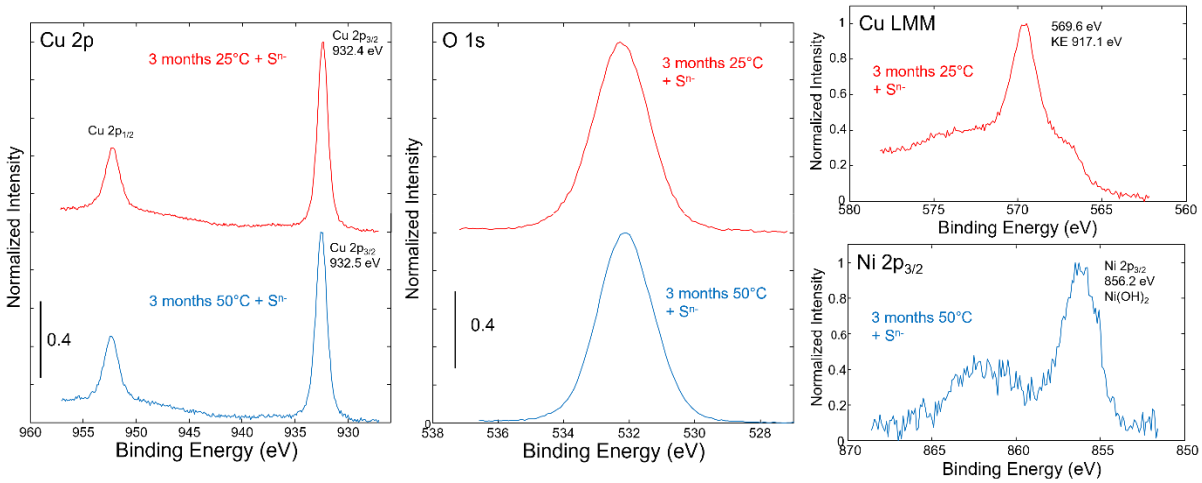

Figure 30 *X-ray photoelectron spectra recorded on Cu-Ni corroded under dynamic conditions (exact conditions are indicated on the individual graphs).*

XPS spectra recorded for selected Cu-Ni coupons for dynamic experiments were shown above in (***Figure 30***). After 3 months at 25°C in the presence of added sulfide, XPS evidenced the presence of Cu **(Karnland O & Motamedi M)** at the corroded coupon surface (***Figure 30***) but no Ni could be detected, corroborating the presence of a Cu-rich layer covering the surface. The Cu speciation is comparable in the experiment performed at 50°C, but the presence of low amounts of Ni, present as hydroxide, could be detected.

The presence of sulfide species (data shown in appendices, ***Figure A11***) could be detected at the surface of both compounds, but in limited amounts, ruling out the presence of copper sulfides in significant amounts. This result compares well with that obtained in experiments under static conditions. Finally, almost no Cu or Ni could be detected at the clay surface, suggesting that CuNi corrosion resulted in the formation of secondary phase with only limited amounts of dissolved Cu or Ni available for interacting with the adjacent bentonite.

The Cu-Ni coupons selected for XPS analysis were shown in (***Figure 31***) for dynamic experiments under different experimental conditions. Relative atomic concentrations using XPS for selected points on exposed surface of CuNi coupons were tabulated in (***Table 21***). A color change like brown green, brownish and blackish was observed on the exposed coupon surface indicating formation of different corrosion products (secondary phases).

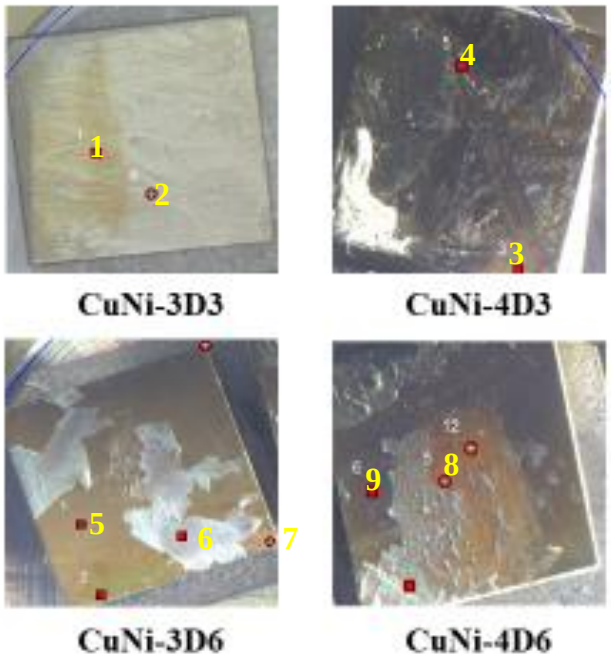

Figure 31 *X-ray photoelectron images of Cu-Ni coupons corroded under dynamic conditions (exact conditions are indicated on the individual sample, details of conditions are available in appendix). Marked points were selected for atomic concentration analysis, quantitative results are provided in* ***Table 21.***

Table 21 *Relative atomic concentrations by XPS analyses at selected points of Cu-Ni coupons for dynamic experiments shown in above* ***Figure31****. Relative errors are estimated to be within ± 10 % (Here each measurement has two type of atomic concentration: one with presence of carbon and one without carbon presence).*

Point	C	N	O	Na	Mg	Al	Si	S	Cl	Fe	Ni	Cu
3D3-1	24.0	0.6	50.0	0.4	0.3	/	12.0	3.2	0.7	/	/	8.9
	/	0.8	65.8	0.6	0.3	/	15.8	4.1	0.9	/	/	11.7
3D3-2	29.0	/	41.4	0.2	0.7	/	8.0	3.7	0.8	/	2.6	13.5
	/	/	58.4	0.3	1.0	/	11.2	5.3	1.1	/	3.7	19.0
4D3-3	9.2	/	60.0	1.0	1.4	8.8	17.4	0.5	/	/	0.8	1.1
	/	**/**	66.0	1.1	1.5	9.7	19.1	0.6	/	/	0.8	1.2
4D3-4	29.8	/	50.2	0.7	0.6	/	12.8	2.0	0.2	/	/	3.7
	/	/	71.5	1.0	0.9	/	18.2	2.9	0.3	/	/	5.3
3D6-5	20.3	/	44.6	/	0.4	/	6.2	3.8	2.4	/	3.4	18.9
	/	/	55.9	/	0.5	/	7.8	4.8	3.0	/	4.3	26.7
3D6-6	8.8	/	76.8	1.2	1.2	10.3	/	/	/	1.3	/	0.4
	/	/	84.2	1.3	1.3	11.3	/	/	/	1.5	/	0.4
3D6-7	27.4	/	36.5	0.5	0.5	/	10.2	/	/	/	/	2.3
	/	/	50.2	0.7	0.7	/	14.1	/	/	/	/	3.2
4D6-8	16.4	/	51.5	/	0.6	/	9.5	3.1	1.7	/	6.4	10.7
	/	/	61.6	/	0.7	/	11.4	3.7	2.0	/	7.7	12.8
4D6-9	7.3	/	60.6	1.2	1.2	7.3	19.6	/	/	/	0.8	0.1
	/	/	65.4	1.2	1.3	7.9	21.2	/	/	/	0.9	0.1

Here (***figure 31***) measurements carried out at different points on the exposed surface of CuNi coupons show different element distribution over the surface. Main elements are copper, oxygen and minor sulphur which form different corrosion products on the exposed surface. The atomic ratio (***Table 21,*** *points 1, 2, 5, 8*) show formation of Cu_xO_y, where as in most of the cases copper and oxygen ratio should be is 2:1. The stoichiometry of copper oxide could not be derived from XPS analysis as the attachment of bentonite to the surface dominates the oxygen content of the interface. It is surprising that the Cu:O atomic ratios are way higher than observed in EDX. This is due to adsorbed bentonite layers partly "hide" Cu-oxide layers, so that the oxygen content of the clay cover dominates the XPS signal more than it is visible in the EDX data, where a higher information depth is achieved.

In some cases, there is possibility of the formation of different corrosion products (Cu_2O + Cu_2S) (***Table 21,*** *point 1, 5, 8*). Thus, exposed corroded surface consist of inhomogeneous distribution of secondary phase on the surface of CuNi coupons for the dynamic experiments. Atomic concentrations of bentonite region as shown in (***Figure 31,*** *point 3, 9*) reveal enrichment of mainly silicon, oxygen, sodium, aluminium, magnesium, iron and minor amount of copper (0.1 to 1 at. %), nickel (0.8 at. %). Overall, results for experiments under dynamic conditions are very comparable to that obtained under static conditions, with the predominant formation of Cu oxide particles as observed from the position of Cu 2p narrow spectra shown in ***Figure30***.

3.1.6 Overall discussion of copper based materials (Cu-Ni alloy)

The study investigates the corrosion behavior of Cu-Ni alloy in contact with MX-80 bentonite under both static and dynamic experimental conditions, with and without the presence of sulfide. Results indicate that Cu and Ni dissolution is primarily due to corrosion of the cupronickel alloy, while Fe, Si, and Al concentrations largely due to bentonite dissolution. Despite variations in temperature, time, and sulfide presence, the concentrations of dissolved metals (particularly Cu and Ni) remained low, often below 1E-6 mol/L, suggesting strong sorption onto clay minerals or formation of secondary phases rather than significant mobilization into solution. ICP-MS analyses support that Cu and Ni are retained on bentonite, limiting their solubility. Corrosion rates were initially high due to residual oxygen but decreased over time, indicating the formation of passivating layers.

Corrosion rates increased with temperature, consistent with enhanced reaction kinetics, and showed comparable values to those reported in long-term in situ studies such as the MaCoTe experiment **(Reddy, Padovani, Rance, et al., 2021).** In static systems, pH and Eh remained relatively stable, while dynamic experiments exhibited increased pH (approaching that of inlet groundwater) and more reducing Eh values, possibly due to system-specific factors or measurement artifacts. Overall, the findings demonstrate limited mobility of corrosion products in bentonite systems, with Cu and Ni primarily retained through interaction with the clay matrix, and confirm that temperature is a key driver for corrosion kinetics rather than sulfide presence under the studied conditions.

Using a combination of SEM-EDX, EBSD, XRD, and XPS analyses, it was found that cuprite (Cu_2O) was the main corrosion product formed in nearly all conditions. This oxide layer formed a dense, protective coating on the alloy surface, which slowed down corrosion over time. Although small amounts of copper sulfide (Cu_2S)/CuS were detected in some samples particularly at higher temperature with added sulfide these were not dominant, and overall sulfur content remained low. Nickel remained mostly in its metallic state (Ni^0) or formed nickel hydroxide ($Ni(OH)_2$) in a few cases, and no significant formation of ni**c**kel sulfide (NiS) was observed.

The analysis also revealed that the distribution of corrosion products was not uniform across the surfaces; some regions were richer in oxides, while others remained relatively uncorroded. This may be also possible due to the sample preparation or handling. Importantly, bentonite clay, which surrounded the samples, did not significantly interact with the dissolved metals only very small amounts of copper and nickel were found on the clay. The results from both static and dynamic experiments were very similar, suggesting that flow conditions did not substantially affect the corrosion process. Overall, the findings confirm that cuprite formation is the primary and stable corrosion mechanism for CuNi alloys in these conditions, and that temperature and sulfide have a minor influence on product type but can affect morphology. This has important implications for using CuNi alloys in nuclear waste containment**,** where long-term corrosion resistance is critical.

3.2 Corrosion of spheroidal graphite iron in MX-80 bentonite

3.2.1 Initial Characterization

The initial characterization of spheroidal graphite iron coupon was carried out to know and compare the morphological changes as corrosion progresses. (***Figure 32***) left side shows the SEM (SE mode) images of polished non-corroded initial spheroidal graphite iron coupon. SEM-EDX results show the chemical composition of the selected areas in the (***Table 22 & 23)***. The bright region of area 1 was Fe, area 2 focussed on the average surface area of coupon that consists of iron and graphite inclusions whereas point 3 focussed on graphite inclusion that consists of mainly carbon and minor amount of iron. SGI is cast iron mainly consisting of iron, carbon, silicon and manganese as chief elements. The obtained composition of SGI coupon by EDX analysis had good match with the composition of the bulk SGI provided on the certificate of analysis from the manufacturer. Finally, the surface roughness of the starting SGI material was assessed by AFM. A value for the root mean square (RMS) roughness of 10± 2 nm was obtained for a scanned area of 20 x 20 μm^2.

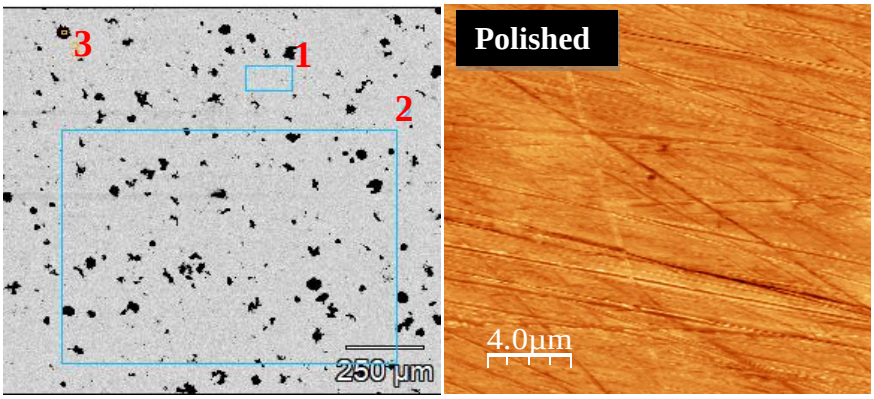

Figure 32 *SEM image on left side and surface roughness image using AFM on right side of the initial SGI coupon.*

Table 22 *Composition of initial SGI coupon obtained by SEM-EDX before experiment with (+/- 3 Sigma) uncertainty.*

Material /Atom %	C	Si	Mn	Al	Mg	Fe
SGI_point 1	4.3±0.5	4.9±0.3	0.4±0.2	0.4±0.1	-	90.0±1.2
SGI_point2	17.3±0.6	4.1±0.2	-	0.2±0.1	-	78.4±1.1
SGI_point3	98.2±1.4	0.1±0.0	-	-	-	1.6± 0.0.1

Table 23 *Chemical composition of the initial SGI coupon with (+/- 3 Sigma) uncertainty.*

Element / wt. %	C	Si	Mn	Al	Mg	Fe
Certificate	3.5	3.4	0.3	-	0.1	92.73
EDX of overall surface(point 1)	1.0±0.1	2.6±0.1	0.5±0.2	0.2±0.1	-	95.7±1.3
EDX of average surface (point 2)	4.4±0.2	2.5±0.1	-	0.1±0.1	-	93.0±1.3
EDX focused onto graphite (point 3)	92.5±1.3	0.3±0.1	-	-	-	7.0±0.6

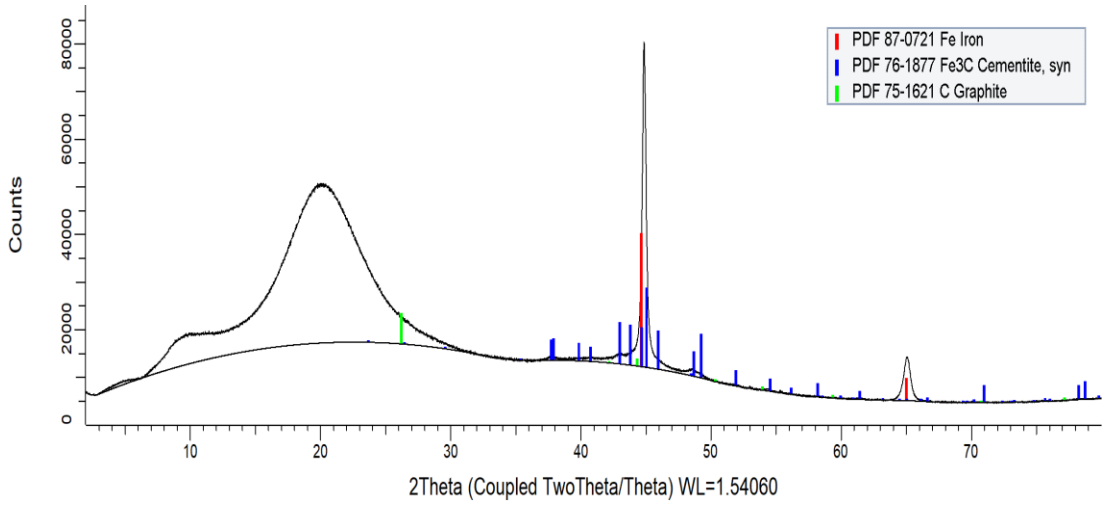

Figure 33 *X-ray diffractogram of the initial SGI coupon before experiment (with air scattering effect).*

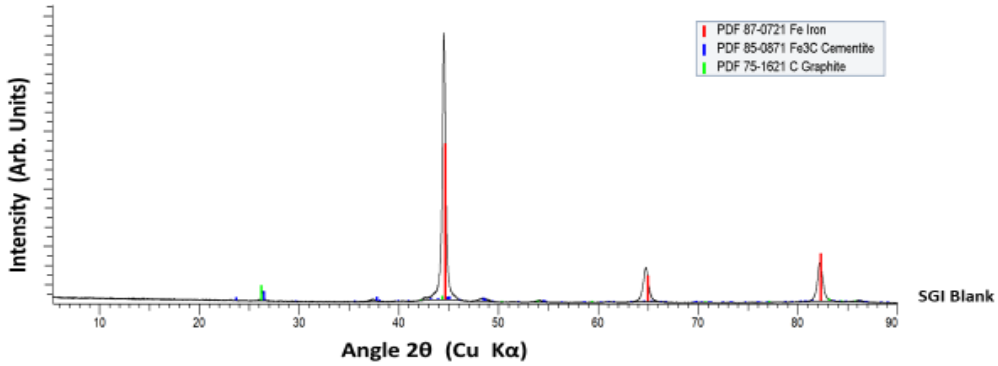

Figure 34 *X-ray diffractogram of the initial SGI coupon before experiment (without air scattering effect).*

The X-ray diffractogram of initial spheroidal graphite iron coupon was shown in the (***Figure 33 & Figure 34).*** The X-ray diffractogram of spheroidal graphite iron (***Figure 33 & Figure34)*** shows a good match with cubic iron (PDF 87-0721), while the small peaks correspond to the cementite (PDF 85-0871) and graphite (PDF 75-1621).

3.2.2 Dissolved metal ions evolution

As already described in the previous section, the concentration of dissolved ions was determined (see appendices section) and only some elements (Fe, Si, Al) are reported here for static (***Table24***) and dynamic experiments (***Table25 and Table26***) of SGI coupons.

At 25°C without hematite, iron concentrations were initially high (8500 µg/L for 3 months) but decrease significantly later, reaching 500 µg/L after 9 months. The same is true for the experiments at 50°C in which the initial Fe- concentration drops from 1100 µg/L to 200 µg/L after 6 months. In both cases the final Fe concentration lies at a low level in the 4-6· E-6 mol/L range. When hematite is present (0.5wt. %), it appears that the opposite temporal evolution occurs. Fe concentrations start from around 4· E-6 mol/L and reach 2-4· E-5 mol/L after 6-9 months. This may point to a slow reductive dissolution of Fe_2O_3 where as a result of the establishment of reducing conditions due to steel corrosion, Fe(III) from the hematite is partially reduced to Fe(II) species of higher solubility.

Table 24 *Dissolved amounts of Fe, Si and Al ions in the pore water solutions in contact with SGI coupons after 3, 6 and 9 months static experiments. Numbers in parentheses correspond to the relative standard deviation in percentage.*

System/ Amounts in µg/L	Fe	Si	Al
3months 25°C w/o hematite	8500(0.1)	14300(2.3)	1500(4.3)
3months 25°C with (0.5 wt.%) hematite	200(0.5)	9600(2.2)	700(3.8)
3months 50°C w/o hematite	1100(3.7)	31100(1.1)	5000(1.6)
3months 50°C with (0.5 wt.%) hematite	200(9.4)	19600(1.1)	800(3.3)
6months 25°C w/o hematite	1300(1.0)	8100(0.7)	700(2.4)
6months 25°C with (0.5 wt.%) hematite	900(1.1)	7600(0.9)	600(6.6)
6months 50°C w/o hematite	200(13)	15200(2.9)	400(27)
6months 50°C with (0.5 wt.%) hematite	2300(0.9)	17000(1.3)	1000(40)
9months 25°C w/o hematite	500(4.9)	12300(0.7)	500(3.7)
9months 25°C with (0.5 wt.%) hematite	1200(3.1)	18200(0.8)	500(5.7)

For static experiments, the concentration of Si is ranging from 7600 to 31100 µg/L, and Al varies in the range 400 to 5000 µg/L. The dissolved Si and Al concentrations were affected slightly by temperature and presence of hematite. There is possibility of adsorption of dissolved silicate species to the hematite surface and thus lowering the silicate concentration a bit as observed during 3 and 6 months at room temperature (25°C) in presence of hematite. Highest Si, Al dissolution was observed at (50°C) elevated temperature for 3 months without hematite. The measured concentration (at least for 9 months) of silicon, and aluminium is quite similar to the concentration of equilibrium bentonite slurry where Si concentration is ~13000 µg/L and Al concentration is ~500 µg/L.

Table 25 *Dissolved amounts of Fe, Si and Al ions in the ground water (solution) in contact with SGI coupons during 3 months dynamic experiment. Numbers in parentheses correspond to the relative standard deviation in percentage.*

25°C w/o hematite (System)/ Amounts in µg/L	**Fe**	**Si**	**Al**
A (4 weeks)	<100	17300(0.7)	900(3.0)
B (5 weeks)	<100	16900(0.8)	800(3.3)
C (6 weeks)	<100	17400(1.6)	1100(4.9)
D (8 weeks)	<100	16800(0.5)	300(1.0)
E (10 weeks)	300(1.4)	18600(0.4)	200(6.0)
F (12weeks)	<100	21400(0.9)	5500(2.0)

25°C with (0.5 wt.%) hematite (System)/ Amounts in µg/L	**Fe**	**Si**	**Al**
A (4 weeks)	<100	16400(0.6)	1500(2.4)
B (5 weeks)	<100	17300(0.9)	1200(2.8)
C (6 weeks)	300(1.2)	18300(1.0)	900(2.1)
D (8 weeks)	<100	17900(1.2)	300(1.3)
E (10 weeks)	<100	20800(0.8)	800(1.3)
F (12 weeks)	<100	21300(0.1)	400(3.1)

50°C with(0.5 wt.%) hematite (System)/ Amounts in µg/L	**Fe**	**Si**	**Al**
A (4 weeks)	600(2.3)	19000(0.6)	1200(2.6)
B (5 weeks)	1900(0.4)	20500(0.4)	1100(4.8)
C (6 weeks)	<100	21800(1.5)	1400(5.9)
D (8 weeks)	2200(1.0)	20900(1.5)	1100(2.0)
E (10 weeks)	<100	23700(0.4)	600(2.3)
F (12 weeks)	500(2.2)	21800(0.1)	300(1.5)

Table 26 *Dissolved amounts of Fe, Si and Al ions in the ground water (solution) in contact with SGI coupons during 6 months dynamic experiment. Numbers in parentheses correspond to the relative standard deviation in percentage.*

25°C w/o hematite (System)/ Amounts in µg/L	**Fe**	**Si**	**Al**
A (6 weeks)	700(5.4)	19200(0.2)	200(2.8)
B (10 weeks)	<200	19300(1.7)	100(2.3)
C (14 weeks)	<200	20700(0.9)	100(0.9)
D (18 weeks)	<100	19400(0.6)	100(11)
E (22 weeks)	<100	19400(0.9)	100(12)
F (26 weeks)	<100	19300(0.7)	100(1.7)

25°C with (0.5 wt.%) hematite (System)/ Amounts in µg/L	Fe	Si	Al
A (6 weeks)	<200	18900(1.2)	100(4.9)
B (10 weeks)	<200	20400(0.9)	200(2.1)
C (14 weeks)	<200	23700(1.7)	100(2.5)
D (18 weeks)	<100	18000(0.5)	100(11)
E (22 weeks)	<100	19900(0.6)	100(16)
F (26 weeks)	<100	19900(1.7)	100(5.3)

50°C with (0.5 wt.%) hematite (System)/ Amounts in µg/L	Fe	Si	Al
A (6 weeks)	200(3.7)	19500(0.2)	300(1.8)
B (10 weeks)	<200	19600(1.4)	400(3.6)
C (14 weeks)	<200	20900(1.7)	600(4.0)
D (18 weeks)	<100	19300(1.6)	500(1.3)
E (22 weeks)	<100	19900(0.9)	500(1.8)
F (26 weeks)	<100	18800(0.4)	400(1.0)

For dynamic experiments, the concentration of Si varies from 16400 to 23700 µg/L which is quite in agreement with concentration of simulated groundwater where Si concentration is ~17000 µg/L (***Table2***). Al concentration is comparable at room and elevated temperature (50°C) and iron concentration is lower in most of the cases but is slightly increased at elevated temperature (50°C) in presence of hematite. Overall, temperature, time and hematite presence do not have significant effect on the concentrations of Fe, Si, and Al. The uncertainties suggest that variations in ions concentration lie within the scatter of the data. Here, Fe dissolution is mainly due to cast iron (SGI) corrosion whereas Si and Al concentrations indicate clay dissolution not iron corrosion.

Overall, results suggest that temperature plays a key role in controlling iron availability in solution, with the presence of hematite influencing iron dynamics, particularly at higher temperatures, where initial dissolution is more pronounced, but long-term concentrations stabilize at low levels. Si and Al exhibiting varying trends in the presence of hematite, temperature and due to interactions between SGI coupons and the bentonite slurry. Overall, the amounts of dissolved iron in dynamic experiments were low compared to static experiments, whereas the amount of dissolved silicon and aluminium in dynamic experiments were relatively comparable with static experiments.

Table 27 Determination of Cu, Ni, Fe, Si and Al concentrations for a bentonite that was in contact with SGI coupons has been digested in acid and the resulting liquid phase has been quantified by using ICP-MS for 6 months dynamic experiment (Numbers in parentheses correspond to the relative standard deviation in percentage).

(Dynamic) System/ Amounts in µg/g	Cu	Ni	Fe	Si	Al
6months 25°C SGI w/o hematite	5 (0.9)	7(1.4)	21740(0.9)	259500(0.9)	45590(0.8)
6months 25°C SGI with 0.5 wt.% hematite	5(1.2)	5(0.2)	23475(1.0)	262250(1.3)	56725(2.3)

Determination of Cu, Ni, Fe, Si and Al concentration for a bentonite that was in contact with SGI coupon with and without hematite has been digested in acid and the resulting liquid phase has been quantified by using ICP-MS for 6 months dynamic experiment. The results shown in ***(Table 27)*** shows variation in concentration (Fe, Si and Al) which was of interest for SGI. The concentration of mainly Fe increases in presence of hematite indicates that Fe(II) release due to iron corrosion and Fe(III) from hematite is mainly sorbed on the clay surface rather than dissolving into the solution. Si and Al are mainly components of bentonite apart Si also present in SGI (3.4 wt. %). The difference in Si concentration for the SGI experimental product and the bentonite is in the range of 4% only, this corresponds to the analytical uncertainty of ICP-MS analysis.

3.2.3 pH / E_h evolution

The accurate pH and E_h values of a system are along dissolved metals amounts crucial parameters allowing identification of thermodynamically stable corrosion phase(s) in *Pourbaix* diagram **(*Figure 2*)** under those conditions.

Table 28 pH / Eh evolution of SGI in contact with MX-80 bentonite slurry after 3, 6 and 9 months exposure time.

System	pH	E_h w.r.t SHE (mV)
3months 25°C w/o hematite	8.17±0.05	-441±50
3months 25°C with (0.5 wt.%) hematite	8.13±0.05	87±50
3months 50°C w/o hematite	8.13±0.05	-254±50
3months 50°C with (0.5 wt.%) hematite	7.91±0.05	-149±50
6months 25°C w/o hematite	7.87±0.10	-47±50
6months 25°C with (0.5 wt.%) hematite	7.74±0.10	-310±50
6months 50°C w/o hematite	7.73±0.10	-430±50
6months 50°C with (0.5 wt.%) hematite	7.80±0.10	-420±50
9months 25°C w/o hematite	7.87±0.10	-250±50
9months 25°C with (0.5 wt.%) hematite	7.95±0.10	14±50

The pH and E_h values of SGI coupons for three, six and nine months of static experiments were shown in (***Table 28***). The *in-situ* pH did not evolve much in SGI corrosion experiments carried out for 3 months (***Table 28***), slightly decreased after 6 months and has similar range after 9 months. Overall, the presence of hematite only had a marginal effect. Metallic corrosion affected the redox potential that became clearly negative after 3 months except at 25°C with hematite present and 9 months with hematite presence, and lower values were recorded after 6 months except in the experiment at 25°C in the absence of α-Fe_2O_3. Hematite is a pure Fe(III) compounds and thus acts as an oxidizing agent. Indeed, after 3 and 9 months, the redox potential is systematically higher when hematite is present. Unfortunately, this trend is less clear after 6 months because at 50°C the difference is within uncertainties and at 25°C E_h is lower for SGI corroded in presence of hematite. Overall, reducing conditions developed as a consequence of steel corrosion, suggesting the formation of Fe(II) bearing compounds. The absence of significant pH change may be related to bentonite acting as pH buffer.

Following *in-situ* pH and E_h measurements, coupons were removed from the vessels for analyses. In some experiments, the SGI/suspension interface exhibited a slight blue/green color (***Figure 42***) indicating that some reaction had occurred. Color is among properties of smectites that is greatly affected by redox reactions, especially for Fe-rich smectites **(Stucki, 2011)**. Indeed, color changes appear because of changes in intra- and intervalence electron transfer transitions involving Fe(II), Fe(III), and O → Fe(III) charge transfer transitions. Structural iron in the starting MX-80 bentonite prevails as ferric ions, and metallic corrosion results in the formation of ferrous ions, which can interact with bentonite in suspension and result in electron transfer. The observed change of color may either suggest reduction of structural iron within the smectite component of the bentonite, or the formation of corrosion products (e.g., green rust compounds).

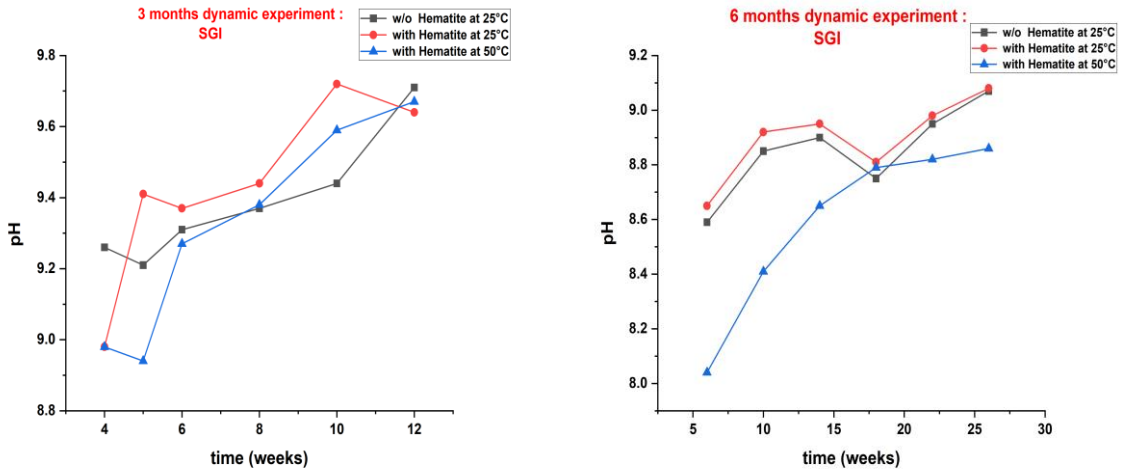

Figure 35 *The pH evolution of the SGI coupons in ground water (solution) during 3 (left side) and 6 months (right side) dynamic experiments (±0.1 is uncertainty).*

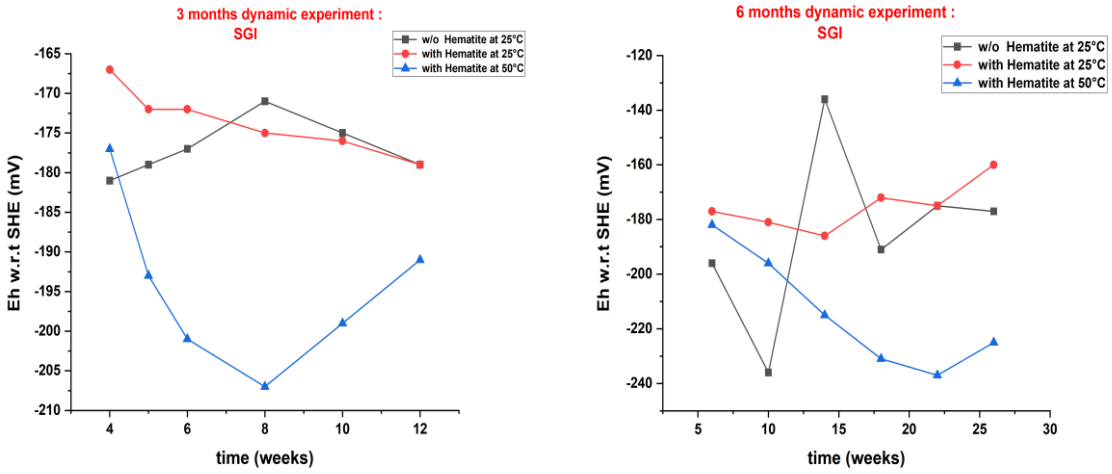

Figure 36 *The Eh evolution of the SGI coupons in ground water (solution) during 3 (left side) and 6 months (right side) dynamic experiments (±50mV is uncertainty).*

The pH and E_h values of SGI coupons for three and six months dynamic experiments were shown in (***Figure 35***) and (***Figure 36***). pH again increases towards the value of the inflowing simulated groundwater. As already outlined in chapter 3.1.3, E_h values lie throughout in the reducing range (-167 mV to -207 mV) in dynamic experiments, partly different to observations in static experiments. Also the presence of hematite does not have a significant impact.

3.2.4 Corrosion rate

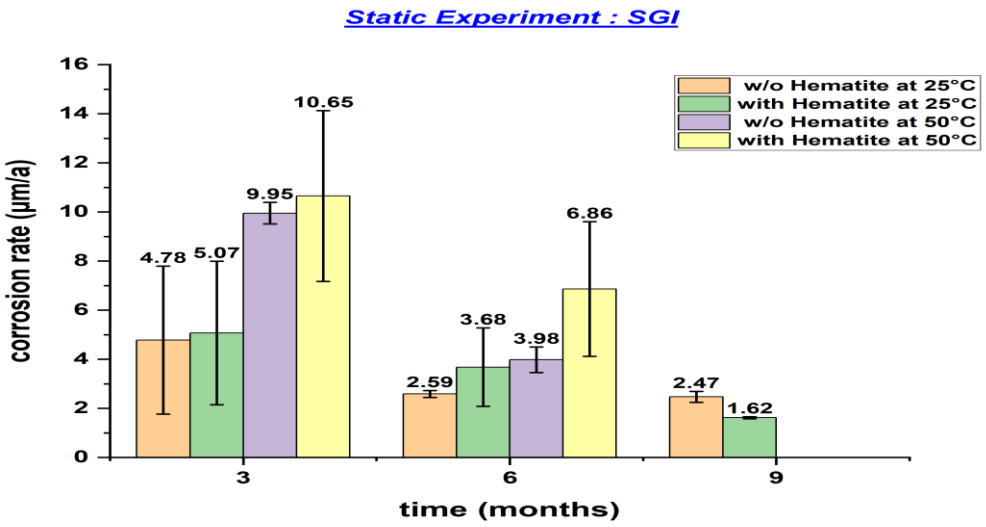

Figure 37 *Corrosion rates of all SGI coupons obtained after 3, 6 and 9 months static experiments.*

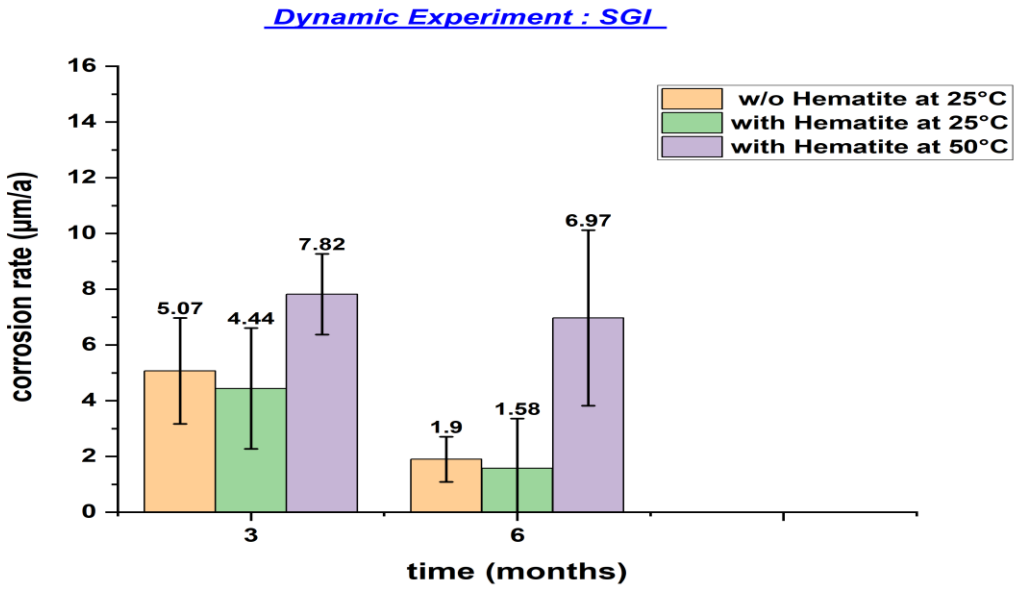

Figure 38 *Corrosion rates of all SGI coupons obtained after 3 and 6 months dynamic experiments.*

The corrosion rates of SGI coupons for static and dynamic experiments were calculated using the weight loss method and are shown in (***Figure 37***) for 3, 6 and 9 months of static experiments and in (***Figure 38***) for 3 and 6 months dynamic experiments. The corrosion rate of SGI mainly varies with temperature and is not much affected by presence of hematite or exposure time. In static and dynamic experiments, the corrosion rate increases with temperature, being higher at 50°C than at 25°C. The corrosion rate of SGI in bentonite suspension for both experiments (static and dynamic) at 25°C, varies in the range between 1.90±0.81 to 5.07±1.90 µm/a which is in agreement with the reported average corrosion rate of carbon steel (~2 µm/a) embedded within compacted MX-80 bentonite and exposed to natural granitic pore water for 394 days in the in situ MaCoTe experiment **(Reddy, Padovani, Rance, et al., 2021)**. The small difference in corrosion rate is due to different material, temperature (25°C vs rock temperature), time and form of bentonite (suspension vs compacted).

In dynamic experiments, the corrosion rate at 50°C varies in the range 6.97±3.15 to 7.82±1.45 µm/a, which is quite comparable with corrosion rate of static experiments (considering experimental uncertainty). Longer exposure time (3 to 6 months) in both experiments show little reduction in corrosion rate that hints at the formation of a protective passivation layer at the coupon surface. Taking uncertainties into account, the results indicate that temperature plays a more significant role in corrosion than hematite content, with higher temperatures leading to increased corrosion over time, especially when hematite is present. The corrosion rates of SGI coupons for dynamic experiments were comparable with static experiments and are in same range (e.g., after 6 months in presence of hematite).

3.2.5 Secondary phase characterization

3.2.5.1 Static condition systems (3, 6 & 9 months)

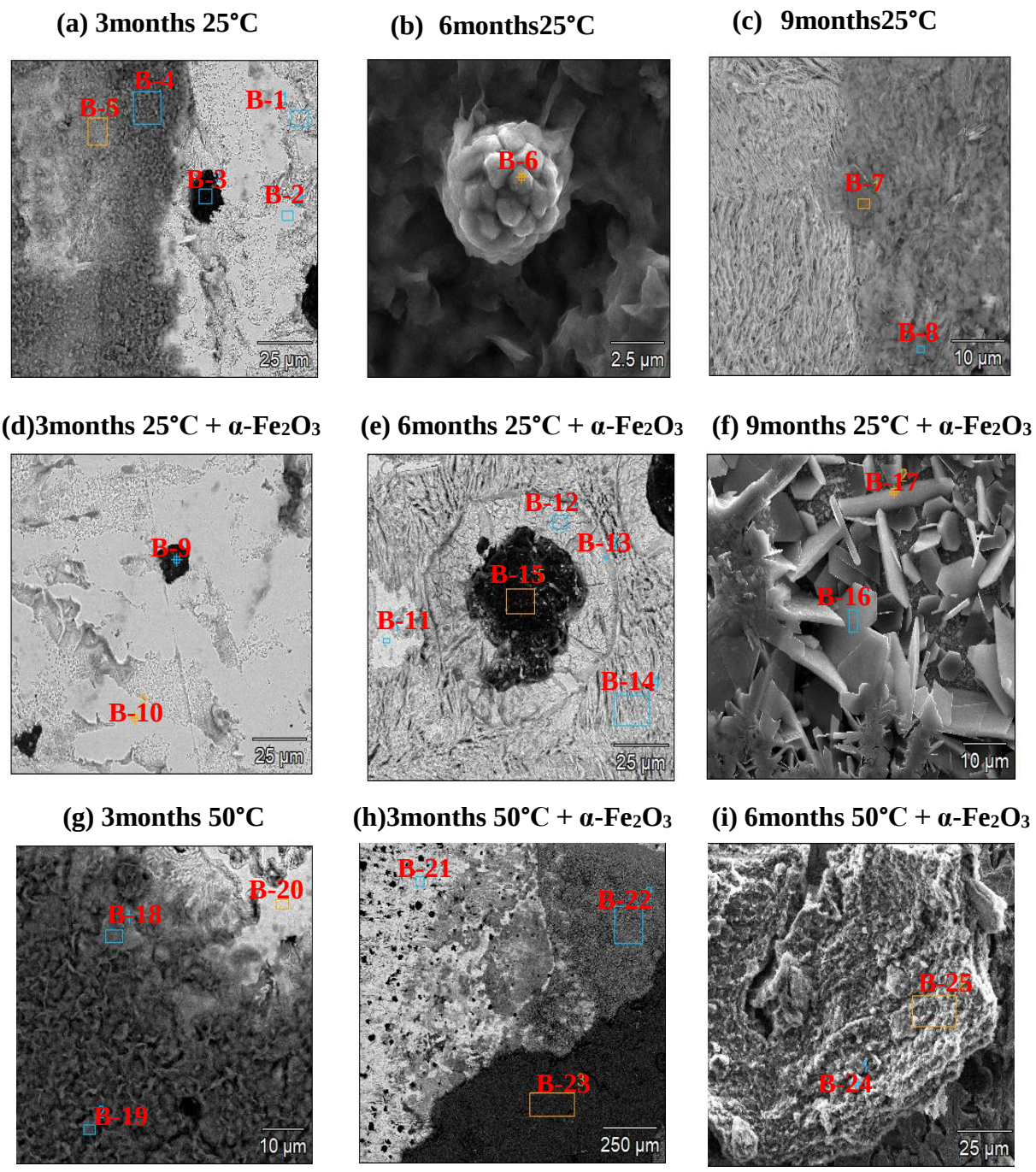

Figure 39 *Scanning electron micrographs (in SE mode) of all SGI coupons corroded for 3, 6 and 9 months under static conditions at different temperatures (exact conditions are indicated above the micrographs). Marked areas were selected for EDXS analysis, quantitative results are provided in* ***Table 29****.*

__Table 29__ Relative atomic concentrations by EDXS analyses at selected areas shown in above __Figure39__. Relative errors are estimated to be within ± 10%.

Area	C	O	Na	Mn	Al	Si	S	Cl	Fe
B-1	7.8	/	/	/	0.2	4.4	/	/	87.6
B-2	12.1	/	/	/	/	0.3	/	/	87.7
B-3	98.3	/	/	/	/	0.3	/	/	1.1
B-4	/	57.0	1.4	/	6.3	17.5	/	0.1	16.2
B-5	2.1	42.4	0.5	/	3.9	11.6	0.3	/	37.8
B-6	7.0	18.7	/	/	0.7	2.0	46.9	/	24.7
B-7	2.4	52.9	0.5	/	6.3	15.9	0.1	0.3	14.4
B-8	1.9	61.4	0.4	/	6.6	15.9	0.1	0.3	12.0
B-9	72.9	24.5	/	/	0.5	1.1	/	/	1.1
B-10	1.7	/	/	0.3	0.2	4.7	/	/	93.0
B-11	10.7	/	/	/	0.7	1.4	/	/	87.2
B-12	4.1	16.9	0.3	/	2.0	7.5	0.4	/	68.1
B-13	6.8	2.6	/	/	0.3	1.1	/	/	89.1
B-14	10.0	/	/	1.0	0.4	3.3	0.6	/	84.7
B-15	78.8	17.5	/	/	0.6	1.6	/	/	1.5
B-16	3.9	63.5	/	/	/	0.7	/	/	31.6
B-17	5.0	62.2	/	/	/	1.6	/	/	30.5
B-18	/	45.1	2.2	/	6.8	15.8	0.1	/	27.9
B-19	/	62.1	1.8	/	7.9	23.2	/	0.1	2.9
B-20	6.9	/	/	/	0.9	1.4	/	/	90.8
B-21	14.9	/	/	0.6	0.4	3.3	/	/	80.9
B-22	6.3	58.8	/	/	0.2	0.9	/	0.2	33.2
B-23	3.0	61.5	1.6	/	7.9	21.1	/	/	3.0
B-24	6.9	59.2	0.6	/	1.4	16.8	/	0.4	13.9
B-25	3.2	52.1	1.0	/	4.1	19.1	/	0.2	19.0

SEM-EDXS analysis for various selected areas were shown in (***Figure 39***) and their atomic concentration results were tabulated in (***Table 29***) for SGI coupons corroded for 3, 6 and 9 months of static experiments. SGI has a pearlitic structure composed of alternating layers of ferrite (α-Fe) and cementite (Fe_3C), and contains graphite inclusions. After 6 months of reaction, the surface is more damaged compared to 3 months, even at 25°C with added hematite (***Figure39e***). The surface is particularly damaged within a small circular area surrounding graphite inclusions, suggesting preferential dissolution of iron without affecting the graphite. This observation may suggest the development of different electrochemical potentials at the surface of the conducting coupon between the inclusion and its immediately surrounding metal, whereby graphite would act as cathodic site. This spatial separation of anodic and cathodic sites results in the development of a galvanic cell **(Schlegel et al., 2018)**, favorable to increasing the metallic corrosion, which thus can account for experimental observations. After 9 months of reaction, at room temperature the exposed surface show clear morphology of secondary phases formed due to corrosion of SGI coupons. At 25°C without hematite iron silicate (***Figure 39c***) formation was observed based on SEM-EDXS and with hematite (***Figure 39f***) addition form mixture of iron oxide, green rust (hexagonal structure) and silicate as corrosion products.

EDXS analyses results of coupons at 25°C after 3 and 9 months without hematite and for coupons at 50°C with hematite after 6 months, selected areas (B-4, B-5, B-7,B-8,B-24 and B-25) shown in ***Figure 39*** indicate formation of iron silicate as corrosion products since Fe: Si ratio is close to 1:1. The atomic concentration values obtained here rule out the presence of only bentonite or hematite and instead may suggest the presence of Fe-rich secondary phases such as phyllosilicates of the kaolinite-serpentine group formed by condensation of one octahedral sheet with one tetrahedral sheet (TO type) confirmed by Fe:Si ratio through SEM-EDXS analysis. This finding would be consistent with usually reported results for iron or steel corroded in contact with clay minerals **(Dzene et al., 2022; Lanson et al., 2012; Lantenois et al., 2005; Schlegel et al., 2018)**. According to reported findings from **(Pignatelli et al., 2013)**, together with the detection of Al presence in the present study, the formation of cronstedtite ($[Fe(II)_{3-x}Fe(III)_x][Fe(III)_xSi_{2-x}]O_5(OH)_4$) in the present work seems rather unlikely. Instead, results may suggest the formation of odinite ($[Fe(II),Fe(III),Mg,Al]_{2.5}[Si,Al]_2O_5(OH)_4$) or ($[Fe(II),Fe(III),Mg,Al]_3[Si,Al]_2O_5(OH)_4$) berthierine. Unfortunately, neither of these compounds could be detected by XRD analysis, very likely due to their low amounts present as discussed in the next section.

It was observed from the (***Figure 39*****a, *39*****c**) that iron silicate was mainly formed in the region close to metal/bentonite interface whereas away from interface base coupon is detected like in areas (B-1, B-2) based on SEM-EDXS and other side regions covered with bentonite (B-19, B-23). The significant presence of oxygen particularly in regions like (B-16, B-17, B-22) shown in (***Figure 39***), suggests the formation of iron oxide-based corrosion products, such as magnetite (Fe3O4), hematite (Fe2O3) or green rust. The SGI coupon corroded for 9 months at 25°C with hematite in bentonite environment may consist of green rust as confirmed by XRD (***Figure 40***) and iron oxide (mostly magnetite) from SEM-EDXS results (***Table 29,*** **B-16, B-17**), because added hematite was reduced and most likely forms (magnetite) after 9 months (long term). In the area with high sulfur for instance region (***Figure39,*** **B-6**) indicates presence of FeS_2 which may come from bentonite. Relatively comparable results were obtained for three, six and nine months of static experiments for SGI coupons. This finding supports that conditions were clearly reducing at the coupon/suspension interface. Thus, SEM-EDXS results provide insights into the corrosion behavior of spheroidal graphite iron (SGI) in bentonite environments, revealing the formation of distinct corrosion products suggested by varying elemental compositions across the analyzed areas.

The XRD analysis of corroded SGI coupons obtained after three, six and nine months of static experiments was carried out and its diffractograms were shown in below (***Figure 40***).

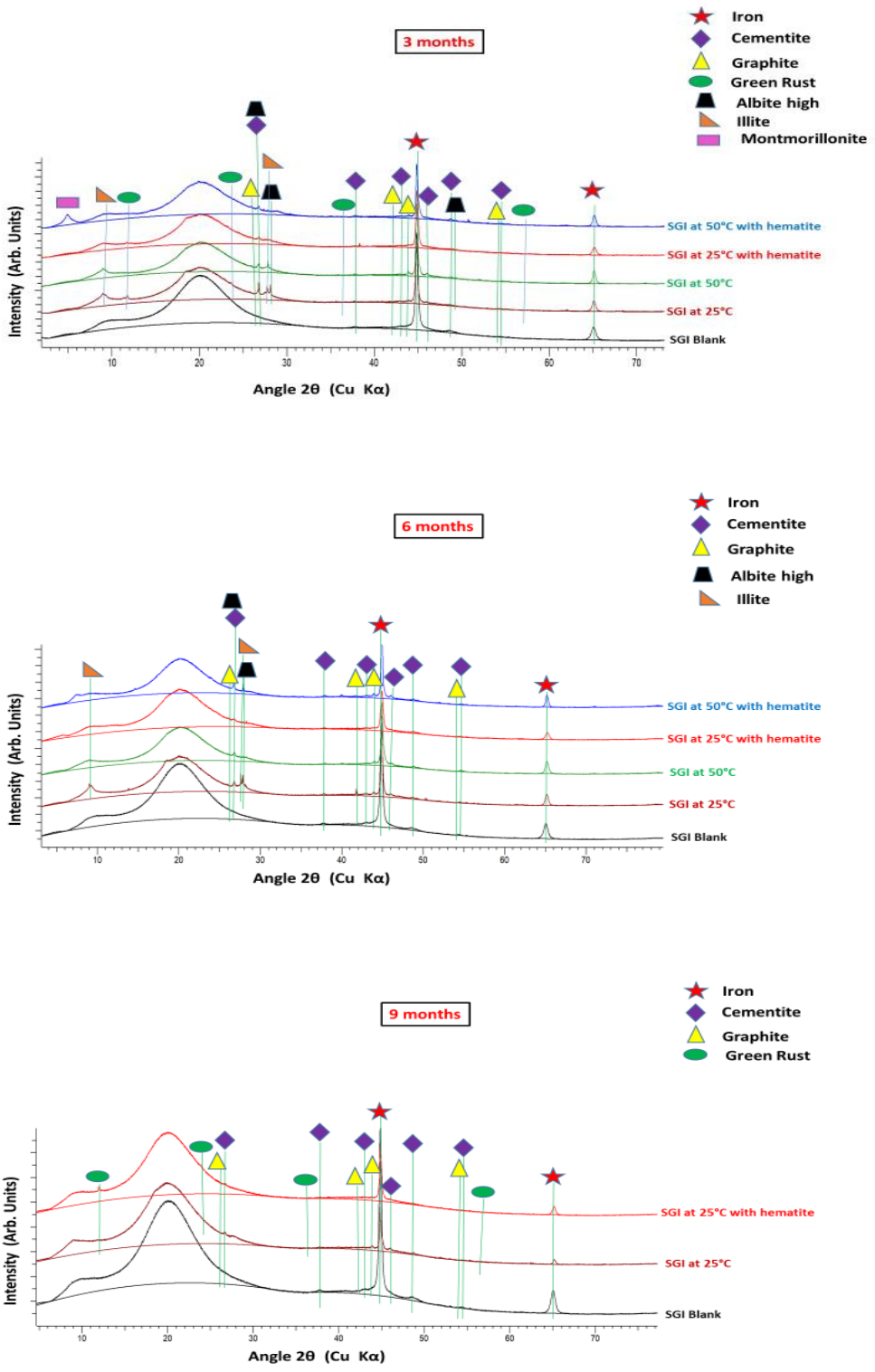

Figure 40 *X-ray diffractograms recorded on the corroded SGI coupons after 3 months (top), 6 months (middle) and 9 months (bottom) reaction time under static conditions (exact conditions are indicated on individual XRD plot).*

The primary peak in the XRD spectrum for three, six and nine months of static experiments likely correspond to theiron (PDF 87-0721), cementite (PDF 85-0871) and graphite phase (PDF 75-1621) which is starting material. Apart from this, other reflections attributable to Montmorillonite, Illite/Albite which are present on the exposed surface especially for three and six months come from the bentonite and remaining peaks correspond to corrosion products or secondary phase green rust (PDF 13-0090) which was detected in most of the samples for three and nine months of static experiments as shown in (***Figure 40***). For six months no secondary phase presence could be detected, suggesting that either their amount was too low, that they are of too low crystallinity, or that they must have been removed when cleaning off the excess suspension.

There is not much difference observed in 9 months coupons compared to three months in terms of secondary phase (corrosion products) from XRD analysis. Findings suggest that secondary phases formed in too low amounts and have heterogeneous distribution over the exposed surface due to difference in experimental conditions (time, temperature and hematite presence). Although hematite is added in some experiments its presence could not be detected in XRD analysis maybe due to low amount or it is converted to magnetite. Overall XRD analysis provides insights into the phases present in SGI coupons after corrosion, which is critical for understanding corrosion process and the stability of the material over time.

XPS analyses provided complementary chemical information as well as speciation information.

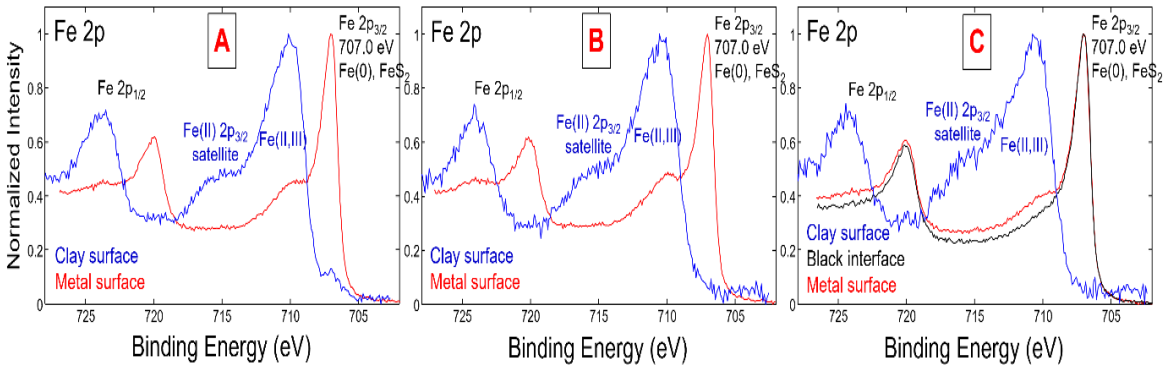

Figure 41 *X-ray photoelectron spectra recorded on the SGI coupons corroded for 3 months at 25°C in absence of α-Fe2O3 (A), SGI corroded for 3 months at 50°C in presence of α-Fe2O3 (B) and SGI corroded for 6 months at 25°C in presence of α-Fe2O3 (C).*

For all analysed samples, findings were very comparable. The Fe 2p spectrum recorded at the metal surface (***Figure 41***) evidenced the presence of metallic Fe, suggesting that no Fe-bearing secondary phase is attached to the surface. Low amounts of sulfide, indicated by the S $2p_{3/2}$ elemental line at 161.8 eV binding energy, were also detected at the coupon surface, most probably as iron sulfide (i.e., due to pyrite naturally present in the bentonite). Reference binding energies **(Moulder et al., 1992)** of the Fe $2p_{3/2}$ elemental line of Fe **(Karnland O & Motamedi M)** (707.0 eV), FeO (709.4 eV) and FeS_2 (706.7 eV) are similar, whereas that of FeS (710.3 – 712.2 eV) or Fe_3O_4 (708.2 eV and 710.4 eV), α-Fe_2O_3 (710.9 eV), and α-FeOOH (711.8 eV) clearly differ. At the clay surface, Fe 2p spectra show shake-up satellites about 5 eV higher binding energies than the Fe 2p main lines, which is characteristic of Fe(II). Shake-up satellites of

Fe(III), expected around 10 eV higher binding energy than the Fe 2p main lines are weak or not present. Interestingly, binding energy of Fe $2p_{3/2}$ lines are at about 710 eV, which is characteristic for iron oxides containing Fe(III), but also for Fe(II) in silicates. Even if Fe and Si have similar Pauling's electronegativity, the oxygen ion at Fe-O-Si may have stronger interaction with tetravalent Si than with Fe(II) or Fe(III) resulting in more positive charge on the Fe ion compared to iron oxides. Thus higher binding energy of Fe 2p photoelectrons emitted from Fe(II)-O-Si(IV) binding is expected **(Seyama & Soma, 1987)**.

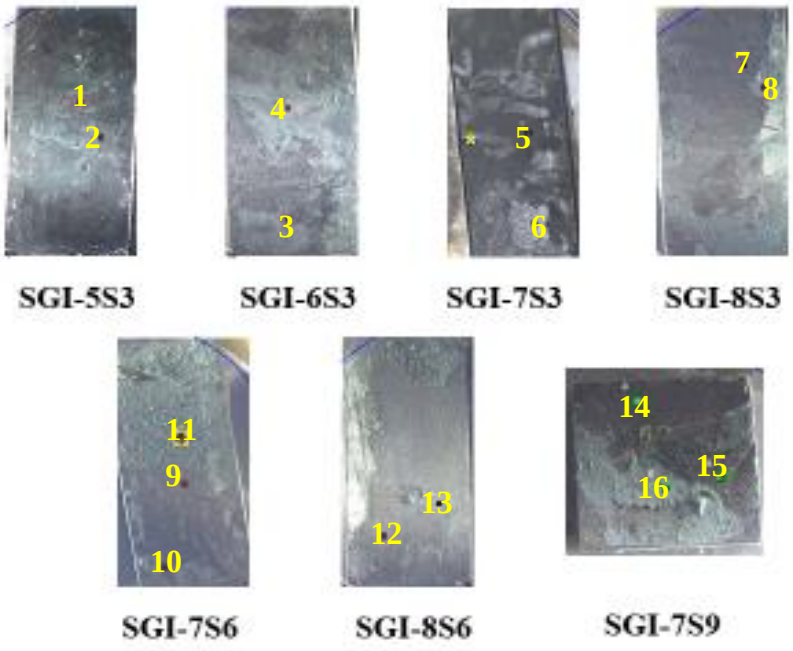

Figure 42 *Pictures taken in XPS chamber of SGI coupons corroded under static conditions (exact conditions are indicated on the individual sample, details of conditions are available in appendix). Marked points were selected for atomic concentration analysis, quantitative results are provided in* ***Table 30****.*

Table 30 *Relative atomic concentrations by XPS analyses at selected points of SGI coupons for static experiments shown in above* ***Figure42****. Relative errors are estimated to be within ± 10% (Here each measurement has two type of atomic concentration: one with presence of carbon and one without carbon presence).*

Point	C	O	Na	Mg	Al	Si	S	Cl	Ca	Mn	Cu	Fe
5A3-1	36.6	29.1	0.4	0.5	/	2.9	1.0	0.5	1.7	/	0.6	25.1
	/	46.0	0.6	0.8	/	4.6	1.6	0.8	2.6	/	1.0	39.7
5A3-2	13.0	55.7	0.6	0.7	2.8	12.2	/	0.5	/	/	/	12.3
	/	64.0	0.7	0.8	3.3	14.0	/	0.5	/	/	/	14.2
6A3-3	23.3	43.7	0.9	0.8	3.2	8.3	1.4	/	/	0.7	/	17.2
	/	57.0	1.2	1.1	4.2	10.8	1.9	/	/	1.0	/	22.4
6A3-4	6.3	62.9	1.3	1.1	5.8	19.9	/	/	0.4	/	/	2.3
	/	67.2	1.4	1.2	6.2	21.2	/	/	0.4	/	/	2.5
7A3-5	5.0	63.8	1.6	1.3	6.5	20.5	/	/	/	/	/	1.4
	/	67.6	1.7	1.4	6.7	21.3	/	/	/	/	/	1.4

7A3-6	41.4	26.1	/	0.6	/	1.6	1.9	0.4	/	/	/	25.9
	/	44.6	/	1.0	/	2.7	3.3	0.7	/	/	/	44.3
8A3-7	20.7	41.6	0.8	0.4	2.9	7.2	2.2	/	/	/	/	23.6
	/	52.5	1.0	0.5	3.7	9.1	2.7	/	/	/	/	29.7
8A3-8	6.9	60.9	1.2	1.2	6.0	20.2	/	/	/	/	/	3.6
	/	65.4	1.2	1.3	6.5	21.7	/	/	/	/	/	3.9
7A6-9	25.3	35.1	1.0	0.7	4.1	6.7	1.0	/	0.3	0.7	/	23.6
	/	47.0	1.4	0.9	5.6	8.9	1.4	/	0.4	0.9	/	31.7
7A6-10	33.5	26.9	/	0.2	/	1.9	1.6	/	/	1.0	/	31.3
	/	40.5	/	0.3	/	2.9	2.4	/	/	1.5	/	47.0
7A6-11	4.5	62.9	1.8	1.2	6.8	19.6	/	/	0.3	/	/	3.0
	/	65.8	1.9	1.2	7.2	20.5	/	/	0.3	/	/	3.1
8A6-12	14.1	56.5	0.6	0.8	3.2	14.0	/	0.1	/	/	/	10.7
	/	65.9	0.7	0.9	3.7	16.3	/	0.1	/	/	/	12.5
8A6-13	11.6	57.7	1.5	0.8	3.9	17.8	/	/	/	/	/	6.9
	/	65.2	1.7	0.9	4.4	20.1	/	/	/	/	/	7.7
7A9-14	36.9	39.8	0.9	/	/	2.4	1.5	0.7	/	/	/	15.6
	/	63.1	1.5	/	/	3.8	2.3	1.2	/	/	/	24.8
7A9-15	18.6	55.6	0.9	/	/	11.1	/	0.8	/	/	/	13.0
	/	68.3	1.1	/	/	13.6	/	0.9	/	/	/	16.0
7A9-16	11.6	60.4	0.7	0.9	4.3	13.0	/	0.6	/	/	/	8.5
	/	68.3	0.7	1.0	4.8	14.7	/	0.7	/	/	/	9.6

The SGI coupons selected for XPS analysis were shown in (***Figure 42***) for static experiments under different experimental conditions. Relative atomic concentrations using XPS for selected points on exposed surface of SGI coupons were tabulated in (***Table 30***). A color change like blue-green, blackish-green was observed on the exposed coupon surface (***Figure 42***) indicating formation of secondary phases. From atomic concentrations (***Table 30***) it is clear most of exposed surface consists of iron, oxygen and silicon as chief elements which form corrosion products. Here atomic ratio (***Table 30,*** point 2, 15) shows the probability of iron silicate formation, since iron and silicon have atomic ratio was 1:1. The atomic concentrations of oxygen are notably high in many samples, reflecting a possible iron oxide layer (Fe_xO_y) formation especially in points like (***Figure 42***, point 1, 3, 6, 7, 9 and 10) and some location of exposed surface was also covered with bentonite. In some cases there are possibilities of formation of iron oxide + iron silicate. Thus, exposed corroded surface consist of inhomogeneous distribution of secondary phase on the surface of SGI coupons for the static experiments. A dense layer of corrosion products like iron silicate and green rust was formed during longer time period (9 months) of static experiments, which decreases the corrosion rate as discussed in corrosion rate measurement (***Figure 37***). The results show the diversity of surface chemistry across the samples, with variations in elemental composition pointing to differences in phase formation and oxidation states. XPS analysis suggests that the surfaces were a mixture of oxide layers, iron silicate and metallic surfaces distributed unevenly over the exposed surface of SGI coupons for static experiments.

3.2.5.2 Dynamic condition systems (3 & 6 months)

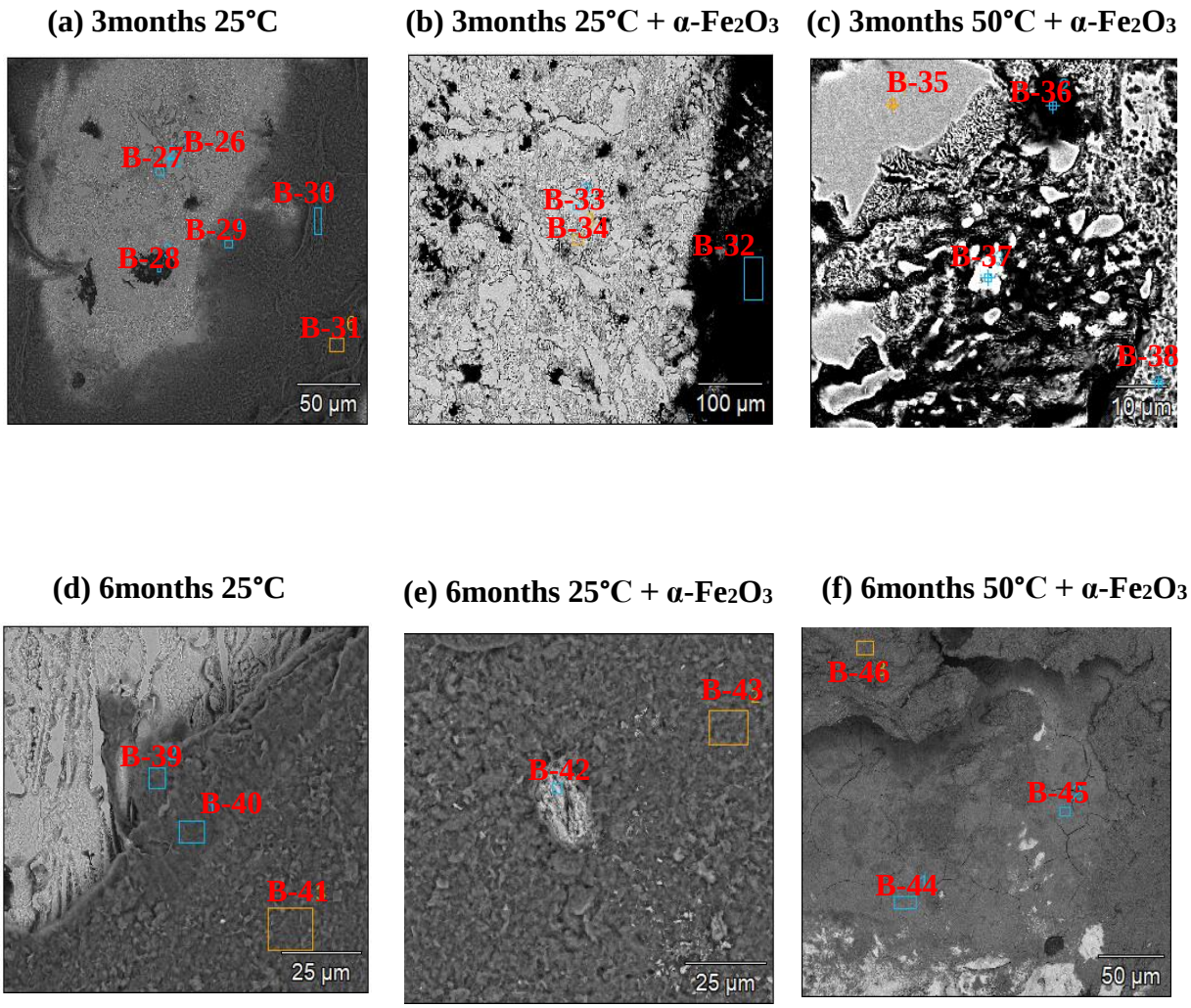

Figure 43 *Scanning electron micrographs (in SE mode) of all SGI coupons corroded for 3 and 6 months under dynamic conditions at different temperatures (exact conditions are indicated above the micrographs). Marked areas were selected for EDXS analysis, quantitative results are provided in* ***Table 31****.*

Table 31 *Relative atomic concentrations by EDXS analyses at selected areas shown in above* ***Figure43****. Relative errors are estimated to be within ± 10%.*

Area	C	O	Na	Mn	Al	Si	S	Cl	Fe
B-26	11.5	/	/	0.7	/	0.3	/	/	87.4
B-27	9.9	11.2	/	0.8	0.2	2.4	0.7	0.7	73.9
B-28	32.8	48.5	1.2	/	3.8	9.3	/	/	3.7
B-29	1.3	46.3	0.4	/	5.9	14.2	/	/	29.4
B-30	1.9	55.8	1.0	/	8.4	25.7	/	/	5.1
B-31	1.5	59.1	1.6	/	8.4	23.6	/	/	2.2
B-32	2.1	57.7	1.5	/	8.0	20.9	/	/	8.1
B-33	12.4	/	/	0.5	/	0.5	/	/	86.5
B-34	4.3	7.3	/	/	0.4	5.9	0.3	/	81.7
B-35	11.8	/	/	0.4	/	0.3	/	/	87.3
B-36	4.6	66.1	1.3	/	6.7	15.6	0.1	0.1	4.1
B-37	10.0	17.0	/	0.5	0.1	0.7	22.5	/	24.4
B-38	4.0	5.1	/	/	0.6	7.1	/	/	83.3
B-39	/	56.0	1.5	/	9.8	26.4	/	0.2	3.9
B-40	3.8	42.4	1.1	/	10.9	27.2	/	0.2	11.6
B-41	2.0	60.2	1.3	/	8.6	22.5	/	0.2	3.2
B-42	3.0	55.8	/	/	0.7	1.7	/	/	38.8
B-43	3.6	57.0	1.4	/	8.5	21.8	/	/	5.9
B-44	1.5	56.5	0.5	/	2.8	18.9	/	/	19.2
B-45	2.9	54.1	0.9	/	0.6	18.0	/	/	23.0
B-46	1.1	55.1	1.3	/	9.1	25.0	/	/	6.9

SEM-EDXS analysis micrographs for various selected areas were shown in (***Figure 43***) and their atomic concentration results were tabulated in (***Table 31***) for SGI coupons corroded for three and six months of dynamic experiments. SEM-EDXS results of areas (B-29, B-44, B-45) shown in (***Figure 43***) led to form iron silicate on the exposed surface. For 6 months coupon at 25°C with added hematite have area such as B-42, data shown in (***Table31***) indicate the presence of iron oxide (Fe_2O_3), on the exposed surface of coupon, which means added hematite was not consumed fully to form more stable corrosion products (magnetite) during exposure. SEM-EDXS results of the areas (B-28, B-31, B-32, B-36, B-41, and B-46) which were enriched with sodium, silicon, aluminum, oxygen and iron can be attributed to bentonite covering the exposed area of SGI coupon. Iron/bentonite interface was most active region for formation of iron silicate as a secondary phase. Overall, based on the EDXS results, it seems that the corrosion products generally present here consist of iron oxides and potentially iron silicates. Based on electron microscopic data, the steel degradation mechanisms under dynamic conditions seem not much different from that under static conditions.

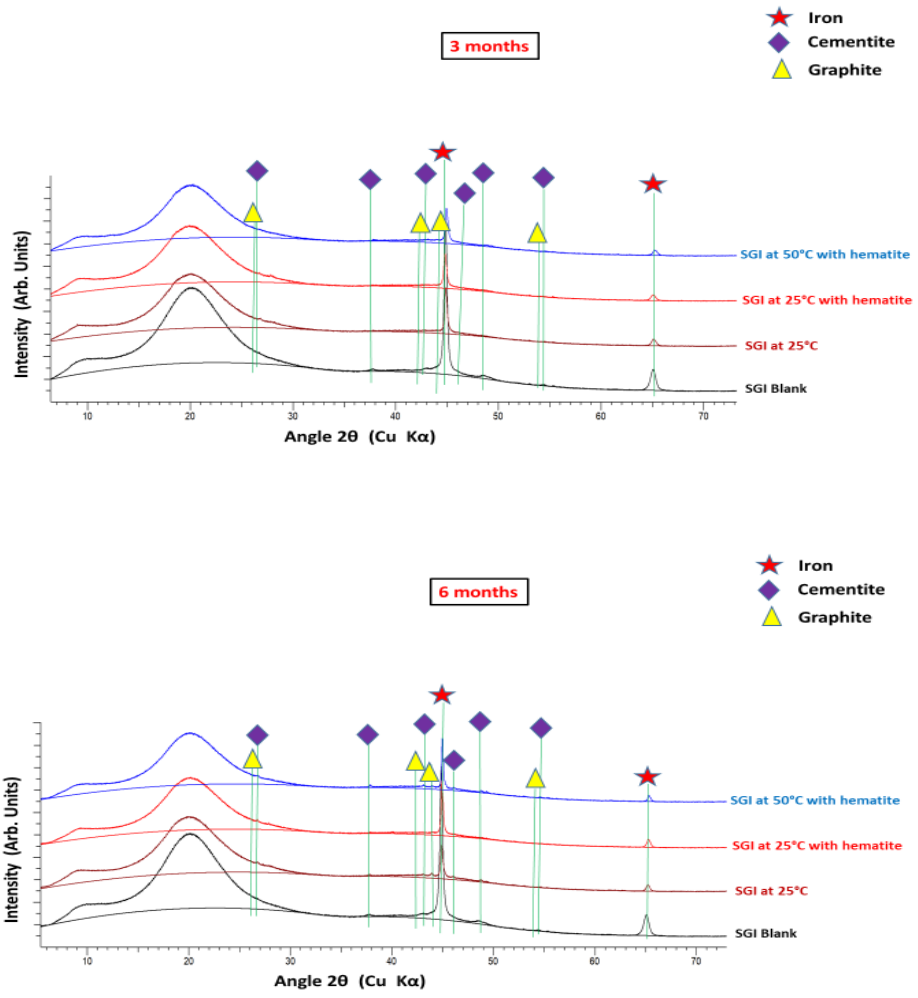

Figure 44 *X-ray diffractograms recorded on the corroded SGI coupons after 3 months (top) and 6 months (down) reaction time under dynamic conditions (exact conditions are indicated on individual XRD plot).*

The XRD analysis of corroded SGI coupons obtained after three and six months of dynamic experiments was carried out, and its diffractograms were shown in (***Figure 44***). XRD analysis of the corroded specimens could only reveal the presence of structures characteristic of the coupon with its components cubic iron (PDF 87-0721), cementite (PDF 85-0871) and graphite (PDF 75-1621) (***Figure 44***). No secondary phase presence could be detected, suggesting that either their amount was too low, that they are of too low crystallinity, or that they must have been removed when cleaning off the excess suspension. There is not much difference observed in six months coupons compared to three months in terms of obtained phase (primary) from XRD analysis. Although hematite was added in some experiment as a transient but due to low amount it was not detected in XRD analysis. XRD analysis results for dynamic experiments were almost comparable with that of static experiments (except green rust formation) for SGI coupons.

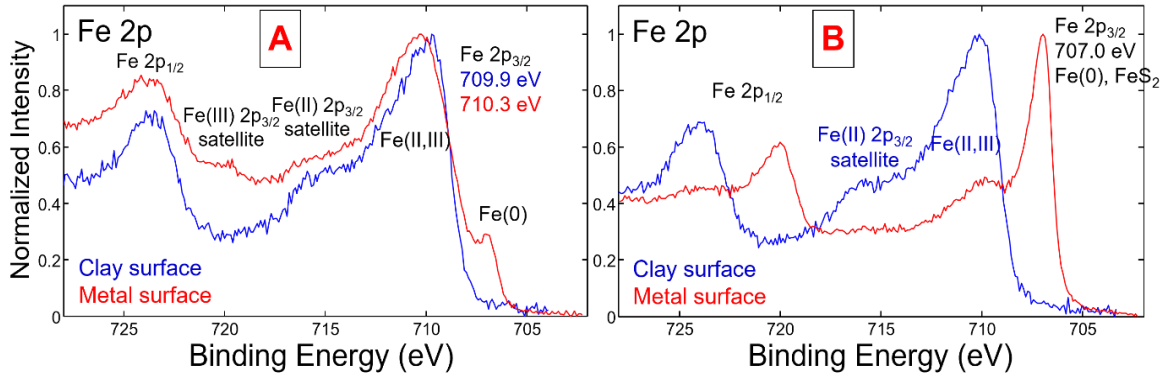

Figure 45 *X-ray photoelectron spectra recorded on SGI corroded under dynamic conditions for 3 months at 25°C in presence of α-Fe2O3 (A) and SGI corroded for 3 months at 50°C in presence of α-Fe2O3 (B).*

XPS spectra recorded for selected SGI coupons for dynamic experiments were shown above in (***Figure 45***). The spectral lines here gave information about oxidation state of iron on metal and clay surface. Iron is present in divalent and trivalent oxidation state at the surface exposed to the suspension for 3 months at 25°C with added hematite present (***Figure 45*-A**). In the parallel experiment at 50°C, the Fe 2p spectrum recorded at the coupon surface agrees with the presence of metallic Fe, suggesting that no Fe-bearing secondary phase was attached to the surface. The sulfur 2p line (**data shown in appendices**) hints at the presence of low amounts of sulfides at the surface of both coupons that may possibly be explained by the presence of admixed pyrite in the bentonite.

At the clay surface, Fe is present as a mixture of Fe(II) and Fe(III), and this result is comparable to that from experiments under static conditions (***Figure 41***). This finding would suggest that Fe(II) formed upon steel corrosion reacted with the contacting bentonite, resulting either in the (partial) reduction of structural Fe(III) of bentonite or the formation of a mixed Fe(II)/Fe(III) compound. Thus, little amount of neoformed Fe-bearing phase could be detected by SEM-EDXS at the coupon/bentonite interface, suggesting a partial reduction of structural Fe of bentonite. This would also be consistent with the measured negative E_h values (***Figure 36***).

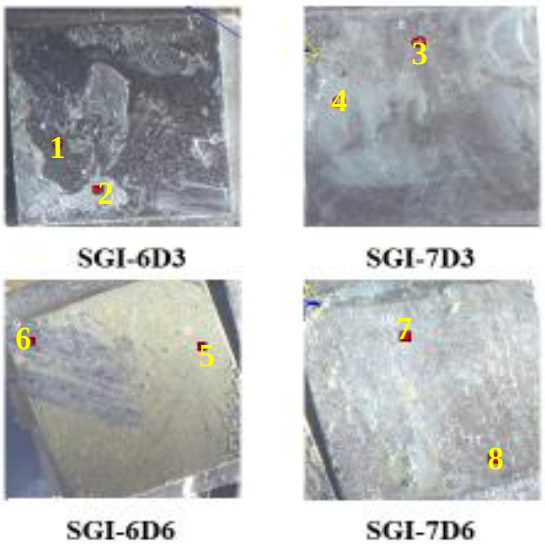

Figure 46 *Pictures taken in XPS chamber of SGI coupons corroded under dynamic conditions (exact conditions are indicated on the individual sample, details of conditions are available in appendix). Marked points were selected for atomic concentration analysis, quantitative results are provided in* ***Table 32****.*

Table 32 *Relative atomic concentrations by XPS analyses at selected points of SGI coupons for dynamic experiments shown in above* ***Figure 46****. Relative errors are estimated to be within ± 10 % (Here each measurement has two type of atomic concentration: one with presence of carbon and one without carbon presence).*

Point	C	O	Na	Mg	Al	Si	S	Cl	Ca	Mn	Cu	Fe
6D3-1	26.2	47.9	1.6	0.3	2.0	4.8	0.5	1.2	0.2	/	/	15.2
	/	64.9	2.2	0.4	2.8	6.5	0.7	1.6	0.3	/	/	20.6
6D3-2	9.3	61.2	0.4	0.9	5.7	18.3	/	/	/	/	/	3.9
	/	67.5	0.4	1.0	6.3	20.2	/	/	/	/	/	4.3
7D3-3	22.1	41.1	/	0.8	2.5	8.0	2.1	0.5	/	/	0.2	21.4
	/	52.8	/	1.0	3.2	10.3	2.7	0.6	/	/	0.2	27.4
7D3-4	6.8	62.3	0.4	0.9	6.0	18.5	/	0.1	/	/	/	5.1
	/	66.9	0.4	0.9	6.4	19.8	/	0.1	/	/	/	5.4
6D6-5	10.8	59.2	0.7	1.0	6.9	19.4	/	0.2	/	/	/	1.6
	/	66.4	0.8	1.2	7.8	21.8	/	0.2	/	/	/	1.8
6D6-6	33.2	39.6	0.5	0.3	1.9	8.2	/	/	/	/	/	16.2
	/	59.3	0.7	0.5	2.9	12.3	/	/	/	/	/	24.3
7D6-7	10.6	58.5	1.1	0.8	6.0	16.9	/	/	/	/	/	6.2
	/	65.4	1.3	0.9	6.7	18.9	/	/	/	/	/	6.9
7D6-8	20.3	44.9	0.3	0.4	3.3	7.6	3.7	0.3	/	0.4	/	18.7
	/	56.4	0.3	0.5	4.1	9.5	4.6	0.4	/	0.5	/	23.5

The SGI coupons selected for XPS analysis were shown in (***Figure 46***) for dynamic experiments under different experimental conditions. Relative atomic concentration using XPS for selected points on exposed surface of SGI coupons were tabulated in (***Table 32***). A color change like blue-green, yellowish-green and blackish was observed on the exposed coupon surface indicating formation of different corrosion products (secondary phases). From atomic concentrations ***(Table 32)*** it is clear most of exposed surface consists of iron, oxygen and silicon as chief elements which form corrosion products.

Here atomic ratios of iron, silicon and oxygen as shown in (***Table 32,*** point 4, 7) show probability of iron silicate formation as corrosion products or bentonite presence. The atomic concentrations of oxygen are notably high in many samples, reflecting a possibility of iron oxide + iron silicate formation, especially at points like (***Figure 46***, Point 1, 3, 6 and 8). XPS analysis suggests that the surfaces were a mixture of oxide layers, iron silicate and metallic surfaces distributed unevenly over the exposed surface of SGI coupons for dynamic experiments. No significant differences were observed between three and six months of dynamic experiments. XPS atomic concentration results of above samples shown in (***Figure46***) corroborated with SEM-EDXS results (***Table 31***). Overall XPS analysis results for dynamic experiments were comparable with that of static experiments for SGI coupons.

3.3 Corrosion of spring steel in MX-80 bentonite

3.3.1 Initial Characterization

The initial characterization of spring steel coupon was carried out to know and compare the morphological changes as corrosion progresses. (***Figure 47***) left side shows the SEM (SE mode) image of polished non-corroded initial spring steel coupon. SEM-EDX results show the chemical composition of the selected areas which focussed on specific points and the average surface area of coupon and their results were shown in the (***Table 33 & Table 34)***. The average area (point 1) of base metal, and point 2 and point 3 are specific points on the surface. The obtained composition of spring steel coupon had good match with the composition compared to the company certificate of the bulk spring steel. Finally, the surface roughness of the starting material was assessed by AFM. A value for the root mean square (RMS) roughness of 10± 2 nm was obtained for a scanned area of 20 x 20 μm^2.

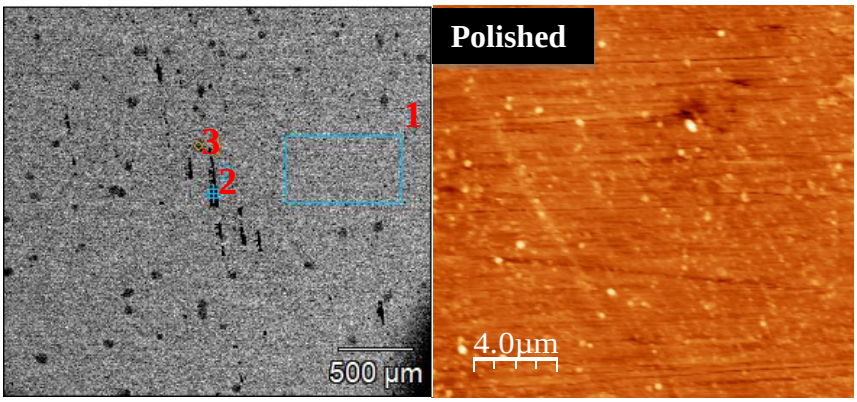

Figure 47 *SEM image on left side and surface roughness image using AFM on right side of the initial SS coupon.*

Table 33 *Composition of initial SS coupon obtained by SEM-EDX before experiment with (+/- 3 Sigma) uncertainty.*

Material /Atom %	C	Si	Mn	Al	Cr	Mo	Fe
SS_point1	2.8±0.5	3.3±0.2	0.9±0.2	0.4±0.1	-	-	92.6±1.2
SS_point2	3.5±0.4	3.1±0.2	0.9±0.2	0.3±0.1	-	-	92.3±1.2
SS_point3	5.4±0.5	3.1±0.2	0.8±0.2	0.2±0.1	-	-	90.5±1.2

Table 34 *Chemical composition of the initial SS coupon with (+/- 3 Sigma) uncertainty.*

Element / wt. %	C	Si	Mn	Al	Ni	Cr	Mo	Fe
Certificate	0.5	1.6	0.8	0.0	0.2	0.2	0.1	96.7
EDX of overall surface (point 1)	0.6±0.1	1.8±0.1	0.9±0.2	0.2±0.1	-	-	-	96.6±1.3
EDX of point 2	0.8±0.1	1.6±0.1	0.9±0.2	0.1±0.1	-	-	-	96.6±1.3
EDX of point 3	1.2±0.1	1.7±0.1	0.8±0.2	0.1±0.1	-	-	-	96.2±1.3

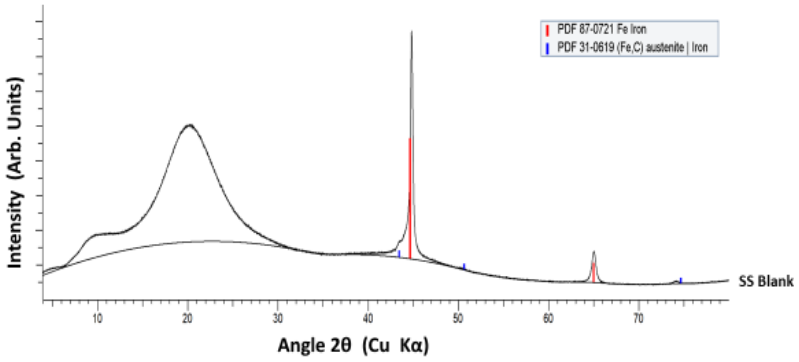

Figure 48 *X-ray diffractogram of the initial SS coupon before experiment (with air scattering effect).*

The X-ray diffractogram of initial spring steel coupon was shown in the (***Figure 48)***. The X-ray diffractogram of spring steel (***Figure 48)*** shows a good match with cubic iron (PDF 87-0721), while the small peaks correspond to the austenite (PDF 31-0619) as expected.

3.3.2 Dissolved metal ions evolution

As already described in the section ***3.1.2***, the concentration of dissolved ions was determined (see appendices section) and only some elements (Fe, Si and Al) are reported here for static (***Table35***) and dynamic experiments (***Table36 and Table37***) of spring steel coupons. In case of spring steel coupons iron evolution is mainly due to steel corrosion whereas silicon and aluminium evolution is due to clay dissolution. In addition, silicon and aluminium are also the components of the pore water and simulated groundwater.

For static experiments, the concentrations of Fe is ranging from 200 to 1500 µg/L, Si varies from 8600 to 28900 µg/L, and Al fluctuates and reaches values up to 4600 µg/L in some case. The measured concentrations of silicon (at least for 9 months w/o scratches), aluminium and iron are quite similar to the concentration of equilibrium bentonite slurry where Si concentration is ~13000 µg/L, Al concentration is ~500 µg/L and Fe concentration is ~400 µg/L. Overall, for static experiments, the results suggests that time, temperature and scratching does not influence significantly the dissolution behavior of Fe, Si, and Al.

Table 35 *Dissolved amounts of Fe, Si and Al ions in the pore water solutions in contact with SS coupons after 3, 6 and 9 months static experiments. Numbers in parentheses correspond to the relative standard deviation in percentage.*

System/ Amounts in µg/L	Fe	Si	Al
3months 25°C w/o scratches	200(4.9)	10800(0.8)	800(1.5)
3months 25°C with scratches	200(6.6)	13600(0.8)	500(3.5)
3months 50°C w/o scratches	1500(2.1)	18600(0.4)	600(1.9)
3months 50°C with scratches	1100(2.4)	28900(1.0)	4600(2.2)
6months 25°C w/o scratches	1200(1.7)	11100(1.8)	900(0.3)
6months 25°C with scratches	800(1.2)	8700(0.4)	700(1.2)
6months 50°C w/o scratches	500(4.9)	18100(0.4)	1500(55)
6months 50°C with scratches	200(4.2)	8600(0.4)	2200(11)
9months 25°C w/o scratches	300(5.2)	12900(0.7)	500(8.6)
9months 25°C with scratches	1100(1.7)	10900(0.7)	600(2.9)

Table 36 *Dissolved amounts of Fe Si and Al ions in the ground water (solution) in contact with SS coupons during 3 months dynamic experiment. Numbers in parentheses correspond to the relative standard deviation in percentage.*

25°C w/o scratches (System)/Amounts in µg/L	Fe	Si	Al
A (4 weeks)	1500(1.6)	17600(0.5)	800(7.1)
B (5 weeks)	<100	18400(1.6)	900(9.9)
C (6 weeks)	<100	20200(2.0)	1100(7.1)
D (8 weeks)	100(8.6)	18500(1.2)	300(2.8)
E (10 weeks)	<100	22300(0.9)	500(1.6)
F (12weeks)	<100	20500(0.8)	300(0.9)

25°C with scratches (System)/Amounts in µg/L	Fe	Si	Al
A (4 weeks)	1500(1.7)	17800(0.8)	900(3.5)
B (5 weeks)	<100	19700(1.7)	1100(6.6)
C (6 weeks)	<100	18500(1.0)	1100(2.5)
D (8 weeks)	100(8.6)	18300(0.4)	300(1.2)
E (10 weeks)	<100	21000(0.7)	300(2.5)
F (12 weeks)	<100	23300(1.4)	400(4.8)

50°C with scratches (System)/Amounts in µg/L	Fe	Si	Al
A (4 weeks)	400(3.1)	16500(1.4)	1000(5.6)
B (5 weeks)	<100	18700(0.5)	1100(2.8)
C (6 weeks)	<100	20100(0.5)	1400(3.4)
D (8 weeks)	150(1.0)	20900(1.0)	800(2.6)
E (10 weeks)	300(2.9)	21100(0.7)	600(4.9)
F (12 weeks)	400(2.5)	21600(0.4)	400(5.4)

Table 37 *Dissolved amounts of Fe Si and Al ions in the ground water (solution) in contact with SS coupons during 6 months dynamic experiment. Numbers in parentheses correspond to the relative standard deviation in percentage.*

25°C w/o scratches (System)/Amounts in µg/L	**Fe**	**Si**	**Al**
A (6 weeks)	<200	19800(1.2)	200(4.8)
B (10 weeks)	<200	19600(0.9)	100(1.9)
C (14 weeks)	<200	21400(0.5)	200(2.1)
D (18 weeks)	<100	18300(1.2)	100(15)
E (22 weeks)	<100	19100(1.6)	100(9.5)
F (26 weeks)	<100	19500(0.7)	100(5.8)

25°C with scratches (System)/Amounts in µg/L	**Fe**	**Si**	**Al**
A (6 weeks)	<200	19500(0.8)	200(1.6)
B (10 weeks)	600(8.4)	18400(0.4)	200(4.2)
C (14 weeks)	<200	21900(0.7)	200(1.0)
D (18 weeks)	<100	19700(1.1)	100(8.9)
E (22 weeks)	<100	19200(1.3)	100(8.9)
F (26 weeks)	<100	20200(1.3)	2500(1.3)

50°C with scratches (System)/Amounts in µg/L	**Fe**	**Si**	**Al**
A (6 weeks)	500(15)	19900(2.2)	400(1.8)
B (10 weeks)	700(5.6)	22500(1.0)	600(1.8)
C (14 weeks)	<200	21100(0.9)	200(1.0)
D (18 weeks)	<100	21700(0.8)	500(1.9)
E (22 weeks)	<100	20900(2.3)	400(1.8)
F (26 weeks)	<100	20100(0.4)	200(5.3)

For dynamic experiments, the concentration of Si varies from 16500 to 23300 µg/L which is quite in agreement with concentration of simulated groundwater where Si concentration is ~17000 µg/L (***Table2***). Al concentration is higher in some cases at elevated temperature (50°C) compared to room temperature and iron concentration is initially high and then lower in most of the cases. Overall, temperature, time and the presence of scratches does not have significant effect on the concentrations of Fe, Si, and Al. The uncertainties suggest that variations in ions concentration lie within the scatter of the data. Here, Fe dissolution is mainly due to steel corrosion whereas Si and Al concentrations indicate clay dissolution not steel corrosion.

Table 38 *Determination of Cu, Ni, Fe, Si and Al concentrations for a bentonite that was in contact with SS coupon has been digested in acid and the resulting liquid phase has been quantified by using ICP-MS for 6 months dynamic experiment (Numbers in parentheses correspond to the relative standard deviation in percentage).*

(Dynamic) System/ Amounts in µg/g	**Cu**	**Ni**	**Fe**	**Si**	**Al**
6months 50°C SS with scratch	8(0.9)	8(1.1)	26110(1.2)	271100(1.5)	51280(2.8)

Determination of Cu, Ni, Fe, Si and Al concentration for a bentonite that was in contact with SS coupon has been digested in acid and the resulting liquid phase has been quantified by using ICP-MS for 6 months dynamic experiment. The result shown in ***(Table 38)*** shows variation in concentration (Fe, Si and Al) for elements that were of interest for spring steel. The concentration of Fe is higher for spring steel compared to carbon steel and without coupon (***Table49***), which release is due to steel corrosion and is mainly sorbed on the clay surface rather than dissolving into the solution. Concentration of Si and Al are comparable and lying within experimental uncertainty.

3.3.3 pH / E_h evolution

The pH and E_h values of spring steel coupons for three, six and nine months of static experiments were shown in (***table 39***).

Table 39 *pH / Eh evolution of SS in contact with MX-80 bentonite slurry after 3, 6 and 9 months exposure time.*

System	pH	E_hw.r.t SHE (mV)
3months 25°C w/o scratches	8.14±0.05	-130±50
3months 25°C with scratches	7.84±0.05	-380±50
3months 50°C w/o scratches	8.21±0.05	-247±50
3months 50°C with scratches	8.47±0.05	-264±50
6months 25°C w/o scratches	7.87±0.10	-268±50
6months 25°C with scratches	7.60±0.05	-376±50
6months 50°C w/o scratches	7.74±0.10	-273±50
6months 50°C with scratches	8.19±0.10	-467±50
9months 25°C w/o scratches	7.91±0.10	-343±50
9months 25°C with scratches	7.88±0.10	-288±50

The *in-situ* pH did not evolve much in spring steel corrosion experiments carried out for 3 months (***Table 39***), slightly decreased after 6 months and has similar range after 9 months. The redox potential of all static experiments with spring steel coupons were clearly negative after 3, 6 and 9 months with and without scratches (***Table 39***). E_h values were not much affected by temperature, but in some cases, significantly lower values were found like for slurry in contact with scratched coupon after 6 months at 50°C (elevated temperature) (-467±50 mV). Overall, reducing conditions developed as a consequence of steel corrosion, suggesting the formation of Fe (II) bearing compounds. The absence of significant pH change may be related to bentonite acting as pH buffer.

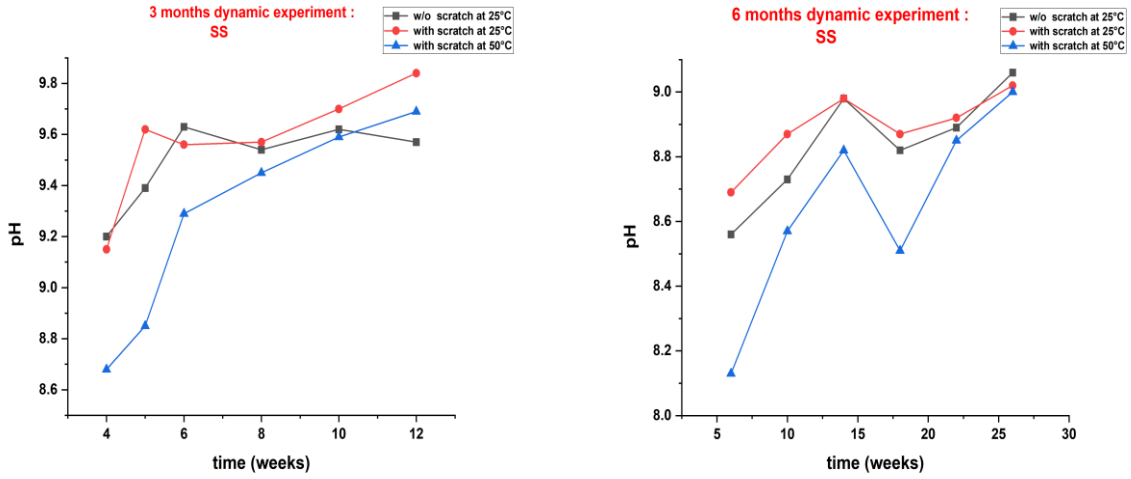

Figure 49 *The pH evolution of the SS coupons in ground water (solution) during 3 (left side) and 6 months (right side) dynamic experiments (±0.1 is uncertainty).*

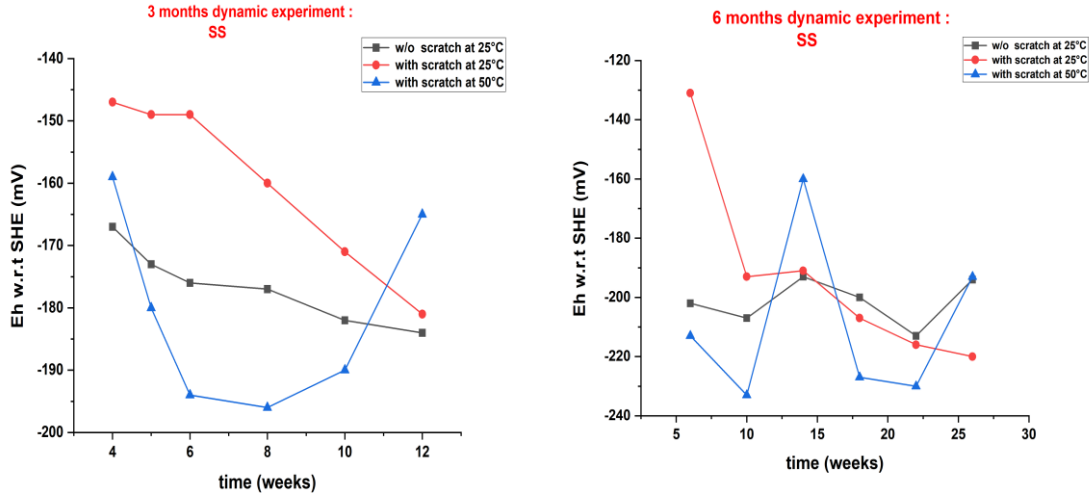

Figure 50 *The Eh evolution of the SS coupons in ground water (solution) during 3 (left side) and 6 months (right side) dynamic experiments (±50mV is uncertainty).*

The pH and E_h values of spring steel coupons for three and six months dynamic experiments were shown in (***Figure 49***) and (***Figure 50***). As already outlined in chapter 3.1.3, pH again increases towards the value of the inflowing simulated groundwater. E_h values lie throughout in the reducing range (-131 mV to -233 mV) in dynamic experiments, partly different to observations in static experiments. Also the scratching the SS coupon surface does not have a significant impact.

3.3.4 Corrosion rate

The corrosion rates of spring steel for static and dynamic experiments were calculated using the weight loss method and are shown in (***Figure 51***) for 3, 6 and 9 months of static experiments and in (***Figure 52***) for 3 and 6 months dynamic experiments.

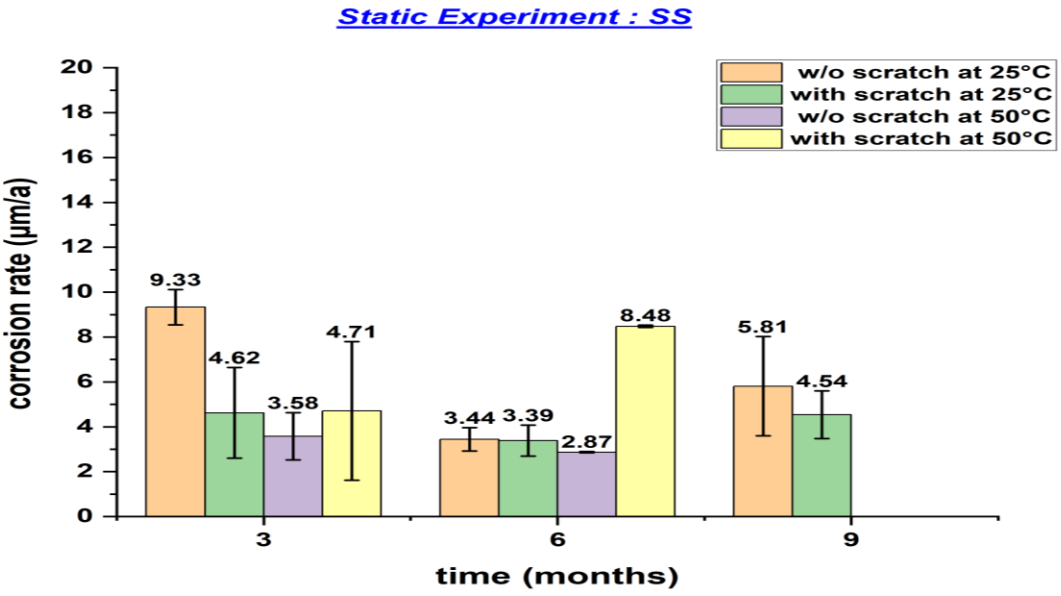

Figure 51 *Corrosion rates of all SS coupons obtained after 3, 6 and 9 months static experiments.*

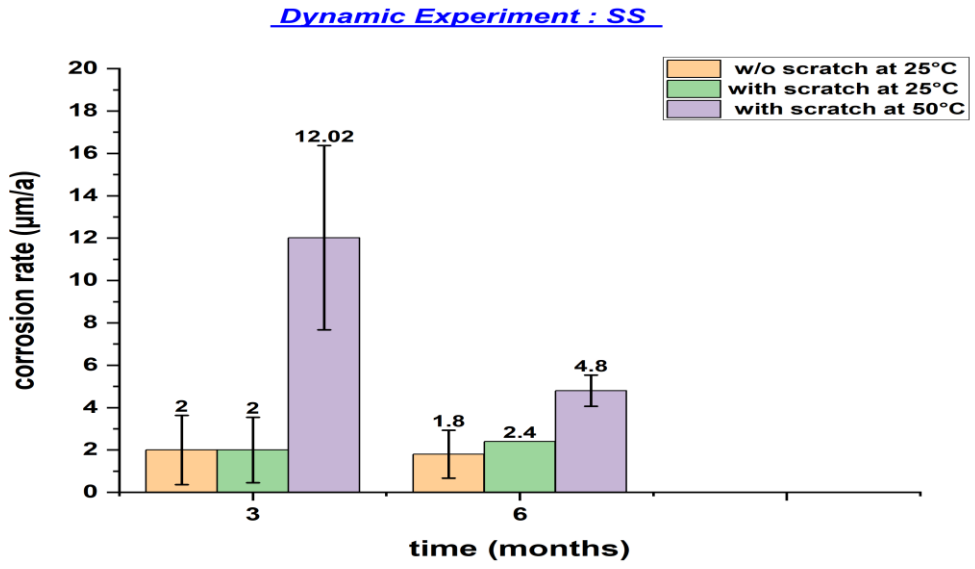

Figure 52 *Corrosion rates of all SS coupons obtained after 3 and 6 months dynamic experiments.*

The corrosion rate of spring steel mainly varies with temperature and is not much affected by presence of surface scratches or exposure time. In static and dynamic experiments, the corrosion rate changes with temperature in most cases, being higher at 50°C than at 25°C. The corrosion rate of spring steel in bentonite suspension for both experiments (static and dynamic) at 25°C, varies in the range between 2.00±1.63 to 5.81±2.21 µm/a which is in agreement with the reported average corrosion rate of carbon steel (~2 µm/a) embedded within compacted MX-80 bentonite and exposed to natural granitic pore water for 394 days in the in situ MaCoTe experiment **(Reddy, Padovani, Rance, et al., 2021)**. Overall, for static experiments, the corrosion behavior of the material varies with mainly temperature and in some cases with exposure duration.

In dynamic experiments, the corrosion rate at 50°C varies in the range 4.80±0.74 to 12.02±4.35 µm/a, which is quite comparable with corrosion rate of static experiments (considering experimental uncertainty). Longer exposure time (3 to 6 months) in both experiments show little variation in corrosion rate that hints at the formation of a protective passivation layer at the coupon surface. Taking uncertainties into account, temperature is the dominant factor influencing corrosion rate, scratching the surface and time has limited effect on corrosion behavior of spring steel coupons in static and dynamic experiments. Overall, the results suggest that higher temperature significantly affect the corrosion rate. Corrosion rate of spring steel for static and dynamic experiments were relatively comparable.

3.3.5 Secondary phase characterization

3.3.5.1 Static condition systems (3, 6 & 9 months)

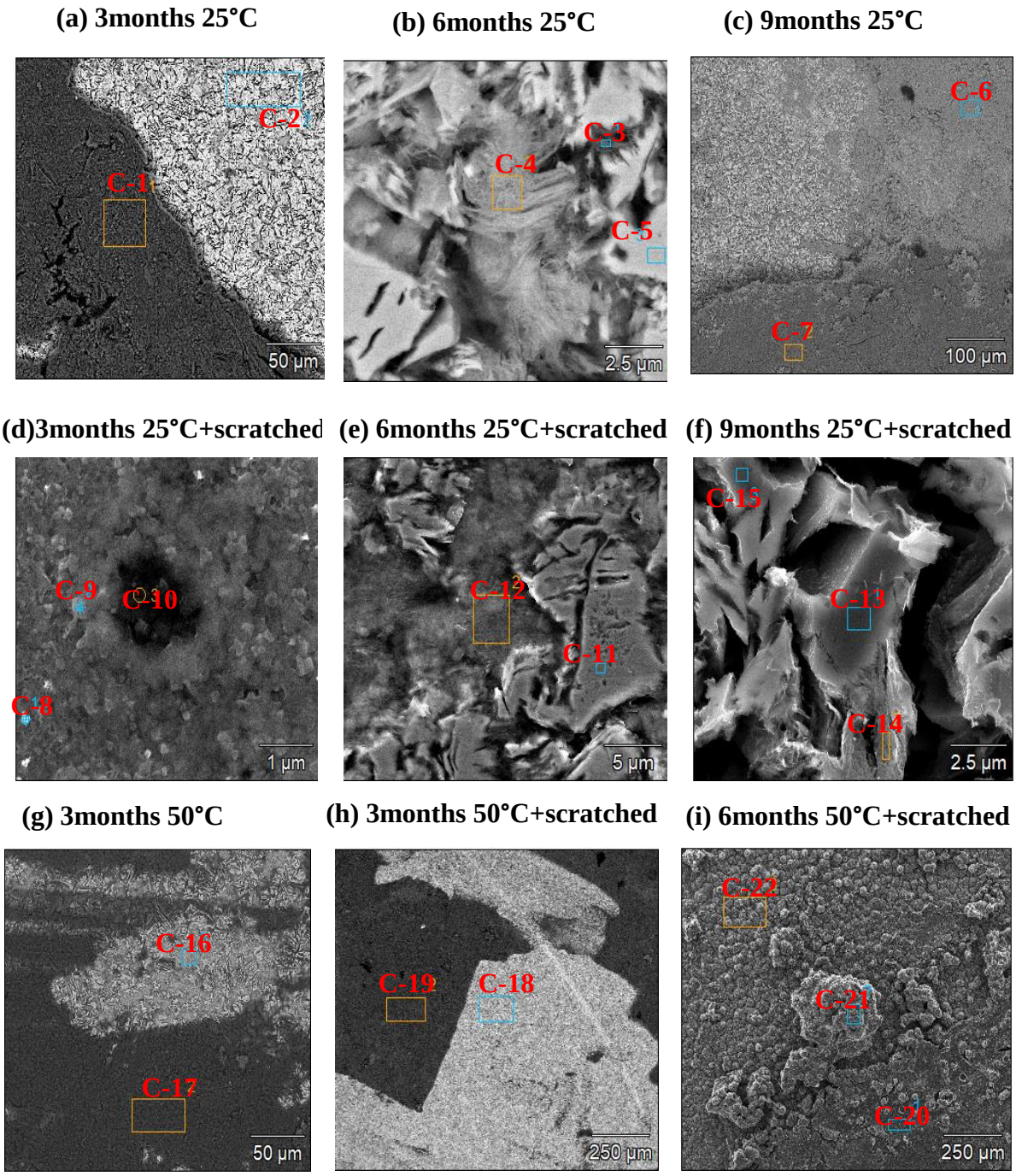

Figure 53 *Scanning electron micrographs (in SE mode) of all SS coupons corroded for 3, 6 and 9 months under static conditions at different temperatures (exact conditions are indicated above the micrographs). Marked areas were selected for EDXS analysis, quantitative results are provided in* ***Table 40****.*

__Table 40__ Relative atomic concentrations by EDXS analyses at selected areas shown in above __Figure 53__. Relative errors are estimated to be within ± 10%. (Here each measurement has two type of atomic concentration: one with presence of carbon and one without carbon presence).

Area	C	O	Na	Mn	Al	Si	S	Cl	Cr	Ni	Fe
C-1	2.0	61.3	1.8	/	5.6	18.6	0.1	0.2	/	/	9.1
C-2	6.5	/	/	0.9	0.3	3.5	0.5	/	0.3	0.5	87.5
C-3	5.4	7.4	/	1.2	/	1.9	/	/	1.1	1.9	78.9
C-4	8.9	9.0	/	1.2	/	1.8	1.2	/	0.9	2.0	73.0
C-5	3.3	/	/	0.9	/	3.7	/	/	/	/	92.1
C-6	6.6	57.5	1.1	/	0.2	0.8	0.2	0.6	/	/	32.5
C-7	1.6	58.8	2.1	/	8.2	21.0	0.3	0.2	/	/	6.2
C-8	8.5	8.2	/	/	0.2	4.7	/	/	/	/	76.5
C-9	5.4	20.9	6.2	/	/	4.0	/	0.2	/	/	63.0
C-10	8.8	32.2	/	/	0.1	3.5	0.4	0.7	/	/	51.8
C-11	3.2	/	/	1.3	0.5	4.0	/	/	/	/	91.0
C-12	6.8	24.3	/	0.9	1.1	3.4	1.0	0.6	0.8	1.4	57.4
C-13	3.0	/	/	0.7	0.2	3.5	/	/	0.2	/	92.3
C-14	12.8	11.3	/	0.8	/	1.6	1.2	0.3	0.9	5.1	63.6
C-15	3.3	/	/	0.8	0.2	3.8	/	/	0.2	/	91.6
C-16	5.6	15.1	/	0.7	2.3	6.4	1.1	/	0.4	0.8	66.2
C-17	2.4	56.8	1.6	/	8.4	22.6	/	0.2	/	/	6.1
C-18	5.7	/	/	0.9	/	2.8	0.9	/	/	/	89.4
C-19	2.4	60.6	1.7	/	7.6	21.8	/	0.3	/	/	3.7
C-20	1.7	63.2	/	/	6.6	16.7	/	/	/	/	10.8
C-21	2.0	61.7	0.9	/	5.8	16.6	/	/	/	/	11.4
C-22	6.5	58.0	/	/	1.4	6.1	0.2	/	/	/	27.5

SEM-EDXS analysis micrographs for various selected areas were shown in (***Figure 53***) and their atomic concentration results were tabulated in (***Table 40***). Spring steel consists of ferrite, austenite, pearlite and small amounts of martensite depending on its heat treatment. Here from the observation (change in microstructure) it seems that non-uniform general corrosion takes place at steel/bentonite interface due to preferential ferrite dissolution. Here most parts of spring steel surface look like needle or lath shape microstructure, which is martensitic phase whereas other bright part was austenite and dark region was voids created due to ferrite dissolution. Apart from these, other black regions at the exposed surface were covered with bentonite clay.

For coupons at 25°C after 3 and 9 months without scratch and for coupons at 50°C with scratch after 6 months, EDXS analyses results for selected areas (C-1, C-7, C-17, C-20, and C-21) shown in (***Figure 53***) show the possibility of iron silicate formation (based on atomic concentration) or presence of iron enriched bentonite layer. It was observed from the result at room temperature the atomic percentage of Fe decreased abruptly at different regions on the surface. Oxygen is also present on the coupon surface after exposure and the amount of silicon slightly increased on coupon surface but larger amounts of silicon were found in the region where surface was covered with bentonite. Iron-based corrosion products, such as iron oxides (Fe_xO_y), are predominant in some areas like (C-6, C-9, C-10 and C-12).

The presence of oxygen alongside iron in these areas would support the formation of Iron (hydr)oxides on the exposed surface as corrosion products when iron is exposed to water saturated bentonite under anoxic conditions. There are certain regions like areas (C-2, C-5, C-11, C-13, C-15, and C-18) where dissolution of iron was limited or less was the base metallic alloy. There was limited effect of scratch on morphology and elements distribution over the exposed surface of spring steel coupons under static experiments.

Overall, the SEM-EDXS results highlight the complex interplay of elements across different areas, suggesting that secondary phases, such as oxides, hydroxide and silicates were likely formed based on the observed elemental distributions. The variations in elemental composition between different areas reflect the heterogeneity of the coupons. The formed secondary phases reflect the interactions of the metal substrates with surrounding environmental (bentonite slurry) and its effect on mineralogical changes and corrosion. Iron (hydr)oxides formed at the coupon surface (***Figure 53,*** **C-6**) and seems to be covered by iron silicates/bentonite transformation products ***(Figure53,*** **C-7**).

The XRD analysis of corroded spring steel coupons obtained after three, six and nine months of static experiments was carried out and its diffractograms were shown in (***Figure 54***). The primary peak in the XRD spectrum for three, six and nine months of static experiments likely correspond to the cubic iron (PDF 87-0721) and austenite phase (PDF 31-0619) which is starting material. Apart from this, other reflections attributable to Montmorillonite, Illite/Albite present on the exposed surface specially for three and six months come from the bentonite. The remaining peaks correspond to corrosion products or secondary phase green rust (PDF 13-0090) which was detected in most of the samples for three, six and nine months of static experiments as shown in (***Figure 54***).

There is not much difference observed in 9 months coupons compared to three and six months in terms of secondary phase (corrosion products) from XRD analysis. The broad reflection around 10 and 20 two theta is due to air scattering effect (***Figure 54***) which was common for all coupons tested under anoxic conditions using anoxic holder. Findings suggest that secondary phases formed in too low amounts and are heterogeneous, which distributed over the exposed surface due to difference in experimental conditions (time, temperature). Scratching the surface of spring steel coupons doesn’t affect much the phase formation.

Overall XRD analysis provides insights into the phases present on spring steel coupons after corrosion, which is critical for understanding the extent of corrosion and deriving a corrosion mechanism.

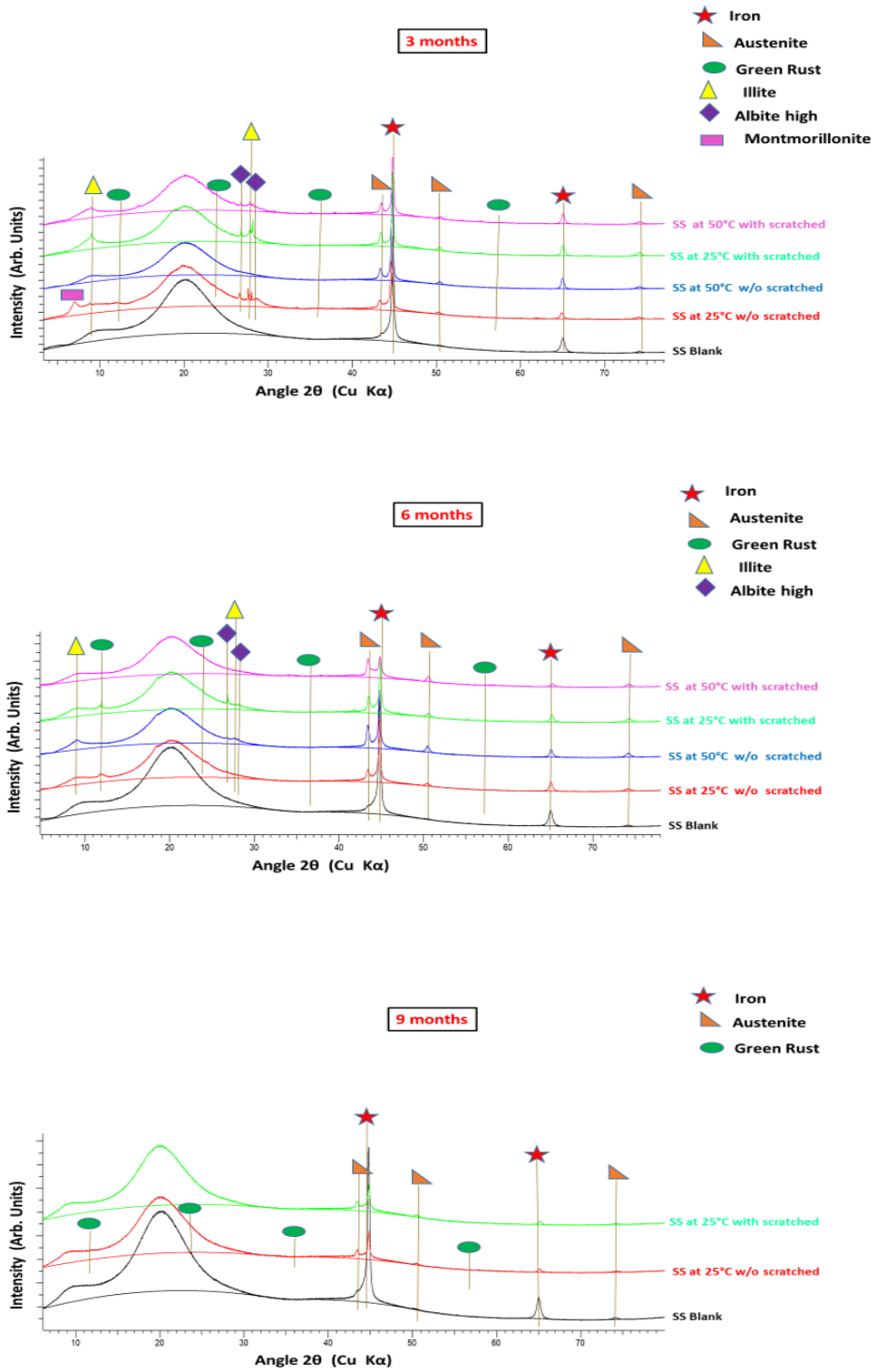

Figure 54 *X-ray diffractograms recorded on the corroded SS coupons after 3 months (top), 6 months (middle) and 9 months (bottom) reaction time under static conditions (exact conditions are indicated on individual XRD plots).*

The spring steel coupons selected for XPS analysis were shown below in (***Figure 55***) for static experiments under different experimental conditions. Relative atomic concentration using XPS for selected points on exposed surface of spring steel coupons were tabulated in (***Table 41***).

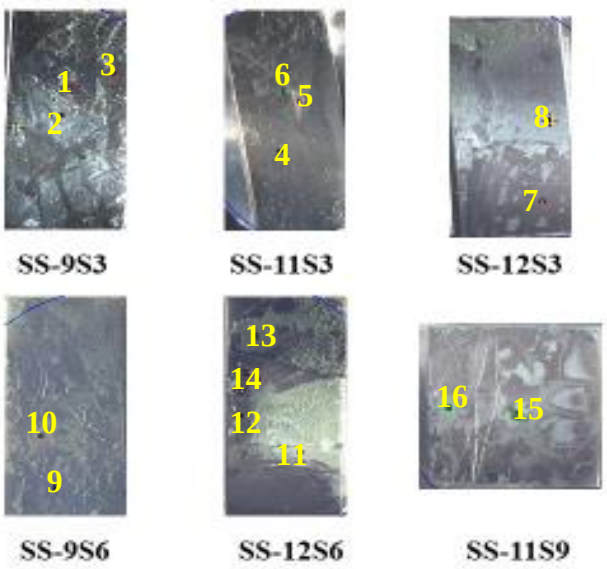

Figure 55 *Pictures taken in XPS chamber of SS coupons corroded under static conditions (exact conditions are indicated on the individual sample, details of conditions are available in appendix). Marked points were selected for atomic concentration analysis, quantitative results are provided in* ***Table 41****.*

Table 41 *Relative atomic concentrations by XPS analyses at selected points of SS coupons for static experiments shown in above* ***Figure55****. Relative errors are estimated to be within ± 10% (Here each measurement has two type of atomic concentration: one with presence of carbon and one without carbon presence).*

Point	C	O	Na	Mg	Al	Si	S	Cl	Cr	Mn	Cu	Ni	Fe
9A3-1	12.3	53.3	2.3	0.7	4.2	12.4	0.2	0.4	/	/	/	0.9	12.6
	/	60.7	2.6	0.8	4.8	14.1	0.3	0.5	/	/	/	1.1	14.4
9A3-2	6.2	62.1	2.0	1.3	6.7	18.5	/	/	/	/	/	/	3.2
	/	66.2	2.2	1.4	7.1	19.7	/	/	/	/	/	/	3.4
9A3-3	12.6	54.7	0.2	0.8	2.7	10.8	/	0.3	/	/	/	/	17.0
	/	62.6	0.2	1.0	3.1	12.3	/	0.4	/	/	/	/	19.4
11A3-4	8.1	63.7	1.7	1.0	6.1	17.4	/	0.2	/	/	/	/	1.8
	/	69.3	1.9	1.1	6.6	19.0	/	0.2	/	/	/	/	2.0
11A3-5	5.3	66.4	1.3	1.2	6.7	18.4	/	/	/	/	/	/	0.7
	/	70.1	1.4	1.3	7.1	19.4	/	/	/	/	/	/	0.7
11A3-6	28.8	43.5	0.8	0.7	/	5.2	1.6	/	/	1.5	1.9	/	15.0
	/	61.1	1.1	1.0	/	7.3	2.3	/	/	2.1	2.7	/	21.1
12A3-7	27.4	39.0	/	0.9	/	4.6	2.3	1.0	/	/	1.7	/	22.7
	/	53.8	/	1.2	/	6.3	3.2	1.3	/	/	2.4	/	31.2

12A3-8	6.6	61.5	1.5	1.3	5.9	19.8	/	/	/	/	/	/	3.4
	/	65.9	1.6	1.3	6.3	21.2	/	/	/	/	/	/	3.6
9A6-9	21.8	38.2	1.4	0.3	3.7	4.8	1.4	/	/	/	0.9	3.3	23.7
	/	48.8	1.8	0.4	4.7	6.2	1.8	/	/	/	1.2	4.2	30.3
9A6-10	11.8	58.7	1.5	0.3	1.0	14.4	/	0.4	/	/	/	/	8.5
	/	66.6	1.7	0.4	4.5	16.4	/	0.4	/	/	/	/	9.6
12A6-11	13.6	59.3	/	0.3	2.0	11.8	/	/	/	/	/	/	13.0
	/	68.6	/	0.4	2.3	13.7	/	/	/	/	/	/	15.1
12A6-12	28.1	39.6	0.3	/	3.6	5.8	/	/	/	/	1.2	1.4	19.9
	/	55.1	0.4	/	5.0	8.0	/	/	/	/	1.7	1.9	27.7
12A6-13	25.8	50.8	0.2	/	/	8.5	0.3	0.3	/	/	0.1	/	13.9
	/	68.4	0.2	/	/	11.4	0.5	0.4	/	/	0.2	/	18.7
12A6-14	32.5	42.0	/	/	/	3.1	0.3	0.5	/	/	0.4	0.4	21.0
	/	62.2	/	/	/	4.5	0.5	0.7	/	/	0.5	0.5	31.0
11A9-15	20.0	58.4	1.6	/	4.3	8.8	0.6	1.2	1.5	/	/	3.0	/
	/	73.0	2.0	/	5.3	11.0	0.7	1.4	1.8	/	/	3.7	/
11A9-16	15.8	57.0	0.9	0.5	2.6	10.5	0.4	1.3	/	/	/	/	10.9
	/	67.8	1.1	0.6	3.1	12.4	0.4	1.5	/	/	/	/	13.0

A color change like blue-green, blackish-green was observed on the exposed coupon surface indicating the formation of different corrosion products. From atomic concentrations (***Table 41***) it is clear most of exposed surface consists of iron, oxygen and silicon as chief elements which can form corrosion products. Here atomic ratio (***Table 41***, point 1 and 16) shows presence of iron silicate/ bentonite layer enriched with iron, since iron and silicon atomic ratio was close to 1:1. The atomic concentrations of oxygen are notably high in many samples, reflecting a possible iron oxide layer (Fe_xO_y) or green rust formation, especially in points like (***Table41***, Point 6, 7, 9, 12 and 14) protecting with bentonite layer at some points like ***Figure55*** (point 9 and12). In some cases (***Figure 55***, point 3, 10 and 13) there are also possibilities of formation of iron oxide + iron silicate. The regions (***Table 41***, ***points*** *2, 4, 8 and 15*) enriched with silicon, oxygen, aluminum, sodium and iron suggest bentonite covering the coupon.

Thus exposed corroded surfaces consist of inhomogeneous distribution of secondary phases on the surface of spring steel coupons for the static experiments. A dense layer of corrosion products like iron silicate and green rust form for longer time period (9 months) of static experiments (***Table 41***, point 16) that results in a decrease of the corrosion rate with increased time as discussed in corrosion rate measurement section. The results show the diversity of surface chemistry across the samples, with variations in elemental composition pointing to differences in phase formation and oxidation states. XPS analysis suggests that the surfaces were a mixture of oxide layers, iron silicate and metallic surfaces distributed unevenly over the exposed surface of spring steel coupons for static experiments.

3.3.5.2 Dynamic condition systems (3 & 6 months)

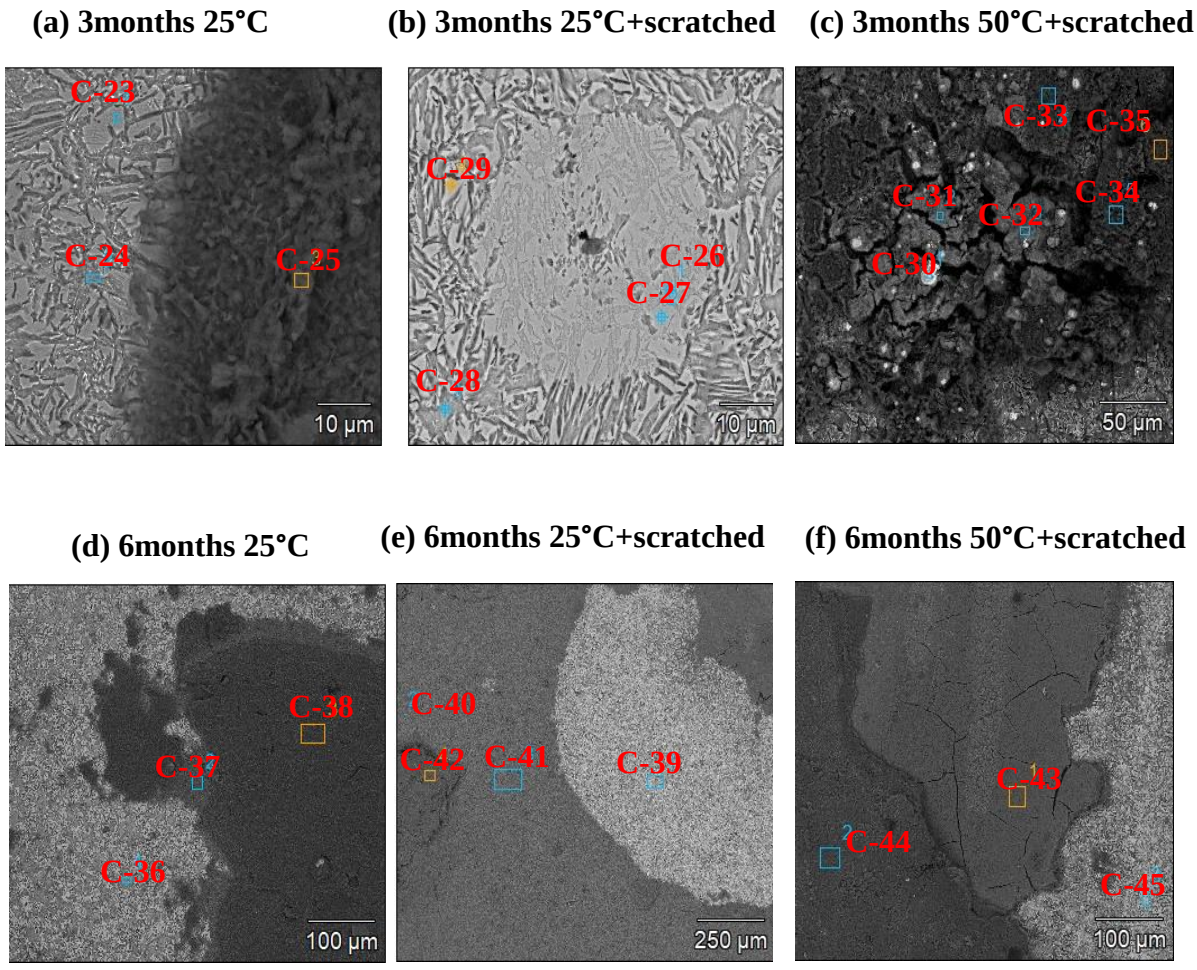

Figure 56 *Scanning electron micrographs (in SE mode) of all SS coupons corroded for 3 and 6 months under dynamic conditions at different temperatures (exact conditions are indicated above the micrographs). Marked areas were selected for EDXS analysis, quantitative results are provided in* ***Table 42****.*

Table 42 Relative atomic concentrations by EDXS analyses at selected areas shown in above Figure56. Relative errors are estimated to be within ± 10%.

Area	C	O	Na	Mn	Al	Si	S	Cl	Cr	Ni	Fe
C-23	4.6	/	/	1.0	0.3	3.3	0.3	/	/	/	90.5
C-24	6.5	4.8	/	0.8	0.4	3.1	1.0	/	/	/	82.9
C-25	3.2	63.3	1.4	/	8.1	20.2	/	0.1	/	/	1.7
C-26	0.9	59.4	/	0.4	0.1	1.1	/	/	0.1	/	38.0
C-27	1.2	59.4	/	0.3	/	1.2	/	/	/	/	38.0
C-28	1.9	58.6	/	0.3	0.2	1.3	/	/	/	0.2	37.2
C-29	1.5	59.0	/	0.3	0.1	1.3	/	/	0.1	/	37.6
C-30	4.2	11.4	/	/	/	/	37.9	/	/	/	7.6
C-31	4.4	44.7	/	/	0.8	2.9	22.0	/	/	/	25.1
C-32	4.2	46.5	/	/	0.9	4.9	19.6	/	/	/	23.6
C-33	2.9	60.6	1.0	/	3.3	17.7	/	/	/	/	13.4
C-34	4.2	59.8	1.0	/	3.3	17.7	/	/	/	/	12.9
C-35	1.9	61.1	1.0	/	4.0	18.0	/	/	/	/	12.8
C-36	7.7	24.9	/	0.7	1.4	4.8	0.9	0.8	0.3	0.7	56.1
C-37	1.6	57.5	/	/	5.7	15.0	0.5	0.6	/	/	18.0
C-38	2.6	60.3	1.7	/	8.2	21.4	/	0.1	/	/	4.1
C-39	7.7	6.7	/	0.9	0.3	3.3	0.9	/	0.5	0.7	77.9
C-40	2.5	61.3	0.5	/	5.7	16.0	/	0.2	/	/	12.5
C-41	2.9	59.3	0.5	/	5.6	17.0	/	0.2	/	/	13.3
C-42	2.3	59.7	1.2	/	7.7	21.5	/	0.1	/	/	5.6
C-43	7.2	55.2	/	/	0.9	16.2	/	0.7	/	/	18.8
C-44	3.0	59.9	1.5	/	8.7	22.6	/	/	/	/	2.6
C-45	4.5	5.3	/	0.8	0.3	3.4	/	/	0.4	9.1	75.2

SEM-EDXS analysis micrographs for various selected areas were shown in (***Figure 56***) and their atomic concentration results were tabulated in (***Table 42***). Spring steel coupons corroded in dynamic conditions were relatively comparable with static conditions. However little differences were observed in certain coupons like shown in (***Figure 56b***) where localized corrosion takes place on specific areas surrounding the scratched region of spring steel (scratched) coupon corroded for 3 months at room temperature (25°C). SEM-EDXS results of areas (C-33, C-34, C-35, C-37, C-40 and C-41) as shown in (***Figure 56***) led to form iron silicate on the exposed surface. For 3 months dynamic spring steel coupon with scratch at 50°C has areas (C-31, C-32) where Fe:S ratio is close to 1:1 indicate formation of iron sulfide. Areas such as (C-26, C-27, C-28, C-29), shown in (***Table42***) indicates formation of iron(hydr)oxides as secondary products on the exposed surface of coupon at 25°C with scratch for 3 months dynamic experiment.

SEM-EDXS results of the areas (C-25, C-38, C-42, and C-44) which were enriched with sodium, silicon, aluminum, oxygen and iron was bentonite clay which covered the exposed area of spring steel coupon. Some amount of dissolved iron was detected on the surface of bentonite clay however, its concentration varies across the exposed surface. The SEM-EDXS results reveal a complex corrosion environment, where the presence of various alloying elements and environmental (bentonite slurry) factors like chloride, sulfur, and residual oxygen significantly influence the corrosion products. Overall, based on the EDXS results, it seems that the corrosion

products obtained here consist of mainly iron (hydr)oxides (hematite, green rust), iron sulfides, and potentially iron silicates which were formed under specific conditions. Based on electron microscopic data, the steel degradation mechanisms under dynamic conditions seem not much different from that under static conditions.

The XRD analysis of corroded spring steel coupons obtained after three and six months of dynamic experiments was carried out, and its diffractograms were shown in (***Figure 57***).

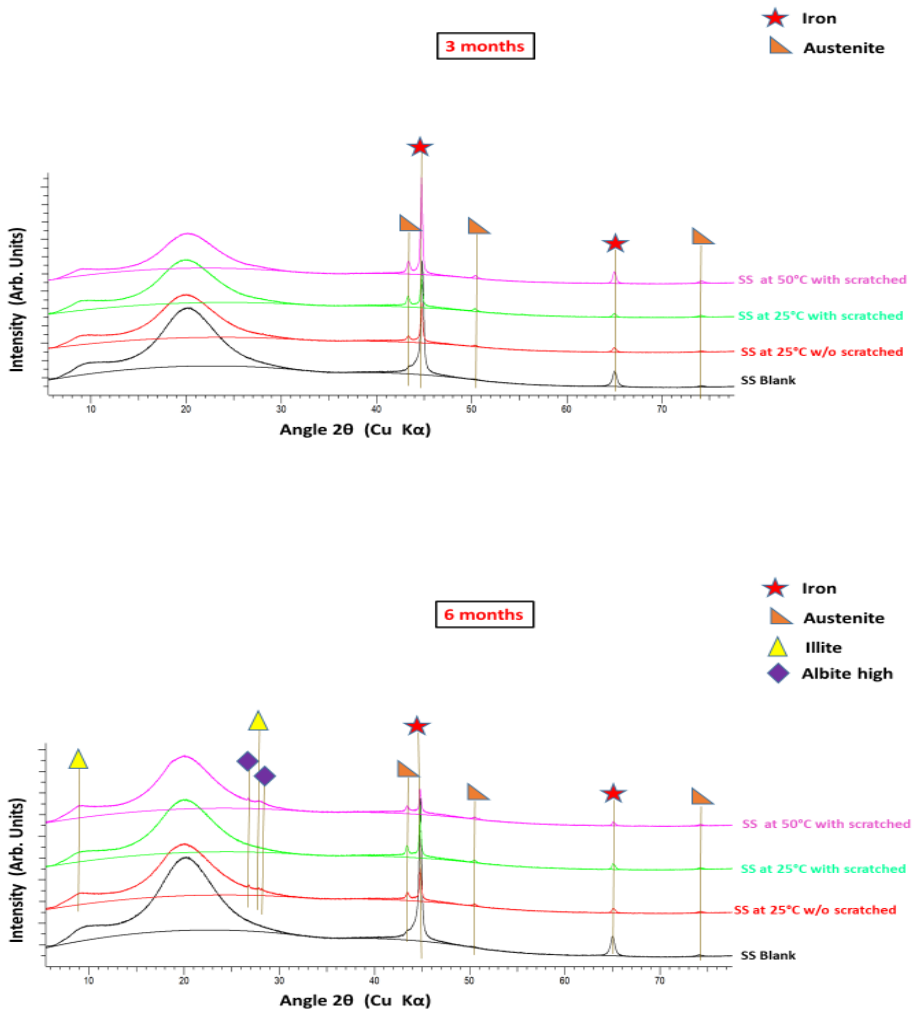

Figure 57 *X-ray diffractograms recorded on the corroded SS coupons after 3 months (top) and 6 months (down) reaction time under dynamic conditions (exact conditions are indicated on individual XRD plot).*

XRD analysis of the corroded specimens could only reveal the presence of structures characteristic of the coupon with its components cubic iron (PDF 87-0721) and austenite (PDF 31-0619) (***Figure 57***) for dynamic experiments. No secondary phase presence could be detected, suggesting that either their amount was too low, that they are of too low crystallinity, or that they must have been removed when cleaning off the excess suspension. There is not much difference observed in six months coupons except bentonite phase compared to three months in terms of

obtained phase (primary) from XRD analysis. XRD analysis results for dynamic experiments show little difference with that of static experiments for spring steel coupons. In static experiments the presence of green rust was evidenced by XRD but was not found in dynamic experiments.

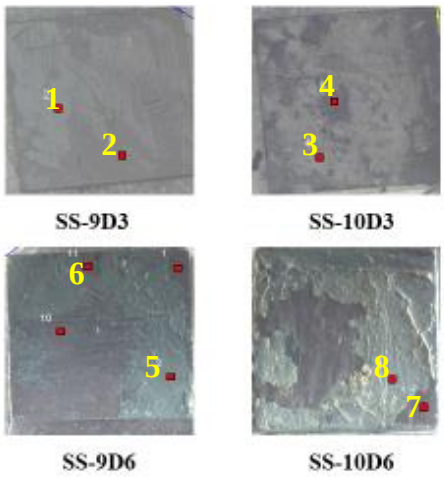

Figure 58 *Pictures taken in XPS chamber of SS coupons corroded under dynamic conditions (exact conditions are indicated on the individual sample, details of conditions are available in appendix). Marked points were selected for atomic concentration analysis, quantitative results are provided in* ***Table 43****.*

Table 43 *Relative atomic concentrations by XPS analyses at selected points of SS coupons for dynamic experiments shown in above* ***Figure 58****. Relative errors are estimated to be within ± 10% (Here each measurement has two type of atomic concentration: one with presence of carbon and one without carbon presence).*

Point	C	O	Na	Mg	Al	Si	S	Cl	Mo	Mn	Cu	Ni	Fe
9D3-1	14.9	57.7	0.9	1.2	5.2	13.5	0.2	/	1.1	/	0.1	/	5.2
	/	67.7	1.1	1.4	6.1	15.9	0.3	/	1.2	/	0.1	/	6.1
9D3-2	7.8	62.8	1.2	1.1	6.2	20.1	/	/	/	/	/	/	1.0
	/	68.1	1.2	1.2	6.7	21.8	/	/	/	/	/	/	1.0
10D3-3	17.6	54.2	/	1.2	2.6	9.2	0.3	1.3	0.3	/	/	/	12.8
	/	65.7	/	1.4	3.1	11.1	0.3	1.6	0.3	/	/	/	15.5
10D3-4	11.2	59.7	0.9	0.8	5.3	19.7	/	/	/	/	/	/	2.3
	/	67.3	1.0	1.0	6.0	22.2	/	/	/	/	/	/	2.6
9D6-5	12.3	57.6	1.5	0.6	3.6	11.7	/	0.4	/	/	/	/	12.2
	/	65.7	1.8	0.6	4.1	13.4	/	0.5	/	/	/	/	13.9
9D6-6	16.3	52.1	1.6	0.5	7.1	12.1	1.1	/	0.3	/	0.7	0.7	7.2
	/	62.3	1.9	0.6	8.4	14.5	1.3	/	0.3	/	0.8	0.8	8.6
10D6-7	23.5	48.6	/	1.0	/	6.1	2.2	/	0.9	/	0.9	0.5	14.2
	/	63.6	/	1.3	/	7.9	2.9	/	1.2	/	1.2	0.7	18.6
10D6-8	6.5	63.3	1.3	1.5	6.5	18.8	/	/	/	/	/	/	2.1
	/	67.0	1.4	1.6	7.0	20.1	/	/	/	/	/	/	2.3

The spring steel coupons selected for XPS analysis were shown in (***Figure 58***) for dynamic experiments under different experimental conditions. Relative atomic concentration using XPS for selected points on exposed surface of spring steel coupons were tabulated in (***Table 43)***. A color change like blue-green, black and grey was observed on the exposed coupon surface indicating formation of different corrosion products (secondary phases). From atomic concentrations (***Table 43***), it is clear most of exposed surface consists of iron, oxygen, aluminium and silicon as chief elements which form corrosion products. The relatively high concentrations of silicon (Si) could point to silicate formation, often seen when corrosion occurs in the presence of silicate-rich environments(bentonite) **(S. Kaufhold et al., 2020)**. Here atomic ratio of iron, silicon and oxygen as shown in (***Table 43***, point 3 and 5) indicate presence of iron enriched bentonite layer which covered the coupon surface and corrosion products.

The atomic concentrations of oxygen are notably high in many samples, reflecting possible iron oxide + iron silicate/ bentonite layer on coupon surface especially in points like (***Figure 58***, Point 1, 6 and 7). Some regions like (***Figure58***, point 2, 4 and 8) enriched with silicon, sodium, oxygen, aluminium, magnesium and some amount of iron indicate bentonite clay region. The varied elemental presence across samples further indicates that these materials have been exposed to different environmental conditions. XPS analysis suggests that the surfaces were a mixture of oxide layers, iron silicate and metallic surfaces distributed unevenly over the exposed surface of spring steel coupons for dynamic experiments. No significant differences were observed between three and six months of dynamic experiments. Overall XPS analysis results for dynamic experiments were comparable with that of static experiments for spring steel coupons.

3.4 Corrosion of Carbon steel in MX-80 bentonite

3.4.1 Initial Characterization

Initial characterization of carbon steel coupon was carried out to know and compare the morphological changes as corrosion progresses. (***Figure 59***) left side shows the SEM (SE mode) images of polished non-corroded initial carbon steel coupon. SEM-EDX results show the chemical composition of the selected areas which focussed on specific points and the average surface area of coupon and their results were shown in the (***Table 44 & Table 45)***. The bright region is average area (point 1) of base metal and point 2 and point 3 are specific points on the surface. All three points have specific composition based on location. Carbon steel here consists of iron, carbon, silicon, manganese and nickel as chief elements. The obtained composition of carbon steel coupon had good match with the composition compared to the company certificate of the bulk carbon steel. Finally, the surface roughness of the starting material was assessed by AFM. A value for the root mean square (RMS) roughness of 18± 2 nm was obtained for a scanned area of 20 x 20 μm^2.

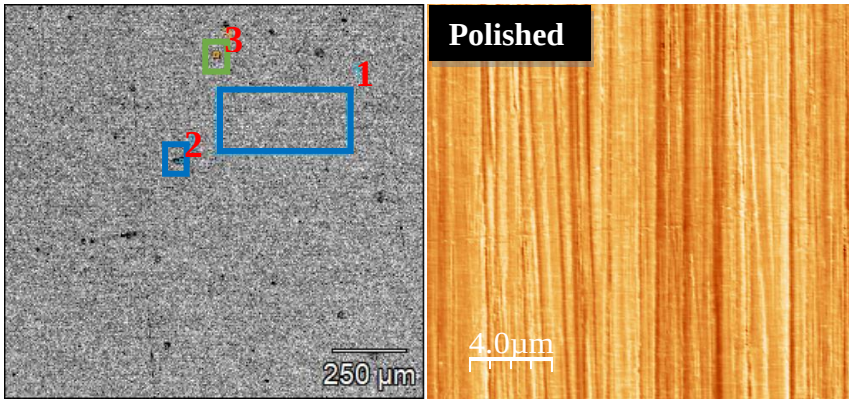

Figure 59 *SEM image on left side and surface roughness image using AFM on right side of the initial CS coupon.*

Table 44 *Composition of initial CS coupon obtained by SEM-EDX before experiment with (+/- 3 Sigma) uncertainty.*

Material /Atom %	C	Si	Mn	Al	Cr	Ni	Fe
CS_point1	2.2±0.4	0.7±0.2	1.6±0.5	0.2±0.1	-	0.6±0.3	94.7±1.3
CS_point2	21.6±0.6	0.5±0.2	1.2±0.4	0.2±0.1	-	-	76.4±1.1
CS_point3	3.9±0.5	0.5±0.1	1.4±0.5	0.3±0.1	-	0.7±0.3	93.2±1.3

Table 45 *Chemical composition of the initial CS coupon with (+/- 3 Sigma) uncertainty.*

Element / wt. %	C	Si	Mn	Al	Cr	Ni	Mo	Fe
Certificate	0.2	0.3	1.6	-	0.06	0.8	0.02	97.1
EDX of overall surface	0.5±0.1	0.3±0.1	1.6±0.5	0.1±0.1	-	0.7±0.3	-	96.8±1.3
EDX of point 2	5.6±0.2	0.3±0.1	1.4±0.5	0.1±0.1	-	-	-	92.5±1.3
EDX of point 3	0.9±0.1	0.2±0.1	1.5±0.5	0.1±0.1	-	0.8±0.3	-	96.5±1.3

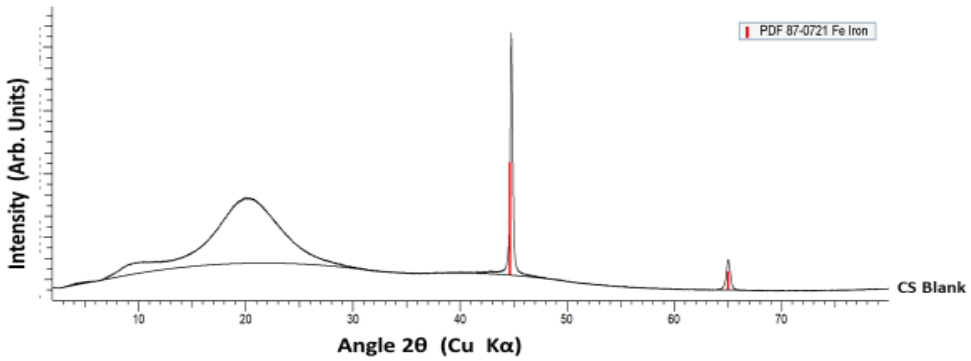

Figure 60 *X-ray diffractogram of the initial CS coupon before experiment (with air scattering effect).*

The X-ray diffractogram of initial carbon steel coupon was shown in the (***Figure 60).*** The X-ray diffractogram of initial carbon steel coupon (***Figure 60)*** shows a good match with cubic iron (PDF 87-0721) as primary phase.

3.4.2 Dissolved metal ions evolution

The quantification of the dissolved ions in the solution after ultracentrifugation at the end of the static and dynamic experiments was done using ICP-OES, Ion chromatography and ICP-MS following the procedure for sample preparation described in methods section ***2.4.4 and 2.2.5***. In case of carbon steel coupons iron evolution is mainly due to steel corrosion whereas silicon and aluminium evolution is due to clay dissolution. In addition, silicon and aluminium are also the components of the pore water and simulated groundwater. Dissolved amount of iron, silicon and aluminium during 3, 6 and 9 months static experiments were shown below in ***Table 46*** and during 3 and 6 months dynamic experiments were shown below in ***Table 47*** and ***Table 48***. Concentrations of other dissolved cations and anions are tabulated in ***appendices section*** since such ions do not have significant effects since their variations lie within experimental uncertainties.

For static experiments, the concentrations of Fe is ranging from 200 to 700 µg/L, Si varies from 7300 to 15600 µg/L, and Al fluctuates and reaches values up to 2400 µg/L in some cases. The measured concentration of silicon (at least for 9 months), aluminium and iron is quite similar to the concentration of equilibrium bentonite slurry where Si concentration is ~13000 µg/L, Al concentration is ~500 µg/L and Fe concentration is ~400 µg/L.

Table 46 *Dissolved amounts of Fe, Si and Al ions in the pore water solutions in contact with CS coupons after 3, 6 and 9 months static experiments. Numbers in parentheses correspond to the relative standard deviation in percentage.*

System/ Amounts in µg/L	Fe	Si	Al
3months 25°C w/o scratches	200(4.0)	9500(1.1)	500(3.1)
3months 25°C with scratches	700 (3.4)	10900(0.3)	1000(1.5)
3months 50°C w/o scratches	700(4.5)	15600(2.8)	2400(10)
3months 50°C with scratches	400(3.6)	14800(1.5)	2000(2.9)
6months 25°C w/o scratches	700(0.3)	8400(0.7)	600(6.8)
6months 25°C with scratches	500(0.6)	7400(1.1)	600(4.1)
6months 50°C w/o scratches	<100	10900(0.6)	2100(18)
6months 50°C with scratches	<100	7300(0.4)	900(17)
9months 25°C w/o scratches	400(5.5)	12200(0.8)	1100(2.1)
9months 25°C with scratches	600(3.6)	9600(1.0)	500(9.6)

Table 47 *Dissolved amounts of Fe, Si and Al ions in the ground water (solution) in contact with CS coupons during 3 months-dynamic experiment. Numbers in parentheses correspond to the relative standard deviation in percentage.*

25°C w/o scratches (System)/Amounts in µg/L	Fe	Si	Al
A (4 weeks)	<100	16900(0.6)	900(3.0)
B (5 weeks)	<100	17500(0.9)	800(5.1)
C (6 weeks)	<100	17500(1.0)	1000(5.1)
D (8 weeks)	1900(0.4)	18100(0.6)	300(5.1)
E (10 weeks)	<100	17300(1.2)	300(3.5)
F (12weeks)	600(2.3)	19600(1.3)	200(4.8)

25°C with scratches (System)/Amounts in µg/L	Fe	Si	Al
A (4 weeks)	<100	17200(1.0)	800(5.8)
B (5 weeks)	<100	17800(1.0)	800(7.2)
C (6 weeks)	<100	20800(0.7)	2900(3.7)
D (8 weeks)	<100	19500(1.9)	200(3.1)
E (10 weeks)	<100	18100(0.3)	200(4.9)
F (12 weeks)	100(5.7)	18800(0.7)	200(1.2)

50°C with scratches (System)/Amounts in µg/L	Fe	Si	Al
A (4 weeks)	500(4.0)	21900(0.7)	31900(1.4)
B (5 weeks)	<100	18200(1.3)	1300(5.6)
C (6 weeks)	<100	19000(1.7)	1400(4.9)
D (8 weeks)	<100	18200(1.6)	800(2.2)
E (10 weeks)	<100	19200(0.8)	800(1.0)
F (12 weeks)	300(0.8)	20300(1.3)	900(2.7)

Table 48 *Dissolved amounts of Fe, Si and Al ions in the ground water (solution) in contact with CS coupons during 6 months-dynamic experiment. Numbers in parentheses correspond to the relative standard deviation in percentage.*

25°C w/o scratches (System)/Amounts in µg/L	**Fe**	**Si**	**Al**
A (6 weeks)	<200	18800(0.3)	100(2.8)
B (10 weeks)	200(41)	19900(1.0)	100(2.7)
C (14 weeks)	1100(5.8)	21200(1.1)	300(1.8)
D (18 weeks)	<100	19200(0.6)	100(5.5)
E (22 weeks)	<100	18700(0.7)	100(6.4)
F (26 weeks)	<100	18400(0.6)	100(11)

25°C with scratches (System)/Amounts in µg/L	**Fe**	**Si**	**Al**
A (6 weeks)	<200	18900(1.3)	100(2.8)
B (10 weeks)	<200	19800(1.5)	100(2.1)
C (14 weeks)	<200	21000(0.4)	200(1.2)
D (18 weeks)	<100	20700(2.0)	100(8.3)
E (22 weeks)	<100	19200(0.5)	100(5.4)
F (26 weeks)	<100	19900(0.3)	100(3.6)

50°C with scratches (System)/Amounts in µg/L	**Fe**	**Si**	**Al**
A (6 weeks)	<200	19100(1.9)	500(10)
B (10 weeks)	200(8.9)	19800(0.9)	700(1.1)
C (14 weeks)	300(17)	20400(1.2)	300(1.2)
D (18 weeks)	<100	18800(0.5)	500(1.4)
E (22 weeks)	<100	19400(0.9)	500(0.5)
F (26 weeks)	<100	19700(0.4)	500(1.6)

For dynamic experiments, the concentration of Si varies from 17300 to 21900 µg/L which is quite in agreement with concentration of simulated groundwater where Si concentration is ~17000 µg/L (***Table2***). Al concentration is higher at elevated temperature (50°C) compared to room temperature and iron concentration is lower in most of the cases. The static experiment shows a more controlled and gradual leaching process compared to the dynamic experiment, which is characterized by faster initial releases and some variability in ion concentrations over time. Overall, temperature, time and the presence of scratches does not have significant effect on the concentrations of Fe, Si, and Al. The uncertainties suggest that variations in ions concentration lie within the scatter of the data. Here, Fe dissolution is mainly due to steel corrosion whereas Si and Al concentrations indicate clay dissolution not steel corrosion.

Overall, Fe concentration observed in the static experiments is at 1E-5 mol/L and in the dynamic experiments even lower at 1E-6 mol/L. Under the experimental pH conditions, solubility concentrations for $Fe(OH)_2$ is around 1E-3 mol/L. This can be taken as a first indication that Fe(II) released due to steel corrosion is bound to clay minerals and cannot be found as dissolved species in solution.

Table 49 Determination of Cu, Ni, Fe, Si and Al concentrations for a bentonite that was in contact with CS coupon and without coupon has been digested in acid and the resulting liquid phase has been quantified by using ICP-MS for 6 months dynamic experiment (Numbers in parentheses correspond to the relative standard deviation in percentage).

(Dynamic) System/ Amounts in µg/g	Cu	Ni	Fe	Si	Al
6months 25°C CS with scratches	7(1.1)	10(1.1)	22330(0.9)	257800(1.5)	43130(3.5)
6months 25°C bentonite w/o coupon	7(1.4)	7(1.2)	16610(1.0)	248400(1.5)	31900(3.0)

Determination of Cu, Ni, Fe, Si and Al concentration for a bentonite that was in contact with CS coupon and without coupon has been digested in acid and the resulting liquid phase has been quantified by using ICP-MS for 6 months dynamic experiment. The results shown in ***(Table 49)*** shows variation in concentration (Fe, Si and Al) which was of interest for carbon steel. The concentration of mainly Fe increases in presence of coupon which indicates that Fe(II) release due to steel corrosion is mainly sorbed on the clay surface rather than dissolving into the solution. Concentration of Si and Al are lying within experimental uncertainty.

3.4.3 pH / E_h evolution

The *in-situ* pH and E_h values for carbon steel for static experiments were shown below in (***Table 50***). The *in-situ* pH did not evolve much in carbon steel corrosion experiments carried out for 3 months, it slightly decreased after 6 months and has similar range after 9 months (***Table50***).

Table 50 pH / Eh evolution of CS in contact with MX-80 bentonite slurry after 3, 6 and 9 months exposure time.

System	pH	E_hw.r.t SHE(mV)
3months 25°C w/o scratches	8.40±0.05	-372±50
3months 25°C with scratches	8.18±0.05	-333±50
3months 50°C w/o scratches	8.03±0.05	-380±50
3months 50°C with scratches	8.12±0.05	-418±50
6months 25°C w/o scratches	7.70±0.10	-285±50
6months 25°C with scratches	7.62±0.10	-314±50
6months 50°C w/o scratches	7.94±0.10	-434±50
6months 50°C with scratches	7.95±0.10	-415±50
9months 25°C w/o scratches	7.88±0.10	-247±50
9months 25°C with scratches	7.82±0.10	-356±50

During the entire reaction time in static conditions, pH and Eh values remains either stable or change slightly. Overall, the abrasion (scratching) of the coupon surface and temperature does not affect the significantly pH and Eh values for carbon steel coupons in static conditions.

The scratched coupon surfaces in some cases exhibit little lower pH values compared to the unscratched surfaces, however the difference is within uncertainties. The pH values at higher temperature are generally lower than those at room temperature because at elevated temperature more solid phase precipitation may occur, thus consuming OH^- ions and reducing pH. Overall, the system exhibits reducing conditions and was buffered as time progresses.

The pH and E_h values of carbon steel coupons for three and six months dynamic experiments were shown below in (***Figure 61***) and (***Figure 62***).

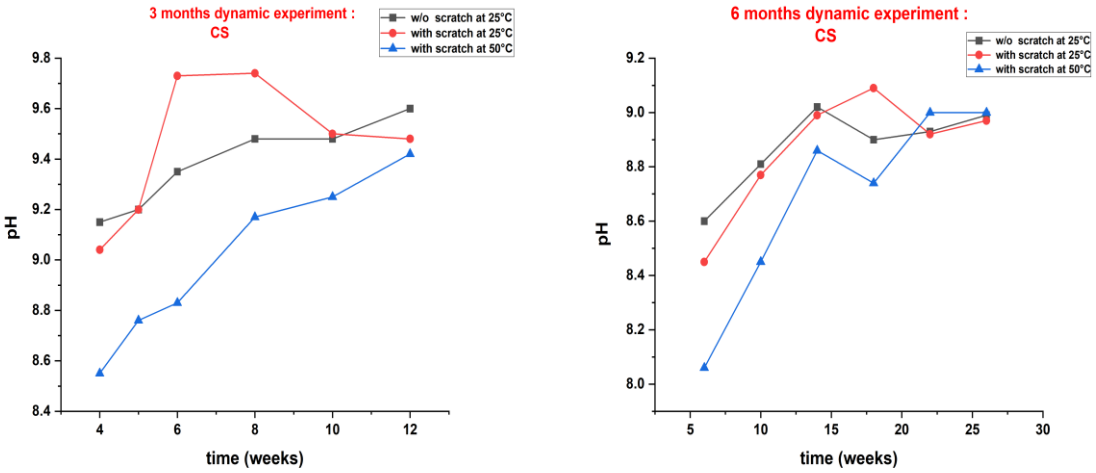

Figure 61 *The pH evolution of the CS coupons in ground water (solution) during 3 (left side) and 6 months (right side) dynamic experiments (±0.1is uncertainty).*

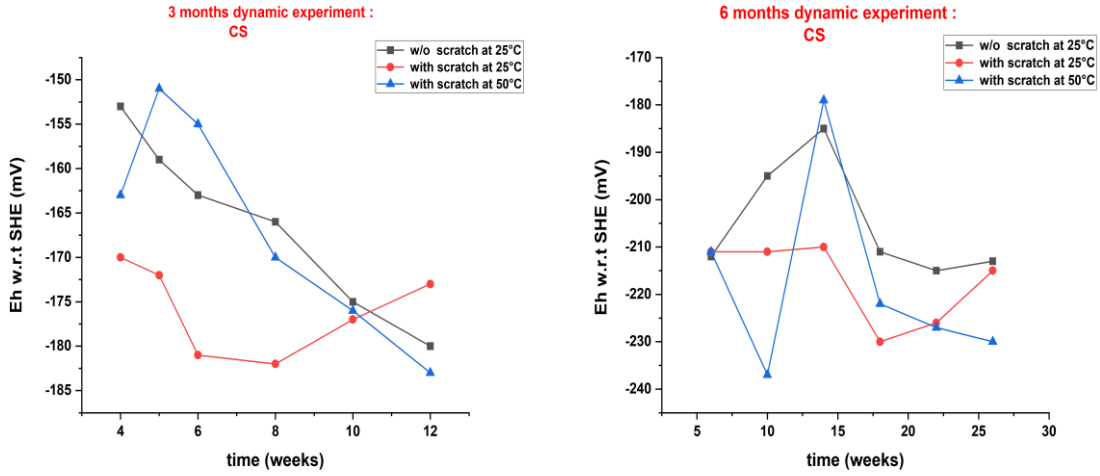

Figure 62 *The Eh evolution of the CS coupons in ground water (solution) during 3 (left side) and 6 months (right side) dynamic experiments (±50mV is uncertainty).*

At the outlet of diffusion cells, the measured pH values increased from about 8.5 in the water collected after 4 weeks of reaction to 9.4 for the last collected water (12 weeks) in three months experiments and from 8.1 in the water collected after 6 weeks to 9.0 for the last collected water after 26 weeks of 6 months dynamic experiments (***Figure 61***). These values are significantly higher than in experiments under static conditions (pH around 8), and scratching the surface or increasing the temperature had no significant impact. The increase of pH is mainly the consequence of the dynamic experimental conditions. While the pH in the water equilibrated with solution initially is buffered by the bentonite at around 8, the pH in the outlet of the setup is dominated by the flowing through simulated groundwater.

The recorded E_h values were all within uncertainties similar and in the range -151 mV to -183 mV for three months and -179 mV to -237 mV for six months of dynamic experiments (***Figure 62***). As the solution in the flow through reactor was continuously exchanged, different to the static experiments, soluble constituents of the bentonite slurry were washed out which was evidenced by eluted dissolved ions concentration. The pH and E_h values of all iron-based materials like SGI, spring steel and carbon steel are in similar range and were comparable. These values suggest the development of reducing conditions, and thus steel corrosion, as in experiments under static conditions

3.4.4 Corrosion rate

The corrosion rates of carbon steel for static and dynamic experiments were calculated using the weight loss method and are shown in (***Figure 63***) for 3, 6 and 9 months of static experiments and in (***Figure 64***) for 3 and 6 months dynamic experiments.

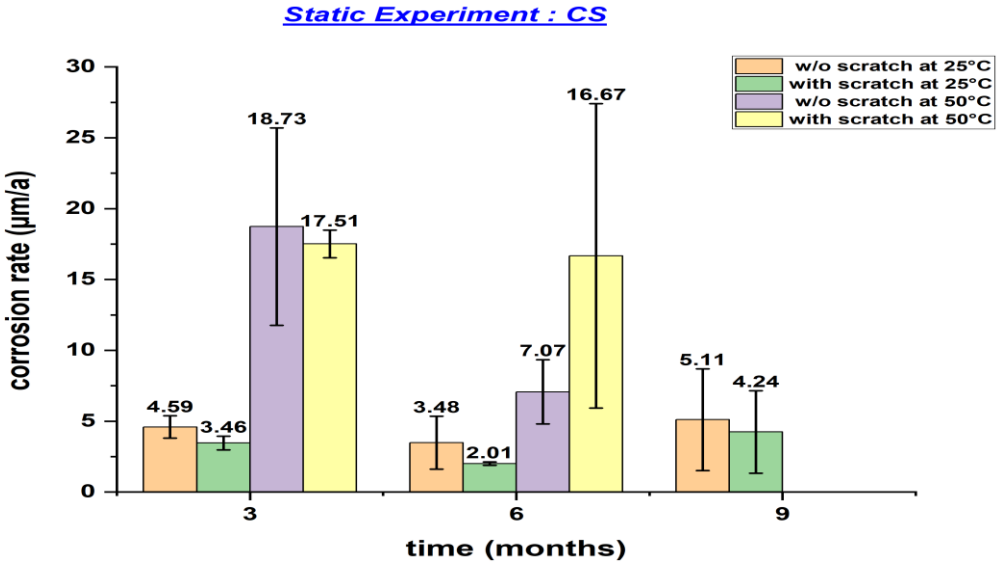

Figure 63 *Corrosion rates of all CS coupons obtained after 3, 6 and 9 months static experiments.*

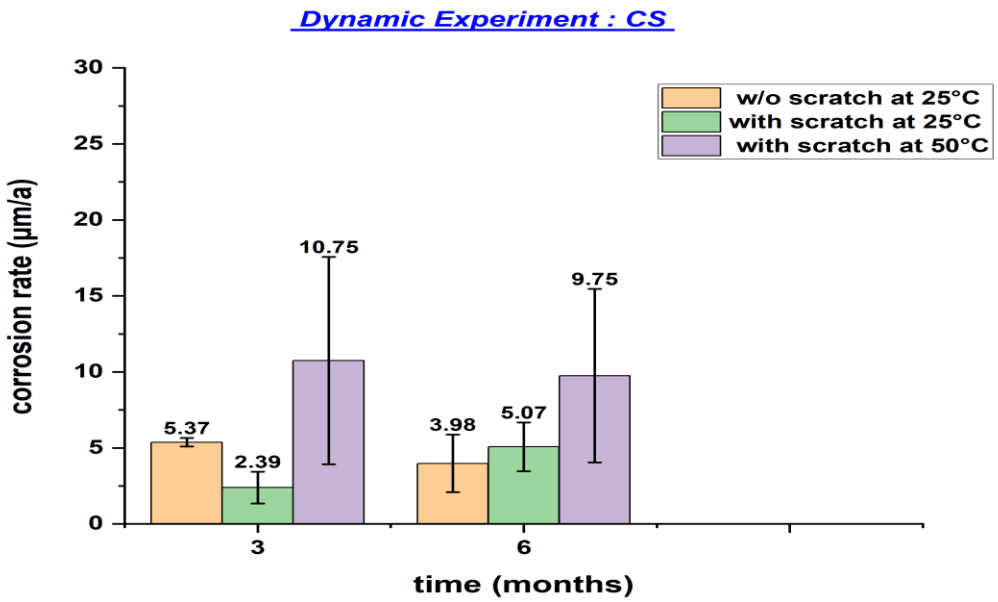

Figure 64 *Corrosion rates of all CS coupons obtained after 3 and 6 months dynamic experiments.*

The corrosion rate of carbon steel mainly varies with temperature and is not much affected by presence of surface scratches or exposure time. In static and dynamic experiments, the corrosion rate increases with temperature, being higher at 50°C than at 25°C. The corrosion rate of carbon steel in bentonite suspension for both experiments (static and dynamic) at 25°C, varies in the range between 2.39±1.05 to 5.11±3.59 µm/a which is in agreement with the reported average corrosion rate of carbon steel (~2 µm/a) embedded within compacted MX-80 bentonite and exposed to natural granitic pore water for 394 days in the in situ MaCoTe experiment **(Reddy, Padovani, Rance, et al., 2021)**. The small difference in corrosion rate is due to different temperature (25°C vs rock temperature), time and form of bentonite (suspension vs compacted).

In dynamic experiments, the corrosion rate at 50°C varies in the range 9.75±5.71 to 10.75±6.82 µm/a, which is quite comparable with corrosion rate of static experiments (considering experimental uncertainty). Longer exposure time (3 to 6 months) in both experiments show little reduction in corrosion rate hints at the formation of a protective passivation layer at the coupon surface. However, formed passive layer may not be fully compact or highly protective. Taking uncertainties into account, temperature is the dominant factor influencing corrosion rate, scratching the surface and time has limited effect on corrosion behavior of carbon steel coupons in static and dynamic experiments.

3.4.5 Secondary phase characterization

3.4.5.1 Static condition systems (3, 6 & 9 months)

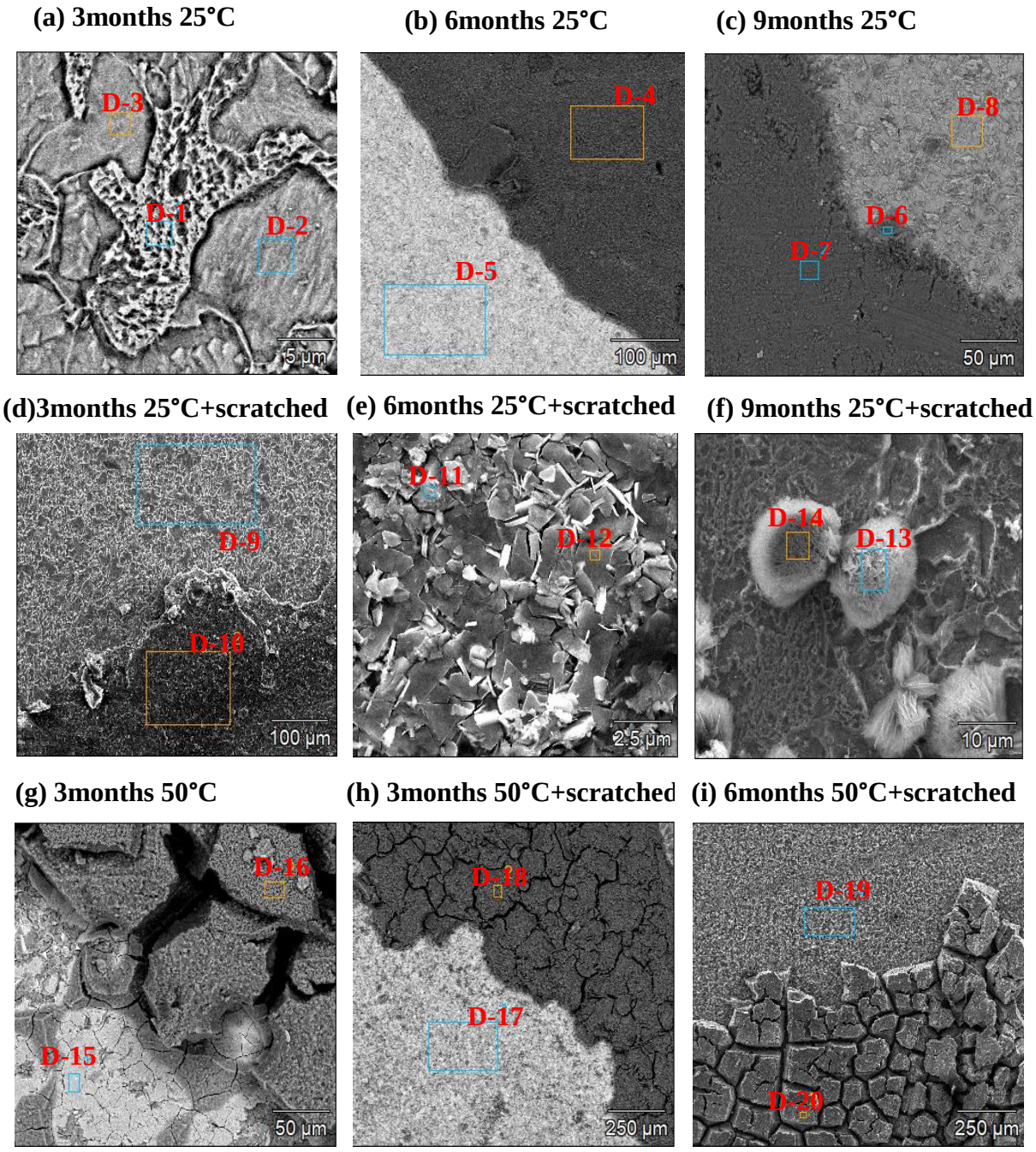

Figure 65 *Scanning electron micrographs (in SE mode) of all CS coupons corroded for 3, 6 and 9 months under static conditions at different temperature (exact conditions are indicated above the micrographs). Marked areas were selected for EDXS analysis, quantitative results are provided in* ***Table 51****.*

Table 51 *Relative atomic concentrations by EDXS analyses at selected areas shown in above* ***Figure 65****. Relative errors are estimated to be within ± 10%.*

Area	C	O	Na	Mn	Al	Si	S	Cl	Ca	Ni	Fe
D-1	4.1	/	/	2.1	/	0.8	/	/	/	1.6	91.1
D-2	2.6	/	/	1.7	/	1.1	/	/	/	2.5	91.8
D-3	2.4	/	/	1.6	/	1.1	/	/	/	2.6	91.3
D-4	1.8	62.1	1.5	/	7.3	20.1	/	0.1	0.1	/	5.6
D-5	5.2	7.8	/	1.5	0.3	1.8	/	0.3	/	2.3	80.5
D-6	1.7	58.5	/	0.3	5.5	13.9	0.3	0.6	0.1	/	18.3
D-7	2.0	60.3	0.4	0.3	5.4	14.5	0.4	0.3	/	/	15.4
D-8	3.8	7.0	/	1.8	0.9	1.6	0.3	0.1	/	1.3	83.2
D-9	6.5	/	/	1.7	0.4	1.5	0.3	/	/	87.2	2.1
D-10	1.9	61.1	1.3	/	7.6	20.4	/	/	0.4	5.8	/
D-11	5.1	52.9	/	/	0.4	0.5	/	1.8	/	/	39.3
D-12	3.4	46.8	/	0.6	0.2	0.5	/	2.5	/	/	45.9
D-13	9.5	62.4	/	0.6	0.2	0.5	/	0.3	/	/	26.3
D-14	7.2	57.2	/	/	/	/	/	0.7	/	/	34.9
D-15	4.4	37.5	/	1.0	/	11.0	1.0	/	/	2.5	42.7
D-16	1.8	60.8	1.2	/	3.2	18.5	/	/	/	/	13.8
D-17	5.9	5.9	/	1.9	/	2.0	0.2	/	/	1.1	83.1
D-18	6.4	58.8	0.6	/	1.4	16.7	/	0.1	0.1	/	15.4
D-19	6.4	15.1	/	1.3	/	2.2	0.3	/	/	1.5	72.8
D-20	2.3	62.7	0.8	/	1.9	16.7	0.1	/	0.1	/	15.0

Scanning electron microscopy was subsequently applied to analyze the carbon steel corroded coupons. SEM-EDXS analysis micrographs for various selected areas were shown in (***Figure 65***) and their atomic concentration results were tabulated in (***Table 51***).

Here from the microstructure observations of coupon surface, most parts of the microstructure consist of ferrite and pearlitic regions. Part of exposed surface is covered with bentonite and formation of corrosion product occurs. Information about chemical composition was provided by SEM-EDXS analysis at selected areas containing enough material to avoid probing simultaneously the adherent particles and the substrate underneath. EDXS analyses results of coupons at 25°C after 6 and 9 months without scratch and for coupons at 50°C with unscratched and scratched after 3,6 months for selected areas (D-4, D-6, D-7, D-16, D-18 and D-20) shown in (***Figure 65***) indicate formation of iron silicate as corrosion products. In various regions the EDX signal for Fe decreased significantly (e.g. D-4, D-10) apparently due to a thick alumino-silicate layer covering the steel surface. D-9 region indicate presence of metallic nickel due to inhomogeneity of the alloy. Oxygen is also present on the coupon surface as well as silicon in the lower percentage range after exposure on coupon surface. Significantly more silicon is found in the region where the surface was covered with bentonite. The carbon content varies only slightly at different positions of the exposed surface.

Dark regions in most areas of the sections shown in (***Figure 65***) correspond to low atomic number or light elements like Al, Ca. Iron-based corrosion products, such as iron oxides (Fe_xO_y), are predominant in some areas like (***Figure65***, D-11, D-12, D-13, D-14).

The presence of oxygen alongside iron in these areas indicates the formation of iron (hydr)oxides on the exposed surface as corrosion products. There are certain regions like areas (D-1, D-2, D-3, D-5, D-8, D-17 and D-19) where of the presence of corrosion products was limited. Overall dissolution of iron was higher at elevated temperature compared to room temperature (see ***Figure63 and Figure 64***). There was a limited effect of scratches on morphology and element distribution over the exposed surface of carbon steel coupons under static experiments. Overall, the SEM-EDXS results highlight the complex interplay of elements across different areas, suggesting that secondary phases, such as oxides, hydroxides, silicates and may be carbonates, were likely forming based on the observed elemental distributions. The variations in elemental composition between different areas reflect the heterogeneity of the coupons. The formed secondary phases reflect the interactions of the metal substrates with surrounding environment (bentonite slurry) and its effect on mineralogical changes and corrosion. Here some areas (***Figure65,*** D-11, D-12) show signs of substantial corrosion with the formation of high amount of Fe(hydr)oxides, others demonstrate the presence of passive oxide layers that provide a degree of protection to the underlying metal.

The XRD analysis of corroded carbon steel coupons obtained after three, six and nine months of static experiments was carried out and its diffractograms were shown in (***Figure 66***). Transfer of coupons and testing was done under anoxic conditions, to avoid exposure to the open atmosphere. The primary peak in the XRD spectrum for three, six and nine months of static experiments likely correspond to the cubic iron phase (PDF 87-0721) which is the starting material. Apart of this, other reflections attributable to Illite which are observed on the exposed surface in (***Figure 66***) mainly for three, six and nine months come from the bentonite. The remaining peaks correspond to corrosion products or secondary phase green rust (PDF 13-0090) which was detected in most of the samples for three, six and nine months of static experiments as shown in (***Figure 66***). Observed secondary phase morphology and atomic concentration was also confirmed by SEM-EDXS analysis which was already discussed in previous section of SEM analysis.

There is not much difference observed in 9 months coupons compared to three and six months in terms of secondary phase (corrosion products) from XRD analysis. Findings suggest that different secondary phases were formed and some of them were too low in amounts due to difference in experimental conditions. Scratching the surface of carbon steel coupons doesn't affect much the phase formation.

Overall XRD analysis provides insights into the phases present on carbon steel coupons after corrosion, which is critical for understanding the extent of corrosion and the stability of the material over time.

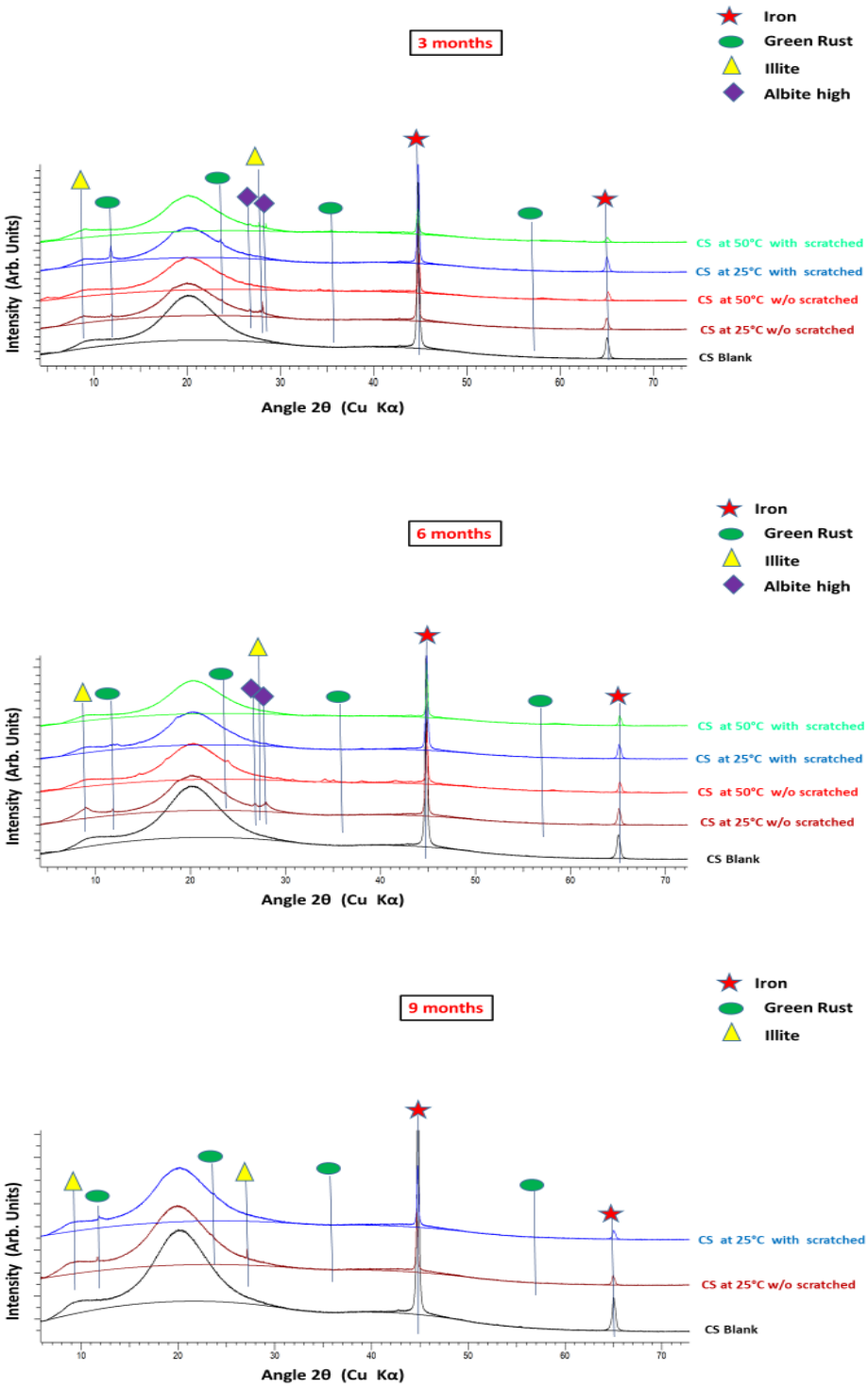

Figure 66 *X-ray diffractograms recorded on the corroded CS coupons after 3 months (top), 6 months (middle) and 9 months (bottom) reaction time under static conditions (exact conditions are indicated on individual XRD plot).*

XPS characterization of the exposed steel surfaces was performed, in order to gain more information on the steel/bentonite/solution interface. Different to EDX, XPS data are much more surface sensitive due to the lower information depth.

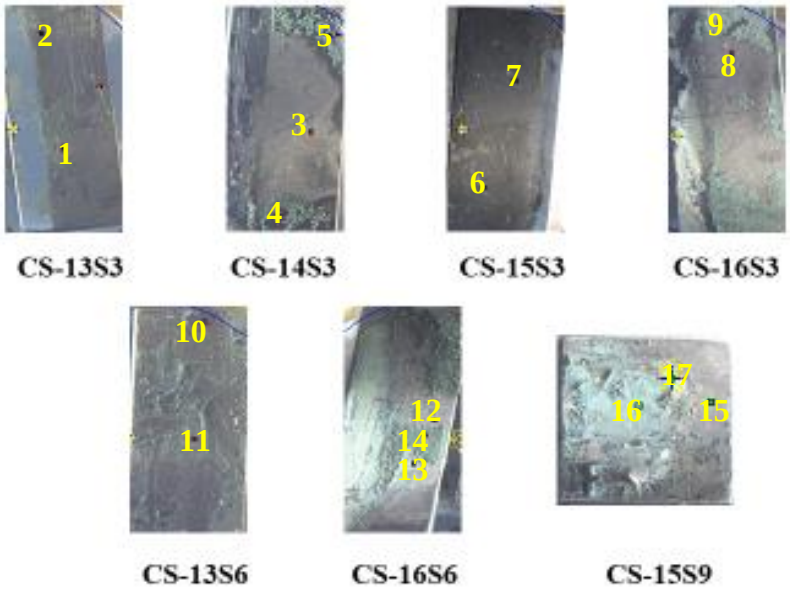

Figure 67 *Pictures taken in XPS chamber of CS coupons corroded under static conditions (exact conditions are indicated on the individual sample, details of conditions are available in appendix). Marked points were selected for atomic concentration analysis, quantitative results are provided in* ***Table 52****.*

Table 52 *Relative atomic concentrations by XPS analyses at selected points of CS coupons for static experiments shown in above* ***Figure67****. Relative errors are estimated to be within ± 10% (Here each measurement has two type of atomic concentration: one with presence of carbon and one without carbon presence).*

Point	C	O	Na	Mg	Al	Si	S	Cl	Cr	Mn	Ca	Ni	Fe
13A3-1	8.6	61.1	2.5	0.9	5.4	17.9	/	0.2	/	/	/	/	3.5
	/	66.8	2.7	1.0	5.9	19.6	/	0.2	/	/	/	/	3.9
13A3-2	24.9	44.6	1.4	0.3	/	4.7	1.0	0.6	0.6	/	/	7.2	14.5
	/	59.4	1.8	0.4	/	6.2	1.4	0.8	0.8	/	/	9.5	19.3
14A3-3	26.3	39.7	/	/	/	3.6	0.6	0.5	0.5	/	/	4.8	24.0
	/	53.8	/	/	/	4.9	0.8	0.6	0.7	/	/	6.4	32.6
14A3-4	14.6	50.4	1.2	/	/	10.4	0.4	0.3	/	/	/	2.6	19.6
	/	59.1	1.4	/	/	12.1	0.5	0.4	/	/	/	3.1	23.0
14A3-5	7.1	60.0	1.5	0.4	/	15.0	/	0.3	/	/	/	/	15.6
	/	64.6	1.7	0.4	/	16.2	/	0.3	/	/	/	/	16.7
15A3-6	11.4	59.4	1.9	0.9	4.8	17.0	/	0.2	/	/	1.1	/	3.4
	/	67.0	2.1	1.0	5.4	19.2	/	0.2	/	/	1.2	/	3.8
15A3-7	27.1	45.5	0.6	0.4	/	5.7	0.7	0.5	0.6	/	/	4.8	13.8
	/	62.4	0.9	0.6	/	7.9	0.9	0.6	0.8	/	/	6.6	18.9
16A3-8	17.4	38.5	0.3	/	/	2.8	0.9	0.3	0.5	/	/	6.3	30.6

	/	46.5	0.4	/	/	3.4	1.1	0.4	0.6	/	/	7.6	37.1
16A3-9	5.6	58.7	0.9	0.7	/	15.8	/	0.2	/	/	/	/	18.1
	/	62.2	1.0	0.8	/	16.7	/	0.2	/	/	/	/	19.2
13A6-10	15.3	55.6	0.3	0.7	3.9	9.4	/	0.8	/	/	/	0.5	13.3
	/	65.6	0.4	0.8	4.7	11.1	/	1.0	/	/	/	0.5	15.7
13A6-11	5.2	63.0	2.0	1.1	6.1	19.5	/	0.1	/	/	/	/	3.0
	/	66.5	2.1	1.1	6.5	20.6	/	0.1	/	/	/	/	3.1
16A6-12	22.3	37.6	/	/	/	2.5	0.9	1.7	/	/	/	6.9	25.8
	/	48.4	/	/	/	3.2	1.1	2.2	/	/	/	8.9	33.2
16A6-13	7.0	61.5	0.5	0.6	2.5	13.6	/	0.8	/	/	/	/	13.6
	/	66.1	0.5	0.6	2.7	14.6	/	0.9	/	/	/	/	14.6
16A6-14	6.7	61.4	1.8	0.4	/	16.1	/	0.6	/	/	/	/	13.1
	/	65.8	1.9	0.5	/	17.2	/	0.6	/	/	/	/	14.0
15A9-15	16.1	56.5	1.7	/	2.3	7.7	/	1.6	0.6	/	/	1.4	12.0
	/	67.4	2.0	/	2.8	9.2	/	1.9	0.7	/	/	1.7	14.3
15A9-16	8.8	61.4	0.8	0.8	5.6	16.4	/	0.5	/	/	/	/	5.4
	/	67.3	1.0	0.8	6.1	18.0	/	0.5	/	/	/	/	5.9
15A9-17	19.3	59.7	0.7	/	/	4.5	/	0.9	/	/	/	/	14.5
	/	74.2	0.8	/	/	5.6	/	1.2	/	/	/	/	18.1

The carbon steel coupons selected for XPS analysis were shown in (***Figure 67***) for static experiments under different experimental conditions. Relative atomic concentration using XPS for selected points on exposed surface of carbon steel coupons were tabulated in (***Table 52***). A color change like blue-green, blackish-green and grey was observed (***Figure 67***) on the exposed coupon surface from visual inspection. From atomic concentrations (***Table 52***) it is clear that most of the exposed surface consists of iron, oxygen and silicon as chief elements which form corrosion products. The variation between the concentrations of elements in different samples indicates potential differences in the formation of secondary phases.

Here, the atomic ratio (***Table 52***, point 5, 9, 10, 13, and 14) shows formation of iron silicate as corrosion products, since iron and silicon atomic ratio was 1:1 in most of the cases. The atomic concentrations of oxygen are notably high in many samples, reflecting a possible iron oxide layer (Fe_xO_y) or green rust formation, especially in points like (***Figure 67***, Point 2, 3, 8, and 12). In some other cases (***Figure 67***, points 4, 7, 15 and 17) there are possibilities of formation of iron oxide + iron silicate. The regions (***Figure 67***, points 1, 6, 11 and 16) enriched with silicon, oxygen, aluminium, sodium and iron represent bentonite clay region. It seems from the visual inspection of carbon steel coupons (***Figure67***) that alteration of bentonite (color change) and corrosion (metallic coupons) took place during static experiments.

Thus, also XPS shows as well as SEM-EDX, that the exposed corroded surfaces consist of inhomogeneous distribution of secondary phase on the surface of carbon steel coupons for the static experiments. XPS analysis allowed to identify a dense and thin layer of corrosion products like iron silicate and green rust forming over longer time periods (6 months) in static experiments (***Figure 67***, point 13). The results show the diversity of surface chemistry across the samples, with variations in elemental composition pointing to differences in phase formation and oxidation

states. In general, XPS confirms the outcome of SEM-EDX analysis that the surfaces were a mixture of oxide layers, iron silicate and metallic surfaces distributed unevenly over the exposed surface of carbon steel coupons for static experiments.

3.4.5.2 Dynamic condition systems (3 & 6 months)

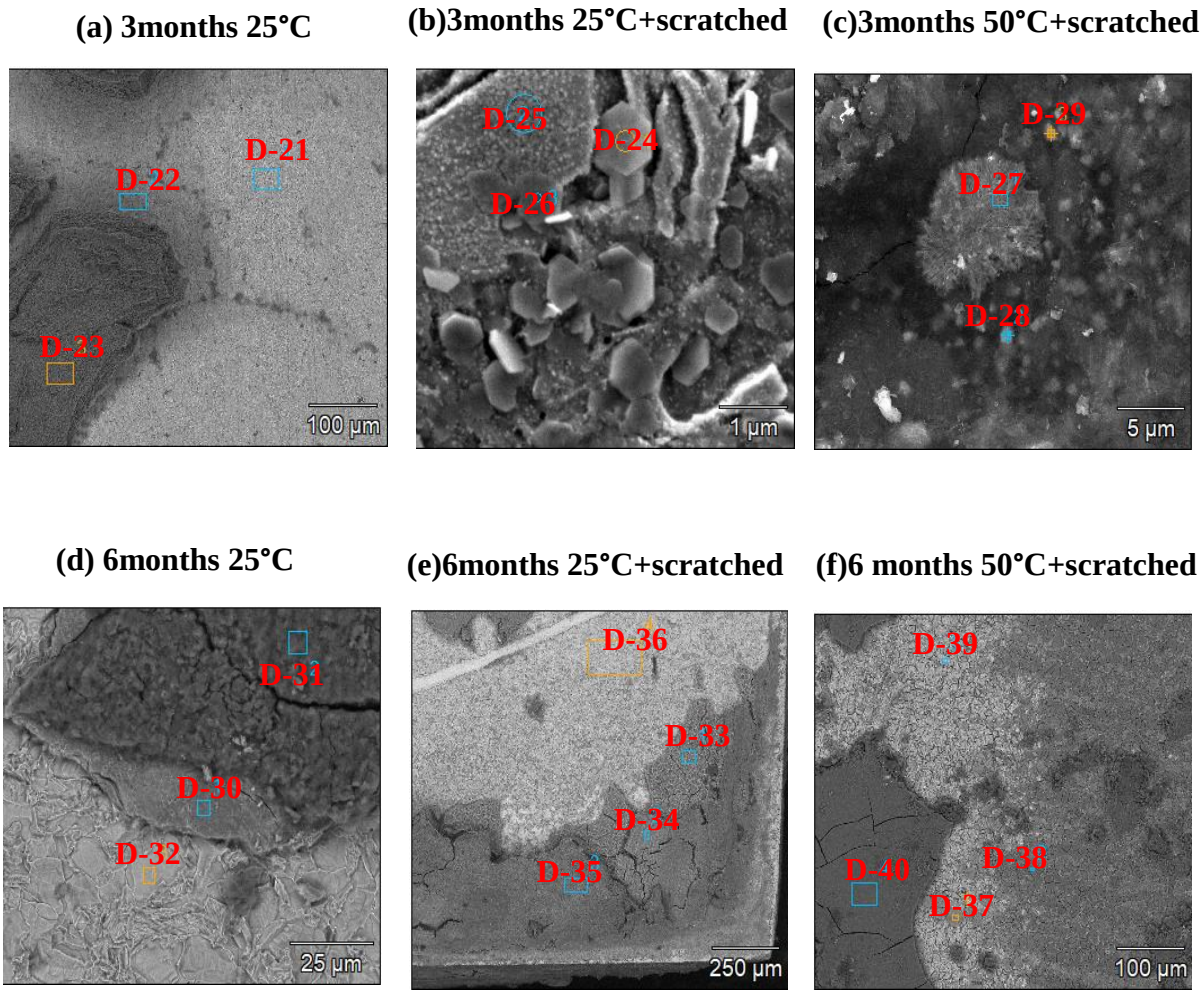

Figure 68 *Scanning electron micrographs (in SE mode) of all CS coupons corroded for 3 and 6 months under dynamic conditions at different temperature (exact conditions are indicated above the micrographs). Marked areas were selected for EDXS analysis, quantitative results are provided in* ***Table 53****.*

__Table 53__ Relative atomic concentrations by EDXS analyses at selected areas shown in above __Figure68__. Relative errors are estimated to be within ± 10%.

Area	C	O	Na	Mn	Al	Si	S	Cl	Ca	Ni	Fe
D-21	7.7	5.4	/	1.8	0.2	1.0	1.3	/	/	2.2	80.4
D-22	7.8	8.2	/	1.7	0.3	1.5	1.3	/	/	1.9	77.1
D-23	2.5	53.6	0.8	/	6.0	20.1	/	0.3	0.7	/	14.9
D-24	1.5	56.2	/	/	0.4	1.8	/	5.4	/	/	34.7
D-25	1.5	59.4	/	/	/	1.4	/	/	/	/	37.7
D-26	1.9	57.8	/	/	0.6	3.1	/	2.4	/	/	33.8
D-27	/	18.4	/	/	0.4	5.7	30.7	/	/	/	10.7
D-28	4.7	48.5	/	/	/	6.1	15.1	/	/	0.9	7.9
D-29	4.6	48.4	/	/	0.2	5.1	16.5	/	/	/	6.5
D-30	9.4	38.6	0.5	0.6	0.4	11.9	1.3	0.2	0.3	2.2	34.5
D-31	7.9	50.8	1.3	0.3	1.8	20.0	/	0.2	0.4	/	16.8
D-32	3.0	/	/	1.7	0.6	0.8	/	/	/	/	94.0
D-33	5.3	55.9	0.5	/	1.6	17.3	/	0.4	0.3	/	18.1
D-34	3.6	54.7	0.5	/	2.2	16.8	/	0.4	0.3	/	20.8
D-35	4.9	54.3	1.1	/	5.9	19.1	/	0.1	0.3	/	13.0
D-36	6.9	16.2	/	1.4	0.2	3.4	0.9	0.2	/	2.9	67.8
D-37	3.7	44.1	/	0.6	/	2.5	0.3	0.2	/	1.2	45.3
D-38	9.0	34.3	0.4	0.6	0.1	9.5	1.2	0.6	/	2.7	39.8
D-39	4.8	/	/	1.6	/	1.0	0.6	/	/	1.6	90.2
D-40	4.1	57.9	0.6	/	1.6	17.1	/	0.2	0.2	/	17.9

SEM-EDXS analysis micrographs for various selected areas were shown in (***Figure 68***) and their atomic concentration results were tabulated in (***Table 53***). SEM microscopy indicates change in surface morphology of the corroded (exposed) surface of carbon steel coupons.

Secondary phases presence was detected in short period (3 months) with clear hexagonal morphology (***Figure68b***) in dynamic experiments compared to static experiments. Surface morphologies of samples from three and six months dynamic experiments as visible by SEM were relatively comparable. The measured elemental compositions suggest uneven distribution of elements like Fe, C, O, S, Si, Na, Mn, Al and other elements on the exposed surface of carbon steel coupons under different experimental conditions. SEM- EDXS results of areas (D-30, D-33, D-34, D-35 and D-40) shown in ***Figure68*** suggest the formation of iron silicate on the exposed surface of carbon steel coupons. For 3 months dynamic experiments, the carbon steel coupon with scratch at 50°C has areas (***Figure68***, D-27, D-28 and D-29) where, the Fe:S atomic ratio indicates the presence of pyrite which may be present in bentonite showing relevance in dynamic experiment compared to static experiment.

In areas such as (***Figure68,*** D-24, D-26, D-37 and D-38), EDXS data shown in (***Table53***) indicate the formation of iron oxide (Fe_xO_y) or green rust as secondary products on the exposed surface of the coupon at 25°C with scratches for 3 months and 50°C with scratches for 6 months dynamic experiment. SEM-EDXS results of the area (D-31) which were enriched with sodium, silicon, aluminum, oxygen and iron suggest presence of bentonite clay covering the corrosion products (iron silicate) and the exposed area of carbon steel coupon. Some amount of dissolved

iron was detected on the surface of bentonite clay however, its concentration varies across the exposed surface. The majority of the surface exhibits high concentrations of iron with areas like D-21, D-22, D-32 and D-39 having notably high iron content and manganese (Mn) presence indicative of iron-based materials (carbon steel), with low coverage of secondary corrosion products.

Areas with high iron content and oxygen likely form iron (hydr)oxides and sulfur-rich areas form iron sulfides. The presence of aluminum, silicon, and iron could contribute to secondary protective layers (iron silicate), but the overall corrosion behavior is heavily influenced by environmental conditions and the interplay of these elements. Overall, based on the EDXS results, it seems that the corrosion products obtained here consist of iron (hydr)oxides (magnetite, green rust), iron sulfides, and potentially iron silicates which were formed under specific conditions. Based on electron microscopic data, the carbon steel degradation mechanisms under dynamic experiments were comparable with static experiments.

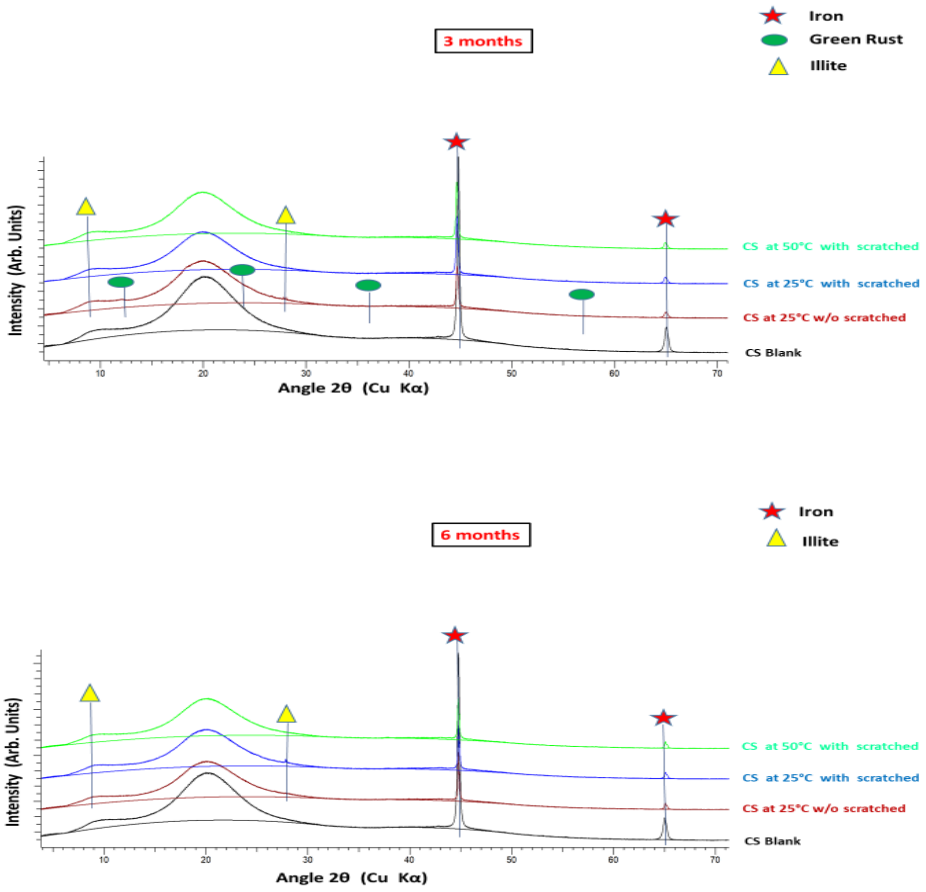

Figure 69 *X-ray diffractograms recorded on the corroded CS coupons after 3 months (top) and 6 months (down) reaction time under dynamic conditions (exact conditions are indicated on individual XRD plot).*

The XRD analysis of corroded carbon steel coupons obtained after three and six months of dynamic experiments was carried out, and its diffractograms were shown in (***Figure 69***). XRD analysis of the corroded specimens reveals the presence of structures characteristic of the coupon with its components cubic iron (PDF 87-0721) (***Figure 69***) on all coupons. Green rust (PDF 13-0090) was detected on carbon steel coupon without scratches at 25°C for 3 months dynamic experiment. Apart from this, only illite was detected on coupons for both three and six months dynamic experiments which comes from bentonite. No other secondary phase presence could be detected for other coupons, suggesting that either their amount was too low, that they are of too low crystallinity, or that they must have been removed when cleaning off the excess suspension. There is not much difference observed in six months coupons compared to three months in terms of obtained phase (primary) from XRD analysis. XRD analysis results for dynamic experiments were comparable with that of static experiments for carbon steel coupons. XRD results of carbon steel coupons were corroborated with SEM analysis for three and six months dynamic experiments.

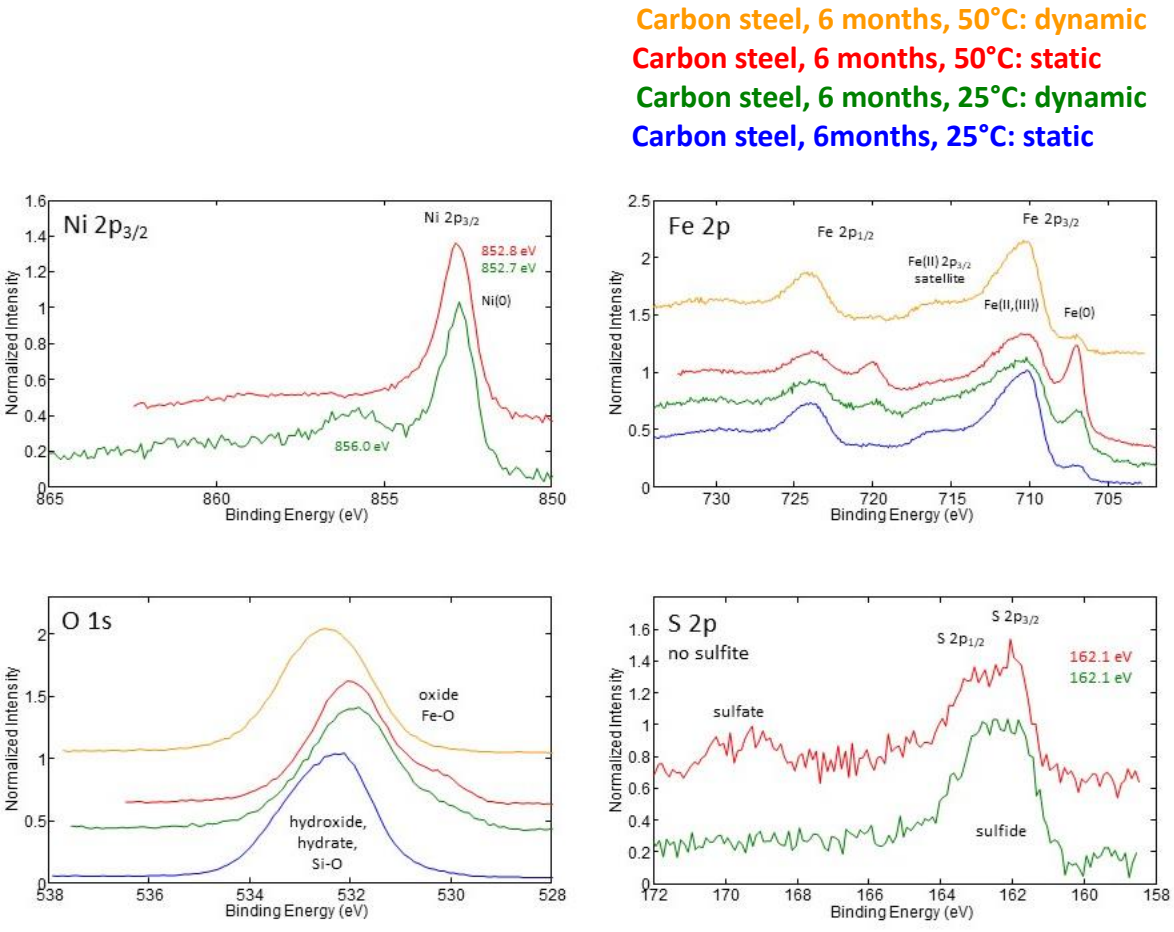

Figure 70 *X-ray photoelectron spectra recorded on CS coupons corroded in MX-80 bentonite under static and dynamic conditions (exact conditions are indicated above the graphs).*

Complementary XPS measurements provided additional speciation information. XPS spectra recorded for selected carbon steel coupons under static and dynamic conditions for 6 months at 25°C and 50°C are shown above in (***Figure 70***). The spectral lines here gave information about oxidation states of iron, nickel and sulfur. For all analyzed samples, findings were very comparable. The Ni $2p_{3/2}$ lines having a binding energy of 852.8 eV for static conditions at 50°C and having a binding energy of 852.7 eV and 856.0 eV for dynamic conditions at 25°C indicating nickel in the carbon steel coupon present in its metallic state or low oxidation state (Ni(0)) **(Kesavan et al., 2017; Siudyga et al., 2020)**. However a low intensity peak on the high binding energy side in dynamic experiments at 25°C indicates the presence of (Ni(II)) which can form $Ni(OH)_2$ as a part of a passive layer **(Dickinson et al., 1977)**. The Fe 2p spectrum recorded at the metal surface for all coupons shown in (***Figure 70***) evidenced the presence of metallic Fe and mixture of (Fe (II) and Fe (III)) which can be due to the presence of different secondary phase like iron silicate, iron oxide and iron sulfide on coupon surface. Interestingly, the binding energy of Fe $2p_{3/2}$ lines are at about 710 eV, which is characteristic for iron oxides containing Fe(III), but also maybe for Fe(II) in silicates. Even if Fe and Si have similar Pauling's electronegativity, the oxygen ion at Fe-O-Si may have stronger interaction with tetravalent Si than with Fe(II) or Fe(III) resulting in more positive charge on the Fe ion compared to iron oxides. Thus higher binding energy of Fe 2p photoelectrons emitted from Fe(II)-O-Si(IV) binding is expected **(Seyama & Soma, 1987)**.

Low amounts of sulfide, indicated by the S $2p_{3/2}$ elemental line at 162.1 eV binding energy **(Nzulu et al., 2024)**, were also detected at the coupon surface for samples from 6 months static experiments at 50°C and 6 months dynamic experiments at 25°C. Sulfide originates most likely from pyrite naturally present in the bentonite and may form iron sulfide at the steel surface. Here the binding energy suggests a relatively reduced state of sulfur. It seems for static conditions at 25°C that sulfate was also present along with sulfide. The O 1s binding energy can correspond to the presence of different types of secondary products like oxide, hydroxide, hydrate and Si-O as shown in (***figure70***). Reference binding energies (**Moulder & Chastain, 1992)** of the Fe $2p_{3/2}$ elemental line of Fe (**Karnland O & Motamedi M**) (707.0 eV), FeO (709.4 eV) and FeS_2 (706.7 eV), whereas that of FeS (710.3 – 712.2) or Fe_3O_4 (708.2 eV and 710.4 eV), α-Fe_2O_3 (710.9 eV), and α-FeOOH (711.8 eV).

The carbon steel coupons selected for XPS analysis were shown in (***Figure 71***) for dynamic experiments under different experimental conditions. Relative atomic concentration using XPS for selected points on exposed surface of carbon steel coupons were tabulated in (***Table 54***). A color change like blue-green, and blackish-grey was observed on the exposed coupon surface (***Figure 71***) indicating formation of different corrosion products (secondary phases). From atomic concentrations (***Table 54***), it is clear that most of exposed surface consists of iron, oxygen, sulfur and silicon as chief elements which form corrosion products and bentonite layer. The relatively high concentrations of silicon (Si) could point to silicate formation, often seen when corrosion occurs in the presence of silicate-rich environments (bentonite).

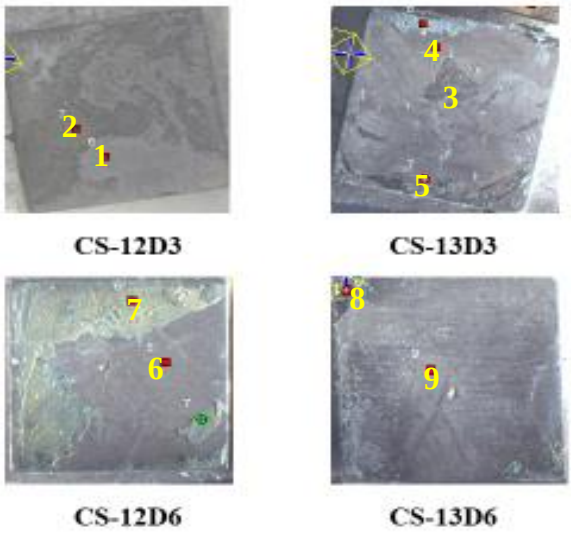

Figure 71 *Pictures taken in XPS chamber of CS coupons corroded under dynamic conditions (exact conditions are indicated on the individual sample, details of conditions are available in appendix). Marked points were selected for atomic concentration analysis, quantitative results are provided in* ***Table 54****.*

Table 54 *Relative atomic concentrations by XPS analyses at selected points of CS coupons for dynamic experiments shown in above* ***Figure 71.*** *Relative errors are estimated to be within ± 10% (Here each measurement has two type of atomic concentration: one with presence of carbon and one without carbon presence).*

Point	C	O	Na	Mg	Al	Si	S	Cl	Cr	Ni	Fe
12D3-1	27.1	46.1	/	/	1.0	1.9	0.2	3.0	/	/	20.8
	/	63.2	/	/	1.3	2.6	0.3	4.1	/	/	28.6
12D3-2	8.3	62.1	0.9	1.0	5.1	17.7	/	0.2	/	/	4.8
	/	67.7	1.0	1.1	5.5	19.3	/	0.2	/	/	5.2
13D3-3	16.2	51.2	0.7	0.6	/	9.3	1.4	1.2	/	1.3	16.0
	/	61.0	0.8	0.7	/	11.1	1.7	1.5	/	1.5	19.1
13D3-4	7.6	60.9	1.9	1.0	2.7	17.2	/	0.4	/	/	8.1
	/	66.0	2.1	1.1	2.9	18.6	/	0.5	/	/	8.7
13D3-5	9.8	60.0	0.7	0.7	3.2	14.0	/	1.0	/	/	10.5
	/	66.5	0.7	0.8	3.6	15.5	/	1.1	/	/	11.7
12D6-6	17.4	46.8	/	0.3	0.7	5.2	1.5	0.9	0.9	4.1	21.4
	/	56.6	/	0.4	0.9	6.3	1.8	1.0	1.1	5.0	25.9
12D6-7	5.8	63.4	1.2	1.2	6.6	19.6	/	/	/	/	2.1
	/	67.3	1.3	1.3	7.0	20.8	/	/	/	/	2.2
13D6-8	18.7	54.7	1.1	0.5	2.6	12.3	/	/	/	/	9.7
	/	67.6	1.3	0.6	3.2	15.2	/	/	/	/	12.0
13D6-9	19.6	45.1	1.0	0.6	1.5	6.8	2.4	1.1	/	4.8	15.8
	/	56.1	1.2	0.7	1.9	8.5	3.0	1.3	/	5.9	19.6

Here atomic ratio of iron, silicon and oxygen as shown in (***Table 54,*** point 4, 5 and 8) indicate formation of iron enriched bentonite layer. The atomic concentrations of oxygen are notably high in many samples, reflecting a possible iron oxide layer (Fe_xO_y) and Pyrite (may be come from bentonite) formation, especially in points like (***Figure 71,*** Point 9). In some cases, there are possibilities of formation of iron oxide + iron silicate (***Figure 71,*** Point 3 and 6). Some regions like (***Figure71,*** point 2 and 7) enriched in silicon, sodium, oxygen, aluminum, magnesium and some amount of iron indicate a bentonite clay region. Overall, the XPS results suggest that the surfaces analyzed have undergone corrosion processes involving oxide, sulfide, and silicate formations, with potential secondary phases like oxides and silicates being present in certain areas. The varied elemental presence across samples further indicates that these materials have been exposed to different environmental conditions.

Thus, exposed corroded surface exhibits an inhomogeneous distribution of secondary phase on the surface of carbon steel coupons subjected to dynamic experimental conditions. The results show the diversity of surface chemistry across the samples, with variations in elemental composition pointing to differences in phase formation and oxidation states. XPS analysis suggests that the surfaces were a mixture of oxide layers, iron silicate and metallic surfaces distributed unevenly over the exposed surface of carbon steel coupons for dynamic experiments. Little differences were observed between three and six months of dynamic experiments in terms of nature of secondary phases and thickness (size) (determined by SEM-EDXS). XPS atomic concentration results of above samples shown in (***Figure 71***) corroborated with SEM-EDXS results (***Table 53***) and XRD. Overall XPS analysis results for dynamic experiments were comparable with that of static experiments for carbon steel coupons.

3.5 Corrosion of Carbon steel in GMZ bentonite

3.5.1 Dissolved metal ions evolution

The dissolved amounts of iron, silicon and aluminium obtained using ICP-OES/MS during 3, 6, 9 and 12 months in presence of carbon steel coupons for GMZ bentonite was shown in ***Table 55*** and ***Table 56*** shows dissolved amounts of iron, silicon and aluminium in the pore water solutions of GMZ and MX-80 bentonite without coupon after one month of equilibrium period.

Table 55 *Dissolved amounts of Fe, Si and Al ions in the pore water solutions of GMZ bentonite in contact with CS coupons after 3, 6, 9 and 12 months static experiments. Numbers in parentheses correspond to the relative standard deviation in percentage.*

System/ Amounts in µg/L	Fe	Si	Al
3months 25°C CS in GMZ bentonite	500(3.6)	12300(0.3)	500(3.0)
3months 50°C CS in GMZ bentonite	100(7.7)	10100(1.2)	400(4.5)
6months 25°C CS in GMZ bentonite	400(8.6)	10400(1.2)	600(1.3)
6months 50°C CS in GMZ bentonite	400(8.4)	12300(0.6)	400(2.1)
9months 25°C CS in GMZ bentonite	300(16)	7900(1.4)	500(2.1)
12months 25°C CS in GMZ bentonite	800(0.8)	12100(0.6)	500(4.0)

Table 56 *Dissolved amounts of Fe Si and Al ions in the pore water solutions of GMZ and MX-80 bentonite without coupon after 1 month of equilibrium period. Numbers in parentheses correspond to the relative standard deviation in percentage.*

System/ Amounts in µg/L	Fe	Si	Al
GMZ bentonite	<100	19300(1.2)	500(3.8)
MX-80bentonite	400(8.2)	19300(0.5)	500(3.1)

There is no significant difference observed with regard to dissolved Fe concentrations in GMZ bentonite (***Table 55***) compared to the data of dissolved Fe concentrations in MX-80 bentonite (***Table 46***). Without coupon, GMZ bentonite shows significantly lower Fe concentrations (<100 µg/L) as seen in ***Table 56***, due to absence to pyrite in GMZ bentonite compared to MX-80, where Fe is present at higher levels (400 µg/L) (due to presence of pyrite). This could be related to differences in mineralogy or the availability of Fe-bearing phases in the two bentonites.

Without coupon GMZ bentonite and MX-80 bentonite shows similar Si and Al concentration as shown in (***Table 56***), although their concentration varies across different time period, but their variations are within experimental uncertainty. Overall, GMZ bentonite and MX-80 bentonite have a higher initial availability of dissolved Si and Al, which is not as significantly influenced by coupon presence.

3.5.2 pH / E_h evolution

The results shown in (***Table 57***) consists of pH values and redox potential (E_h) measurements with respect to the standard hydrogen electrode (SHE), for a carbon steel (CS) coupon in GMZ bentonite under static conditions over various time periods (3 months, 6 months, 9 months, and 12 months) at temperatures of 25°C and 50°C.

Table 57 *pH / Eh evolution of CS in contact with GMZ bentonite slurry after 3, 6, 9 and 12 months exposure time.*

System	pH	E_hw.r.t SHE (mV)
3months 25°C CS in GMZ bentonite	8.17±0.10	-415±50
3months 50°C CS in GMZ bentonite	8.08±0.10	-272±50
6months 25°C CS in GMZ bentonite	8.27±0.10	-298±50
6months 50°C CS in GMZ bentonite	7.95±0.10	30±50
9months 25°C CS in GMZ bentonite	8.09±0.10	-353±50
12months 25°C CS in GMZ bentonite	8.08±0.10	-460±50

The pH values are relatively stable over time and temperature, ranging from 7.95 to 8.27 throughout the 12 months period, certainly due to buffering capacity of the GMZ bentonite. The E_h values (***Table 57***) suggest a typical corrosion behavior of carbon steel, where the system remains predominantly in a reducing environment over time, but temperature and time influence the corrosion dynamics. The positive E_h values at 50°C for six months experiments may be due to data scattering, but the overall system shows signs of maintaining reducing environment over longer periods, possibly due to the formation of protective corrosion products or passivating layers on the carbon steel surface. Overall pH and E_h results of carbon steel in GMZ bentonite (***Table 57***) were comparable with pH and E_h results of carbon steel in MX-80 bentonite (***Table 50***) for experiments under static conditions. Both bentonites show buffering property over different experimental conditions (time and temperature).

3.5.3 Corrosion rate

The corrosion rates of carbon steel in contact with GMZ bentonite were calculated using the weight loss method and are shown in (***Figure 72***) for 3, 6, 9 and 12 months of static experiments whereas (***Figure 63***) shows corrosion rates of carbon steel coupons in MX-80 for 3, 6 and 9 months of static experiments. The corrosion rate results obtained across different conditions reveal a noticeable variation in the material's behavior over temperature and time.

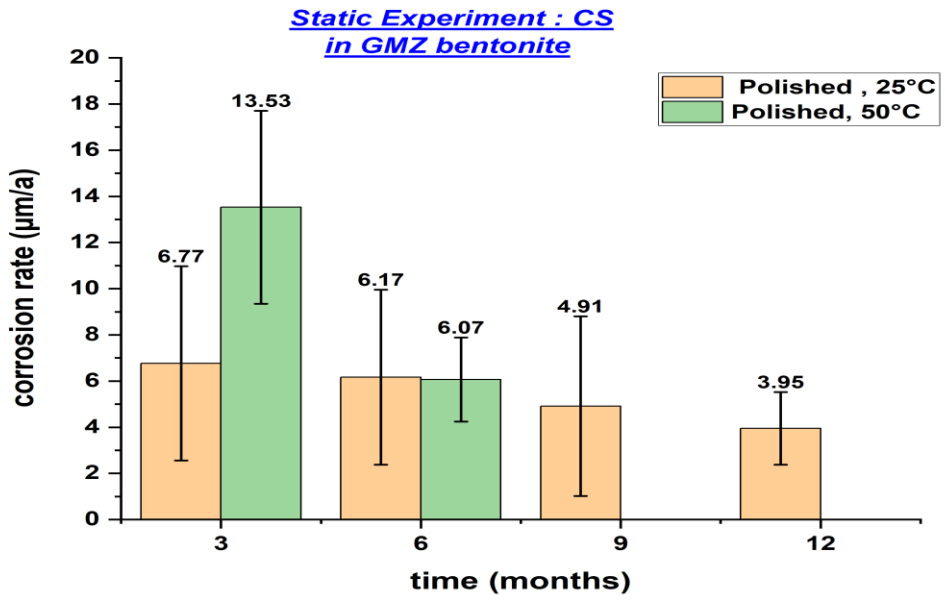

Figure 72 *Corrosion rates of all CS coupons for GMZ bentonite obtained after 3, 6, 9 and 12 months static experiments.*

At 25°C, GMZ bentonite exhibits a general decreasing trend in corrosion rates over time, showing a more pronounced and steady decrease from 6.77±4.21 µm/a after 3 months to 3.95±1.57 µm/a after 12 months. Comparing corrosion rate of carbon steel in GMZ bentonite with MX-80, there might be initially enhanced corrosion rates visible in GMZ at room temperature (25°C) which level out after 9 months. At 50°C a decrease in corrosion rates for carbon steel in GMZ bentonite (***Figure 72***) with time is more pronounced as compared to experiment with MX-80 bentonite (***Figure63***), however the variation seems to be within experimental uncertainty range.

The significant temperature effect on corrosion is evident, with the 50°C measurements generally being higher, particularly in the early months. Overall, both (GMZ and MX-80) bentonites show a general reduction in corrosion rate over time, GMZ demonstrates a more stable and predictable pattern, while MX-80 experiences greater variability, especially in response to different temperature (25°C and 50°C). Overall, the variation in corrosion rates observed in GMZ and MX-80 bentonites can be explained by differences in their mineral composition, their ability to form protective layers, their ion-exchange properties, and their effects on pH and pore-water chemistry, all of which interact with the temperature and time of exposure. GMZ bentonite seems to provide more consistent protection for carbon steel, MX-80 bentonite 's higher initial corrosion rates and fluctuations may result from its different composition, less stable protective film formation, and greater sensitivity to experimental conditions.

3.5.4 Secondary phase characterization

3.5.4.1 Static condition systems (3, 6, 9 & 12 months)

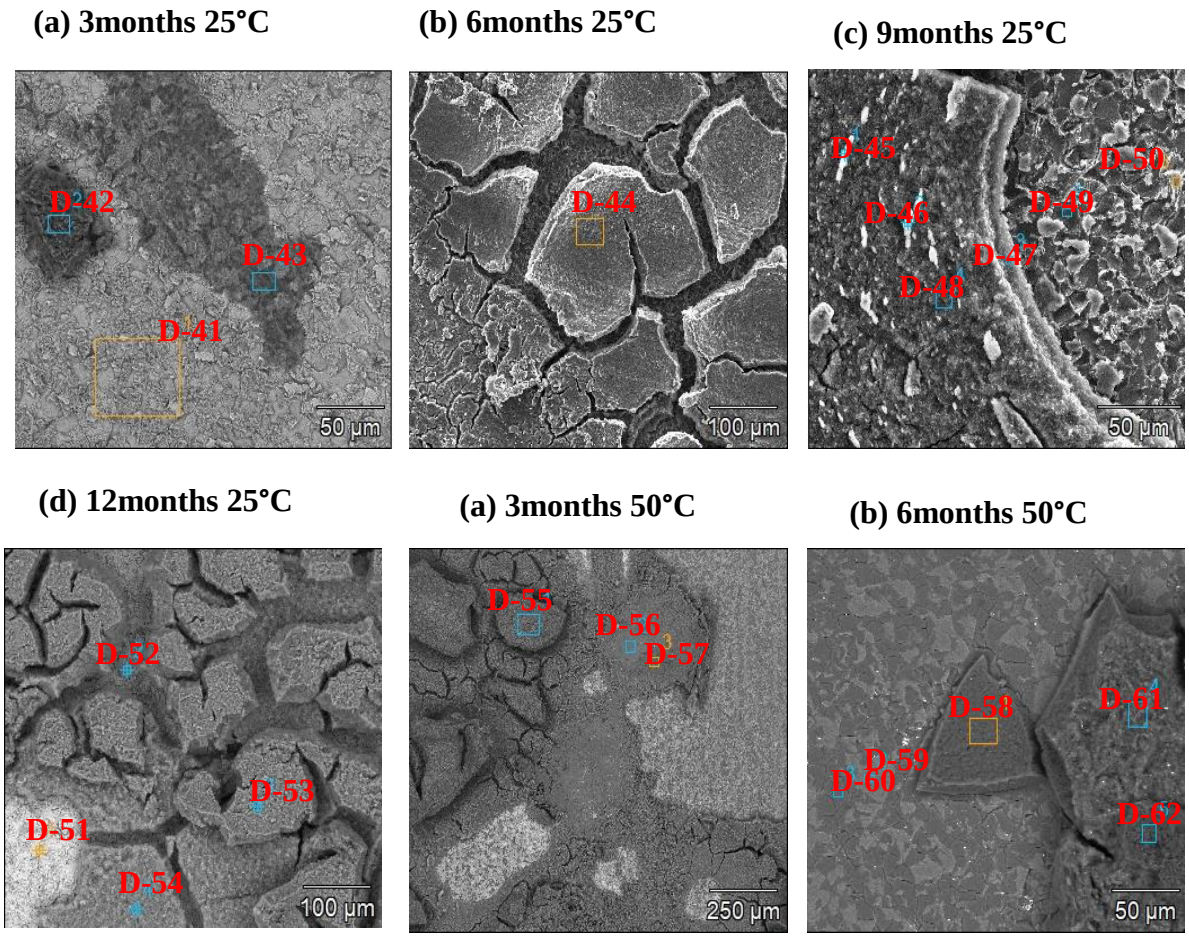

Figure 73 *Scanning electron micrographs (in SE mode) of all CS coupons in GMZ bentonite corroded for 3, 6, 9 and 12 months under static conditions at different temperature (exact conditions are indicated above the micrographs).Marked areas were selected for EDX analysis, quantitative results are provided in* ***Table 58****.*

Table 58 Relative atomic concentrations by EDXS analyses at selected areas shown in above Figure 73. Relative errors are estimated to be within ± 10%.

Area	C	O	Na	Mn	Al	Si	S	Cl	Ca	Ni	Fe
D-41	5.5	20.2	/	1.3	/	1.3	/	/	/	1.0	70.8
D-42	8.0	59.8	0.6	/	1.5	14.9	/	0.2	/	/	14.4
D-43	7.6	41.1	/	0.8	0.6	8.0	/	0.4	/	/	40.9
D-44	2.6	54.6	0.7	/	2.9	19.4	/	/	/	/	19.0
D-45	7.4	57.6	0.5	0.2	1.2	16.0	/	0.2	/	/	16.5
D-46	7.5	57.4	0.5	/	1.4	16.5	/	0.2	/	/	16.2
D-47	11.0	50.7	0.4	0.6	0.4	10.1	/	0.2	/	0.7	25.8
D-48	7.3	54.7	0.5	/	0.9	17.1	/	0.2	0.1	/	18.8
D-49	4.7	33.5	/	0.8	0.2	4.7	/	0.3	/	0.6	53.6
D-50	9.1	20.8	/	2.4	/	1.7	/	/	/	2.4	62.5
D-51	2.0	2.4	/	1.5	0.2	0.9	/	/	/	0.5	92.5
D-52	0.5	6.6	/	2.2	0.1	2.0	/	/	/	1.0	87.4
D-53	2.3	62.4	0.5	0.2	1.3	16.6	/	0.2	0.1	0.1	15.9
D-54	2.3	59.0	0.5	0.2	0.6	17.4	/	0.1	0.1	/	19.5
D-55	3.3	54.0	/	/	3.4	16.6	/	0.2	/	/	21.3
D-56	2.4	58.7	/	/	1.2	16.8	/	0.2	/	/	20.3
D-57	3.0	57.8	/	/	4.3	17.3	/	0.2	/	/	16.2
D-58	8.4	55.1	0.5	0.2	0.3	18.2	/	0.3	0.1		16.4
D-59	6.7	42.3	1.3	1.1	/	15.2	/	0.1	/	1.2	31.4
D-60	5.5	53.8	0.9	0.2	/	18.4	/	0.2	/	0.7	19.6
D-61	5.9	54.6	0.5	/	1.1	20.1	/	0.3	0.1	/	16.7
D-62	3.6	54.7	0.9	/	5.8	25.8	/	0.1	/	/	6.0

Scanning electron microscopy was subsequently applied to analyze the carbon steel corroded coupons in contact with GMZ bentonite. SEM-EDXS analysis micrographs for various selected areas were shown in (***Figure 73***) and their atomic concentration results were tabulated in (***Table 58***). SEM microscopy reveals presence of different secondary phases under different experimental conditions. For instance, as shown in appendices (***Figure A10d***) octahedral shape corrosion product for carbon steel coupon was observed at room temperature after 12 months. EDXS analyses results of all carbon steel coupons in GMZ bentonite at 25°C (3, 6, 9, and 12 months) and 50°C after 3, 6 months for selected areas (D-42, D-44, D-45, D-46, D-48, D-53, D-54, D-55, D-56, D-57, D-58, D-60, and D-61) shown in (***Figure 73***) indicate the formation of iron silicate as corrosion products. Oxygen is also present on the coupon surface after exposure and the amount of silicon slightly increased on coupon surface in the region where surface was covered with bentonite.

Iron-based corrosion products, such as iron oxides (Fe_xO_y), are predominant in some areas like (***Figure73,*** D-49 and D-50). The presence of oxygen alongside iron in these areas may also support the formation of iron (hydr)oxides on the exposed surface as corrosion products when iron exposed to water saturated bentonite under anoxic conditions. Formation of iron silicate and iron oxide was mainly observed on the exposed surface of corroded carbon steel coupons in GMZ bentonite. SEM analysis of carbon steel in GMZ and MX-80 bentonite were relatively comparable, however the iron silicate formation in GMZ bentonite seems to be more prominent

compared to MX-80 bentonite under static conditions. It seems that iron silicate formed on carbon steel coupon surface was more protective for GMZ bentonite than MX-80 bentonite under elevated temperature conditions for static experiments which was evidenced by corrosion rate measurements. Also, magnetite formation was detected in presence of GMZ bentonite but was not observed in presence of MX-80 bentonite (although it contains high soluble silica) for carbon steel coupons. In contrast Pyrite was detected in MX-80 bentonite but was not observed in GMZ bentonite for carbon steel coupons under static conditions. So, different types of corrosion products were formed in different types of bentonite (MX-80 and GMZ) which affects the corrosion behavior of carbon steel in given bentonite. Overall MX-80 and GMZ bentonite were relatively comparable in buffering the system under static conditions.

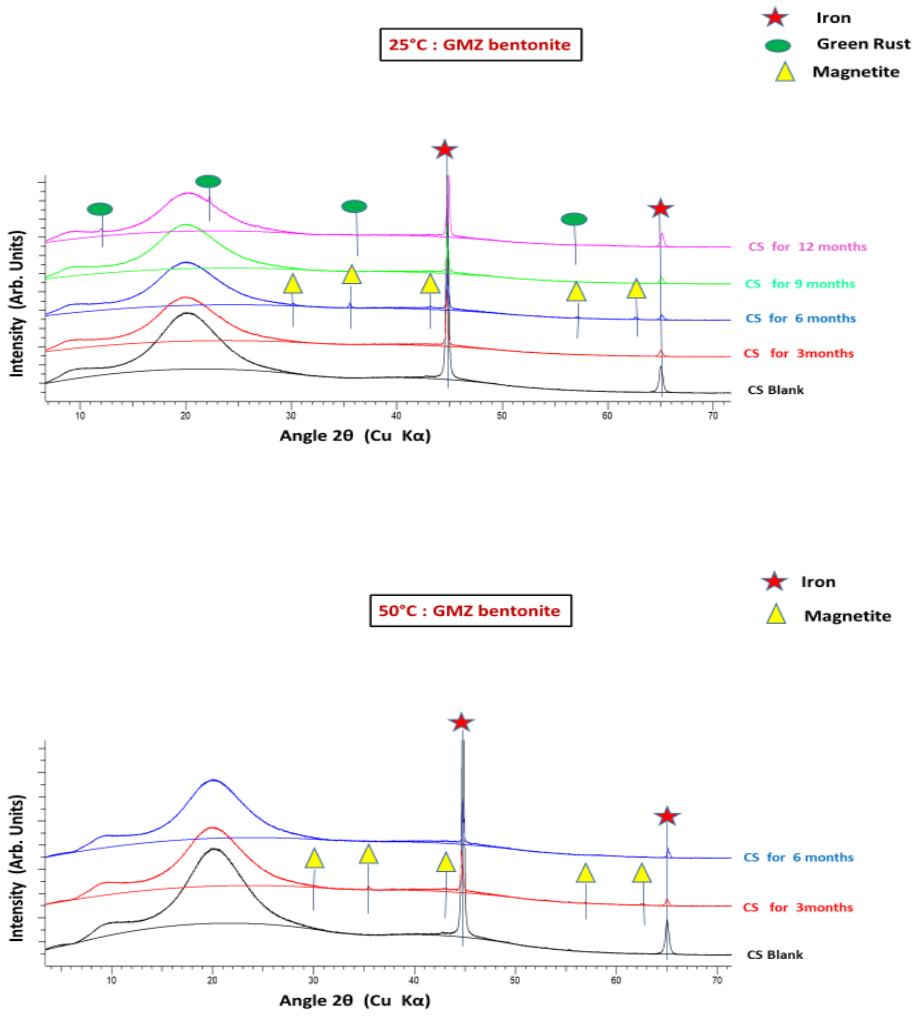

Figure 74 *X-ray diffractograms recorded on the corroded CS coupons in GMZ bentonite at room temperature for 3, 6, 9 an 12 months (top) and at elevated temperature for 3 and 6 months (down) reaction time under static conditions (exact conditions are indicated on individual XRD plot).*

The XRD analysis of corroded carbon steel coupons in GMZ obtained after three, six, nine and twelve months of static experiments was carried out and its diffractograms were shown in ***(Figure 74)***. The primary peak in the XRD spectrum for three, six, nine and twelve months of static experiments likely correspond to the cubic iron phase (PDF 87-0721), which is starting material. Apart from this, other reflections correspond to corrosion products like magnetite (PDF 79-0419) which was observed on the exposed surface as shown in (***Figure 74***) specially for six months at room temperature (25°C) and in three months coupon at elevated temperature(50°C). Green rust (PDF 13-0090) as corrosion product (secondary phase) was also observed on carbon steel coupon surface after 12 months at room temperature. Findings suggest that secondary phases may be also formed on other coupons but since it was in too low amounts, so not able to detect through XRD analysis but were evidenced by XPS and SEM-EDXS analysis.

There was not much difference observed on carbon steel coupon surface at room and elevated temperature after three and six months in terms of secondary phase (corrosion products) from XRD analysis. Overall, XRD analysis of carbon steel corroded coupons in GMZ bentonite and MX-80 bentonite were relatively comparable. In both (GMZ and MX-80) bentonites green rust was detected as corrosion product. In contrast, magnetite was detected in GMZ bentonite but was not found in MX-80 bentonite for carbon steel coupons under static conditions using XRD analysis.

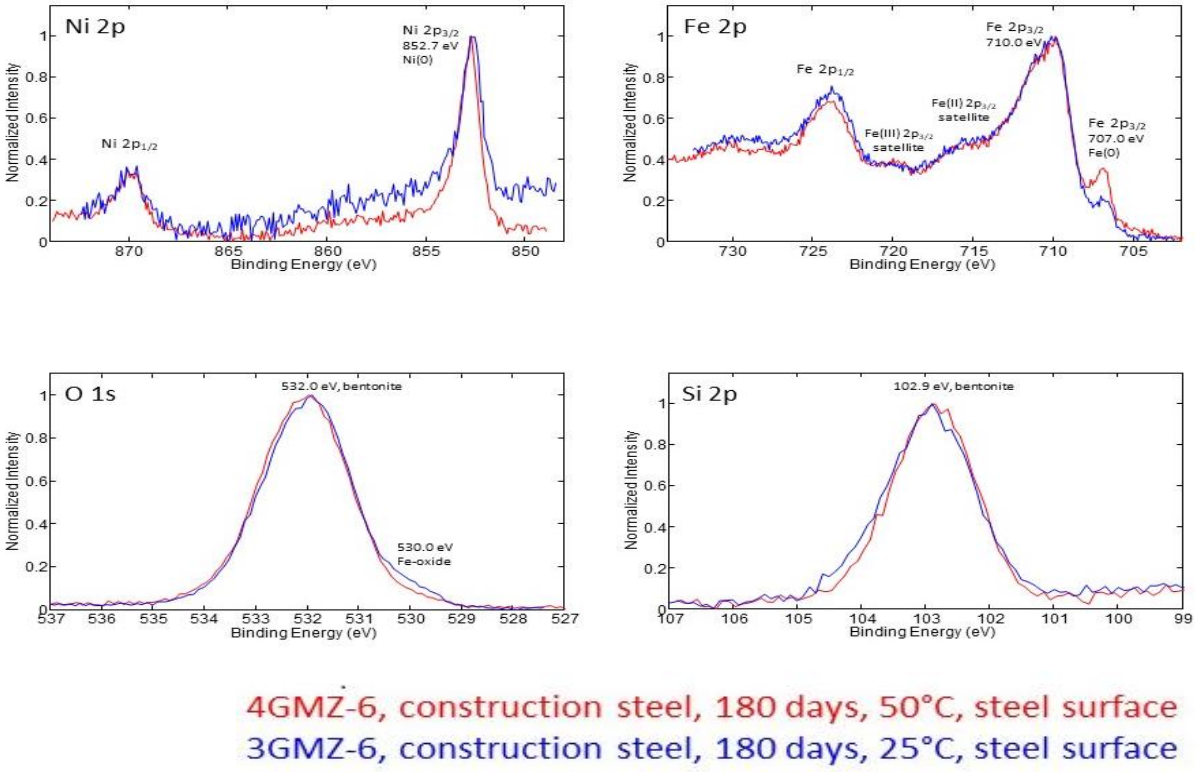

Figure 75 *X-ray photoelectron spectra recorded for speciation on CS coupons corroded in GMZ bentonite under static conditions (exact conditions are indicated below the graphs).*

XPS spectra recorded for selected carbon steel coupons in contact with GMZ bentonite under static conditions for 6 months at 25°C and 50°C are shown above in (***Figure 75***). The Ni $2p_{3/2}$ lines having a binding energy of 852.7 eV for both coupons at 25°C and 50°C indicate nickel in the carbon steel coupon is present in its metallic state. The Fe 2p spectrum recorded at the metal surface for all coupons shown in (***Figure 75***) evidenced the presence of metallic Fe and mixture of (Fe (II) and Fe (III)) which originate from different secondary phase like iron silicate and iron oxide on coupon surface. Interestingly, binding energy of Fe $2p_{3/2}$ lines are at about 710 eV, which is characteristic for iron oxides containing Fe(III), but also for Fe(II) in silicates. However, the Fe $2p_{3/2}$ spectra are sometimes complex due to multiplet splitting and satellite features **(Hughes et al., 2024)**.

The peak at 707 eV suggests that there is Fe(II) present possibly from Fe_3O_4. The satellite peak supports the presence of Fe(III) and Fe(II) species, confirming the possible iron oxide or silicate in mixed valence state. The binding energy of Si 2p lines at about 102.9 eV suggests the presence of silicon in partially oxidized state (silicon in an oxidation state between 0 and +4) or non-stoichiometric oxide layer (i.e., naturally present in the bentonite). It seems for static conditions at 25°C and 50°C, the oxygen binding energy (530 eV) corresponds to more stable (O^{2-}), bonded to form (metal oxide) whereas binding energy at 532 eV correspond to oxygen in a weaker such as hydroxyl group (OH^-) or adsorbed oxygen species (water), more loosely bound state. For all analyzed samples, findings were very comparable with MX-80 bentonite (***Figure 70***).

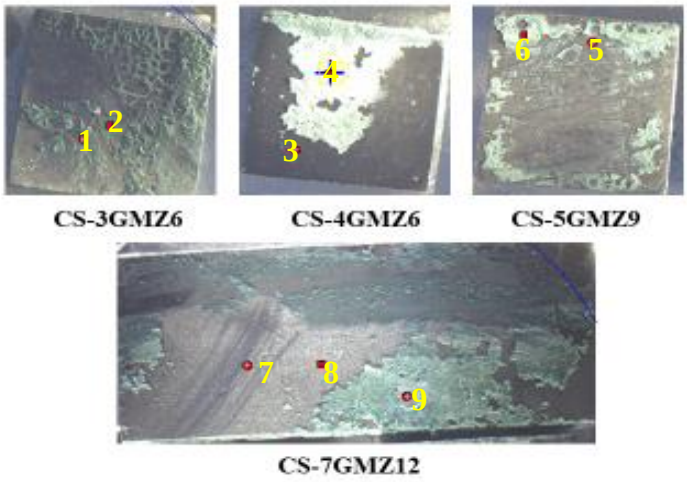

Figure 76 *Pictures taken in XPS chamber of CS coupons in GMZ bentonite corroded under static conditions (exact conditions are indicated on the individual sample, details of conditions are available in appendix). Marked points were selected for atomic concentration analysis, quantitative results are provided in* ***Table 59****.*

Table 59 *Relative atomic concentrations by XPS analyses at selected points of CS coupons for static experiments shown in above* ***Figure 76****. Relative errors are estimated to be within ± 10 % (Here each measurement has two type of atomic concentration: one with presence of carbon and one without carbon presence).*

Point	C	O	Na	Mg	Al	Si	S	Cl	Cr	Ni	Fe
3GMZ6-1	14.0	59.8	0.4	0.4	1.7	11.1	/	0.4	/	1.1	10.5
	/	69.6	0.4	0.5	2.0	12.9	/	0.5	/	1.3	12.2
3GMZ6-2	8.3	62.6	0.3	0.7	3.2	14.3	/	0.4	/	/	10.2
	/	68.2	0.3	0.8	3.5	15.6	/	0.5	/	/	11.1
4GMZ6-3	14.3	49.3	0.7	/	/	11.9	/	/	/	3.1	20.3
	/	57.6	0.8	/	/	13.9	/	/	/	3.6	23.7
4GMZ6-4	3.9	63.1	1.4	1.6	4.9	18.2	/	/	/	/	6.1
	/	65.7	1.5	1.6	5.1	18.9	/	/	/	/	6.3
5GMZ9-5	16.3	50.1	/	/	/	5.8	/	0.4	0.4	1.5	24.8
	/	59.9	/	/	/	6.9	/	0.4	0.5	1.8	29.7
5GMZ9-6	5.9	61.2	1.0	/	/	17.9	/	0.5	/	/	13.4
	/	65.1	1.1	/	/	19.0	/	0.6	/	/	14.2
7GMZ12-7	22.5	44.0	/	/	/	3.6	/	1.9	/	/	28.0
	/	56.8	/	/	/	4.6	/	2.5	/	/	36.1
7GMZ12-8	20.5	46.8	/	/	/	4.4	/	1.3	/	1.2	24.4
	/	58.9	/	/	/	5.6	/	1.6	/	1.6	30.7
7GMZ12-9	5.9	61.8	1.0	0.1	/	15.0	/	0.6	/	/	15.7
	/	65.6	1.0	0.1	/	15.9	/	0.6	/	/	16.7

The carbon steel coupons in GMZ bentonite selected for XPS analysis for static experiments under different experimental conditions were shown in (***Figure76***). Relative atomic concentrations using XPS for selected points on exposed surface of carbon steel coupons were tabulated in (***Table 59***). Here atomic ratio of iron, silicon and oxygen as shown in (***Table 59,*** Point 1, 2, 6 and 9) indicate formation of iron enriched bentonite layer/silicate. The atomic concentrations of oxygen are notably high in many samples, reflecting a possible iron oxide layer (Fe_xO_y) formation, especially in points like (***Figure 76***, Point 5, 7 and 8). In some cases, there are possibilities of formation of iron oxide + iron silicate (***Figure 76,*** Point 3). Some region like (***Figure76,*** Point 4) is enriched with silicon, sodium, oxygen, aluminum, magnesium and some amount of iron indicating the presence of bentonite. Overall, the XPS results suggest that the surfaces analyzed have undergone corrosion processes involving hydroxyl/oxide, and silicate formations, with varied elemental compositions across samples, further indicating that these materials have been exposed to different environmental conditions.

Overall XPS analysis results of carbon steel coupons in GMZ bentonite were comparable with that in MX-80 bentonite for experiments under static conditions. However, there was little changes like, iron sulfide (FeS) was not detected in presence of GMZ bentonite but was observed in MX-80 bentonite for static experiments.

3.6 Alteration of MX-80 Bentonite (for iron based materials)

X-ray absorption near edge structure (XANES) spectroscopy which is highly sensitive technique for studying the electronic structure and chemical speciation of elements, was applied to probe the Fe K-edge for selected samples of altered bentonite from 6 months dynamic experiments.

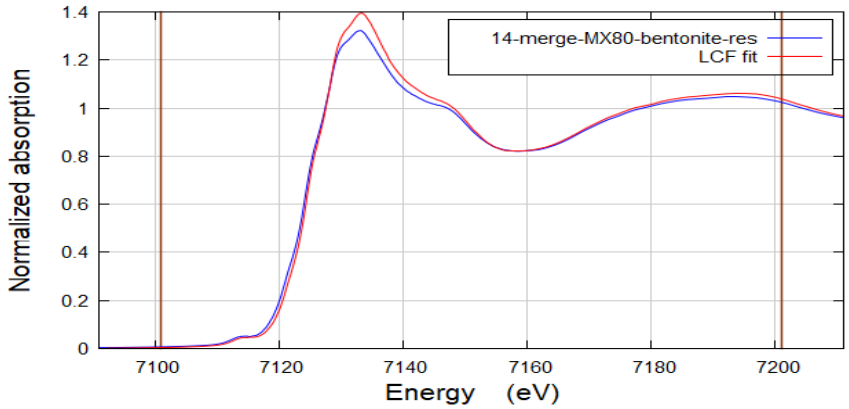

Figure 77 *XANES spectra of reference MX-80 bentonite without coupon for 6 months dynamic experiments (blue line is experimental data, red line is fit).*

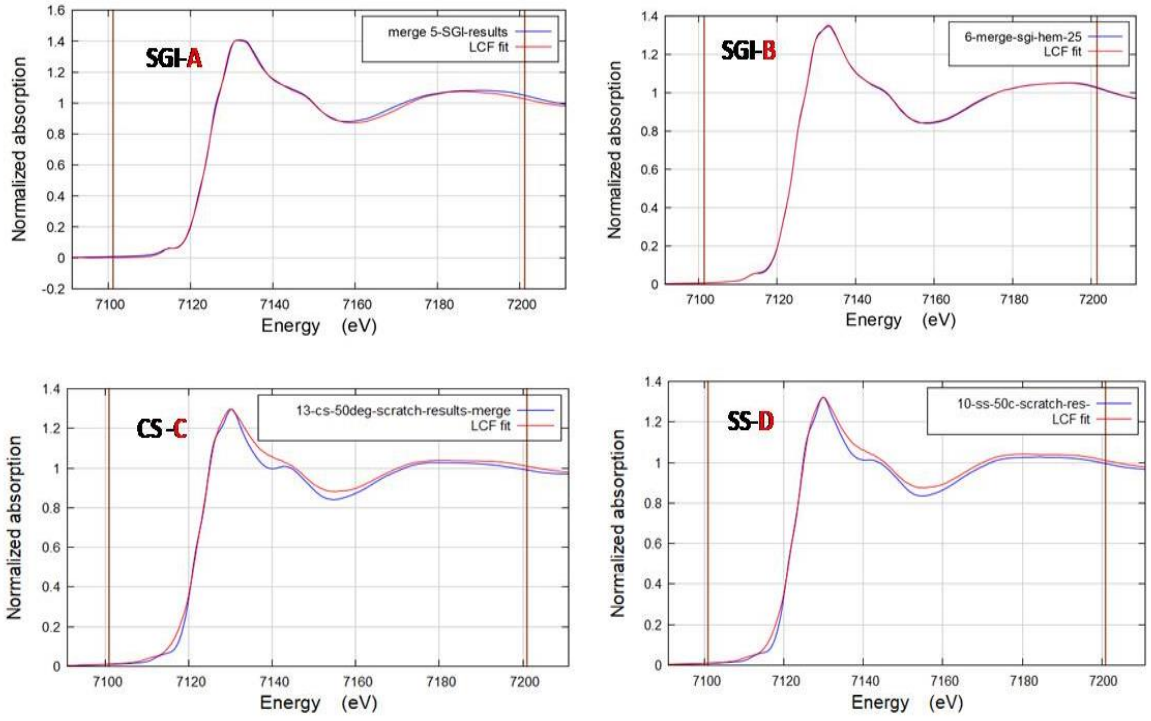

Figure 78 *The XANES (Fe) spectra of the corrosion products in altered bentonite contact with different coupons like SGI-A (spheroidal graphite iron at 25°C without hematite), SGI-B (spheroidal graphite iron at 25°C with 0.5wt%. hematite), CS-C (carbon steel at 50°C with scratched) and SS-D (spring steel at 50°C with scratched) for 6 months dynamic experiments (blue line is experimental data, red line is fit).*

When analyzing altered bentonite having been in contact with steel and cast iron coupons under anoxic conditions, XANES offers valuable insight into the alteration processes of bentonite and the secondary phases formed due to interaction with these materials (iron and steel). The Fe K-edge XANES spectrum of the reference MX-80 bentonite without coupon was shown in (***Figure 77***). Bentonite was analyzed to determine the Fe speciation in the altered bentonite sample having been interacted with different corroding coupons like SGI-A (spheroidal graphite iron at 25°C without hematite), SGI-B (spheroidal graphite iron at 25°C with 0.5wt% hematite), CS-C (carbon steel at 50°C with scratched) and SS-D (spring steel at 50°C with scratched) for 6 months dynamic experiments were shown in (***Figure78***).

A color change was observed on the surface of altered bentonite after corrosion experiments, suggesting an alteration of bentonite and/or possible Fe corrosion products presence. For LCF analysis, XANES data of reference compounds of known composition were already available **(Finck et al., 2023)**. MX-80 is an assemblage of mineral phases, and among those present (***Table3***) only clay minerals (montmorillonite, illite, muscovite) and pyrite contain Fe. The pyrite content is very low, implying a negligible contribution to the Fe K-edge XANES spectrum recorded on MX-80. Montmorillonite, illite and muscovite have all a comparable crystal structure, made of one octahedral layer sandwiched between two tetrahedral layers (i.e., TOT type structure), in which Fe occupies an octahedral position. The spectrum recorded on MX-80 thus corresponds dominantly to octahedral Fe located in a TOT environment, more precisely in montmorillonite that makes >80wt%. of the mineral assemblage.

For sample SGI-A (spheroidal graphite iron at 25°C without hematite), LCF fit results hint at the presence of MX-80 (39%), magnetite (34%) and berthierine (27%). The experimental XANES spectrum of the sample interacted with SGI-B (spheroidal graphite iron at 25°C with 0.5wt%. hematite) could be reconstructed using spectra recorded on MX-80 (85 %) and chukanovite (17 %), and the XANES spectrum of the sample interacted with CS-C (carbon steel at 50°C with scratched) using MX-80 (43 %), green rust (10 %) and chukanovite (47%). Finally, results of fits to the Fe K-edge XANES spectrum recorded on sample SS-D (spring steel at 50°C with scratch) hint at the presence of MX-80 (31%), green rust (40%) and chukanovite (29%).

Bentonite alteration is mainly because of (partial) reduction of structural iron from Fe^{+3} to $Fe^{+2.}$ The color change observed around steel/bentonite contact region indicates bentonite alteration and formation of Fe-bearing compounds like magnetite, green rust, berthierine and chukanovite. However, their formation and concentration depend on experimental conditions and materials. XANES gives information about alteration of bentonite and presence of secondary corrosion products in the altered bentonite. Thus, information about the nature of Fe-bearing phases present at the coupon/bentonite interface was obtained using XANES analysis. Differences were observed due to change in experimental parameter and type of materials (SGI, SS and CS).

3.7 Overall discussion of iron based materials (SGI, SS and CS)

For iron based materials, the experimental results from both static and dynamic conditions indicate that iron (Fe) dissolution is primarily governed by steel corrosion (SGI, carbon steel, and spring steel), while silicon (Si) and aluminum (Al) mobilization originates mainly due to clay (bentonite) dissolution. In static experiments for SGI without hematite, Fe concentrations initially peak but decrease over time, stabilizing at low levels (~4–6 × E-6 mol/L), indicating progressive sorption or precipitation. In contrast, in the presence of hematite (0.5 wt.%), Fe concentrations increase over time, suggesting slow reductive dissolution of Fe(III) from hematite to soluble Fe(II) under reducing conditions induced by corrosion. Despite changes in temperature and hematite presence, Si and Al concentrations remain within the range of experimental uncertainty mostly, implying minimal influence from these variables. Si and Al dissolution patterns reflect bentonite behavior, aligning with equilibrium slurry or simulated groundwater values. Dynamic experiments consistently show lower Fe concentrations than static, further suggesting sorption of Fe(II) onto clay minerals, supported by solubility limits under experimental pH (~1 × E-3 mol/L) for $Fe(OH)_2$. Comparative results from MX-80 and GMZ bentonite reveal higher Fe levels in MX-80, attributed to pyrite content, while Si and Al remain comparable across both clays. Overall, temperature and hematite presence primarily affect Fe concentration, while Si and Al behavior is controlled by bentonite dissolution, independent of coupon type or experimental condition, with variations falling within analytical uncertainty.

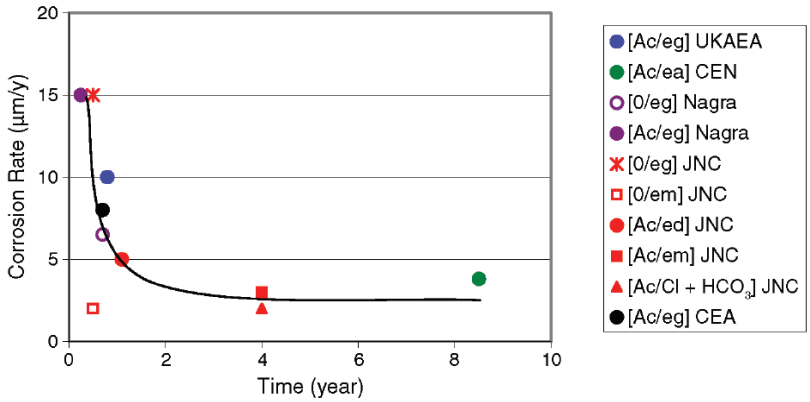

Figure 79 *Evolution of average generalized corrosion rate of carbon steels as a function of time in fairly reducing conditions at 80°C or 85°C. G: granite; Ac: compacted clay; O: immersion; ed: distilled water; eg: granite water; em: seawater; ea: clay water (**Féron et al., 2008**).*

Those findings (***Figure 79***) shown in literature **(Féron et al., 2008)** appear to suggest that the rate determining step is the corrosion reaction, i.e. the release of metal ions to solution. Sorption reactions are known to be rapid.

Here in this study, the experimental results demonstrate that temperature is the dominant factor influencing the corrosion behavior of iron-based materials (SGI, spring steel, and carbon steel) in bentonite suspensions, with corrosion rates significantly higher (~4-8 µm/a) at 50°C compared to 25°C, in agreement with reported findings **(Hesketh et al., 2023)**. The presence of hematite, surface scratches, and exposure duration had comparatively minor effects on both corrosion rate and electrochemical parameters (pH and E_h). Across static and dynamic conditions, reducing environments consistently developed due to steel corrosion, indicated by negative E_h values. However, pH remained relatively stable over time, largely due to the buffering capacity of bentonite. This buffering effect was evident in both static and dynamic experiments and minimized the influence of corrosion processes on pH, even under conditions that promoted redox changes and solid phase precipitation.

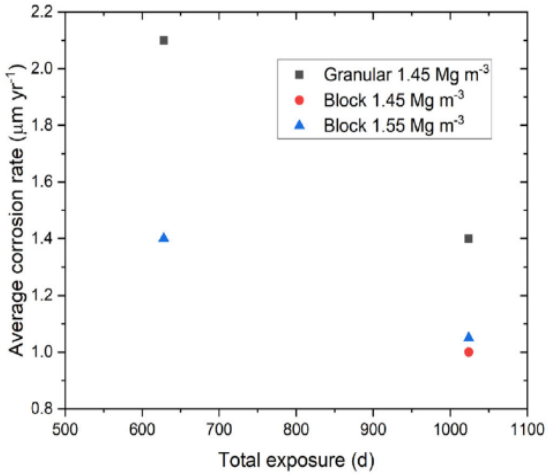

Figure 80 *Average corrosion rates (derived from weight loss) of corrosion coupons extracted from the IC-A experiment after 1.7 and 2.7 years* ***(Wersin et al., 2023).***

The corrosion rates data (***Figure80***) shown in literature **(Wersin et al., 2023)** tend to decrease over time. Here the corrosion rate for granular bentonite is higher than that of compacted bentonite, which also depends on water volume. In current study, the corrosion rate of all iron-based materials (SGI, spring steel, and carbon steel) at room temperature (25°C) in MX-80 bentonite suspension lies in the range ~2-6 µm/a after 9 months for static/dynamic experiments. The obtained corrosion rate values were quite similar to that reported corrosion rate (~2 µm/a) for carbon steel embedded within compacted MX-80 and exposed to natural granitic pore water for 394 days in the MaCoTe experiment **(Reddy, Padovani, Rance, et al., 2021)**. Both the difference in reaction time (270 days vs 394 days) and the difference in temperature (25°C vs rock temperature) can account for small differences in corrosion rates. In addition, the use of a suspension instead of compacted bentonite also plays a role because of the larger amount of water available.

When comparing the type of bentonites like MX-80 and GMZ bentonite, both materials demonstrated the ability to buffer pH and maintain reducing conditions over time, but little differences in corrosion trends were observed. GMZ bentonite provided more stable and

predictable corrosion behavior, particularly for carbon steel, with a gradual decrease in corrosion rate over time, likely due to the formation of more uniform and protective corrosion products.

In contrast, MX-80 bentonite exhibited some variability in corrosion rates, particularly at elevated temperatures, potentially due to differences in mineral composition, ion exchange capacity, and interaction with corrosion products. Overall, both bentonites are effective as corrosion mitigating media in engineered barrier systems and may offer more consistent long-term performance under thermal and geochemical gradients relevant to deep geological disposal conditions.

For SGI corroded coupons, the finding would agree with the visual observation of a blue/green coloration at the coupon/suspension interface suggesting a possible reduction of structural Fe(III) within smectite. In addition, this finding would also agree with the presence of mixed Fe(II)/Fe(III) bearing secondary phase such as berthierine and magnetite suggested from XANES and SEM-EDXS analysis. The presence of hematite had no significant impact on the Fe speciation, XPS data suggest it prevails in divalent and in trivalent oxidation state at the coupon/bentonite interface in all experiments.

The formation of iron silicates could be detected in some samples, especially at 50°C. This finding suggests that dissolved silica must have been available in the system **(Stephan Kaufhold et al., 2020)**, certainly favored by the slightly elevated temperature and the prevailing pH condition. Interestingly, data also indicate that neoformed iron silicates contain some aluminum meaning that the availability of dissolved silica alone cannot account for the observed secondary phases. Consequently, the reaction pathway may not simply consist in precipitation from dissolved species but may be more complex and possibly involve some kind of dissolution-reprecipitation mechanism. Layered Fe-bearing compounds have also been detected at the coupon/suspension interface, suggesting that not enough silica must have been available for the formation of only Fe silicates. Most probably, steel corrosion resulted in larger amounts of dissolved Fe(II) than dissolved silica available, thus resulting in the simultaneous formation of Fe (hydr)oxides in addition to Fe silicates.

Fe(II) has a good affinity for hematite under the given pH conditions **(Larese-Casanova & Scherer, 2007; Williams & Scherer, 2004)** and reported data showed that ferrous ions uptake results in electron transfer with structural Fe(III) in hematite. In the long term, this may result in quantitative transformation of hematite into mixed Fe(II)/Fe(III) compounds. Outcomes suggest that the starting pre-equilibrated suspension was diluted during the 3 and 6 months reaction time for dynamic experiments, implying that dissolved amounts of Fe(II) formed upon steel corrosion very likely did not accumulate in significant amounts within the reactor. Though results showed that a fraction of formed Fe(II) reacted with the contacting bentonite, the remaining was transported away with the water. Under these conditions no protective passive layer may be able to develop and protect the coupon surface, resulting in corrosion progressing over time. In any case, no experimental finding supports the hypothesis of a steel degradation mechanism (dynamic conditions) differing from that under static conditions.

The findings from SEM-EDXS, XRD, and XPS analyses of corroded spring steel coupons exposed to static and dynamic conditions in a bentonite slurry reveal significant insights into the corrosion mechanisms. In the static system, corrosion products such as iron (hydr)oxides, iron silicates, green rust, and iron sulfides were identified, with a more heterogeneous distribution of secondary phases over time, especially after nine months of exposure. These products, particularly iron silicates and green rust, formed dense protective layers that slowed down the corrosion rate with elemental compositions indicating complex interactions between the metal coupons and the surrounding environment (bentonite). In contrast, the dynamic system showed minimal secondary phase formation, with XRD analysis only detecting the primary phases of cubic iron and austenite, and no significant corrosion products like green rust. The dynamic system likely had lower amounts of corrosion products due to the mechanical movement and possible removal of phases during continuous flow of ground water, leading to less phase development compared to the static system. Overall, the finding demonstrates that environmental factors, particularly the duration of exposure and the presence of bentonite, significantly influence the formation and distribution of corrosion products. The corrosion rates decrease with longer exposure times due to the buildup of protective layers, which is consistent with the observed elemental and phase changes.

Comprehensive characterization using SEM-EDXS, XRD, XPS, and XANES has revealed that carbon steel corrosion under anoxic conditions in contact with bentonite (MX-80 and GMZ) results in the formation of spatially heterogeneous and chemically complex secondary phases. These primarily include iron (hydr)oxides, iron silicates, green rust, and particularly in the case of MX-80, iron sulfides such as FeS/FeS_2 (pyrite naturally present in MX-80). The corrosion products form via localized interactions between the steel surface and bentonite, influenced by factors such as temperature, exposure time, and surface condition (scratched or unscratched). SEM-EDXS showed areas depleted in iron but enriched in silicon and aluminum, indicative of aluminosilicate or iron silicate layer formation, particularly under bentonite coverage. XRD confirmed the persistence of the primary metallic phase with the emergence of crystalline corrosion products like magnetite and green rust under certain conditions, while many amorphous or poorly crystalline products were detected by surface sensitive XPS/XAS.

XPS and XANES provided insights into the oxidation states and coordination environments of Fe, Ni, and S. Mixed valence states of Fe (Fe(II)/Fe(III)) were observed, with Fe 2p binding energies suggesting the presence of iron oxides, silicates, and potentially non-stoichiometric mixed phases. Ni remained mostly in the metallic state, while trace amounts of Ni(II) indicated passive layer formation. XANES spectra of altered bentonites confirmed partial reduction of structural Fe(III) to Fe(II), indicating chemical alteration of the bentonite matrix due to interaction with corroding steel. Secondary Fe-bearing phases such as chukanovite, berthierine, magnetite and green rust were detected at the steel/bentonite interface in MX-80 bentonite.

The findings of both static and dynamic experiments reveal that temperature and time of exposure play a pivotal role in influencing the dissolution and corrosion behavior of iron based materials (SGI, spring steel, and carbon steel) in bentonite suspension. Higher temperatures notably affect the concentrations of Fe, Si and Al dissolved ions, particularly accelerating the release of Fe and Si, especially at 50°C. The corrosion rate shows a clear increase with temperature, highlighting the significant role of thermal energy in driving corrosion processes. Studies have demonstrated that higher temperatures not only affect the solubility of oxygen but

also promote ion transport, facilitating the formation of corrosion products that can influence the overall corrosion process **(Qi et al., 2014)**. Over time, the corrosion rates under static and dynamic conditions were relatively comparable for all iron based materials.

Table 60 *Comparison of results of corrosion layer analysis from the in-situ steel/bentonite interface samples in literature and current study. Abbrevations : Fe-S, (unidentified) FeS compound; goe, goethite; hem, haematite; lep, lepidocrocite; mag, magnetite; mah, maghemite; ma., maximum; n.d., not determined; sid, siderite* ***(Wersin et al., 2023)***.

Experi-ments	Maximum temperature (°C)	Duration (year)	Redox conditions	Average Corrosion rate(µm/a)	Corrosion products	References
IC-A	14	1.7	Anoxic	1.4-3.4	mag, hem	**(Smart et al., 2017)**
	14	2.8	Anoxic	0.9-2.1	mag, hem, Fe-S	**(Reddy, Padovani, Smart, et al., 2021)**
FEBEX	70	18	Mixed	6-11	goe, hem, mag, sid, lep, mah	**(Hadi et al., 2019)**
ABM1	115	2.4	Mixed	5-8	Mag, hem, sid, goe, lep	**(Wersin et al., 2015)**
ABM2	130	5.5	Mixed	n.d.	Mag, sid	**(Kaufhold et al., 2017; Wersin et al., 2021b)**
This study	25, 50	0.5, 1	Anoxic	2-6, 4-18	mag, hem ,green rust, Fe-hydroxide, Fe-silicate, Fe-S	/

Overall, the findings demonstrate that bentonite based systems effectively mitigate corrosion and which could limit radionuclide mobility, supporting the long-term stability of iron based materials (SGI and steel alloys) in geological disposal environments. Overall, corrosion rates and most of corrosion products obtained in this study for all candidate canister materials were comparable with in situ experiments and literature data **(Wersin et al., 2023)** as shown above in (***Table60***).

4. Conclusions and Outlook

This PhD thesis addresses the corrosion behavior of three iron-based and one copper-based candidate canister materials in contact with bentonite under anoxic and water saturated conditions. Note, however, that under given experimental conditions even when working under inert gas atmosphere, traces of oxygen may still be present at least initially. The corrosion behavior of these materials has been systematically evaluated using static and dynamic batch experiments at room (25°C) and elevated temperature (50°C) for three, six and nine months. The corrosion rate is determined for the selected materials and a special attention is given to understanding in detail the corrosion mechanism from the identification of corrosion products formed under the applied conditions and to unravel the effect of specific experimental parameters on the corrosion behavior of these materials in bentonite environment.

For the cupronickel alloy a special attention is given to the effect of added sulfide on the corrosion behavior, for the cast iron the effect of added ferric compound mimicking the presence of oxic phase corrosion products on the anoxic corrosion behavior was investigated, and for both other materials (spring steel and carbon steel) the effect of surface roughness (i.e., scratch) was of interest. Furthermore, the effect of bentonite chemistry on carbon steel corrosion was investigated by performing parallel experiments with an additional bentonite (GMZ). All experiments were performed with synthetic Grimsel groundwater and MX-80 was the generally used bentonite to allow comparison with in-situ experiments at the Grimsel Test Site. Due to technical difficulties, the bentonite was not used in compacted form but rather in form of slurry in both static and dynamic batch experiments.

The experimental findings at elevated temperature simulate exemplary the impact of the transient and thermal phase. Effects are:

- The corrosion rate was higher initially in almost all cases, with a tendency to decrease over time.
- The experimental results demonstrate that temperature is the primary driver of corrosion kinetics for all systems (static and dynamic), significantly higher corrosion rates observed at elevated temperatures (50°C) compared to room temperature (25^{o}C).
- Temperature affects the nature and types of corrosion products, formed on steel in contact with bentonite under anoxic, transient and thermal conditions.
- Under such conditions steel corrosion yields magnetite, iron hydroxide, green rust and iron silicate as corrosion products and cupronickel corrosion yields cuprite, nickel hydroxide and copper (I/II) sulfide as corrosion products. The corrosion products formed protective layer reducing further corrosion.

In case of SGI coupons, corrosion processes in presence of initially present oxygen was simulated by addition of hematite which act as a potential oxidant had a measurable but limited influence on corrosion behavior. Measured redox potentials are partly higher in presence of hematite, thus Fe(II)-bearing compounds are not stable. Additionally, graphite inclusions in SGI likely act as

cathodic sites where water is reduced, with the coupled anodic reaction corresponding to preferential ferrite oxidation. Over time, as metallic corrosion progresses, hematite likely converted into mixed Fe(II)/Fe(III) corrosion products (magnetite). A significant enhancement of corrosion rates in presence of hematite could however not be stated.

For Cu-Ni coupons, impact of microbial corrosion was partly simulated by the addition of sulfide in static and dynamic experiments. The presence of added sulfide had no significant effect in static experiments but seems to be effective at elevated temperature in dynamic experiment which was evidenced by formation of Cu_2S/CuS as corrosion products by breaking passive layer of copper oxides and nickel hydroxide. pH, redox potential and corrosion rate are not much affected in presence of sulfide in both system (static and dynamic).

Since a repository is not a closed system, experiments have been performed under dynamic conditions implying water flowing at low rate in order to mimic the intrusion of groundwater. Such conditions simulate partly a scenario where bentonite is eroding and low mineralized groundwater accesses the metal surface. Dynamic system showed reduced secondary phase formation compared to static system due to continuous groundwater flow removing soluble products and inhibiting layer buildup affecting corrosion behavior.

Iron corrosion in bentonite clay lead to form magnetite, green rust and mostly silicate based corrosion products at metal/bentonite interface under anoxic conditions. Alteration of bentonite (Reduction of Fe (III)) and color change was observed after corrosion experiments. Identification of admixed corrosion products (berthierine, green rust, magnetite and chukanovite) on altered bentonite was evidenced by XAS (XANES) analysis and change in elemental composition of altered bentonite was evidenced by acid digestion and ICP-MS analysis.

These corrosion products formed due to bentonite alteration can buffer Fe^{2+} ion concentrations at the steel/bentonite surface and act as a driver for Fe^{2+} diffusion and sorption on clay. Overall amalgamation of iron into bentonite alteration products could act as a pump to accelerate corrosion **(Savage et al., 2010)**. However, pump effect was not much affected in this study may be due to short-term nature of laboratory experiments.

The analysis of dissolved metal ions (Fe, Ni and Cu) in the solution shows that concentrations remained pretty low (E-6 mol/L) across all conditions, typically below those assumed for the solubility of $Fe(OH)_2$, $Ni(OH)_2$ or Cu-oxides, suggesting strong retention by bentonite through surface sorption and/or mixed secondary phase formation.

The in-situ measured pH does not change much for all material coupons for static experiments. pH slightly decreases at elevated temperature compared to room temperature for most of the coupons. The pH in dynamic experiments increases with time and evolves towards inlet groundwater (pH 9.8) for all material coupons indicating moderate alkaline conditions. The redox potential (E_h) for all iron based candidate canister materials was negative indicating reducing conditions hinting at the formation of Fe(II)-bearing secondary phases which can remain stable under anoxic conditions. Redox potentials (E_h) in experiments with cupronickel coupons remained positive even with added sulfide in static conditions and lie in the stability region of metallic copper based on the Pourbaix diagram (**Figure 3**) in dynamic conditions.

The corrosion rate of cupronickel coupons was lower at room temperature (25°C) in the range 0.1-0.2 µm/a compared to elevated temperature (50°C) for 270 days. The obtained corrosion rates are comparable with in-situ Grimsel experiments in which copper in the range 0.1-0.3 µm/a for 394 days. Residual oxygen plays an important role in increasing corrosion rate initially during exposure. For the same materials the corrosion rate in dynamic experiments are comparable with static experiments, little differences observed are within experimental uncertainty ranges.

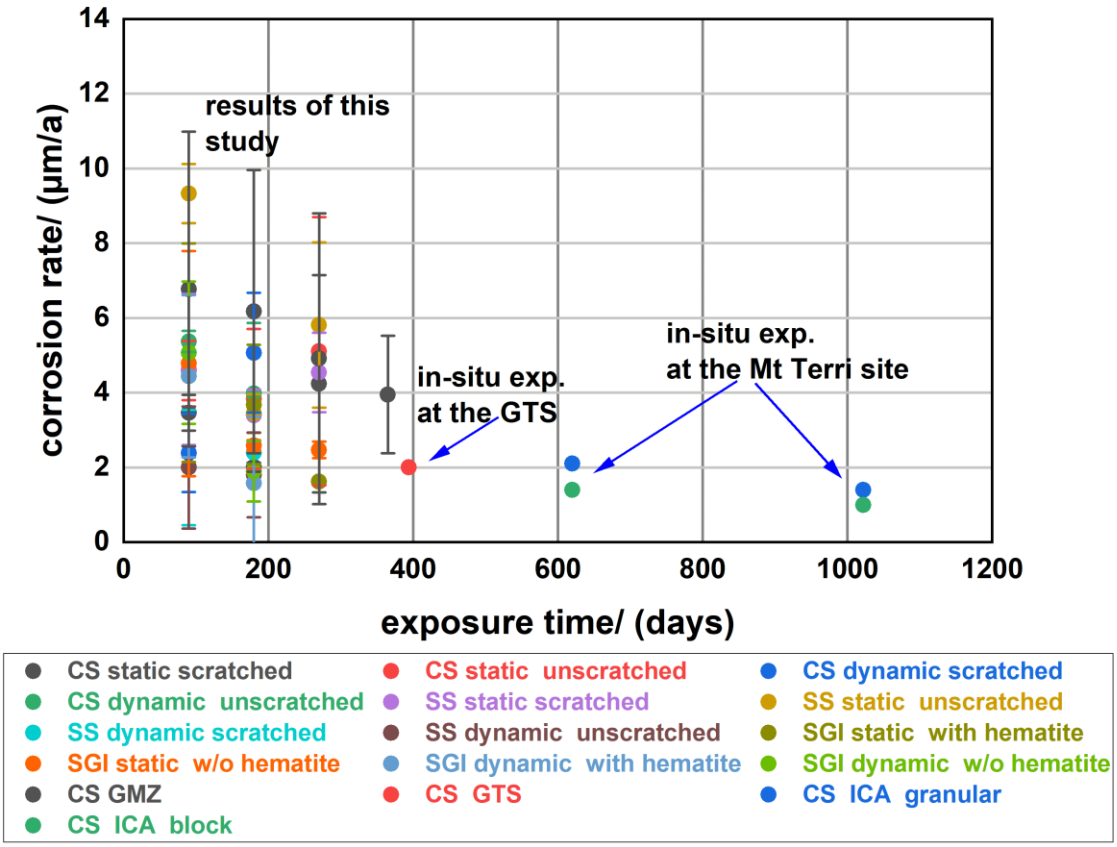

Figure 81 *Comparison of corrosion rates results from this study with the in-situ literature data.*

At room temperature (25°C), the corrosion rate of the selected iron based candidate materials (carbon steel, spheroidal graphite iron and spring steel) in this study was shown for 365 days at maximum. The corrosion rate data obtained in this study represent rather an initial "transient" phase. Overall, it is visible from present studies, that corrosion rates decrease with time and moving towards the corrosion rate data found in in-situ studies.

Initial corrosion rates of the present work are in general higher than those found in in-situ experiments after longer observation time scales. In experiments described in literature **(Wersin et al., 2023)**, corrosion rates are found to be higher in experiments with granular bentonite than with compacted material, where the water volume access is limited by diffusion. Present

experiments described in this thesis might therefore result in somewhat higher corrosion rate as no water access limitations exist.

At elevated temperatures (50°C), the corrosion rates of iron based materials (carbon steel, spheroidal graphite iron and spring steel) were significantly higher in the range ~ 4-18 µm/a with experimental data scattering. The impact of scratches at the surface or the presence of hematite did not have a significant impact. Corrosion rate of carbon steel in MX-80 and GMZ bentonite were quite comparable. Overall, the corrosion rate increases with temperature and decreases with time in most of the cases. Corrosion rates in the present study in presence of bentonite are not really enhanced in comparison to those in absence of bentonite **(Féron et al., 2008**) .

In the present study, under the prevailing pH and E_h conditions, the nature of the detected corrosion products in CuNi alloy corrosion experiments agree with the reported Pourbaix diagrams **(Puigdomenech & Taxén, 2000)**. Formation of secondary phases like cuprite (Cu_2O), copper sulfide (Cu_2S) and nickel hydroxide ($Ni(OH)_2$) was evidenced by SEM-EDXS, XRD and XPS analysis of CuNi coupons. During the long-term evolution under repository conditions, it can be attributed that once the protective film of nickel hydroxide and copper oxide breaks by reacting with dissolved sulfide, it leads to degradation of CuNi alloy and form copper sulfide as corrosion products.

For iron-based materials (carbon steel, spheroidal graphite iron and spring steel) advanced surface and bulk characterization techniques (SEM-EDXS, XRD, XPS) confirmed the formation of corrosion products like iron (hydr)oxides, iron silicates, green rust (sulfate based), and in some cases, iron sulfides. The formation of mixed Fe(II)/Fe(III) phases and iron silicates indicates that steel corrosion not only affects the metal surface but also alters the surrounding bentonite matrix through redox reactions and dissolution and re-precipitation mechanisms.

Comparative analysis between MX-80 and GMZ bentonites revealed that while both clays buffered pH and maintained reducing conditions effectively, GMZ bentonite supported more uniform and protective corrosion product formation, particularly for carbon steel. This is attributed to its mineralogical composition and possibly lower pyrite content compared to MX-80 bentonite, which exhibited greater variability in corrosion behavior.

It may be implied from the observed results that change in the surface roughness due to scratches, which can occur during canister handling, will not affect significantly the corrosion behavior of candidate canister materials (carbon steel and spring steel). In all experiments, the main corrosion products were identified, being very diverse and highly dependent on the specific material, experimental parameters and environmental conditions. Overall, obtained corrosion rates and most of corrosion products for all materials used in this study were comparable with in situ experiments (MaCoTe) **(Reddy, Padovani, Rance, et al., 2021)** and literature data **(Wersin et al., 2023)**. No significant difference was observed between static and dynamic experiments.

The current research was based on 12 months duration at maximum and under controlled experimental conditions due to technical difficulties that may not fully reflect long-term corrosion behavior in real geological environments. The results, based on short-term observations in simulated anoxic, water-saturated bentonite environments, may not capture the influence of

varying factors like pressure, temperature fluctuations, the chemical composition of ground/porewater found in actual geological sites and most importantly, long-term kinetics in all involved reactions.

Information about formation of long-term stable corrosion products can be provided by geochemical modeling using experimental findings from short-term experiments as starting points of modeling. Although few studies are available but still, there was lack of detailed study in this direction (geochemical modeling). Additionally, the study simplified bentonite composition but excluded actual microbial impacts (which however more or less excluded in compacted bentonite environment) and irradiation (experiments at elevated temperature with radioactive source for gamma rays), which can significantly affect corrosion.

Future studies could focus more specifically on predictive modeling of the long-term evolution periods, particularly in the context of deep geological repository considering corrosion mechanism and products (metallurgical modifications) forming in the short to long term in account. Future research should explore the behavior of alternative container materials, including their cost-effectiveness and suitability for use in nuclear waste containment systems.

Focusing only on steel and copper, the research didn't assess other materials (relevant titanium alloys and alloy steel) in context with bentonite environment including their mechanisms, limiting the broader applicability (weld susceptibility, stress and pressure) and depth of the findings. Overall, while cupronickel has demonstrated superior corrosion resistance in the studied conditions, ongoing research into long-term effects, microbial influence, alternative materials, and protective strategies will be essential to ensure the safety and stability of materials used in nuclear waste disposal systems for million years.

Corrosion rate slowing down due to the formation of a protective layer (iron silicate) with time in the presence of bentonite was observed. Bentonite can act as buffer material (buffering pH and corrosion products) for nuclear waste disposal. Secondary phases formed due to corrosion process have an impact on the corrosion behavior of the candidate materials on long term, as observed by the decrease of the corrosion rate. These secondary phases can also sorb radionuclides thus prevent their migration to biosphere in long term. Thus, secondary phases found in corrosion studies should be used for radionuclides uptake studies.

Overall, the outcome of thesis give idea about the repository near-field environment after corrosion has taken place. The formation of secondary corrosion phases will have possible impact on the porosity of the geotechnical or geological barrier and which modify mineralogy in this area. Both could influence radionuclide migration/retention in the repository near field.

References

"Alexander, W. R., "Frieg, B., & "Ota, K. (2009). Grimsel test site investigation Phase IV. The Nagra-JAEA in situ study of safety relevant radionuclide retardation in fractured crystalline rock. III: The RRP project final report.

Alzamel, M., Fall, M., & Haruna, S. (2022). Swelling ability and behaviour of bentonite-based materials for deep repository engineered barrier systems: Influence of physical, chemical and thermal factors. Journal of Rock Mechanics and Geotechnical Engineering, 14(3), 689-702. https://doi.org/https://doi.org/10.1016/j.jrmge.2021.11.009

Aromaa, J. K., Muhammad Kamran ; Aji, Arif Tirto et al. (2021). Corrosion rate of copper canisters used for final disposal of nuclear waste, in synthetic ground water and bentonite clay pore water. Current Topics in Electrochemistry, 23, 81-96.

Attinger, R. O., Knecht, B., Mercier, O., Rosselet, A., & Simpson, J. P. (1991). Residual stresses and stress corrosion effects in cast steel nuclear waste overpacks. Nuclear Engineering and Design, 129(1), 89-99. https://doi.org/https://doi.org/10.1016/0029-5493(91)90330-K

Bailey, S. W. (1988). Structures and compositions of other trioctahedral 1:1 phyllosilicates. Reviews in Mineralogy and Geochemistry, 19(1), 169-188.

Bard, A. J., & Faulkner, L. R. (2012). Electrochemical Methods: Fundamentals and Applications. Wiley. https://books.google.de/books?id=hQocAAAAQBAJ

Barry, P. H. (1994). JPCalc, a software package for calculating liquid junction potential corrections in patch-clamp, intracellular, epithelial and bilayer measurements and for correcting junction potential measurements. Journal of Neuroscience Methods, 51(1), 107-116. https://doi.org/https://doi.org/10.1016/0165-0270(94)90031-0

Bayol, E., Kayakırılmaz, K., & Erbil, M. (2007). The inhibitive effect of hexamethylenetetramine on the acid corrosion of steel. Materials Chemistry and Physics, 104(1), 74-82. https://doi.org/https://doi.org/10.1016/j.matchemphys.2007.02.073

Biesinger, M. C. (2017). Advanced analysis of copper X-ray photoelectron spectra. Surface and Interface Analysis, 49(13), 1325-1334. https://doi.org/https://doi.org/10.1002/sia.6239

Binns, W. J., Behazin, M., Briggs, S., & Keech, P. G. (2023). An overview of the Canadian nuclear waste corrosion program. Materials and Corrosion, 74(11-12), 1580-1586. https://doi.org/https://doi.org/10.1002/maco.202313763

Birgersson, M., & Karnland, O. (2009). Ion equilibrium between montmorillonite interlayer space and an external solution—Consequences for diffusional transport. Geochimica et Cosmochimica Acta, 73(7), 1908-1923. https://doi.org/https://doi.org/10.1016/j.gca.2008.11.027

Bourdelle, F., Mosser-Ruck, R., Truche, L., Lorgeoux, C., Pignatelli, I., & Michau, N. (2017). A new view on iron-claystone interactions under hydrothermal conditions (90°C) by monitoring in situ pH evolution and H2 generation. Chemical Geology, 466, 600-607. https://doi.org/https://doi.org/10.1016/j.chemgeo.2017.07.009

Boyle, C. H., & Meguid, S. A. (2015). Mechanical performance of integrally bonded copper coatings for the long term disposal of used nuclear fuel. Nuclear Engineering and Design, 293, 403-412. https://doi.org/https://doi.org/10.1016/j.nucengdes.2015.08.011

Bracke, G., & Fischer-Appelt, K. (2015). Methodological approach to a safety analysis of radioactive waste disposal in rock salt: An example. Progress in Nuclear Energy, 84, 79-88.

Briggs, S., Lilja, C., & King, F. (2021). Probabilistic model for pitting of copper canisters. Materials and Corrosion, 72(1-2), 308-316. https://doi.org/https://doi.org/10.1002/maco.202011784

Brindley, G. (1982). Chemical compositions of berthierines—A review. Clays and Clay Minerals, 30(2), 153-155.

Cabrera, V., López-Vizcaíno, R., Yustres, Á., & Navarro, V. (2024). Reactive transport model for bentonites in COMSOL multiphysics: Benchmark and validation exercise. Chemosphere, 350, 141050. https://doi.org/10.1016/j.chemosphere.2023.141050

Chaparro, M. C., Finck, N., Metz, V., & Geckeis, H. (2021). Reactive Transport Modelling of the Long-Term Interaction between Carbon Steel and MX-80 Bentonite at 25 °C. Minerals, 11(11), 1272. https://www.mdpi.com/2075-163X/11/11/1272

Chen, J., Qin, Z., & Shoesmith, D. W. (2011). Rate controlling reactions for copper corrosion in anaerobic aqueous sulphide solutions. Corrosion Engineering, Science and Technology, 46(2), 138-141. https://doi.org/10.1179/1743278210y.0000000007

Cloet, V., Pekala, M., Smith, P., Wersin, P., & Diomidis, N. (2017). An evaluation of sulphide fluxes in the near field of a HLW repository.

Demers, H., Poirier-Demers, N., Couture, A. R., Joly, D., Guilmain, M., de Jonge, N., & Drouin, D. (2011). Three-dimensional electron microscopy simulation with the CASINO Monte Carlo software. Scanning, 33(3), 135-146. https://doi.org/https://doi.org/10.1002/sca.20262

Dickinson, T., Povey, A. F., & Sherwood, P. M. A. (1977). Dissolution and passivation of nickel. An X-ray photoelectron spectroscopic study [10.1039/F19777300327]. Journal of the Chemical Society, Faraday Transactions 1: Physical Chemistry in Condensed Phases, 73(0), 327-343. https://doi.org/10.1039/F19777300327

Diomidis, N., & Reddy, B. (2021). In situ corrosion of canister materials in bentonite: the IC-A experiment at Mont Terri. Saf. Nucl. Waste Disposal, 1, 89-89. https://doi.org/10.5194/sand-1-89-2021

Drake, H., Hallbeck, L., Pedersen, K., Rosdahl, A., Tullborg, E.-L., Wallin, B., Sandberg, B., & Blomfeldt, T. (2013). Investigation of sulphide production in core-drilled boreholes in Äspö Hard Rock Laboratory. Boreholes KA3110A, KA3385A and KA3105A.

Drissi, S. H., Refait, P., Abdelmoula, M., & Génin, J. M. R. (1995). The preparation and thermodynamic properties of Fe(II)/Fe(III) hydroxide-carbonate (green rust 1); Pourbaix diagram of iron in carbonate-containing aqueous media. Corrosion Science, 37(12), 2025-2041. https://doi.org/https://doi.org/10.1016/0010-938X(95)00096-3

Dunn, D. S., Pan, Y. M., Chiang, K. T., Yang, L., Cragnolino, G. A., & He, X. (2005). The localized corrosion resistance and mechanical properties of alloy 22 waste package outer containers. JOM, 57(1), 49-55. https://doi.org/10.1007/s11837-005-0064-7

Duquette, D. J., Latanision, R. M., Di Bella, C. A. W., & Kirstein, B. E. (2009). Corrosion Issues Related to Disposal of High-Level Nuclear Waste in the Yucca Mountain Repository—Peer Reviewers' Perspective. Corrosion, 65(4), 272-280. https://doi.org/10.5006/1.3319133

Dzene, L., Dutournie, P., Brendle, J., Limousy, L., Le Meins, J.-M., Michelin, L., Vidal, L., Gree, S., Abdelmoula, M., Martin, C., & Michau, N. (2022). Characterization of Iron-Rich Phyllosilicates Formed at Different Fe/Si Ratios. Clays and Clay Minerals, 70(4), 580-594. https://doi.org/10.1007/s42860-022-00204-6

Einfeld, K., & Popp, F. W. (1988). The POLLUX cask system. http://inis.iaea.org/search/search.aspx?orig_q=RN:21037081

El Mendili, Y., Abdelouas, A., Ait Chaou, A., Bardeau, J. F., & Schlegel, M. L. (2014). Carbon steel corrosion in clay-rich environment. Corrosion Science, 88, 56-65. https://doi.org/https://doi.org/10.1016/j.corsci.2014.07.020

Féron, D., Crusset, D., & Gras, J.-M. (2008). Corrosion issues in nuclear waste disposal. Journal of Nuclear Materials, 379(1), 16-23. https://doi.org/https://doi.org/10.1016/j.jnucmat.2008.06.023

Finck, N., Morelová, N., Cakir-Wuttke, P., Polly, R., & Schild, D. (2021). Korrosions- und Sorptionsprozesse an Stahloberflächen bei hohen Temperaturen und Drücken im anaeroben salinaren Milieu (KORSO): Abschlussbericht Teilprojekt B, KIT-INE.

Finck, N., Morelová, N., Schlegel, M. L., Schild, D., Reguer, S., Dardenne, K., & Geckeis, H. (2023). Corrosion of austenitic stainless steel at 90 °C under highly saline and anoxic conditions: A microspectroscopic study. Corrosion Science, 220, 111265. https://doi.org/https://doi.org/10.1016/j.corsci.2023.111265

Francisco, P. C. M., Mitsui, S., Ishidera, T., Tachi, Y., Doi, R., & Shiwaku, H. (2020). Interaction of FeII and Si under anoxic and reducing conditions: Structural characteristics of ferrous silicate co-precipitates. Geochimica et Cosmochimica Acta, 270, 1-20. https://doi.org/https://doi.org/10.1016/j.gca.2019.11.009

Galai, L., Marchetti, L., Miserque, F., Frugier, P., Godon, N., Brackx, E., Remazeilles, C., & Refait, P. (2023). Effect of dissolved Si on the corrosion of iron in deaerated and slightly alkaline solutions (pH ≈ 8.1) at 50 °C. Corrosion Science, 210, 110790. https://doi.org/https://doi.org/10.1016/j.corsci.2022.110790

García-Romero, E., María Manchado, E., Suárez, M., & García-Rivas, J. (2019). Spanish Bentonites: A Review and New Data on Their Geology, Mineralogy, and Crystal Chemistry. Minerals, 9(11), 696. https://www.mdpi.com/2075-163X/9/11/696

Gey, M. (2008). Instrumentelle Analytik und Bioanalytik, 2., überarb. u. erw. Aufl. In: Springer, Berlin.

González-Siso, M. R., Gaona, X., Duro, L., Altmaier, M., & Bruno, J. (2018). Thermodynamic model of Ni (II) solubility, hydrolysis and complex formation with ISA. Radiochimica Acta, 106(1), 31-45.

Guo, X., Gin, S., & Frankel, G. S. (2020). Review of corrosion interactions between different materials relevant to disposal of high-level nuclear waste. npj Materials Degradation, 4(1), 34. https://doi.org/10.1038/s41529-020-00140-7

Guo, X., Lei, P., Mohanty, C., Yao, T., Lian, J., & Frankel, G. S. (2022). Enhanced crevice corrosion of stainless steel 316 by degradation of Cr-containing hollandite crevice former. Corrosion Science, 205, 110462. https://doi.org/https://doi.org/10.1016/j.corsci.2022.110462

Hadi, J., Wersin, P., Serneels, V., & Greneche, J.-M. (2019). Eighteen years of steel–bentonite interaction in the FEBEX in situ test at the Grimsel Test Site in Switzerland. Clays and Clay Minerals, 67(2), 111-131. https://doi.org/10.1007/s42860-019-00012-5

Hedin, A., Johansson, A. J., Lilja, C., Boman, M., Berastegui, P., Berger, R., & Ottosson, M. (2018). Corrosion of copper in pure O2-free water? Corrosion Science, 137, 1-12. https://doi.org/https://doi.org/10.1016/j.corsci.2018.02.008

Henshall, G. A. (1992). Modeling pitting corrosion damage of high-level radioactive-waste containers using a stochastic approach. Journal of Nuclear Materials, 195(1), 109-125. https://doi.org/https://doi.org/10.1016/0022-3115(92)90367-T

Hesketh, J., Haynes, H., Reddy, B., Rance, A., Bevas, C., Padovani, C., & Diomidis, N. (2023). Carbon steel corrosion in a bentonite buffer: A comparison between in situ exposure and lab based experiments. Materials and Corrosion, 74(11-12), 1728-1745. https://doi.org/https://doi.org/10.1002/maco.202313767

Hofstetter, T. B., Sosedova, Y., Gorski, C., Voegelin, A., & Sander, M. (2014). Redox properties of iron-bearing clays and MX-80 bentonite–Electrochemical and spectroscopic characterization.

Hsu, C.-H., & Chen, M.-L. (2010). Corrosion behavior of nickel alloyed and austempered ductile irons in 3.5% sodium chloride. Corrosion Science, 52(9), 2945-2949. https://doi.org/https://doi.org/10.1016/j.corsci.2010.05.006

Hua, F., Pasupathi, P., Brown, N., & Mon, K. (2005). Some Materials Degradation Issues in the U.S. High-Level Nuclear Waste Repository Study (The Yucca Mountain Project). https://www.osti.gov/biblio/840143

Hua, F., Sarver, J., & Mohn, W. (2001). Crevice Corrosion Behavior of Candidate Nuclear Waste Container Materials in Repository Environment. https://www.osti.gov/biblio/840361

Hughes, A. E., Easton, C. D., Gengenbach, T. R., Biesinger, M. C., & Laleh, M. (2024). Interpretation of complex x-ray photoelectron peak shapes. I. Case study of Fe 2p3/2 spectra. Journal of Vacuum Science & Technology A, 42(5). https://doi.org/10.1116/6.0003804

Hung, C.-C., Wu, Y.-C., & King, F. (2017). Corrosion assessment of canister for the disposal of spent nuclear fuel in crystalline rock in Taiwan. Corrosion Engineering, Science and Technology, 52(1_suppl), 194-199. https://doi.org/10.1080/1478422x.2017.1285855

Hunter, F. B., Fiona; Heath, Tim; Hoch, Andrew (2007). Geochemical investigation of iron transport into bentonite as steel corrodes.

Huttunen-Saarivirta, E., Rajala, P., & Carpén, L. (2016). Corrosion behaviour of copper under biotic and abiotic conditions in anoxic ground water: electrochemical study. Electrochimica Acta, 203, 350-365. https://doi.org/https://doi.org/10.1016/j.electacta.2016.01.098

International, A. (2003). G1-03 Standard Practice for Preparing, Cleaning, and Evaluating Corrosion Test Specimens. West Conshohocken, PA; ASTM International https://doi.org/https://doi.org/10.1520/G0001-03

Ishidera, T., Ueno, K., Kurosawa, S., & Suyama, T. (2008). Investigation of montmorillonite alteration and form of iron corrosion products in compacted bentonite in contact with carbon steel for ten years. Physics and Chemistry of the Earth, Parts A/B/C, 33, S269-S275. https://doi.org/https://doi.org/10.1016/j.pce.2008.10.062

Johnson, L., & King, F. (2008). The effect of the evolution of environmental conditions on the corrosion evolutionary path in a repository for spent fuel and high-level waste in Opalinus Clay. Journal of Nuclear Materials, 379(1), 9-15. https://doi.org/https://doi.org/10.1016/j.jnucmat.2008.06.003

Johnson, L. H., & King, F. (2003). Canister options for the disposal of spent fuel (1015-2636). http://inis.iaea.org/search/search.aspx?orig_q=RN:50044662

Jones, A. M., Murphy, C. A., Waite, T. D., & Collins, R. N. (2017). Fe(II) Interactions with Smectites: Temporal Changes in Redox Reactivity and the Formation of Green Rust. Environmental Science & Technology, 51(21), 12573-12582. https://doi.org/10.1021/acs.est.7b01793

"Karnland, O. (2010). Chemical and mineralogical characterization of the bentonite buffer for the acceptance control procedure in a KBS-3 repository.

Karnland O, S. T., Johannesson L-E, Eriksen T E, Jansson M, Wold S, Pedersen K,, & Motamedi M, R. B., 2000. (2000). Long term test of buffer material. Final report on the pilot parcels.SKB TR-00-22, Svensk Kärnbränslehantering AB.

Kaufhold, S., Dohrmann, R., Götze, N., & Svensson, D. (2017). CHARACTERIZATION OF THE SECOND PARCEL OF THE ALTERNATIVE BUFFER MATERIAL (ABM) EXPERIMENT – I MINERALOGICAL REACTIONS. Clays and Clay Minerals, 65(1), 27-41. https://doi.org/10.1346/CCMN.2016.064047

Kaufhold, S., Hassel, A. W., Sanders, D., & Dohrmann, R. (2015). Corrosion of high-level radioactive waste iron-canisters in contact with bentonite. Journal of Hazardous Materials, 285, 464-473. https://doi.org/https://doi.org/10.1016/j.jhazmat.2014.10.056

Kaufhold, S., Klimke, S., Schloemer, S., Alpermann, T., Renz, F., & Dohrmann, R. (2020). About the Corrosion Mechanism of Metal Iron in Contact with Bentonite. ACS Earth and Space Chemistry, 4(5), 711-721. https://doi.org/10.1021/acsearthspacechem.0c00005

Kaufhold, S., Schippers, A., Marx, A., & Dohrmann, R. (2020). SEM study of the early stages of Fe-bentonite corrosion—The role of naturally present reactive silica. Corrosion Science, 171, 108716. https://doi.org/https://doi.org/10.1016/j.corsci.2020.108716

Keech, P. G., Behazin, M., Binns, W. J., & Briggs, S. (2021). An update on the copper corrosion program for the long-term management of used nuclear fuel in Canada. Materials and Corrosion, 72(1-2), 25-31. https://doi.org/https://doi.org/10.1002/maco.202011763

Kesavan, J. K., Luisetto, I., Tuti, S., Meneghini, C., Battocchio, C., & Iucci, G. (2017). Ni supported on YSZ: XAS and XPS characterization and catalytic activity for CO2 methanation. Journal of Materials Science, 52(17), 10331-10340. https://doi.org/10.1007/s10853-017-1179-2

Kiczka, M., Alt-Epping, P., Hadi, J., Wersin, P., Leupin, O. X., & Diomidis, N. (2024). Reactive transport modelling of iron bentonite interaction in the FEBEX in situ experiment. Applied Geochemistry, 170, 106057. https://doi.org/https://doi.org/10.1016/j.apgeochem.2024.106057

King, F. (1995). A natural analogue for the long-term corrosion of copper nuclear waste containers—reanalysis of a study of a bronze cannon. Applied Geochemistry, 10(4), 477-487. https://doi.org/https://doi.org/10.1016/0883-2927(95)00019-G

King, F. (2008). Corrosion of carbon steel under anaerobic conditions in a repository for SF and HLW in Opalinus Clay Technical report 08-12 (1015-2636). http://inis.iaea.org/search/search.aspx?orig_q=RN:41030156

King, F. (2013). Container Materials for the Storage and Disposal of Nuclear Waste. Corrosion, 69(10), 986-1011. https://doi.org/10.5006/0894

King, F., Ahonen, L., Taxen, C., Vuorinen, U., & Werme, L. (2001). Copper corrosion under expected conditions in a deep geologic repository (1404-0344). http://www.ski.se/dynamaster/file_archive/011219/7958921098/01%2d40.pdf

King, F., & Kolar, M. (1997). Corrosion of copper containers prior to saturation of a nuclear fuel waste disposal vault. http://inis.iaea.org/search/search.aspx?orig_q=RN:31010380

King, F., & Kolář, M. (2018). Lifetime Predictions for Nuclear Waste Disposal Containers. Corrosion, 75(3), 309-323. https://doi.org/10.5006/2994

King, F., Kolàř, M., Briggs, S., Behazin, M., Keech, P., & Diomidis, N. (2024). Review of the Modelling of Corrosion Processes and Lifetime Prediction for HLW/SF Containers—Part 2: Performance Assessment Models. Corrosion and Materials Degradation, 5(2), 289-339.

King, F., Lilja, C., Pedersen, K., Vähänen, M., & Pitkänen, P. (2010). An update of the state-of-the-art report on the corrosion of copper under expected conditions in a deep geologic repository.

King, F., Lilja, C., Pedersen, K., Vähänen, M., & Pitkänen, P. (2012). An Update of the State-of-the-art Report on the Corrosion of Copper under Expected Conditions in a Deep Geologic Repository.

King, F., Lilja, C., & Vähänen, M. (2013). Progress in the understanding of the long-term corrosion behaviour of copper canisters. Journal of Nuclear Materials, 438(1), 228-237. https://doi.org/https://doi.org/10.1016/j.jnucmat.2013.02.080

King, F., & Padovani, C. (2011). Review of the corrosion performance of selected canister materials for disposal of UK HLW and/or spent fuel. Corrosion Engineering, Science and Technology, 46(2), 82-90. https://doi.org/10.1179/1743278211y.0000000005

Kirfel, A., & Eichhorn, K. (1990). Accurate structure analysis with synchrotron radiation. The electron density in Al2O3 and Cu2O. Acta Crystallographica Section A, 46(4), 271-284. https://doi.org/https://doi.org/10.1107/S0108767389012596

Kong, D., Dong, C., Xu, A., Man, C., He, C., & Li, X. (2017). Effect of Sulfide Concentration on Copper Corrosion in Anoxic Chloride-Containing Solutions. Journal of Materials Engineering and Performance, 26(4), 1741-1750. https://doi.org/10.1007/s11665-017-2578-x

Kong, M., Lee, M., Kim, G.-Y., Jang, J., & Kim, J.-S. (2023). Characterization of Compacted Ca- and Na-Bentonite with Copper Corrosion Products in the KAERI Underground Research Tunnel. Minerals, 13(7), 898. https://www.mdpi.com/2075-163X/13/7/898

Kosec, T., Qin, Z., Chen, J., Legat, A., & Shoesmith, D. W. (2015). Copper corrosion in bentonite/saline groundwater solution: Effects of solution and bentonite chemistry. Corrosion Science, 90, 248-258. https://doi.org/https://doi.org/10.1016/j.corsci.2014.10.017

Kursten, B., Smailos, E., Azkarate, I., Werme, L., Smart, N., & Santarini, G. (2004). COBECOMA. State of the art document on the Corrosion Behaviour of Container Materials.

Lanson, B., Lantenois, S., van Aken, P. A., Bauer, A., & Plançon, A. (2012). Experimental investigation of smectite interaction with metal iron at 80 °C: Structural characterization of newly formed Fe-rich phyllosilicates. American Mineralogist, 97(5-6), 864-871.

Lantenois, S., Lanson, B., Muller, F., Bauer, A., Jullien, M., & Plançon, A. (2005). Experimental Study of Smectite Interaction with Metal Fe at Low Temperature: 1. Smectite Destabilization. Clays and Clay Minerals, 53(6), 597-612. https://doi.org/10.1346/CCMN.2005.0530606

Larese-Casanova, P., & Scherer, M. M. (2007). Fe(II) sorption on hematite: new insights based on spectroscopic measurements. Environ Sci Technol, 41(2), 471-477. https://doi.org/10.1021/es0617035

Lazo, C., Karnland, O., Tullborg, E.-L., & Puigdomenech, I. (2011). Redox properties of MX-80 and Montigel bentonite-water systems. MRS Online Proceedings Library, 757(1), 81. https://doi.org/10.1557/PROC-757-II8.1

Legrand, D. L., Nesbitt, H. W., & Bancroft, G. M. (1998). X-ray photoelectron spectroscopic study of a pristine millerite (NiS) surface and the effect of air and water oxidation. American Mineralogist, 83(12), 1256-1265. https://doi.org/doi:10.2138/am-1998-1214

Leupin, O. X., Smart, N. R., Zhang, Z., Stefanoni, M., Angst, U., Papafotiou, A., & Diomidis, N. (2021). Anaerobic corrosion of carbon steel in bentonite: An evolving interface. Corrosion Science, 187, 109523. https://doi.org/https://doi.org/10.1016/j.corsci.2021.109523

Liu, T., Tian, X.-F., Zhao, Y., & Gao, T. (2010). Swelling of K+, Na+ and Ca2+-montmorillonites and hydration of interlayer cations: a molecular dynamics simulation. Chinese Physics B, 19(10), 109101. https://doi.org/10.1088/1674-1056/19/10/109101

Macdonald, D., & Lei, X. (2016). Theoretical Interpretation of Anion Size Effects in Passivity Breakdown. Journal of The Electrochemical Society, 163, C738-C744. https://doi.org/10.1149/2.0571613jes

Mani Mathew, P., & Krueger, P. A. (1989). Galvanic Corrosion of Lead Coupled with Titanium for Nuclear Fuel Waste Disposal. Canadian Metallurgical Quarterly, 28(1), 89-99. https://doi.org/10.1179/cmq.1989.28.1.89

Marsh, G. P., Taylor, K. J., Bland, I. D., Westcott, C., Tasker, P. W., & Sharland, S. M. (1986). Evaluation of the localized corrosion of carbon steel overpacks for nuclear waste disposal in granite environments. Materials Research Society Symposia Proceedings, 421-428. http://inis.iaea.org/search/search.aspx?orig_q=RN:17090143

Martin, F. A., Bataillon, C., & Schlegel, M. L. (2008). Corrosion of iron and low alloyed steel within a water saturated brick of clay under anaerobic deep geological disposal conditions: An integrated experiment. Journal of Nuclear Materials, 379(1), 80-90. https://doi.org/https://doi.org/10.1016/j.jnucmat.2008.06.021

Morelová, N., Dardenne, K., Finck, N., Heberling, F., Metz, V., Schild, D., Geckeis, H., & Diomidis, N. (2021). Anaerobic corrosion of carbon steel in compacted bentonite exposed to natural Opalinus clay porewater: Bentonite alteration study. Saf. Nucl. Waste Disposal, 1, 103-104. https://doi.org/10.5194/sand-1-103-2021

Moulder, J. F., & Chastain, J. (1992). Handbook of X-ray Photoelectron Spectroscopy: A Reference Book of Standard Spectra for Identification and Interpretation of XPS Data. Physical Electronics Division, Perkin-Elmer Corporation. https://books.google.de/books?id=A_XGQgAACAAJ

Moulder, J. F., Stickle, W. F., Sobol, W. M., & Bomben, K. D. (1992). Handbook of X-Ray Photoelectron Spectroscopy.

Muhammad, N., & Siddiqua, S. (2022). Calcium bentonite vs sodium bentonite: The potential of calcium bentonite for soil foundation. Materials Today: Proceedings, 48, 822-827. https://doi.org/https://doi.org/10.1016/j.matpr.2021.02.386

Muñoz, A. G., Abdelouas, A., Alonso, U., Fernández, A. M., Bernier-Latmani, R., Cherkouk, A., Gaggiano, R., Hesketh, J., Smart, N., Padovani, C., Mijnendonckx, K., Montoya, V., Idiart, A., Pont, A., Riba, O., Finck, N., Singh, A. R., King, F., & Diomidis, N. (2024). WP15 ConCorD state-of-the-art report (container corrosion under disposal conditions) [Review]. Frontiers in Nuclear Engineering, 3. https://doi.org/10.3389/fnuen.2024.1404739

Nakayama, G., Wakamatsu, H., & Akashi, M. (1992). Effects of Chloride, Bromide, and Thiosulfate Ions on the Critical Conditions for Crevice Corrosion of Several Stainless Alloys as a Material for Geological Disposal Packages for Nuclear Waste. MRS Online Proceedings Library, 294(1), 323-328. https://doi.org/10.1557/PROC-294-323

Ning, Z. a. Z., Qulan and Li, Na and Macdonald, Digby D., . (2024). Influence of Bentonite on Copper Corrosion in Simulated Repository Electrolyte. SSRN. https://doi.org/http://dx.doi.org/10.2139/ssrn.4727765

Nzulu, G., Högberg, H., Eklund, P., Hultman, L., Nude, P., Yaya, A., & Magnuson, M. (2024). Chemical Reactivity and Alteration of Pyrite Mineral in the Kubi Gold Concession in Ghana. Mining, Metallurgy & Exploration, 41. https://doi.org/10.1007/s42461-024-00932-4

Olesik, J. W. (1991). Elemental analysis using icp-oes and icp/ms. Analytical Chemistry, 63(1), 12A-21A.

Padovani, C., King, F., Lilja, C., Féron, D., Necib, S., Crusset, D., Deydier, V., Diomidis, N., Gaggiano, R., Ahn, T., Keech, P. G., Macdonald, D. D., Asano, H., Smart, N., Hall, D. S., Hänninen, H., Engelberg, D., Noël, J. J., & Shoesmith, D. W. (2017). The corrosion behaviour of candidate container materials for the disposal of high-level waste and spent fuel – a summary of the state of the art and opportunities for synergies in future R&D. Corrosion Engineering, Science and Technology, 52(1_suppl), 227-231. https://doi.org/10.1080/1478422x.2017.1356973

Pedersen, K. (2010). Analysis of copper corrosion in compacted bentonite clay as a function of clay density and growth conditions for sulfate-reducing bacteria. Journal of Applied Microbiology, 108(3), 1094-1104. https://doi.org/10.1111/j.1365-2672.2009.04629.x

Pedersen, K., Motamedi, M., Karnland, O., & Sandén, T. (2000). Mixing and sulphate-reducing activity of bacteria in swelling, compacted bentonite clay under high-level radioactive waste repository conditions. Journal of Applied Microbiology, 89(6), 1038-1047. https://doi.org/https://doi.org/10.1046/j.1365-2672.2000.01212.x

Pignatelli, I., Mugnaioli, E., Hybler, J., Mosser-Ruck, R., Cathelineau, M., & Michau, N. (2013). A Multi-Technique Characterization of Cronstedtite Synthesized by Iron-Clay Interaction in a Step-By-Step Cooling Procedure. Clays and Clay Minerals, 61(4), 277-289. https://doi.org/10.1346/CCMN.2013.0610408

Pourbaix, M. (1974). Atlas of Electrochemical Equilibria in Aqueous Solutions. National Association of Corrosion Engineers. https://books.google.de/books?id=QjxRAAAAMAAJ

Puigdomenech, I., & Taxén, C. (2000). Thermodynamic data for copper. Implications for the corrosion of copper under repository conditions.

Qi, Y., Luo, H., Zheng, S., Chen, C., Lv, Z., & Xiong, M. (2014). Effect of Temperature on the Corrosion Behavior of Carbon Steel in Hydrogen Sulphide Environments. International journal of electrochemical science, 9, 2101-2112. https://doi.org/10.1016/S1452-3981(23)07914-2

Ravel, B., & Newville, M. (2005). ATHENA, ARTEMIS, HEPHAESTUS: data analysis for X-ray absorption spectroscopy using IFEFFIT. Journal of Synchrotron Radiation, 12(4), 537-541. https://doi.org/doi:10.1107/S0909049505012719

Reddy, B., Padovani, C., Rance, A. P., Smart, N. R., Cook, A., Haynes, H. M., Milodowski, A. E., Field, L. P., Kemp, S. J., Martin, A., & Diomidis, N. (2021). The anaerobic corrosion of candidate disposal canister materials in compacted bentonite exposed to natural granitic porewater containing native microbial populations. Materials and Corrosion, 72(1-2), 361-382. https://doi.org/https://doi.org/10.1002/maco.202011798

Reddy, B., Padovani, C., Smart, N. R., Rance, A. P., Cook, A., Milodowski, A., Field, L., Kemp, S., & Diomidis, N. (2021). Further results on the in situ anaerobic corrosion of carbon steel and copper in compacted bentonite exposed to natural Opalinus Clay porewater containing native microbial populations. Materials and Corrosion, 72(1-2), 268-281. https://doi.org/https://doi.org/10.1002/maco.202011785

Refait, P., & Génin, J. M. R. (1993). The oxidation of ferrous hydroxide in chloride-containing aqueous media and pourbaix diagrams of green rust one. Corrosion Science, 34(5), 797-819. https://doi.org/https://doi.org/10.1016/0010-938X(93)90101-L

Ritgen, U. (2023). Analytical Chemistry I. Springer Nature.

Rothe, J., Butorin, S., Dardenne, K., Denecke, M. A., Kienzler, B., Löble, M., Metz, V., Seibert, A., Steppert, M., Vitova, T., Walther, C., & Geckeis, H. (2012). The INE-Beamline for actinide science at ANKA. Review of Scientific Instruments, 83(4). https://doi.org/10.1063/1.3700813

Samper, J., Lu, C., & Montenegro, L. (2008). Reactive transport model of interactions of corrosion products and bentonite. Physics and Chemistry of the Earth, Parts A/B/C, 33, S306-S316. https://doi.org/https://doi.org/10.1016/j.pce.2008.10.009

Savage, D., Watson, C., Benbow, S., & Wilson, J. (2010). Modelling iron-bentonite interactions. Applied Clay Science, 47(1), 91-98. https://doi.org/https://doi.org/10.1016/j.clay.2008.03.011

Schlegel, M. L., Martin, C., Brucker, F., Bataillon, C., Blanc, C., Chorro, M., & Jollivet, P. (2016). Alteration of nuclear glass in contact with iron and claystone at 90 °C under anoxic conditions: Characterization of the alteration products after two years of interaction. Applied Geochemistry, 70, 27-42. https://doi.org/https://doi.org/10.1016/j.apgeochem.2016.04.009

Schlegel, M. L., Martin, F., Fenart, M., Blanc, C., Varlet, J., & Foy, E. (2021). Corrosion of carbon steel in clay compact environments at 90 °C: Effect of confined conditions. Corrosion Science, 184, 109368. https://doi.org/https://doi.org/10.1016/j.corsci.2021.109368

Schlegel, M. L., Necib, S., Daumas, S., Labat, M., Blanc, C., Foy, E., & Linard, Y. (2018). Corrosion at the carbon steel-clay borehole water interface under anoxic alkaline and fluctuating temperature conditions. Corrosion Science, 136, 70-90. https://doi.org/https://doi.org/10.1016/j.corsci.2018.02.052

Scientific, T. F. (2020). Comparison of ICP-OES and ICP-MS for Trace Element Analysis. ThermoFisher Scientific.

Senior, N. A., Newman, R. C., Artymowicz, D., Binns, W. J., Keech, P. G., & Hall, D. S. (2019). Communication—A Method to Measure Extremely Low Corrosion Rates of Copper Metal in Anoxic Aqueous Media. Journal of The Electrochemical Society, 166(11), C3015. https://doi.org/10.1149/2.0031911jes

Seyama, H., & Soma, M. (1987). Fe 2p spectra of silicate minerals. Journal of Electron Spectroscopy and Related Phenomena, 42(1), 97-101. https://doi.org/https://doi.org/10.1016/0368-2048(87)85010-7

Shao, H., Wang, J., Schäfer, T., Zhang, C.-L., Geckeis, H., Nagel, T., Düsterloh, U., Kolditz, O., & Shao, H. (2024). Introduction. In H. Shao, J. Wang, T. Schäfer, C.-L. Zhang, H. Geckeis, T. Nagel, U. Düsterloh, O. Kolditz, & H. Shao (Eds.), Thermo-Hydro-Mechanical-Chemical (THMC) Processes in Bentonite Barrier Systems (pp. 1-4). Springer Nature Switzerland. https://doi.org/10.1007/978-3-031-53204-7_1

Shoesmith, D. W. (2006). Assessing the Corrosion Performance of High-Level Nuclear Waste Containers. Corrosion, 62(8), 703-722. https://doi.org/10.5006/1.3278296

Shoesmith, D. W., Hocking, W. H., Ikeda, B. M., King, F., Noël, J. J., & Sunder, S. (1997). Application of electrochemical methods in the development of models for fuel dissolution and container corrosion under nuclear waste disposal conditions. Canadian Journal of Chemistry, 75(11), 1566-1584. https://doi.org/10.1139/v97-188

Siudyga, T., Kapkowski, M., Janas, D., Wasiak, T., Sitko, R., Zubko, M., Szade, J., Balin, K., Klimontko, J., Lach, D., Popiel, J., Smoliński, A., & Polanski, J. (2020). Nano-Ru Supported on Ni Nanowires for Low-Temperature Carbon Dioxide Methanation. Catalysts, 10, 513. https://doi.org/10.3390/catal10050513

Smailos, E., & Kienzler, B. (2005). Galvanic Corrosion Between the Nuclear Waste Disposal Container Material Pairs of Copper-Nickel Alloys and Carbon Steel in Salt Brines. Corrosion, 61(3), 230-236. https://doi.org/10.5006/1.3280632

Smart, N., Blackwood, D., Marsh, G., Naish, C., O'Brien, T., Rance, A., & Thomas, M. (2004). The anaerobic corrosion of carbon and stainless steels in simulated cementitious repository environments: a summary review of Nirex research. AEAT/Erra-0313, AEA Technology, Harwell, United Kingdom.

Smart, N. R., Blackwood, D. J., & Werme, L. (2001). The anaerobic corrosion of carbon steel and cast iron in artificial groundwaters (1404-0344). http://www.skb.se/uploads/pdf/TR-01-22.pdfhttp://inis.iaea.org/search/search.aspx?orig_q=RN:32056044

Smart, N. R., Blackwood, D. J., & Werme, L. (2002a). Anaerobic Corrosion of Carbon Steel and Cast Iron in Artificial Groundwaters: Part 1—Electrochemical Aspects. Corrosion, 58(7), 547-559. https://doi.org/10.5006/1.3277646

Smart, N. R., Blackwood, D. J., & Werme, L. (2002b). Anaerobic Corrosion of Carbon Steel and Cast Iron in Artificial Groundwaters: Part 2—Gas Generation. Corrosion, 58(8), 627-637. https://doi.org/10.5006/1.3287691

"Smart, N. R., "Fennell, P. A. H., "Rance, A. P., & "Werme, L. O. (2004). Galvanic corrosion of copper-cast iron couples in relation to the Swedish radioactive waste canister concept. ; Societe de Chimie Industrielle (SCI), 28 Rue Saint Dominique, F-75007 Paris (France). https://doi.org/https://doi.org/ TRN: FR0503886105077 FRN

Smart, N. R., Rance, A. P., & Werme, L. O. (2003). Anaerobic Corrosion of Steel in Bentonite. MRS Online Proceedings Library, 807(1), 660-665. https://doi.org/10.1557/PROC-807-441

Smart, N. R., Reddy, B., Rance, A. P., Nixon, D. J., Frutschi, M., Bernier-Latmani, R., & Diomidis, N. (2017). The anaerobic corrosion of carbon steel in compacted bentonite exposed to natural Opalinus Clay porewater containing native microbial populations. Corrosion Engineering, Science and Technology, 52(1_suppl), 101-112. https://doi.org/10.1080/1478422x.2017.1315233

Smith, J. M., Wren, J. C., Odziemkowski, M., & Shoesmith, D. W. (2007). The Electrochemical Response of Preoxidized Copper in Aqueous Sulfide Solutions. Journal of The Electrochemical Society, 154(8), C431. https://doi.org/10.1149/1.2745647

Soltermann, D., Baeyens, B., Bradbury, M. H., & Fernandes, M. M. (2014). Fe(II) Uptake on Natural Montmorillonites. II. Surface Complexation Modeling. Environmental Science & Technology, 48(15), 8698-8705. https://doi.org/10.1021/es501902f

Stoulil, J., Pavlova, L., & Kouřil, M. (2021). LOCALISED CORROSION OF STAINLESS STEELS 316L AND 2205 IN SYNTHETIC BENTONITE PORE WATER AND BENTONITE SLURRY. Acta Metallurgica Slovaca, 25(1), 24-32. https://doi.org/10.36547/ams.25.1.4

Stroes-Gascoyne, S. (2010). Microbial occurrence in bentonite-based buffer, backfill and sealing materials from large-scale experiments at AECL's Underground Research Laboratory. Applied Clay Science, 47(1), 36-42. https://doi.org/https://doi.org/10.1016/j.clay.2008.07.022

Stucki, J. W. (2011). A review of the effects of iron redox cycles on smectite properties. Comptes Rendus Geoscience, 343(2), 199-209. https://doi.org/https://doi.org/10.1016/j.crte.2010.10.008

Syrett, B. C. (1981). The mechanism of accelerated corrosion of copper-nickel alloys in sulphide-polluted seawater. Corrosion Science, 21(3), 187-209. https://doi.org/https://doi.org/10.1016/0010-938X(81)90030-5

Tully, C., Zagidulin, D., Binns, W., & Noel, J. (2020). (Invited) Effect of Bentonite Dry Density on Corrosion of Embedded Copper. ECS Meeting Abstracts, MA2020-02, 1284-1284. https://doi.org/10.1149/MA2020-02121284mtgabs

Van Iseghem, P. (2012). 26 - Corrosion issues of radioactive waste packages in geological disposal systems. In D. Féron (Ed.), Nuclear Corrosion Science and Engineering (pp. 939-987). Woodhead Publishing. https://doi.org/https://doi.org/10.1533/9780857095343.6.939

Wang, X., Xiao, W., Wang, J., Jones, A. M., & Collins, R. N. (2023). The formation of sulfate-green rust through Fe(II) sorption to montmorillonite: Impacts on abiotic nitrate reduction. Science of The Total Environment, 868, 161496. https://doi.org/https://doi.org/10.1016/j.scitotenv.2023.161496

Wei, X., Dong, J., Chen, N., Yadav, A. P., Ren, Q., Wei, J., Wang, C., Ma, R., & Ke, W. (2021). Effects of bentonite content on the corrosion evolution of low carbon steel in simulated geological disposal environment. Journal of Materials Science & Technology, 66, 46-56. https://doi.org/https://doi.org/10.1016/j.jmst.2020.04.071

Wei, X., Dong, J., & Ke, W. (2021). Progress on a corrosion study of low carbon steel for HLW container in a simulated geological disposal environment in China. Corrosion Communications, 1, 10-17. https://doi.org/https://doi.org/10.1016/j.corcom.2021.05.002

Wersin, P., Hadi, J., Jenni, A., Svensson, D., Grenèche, J.-M., Sellin, P., & Leupin, O. X. (2021a). Interaction of Corroding Iron with Eight Bentonites in the Alternative Buffer Materials Field Experiment (ABM2). Minerals, 11(8), 907. https://www.mdpi.com/2075-163X/11/8/907

Wersin, P., Hadi, J., Jenni, A., Svensson, D., Grenèche, J.-M., Sellin, P., & Leupin, O. X. (2021b). Interaction of Corroding Iron with Eight Bentonites in the Alternative Buffer Materials Field Experiment (ABM2). Minerals, 11(8).

Wersin, P., Hadi, J., Kiczka, M., Jenni, A., Grenèche, J.-M., Diomidis, N., Leupin, O. X., Svensson, D., Sellin, P., Reddy, B., Smart, N., & Zhang, Z. (2023). Unravelling the corrosion processes at steel/bentonite interfaces in in situ tests. Materials and Corrosion, 74(11-12), 1716-1727. https://doi.org/https://doi.org/10.1002/maco.202313755

Wersin, P., Jenni, A., & Mäder, U. K. (2015). Interaction of Corroding Iron with Bentonite in the ABM1 Experiment at Äspö, Sweden: A Microscopic Approach. Clays and Clay Minerals, 63(1), 51-68. https://doi.org/10.1346/CCMN.2015.0630105

Wersin, P., Spahiu, K., & Bruno, J. (1994). Kinetic modelling of bentonite-canister interaction Long-term predictions of copper canister corrosion under oxic and anoxic conditions (0284-3757). http://inis.iaea.org/search/search.aspx?orig_q=RN:26040358

Williams, A. G. B., & Scherer, M. M. (2004). Spectroscopic Evidence for Fe(II)−Fe(III) Electron Transfer at the Iron Oxide−Water Interface. Environmental Science & Technology, 38(18), 4782-4790. https://doi.org/10.1021/es049373g

Yalçıntaş, E., Gaona, X., Scheinost, A. C., Kobayashi, T., Altmaier, M., & Geckeis, H. (2015). Redox chemistry of Tc(VII)/Tc(IV) in dilute to concentrated NaCl and MgCl2 solutions. Radiochimica Acta, 103(1), 57-72. https://doi.org/doi:10.1515/ract-2014-2272

Yoo, M., Choi, H.-j., Lee, M.-s., & Lee, S.-y. (2016). Measurement of Properties of Domestic Bentonite for a Buffer of an HLW Repository. Journal of Nuclear Fuel Cycle and Waste Technology (JNFCWT), 14(2), 135-147.

Yun, T. H., Kim, T., Kim, S., & Kim, J. (2024). Investigation of Corrosion Behavior of Oxygen-Free Copper Canisters in Groundwater Chemistry of Deep Geological Repositories. Materials, 17(1), 74. https://www.mdpi.com/1996-1944/17/1/74

Zhang-Gang, Y., Jun-hua, D., Wei, K., & Nan, C. (2012). EFFECTS OF HCO3- AND SO42- ON THE PITTING CORROSION BEHAVIOR OF Cu. Acta Metallurgica Sinica, 48, 85-93.

Zhang, F., Örnek, C., Liu, M., Müller, T., Lienert, U., Ratia-Hanby, V., Carpén, L., Isotahdon, E., & Pan, J. (2021). Corrosion-induced microstructure degradation of copper in sulfide-containing simulated anoxic groundwater studied by synchrotron high-energy X-ray diffraction and ab-initio density functional theory calculation. Corrosion Science, 184, 109390. https://doi.org/https://doi.org/10.1016/j.corsci.2021.109390

Zhang, Q., Jiang, Y., Zhao, X., Duan, J., Chen, L., & Xu, Y. (2023). A new research proposal to prevent hydrogen embrittlement for nuclear waste container by bacteria-a mini review

[Mini Review]. Frontiers in Microbiology, Volume 14 - 2023. https://www.frontiersin.org/journals/microbiology/articles/10.3389/fmicb.2023.1304703

Zhao, G., Zhang, H., Fan, Q., Ren, X., Li, J., Chen, Y., & Wang, X. (2010). Sorption of copper(II) onto super-adsorbent of bentonite–polyacrylamide composites. Journal of Hazardous Materials, 173(1), 661-668. https://doi.org/https://doi.org/10.1016/j.jhazmat.2009.08.135

Zhu, T., Wang, L., Sun, W., Yang, Z., Wang, S., Zhao, L., Xiao, G., Wang, G., Liu, Z., Shu, X., & Liu, G. (2019). Local scaling of CaCO3 on carbon steel surface with different corrosion types. Powder Technology, 356, 990-1000. https://doi.org/https://doi.org/10.1016/j.powtec.2019.09.021

Appendices

Design of corrosion batch experiments under static and dynamic conditions

Table A 1 *Design of experiment at 25°C and 50°C under static conditions for three, six, nine and twelve months.*

Static Experiments	Material	Condition	T/(°C)	Exposure
CuNi-1S3	Cu-Ni alloy	50ml MX-80 slurry	25	3 months
CuNi-2S3	Cu-Ni alloy	50ml MX-80 slurry	50	3 months
CuNi-3S3	Cu-Ni alloy	50ml MX-80 slurry with 3µM sulfide	25	3 months
Cu-Ni-4S3	Cu-Ni alloy	50ml MX-80 slurry with 3µM sulfide	50	3 months
SGI-5S3	Spheroidal Graphite Iron	50ml MX-80 slurry	25	3 months
SGI-6S3	Spheroidal Graphite Iron	50ml MX-80 slurry	50	3 months
SGI-7S3	Spheroidal Graphite Iron	50ml MX-80 slurry with (0.5 wt.%) α-Fe_2O_3	25	3 months
SGI-8S3	Spheroidal Graphite Iron	50ml MX-80 slurry with (0.5 wt.%) α-Fe_2O_3	50	3 months
SS-9S3	Spring steel	50ml MX-80 slurry + unscratched coupons	25	3 months
SS-10S3	Spring steel	50ml MX-80 slurry + unscratched coupons	50	3 months
SS-11S3	Spring steel	50ml MX-80 slurry + scratched coupons	25	3 months
SS-12S3	Spring steel	50ml MX-80 slurry + scratched coupons	50	3 months
CS-13S3	Construction steel	50ml MX-80 slurry + unscratched coupons	25	3 months
CS-14S3	Construction steel	50ml MX-80 slurry + unscratched coupons	50	3 months
CS-15S3	Construction steel	50ml MX-80 slurry + scratched coupons	25	3 months
CS-16S3	Construction steel	50ml MX-80 slurry + scratched coupons	50	3 months
T1-S3	Without coupon	50ml MX-80 slurry	25	3 months
T2-S3	Without coupon	50ml MX-80 slurry	50	3 months
CuNi-1S6	Cu-Ni alloy	50ml MX-80 slurry	25	6 months
CuNi-2S6	Cu-Ni alloy	50ml MX-80 slurry	50	6 months
CuNi-3S6	Cu-Ni alloy	50ml MX-80 slurry with 3µM sulfide	25	6 months
Cu-Ni-4S6	Cu-Ni alloy	50ml MX-80 slurry with 3µM sulfide	50	6 months
SGI-5S6	Spheroidal Graphite Iron	50ml MX-80 slurry	25	6 months

SGI-6S6	Spheroidal Graphite Iron	50ml MX-80 slurry	50	6 months
SGI-7S6	Spheroidal Graphite Iron	50ml MX-80 slurry with (0.5 wt.%) α-Fe_2O_3	25	6 months
SGI-8S6	Spheroidal Graphite Iron	50ml MX-80 slurry with (0.5 wt.%) α-Fe_2O_3	50	6months
SS-9S6	Spring steel	50ml MX-80 slurry + unscratched coupons	25	6 months
SS-10S6	Spring steel	50ml MX-80 slurry + unscratched coupons	50	6 months
SS-11S6	Spring steel	50ml MX-80 slurry + scratched coupons	25	6 months
SS-12S6	Spring steel	50ml MX-80 slurry + scratched coupons	50	6 months
CS-13S6	Construction steel	50ml MX-80 slurry + unscratched coupons	25	6 months
CS-14S6	Construction steel	50ml MX-80 slurry + unscratched coupons	50	6 months
CS-15S6	Construction steel	50ml MX-80 slurry + scratched coupons	25	6 months
CS-16S6	Construction steel	50ml MX-80 slurry + scratched coupons	50	6 months
T1-S6	Without coupon	50ml MX-80 slurry	25	6 months
T2-S6	Without coupon	50ml MX-80 slurry	50	6months
CuNi-1S9	Cu-Ni alloy	50ml MX-80 slurry	25	9months
CuNi-3S9	Cu-Ni alloy	50ml MX-80 slurry with 3μM sulfide	25	9months
SGI-5S9	Spheroidal Graphite Iron	50ml MX-80 slurry	25	9months
SGI-7S9	Spheroidal Graphite Iron	50ml MX-80 slurry with (0.5 wt.%) α-Fe_2O_3	25	9months
SS-9S9	Spring steel	50ml MX-80 slurry + unscratched coupons	25	9months
SS-11S9	Spring steel	50ml MX-80 slurry + scratched coupons	25	9months
CS-13S9	Construction steel	50ml MX-80 slurry + unscratched coupons	25	9months
CS-15S9	Construction steel	50ml MX-80 slurry + scratched coupons	25	9months
T1-S9	Without coupon	50ml MX-80 slurry	25	9months
CS-1GMZ3	Construction steel	50ml GMZ slurry	25	3months
CS-2GMZ3	Construction steel	50ml GMZ slurry	50	3months
CS-3GMZ6	Construction steel	50ml GMZ slurry	25	6 months
CS-4GMZ6	Construction steel	50ml GMZ slurry	50	6 months
CS-5GMZ9	Construction steel	50ml GMZ slurry	25	9months
CS-7GMZ12	Construction steel	50ml GMZ slurry	25	12months

Table A 2 Design of experiment at 25°C and 50°C under dynamic conditions for three and six months.

Dynamic Experiments	Material	Condition	T/(°C)	Exposure
CuNi-1D3	Cu-Ni alloy	3.1 ml MX-80 slurry	25	3 months
CuNi-2D3	Cu-Ni alloy	3.1 ml MX-80 slurry	50	3 months
CuNi-3D3	Cu-Ni alloy	3.1 MX-80 slurry with 1-2-3μM sulfide	25	3 months
CuNi-4D3	Cu-Ni alloy	3.1 MX-80 slurry with 1-2-3μM sulfide	50	3 months
SGI-5D3	Spheroidal Graphite Iron	3.1 ml MX-80 slurry	25	3 months
SGI-6D3	Spheroidal Graphite Iron	3.1 ml MX-80 slurry with (0.5 wt.%) α-Fe_2O_3	25	3 months
SGI-7D3	Spheroidal Graphite Iron	3.1 ml MX-80 slurry with (0.5 wt.%) α-Fe_2O_3	50	3 months
SS-8D3	Spring steel	3.1 ml MX-80 slurry+ unscratched coupons	25	3 months
SS-9D3	Spring steel	3.1 ml MX-80 slurry+ scratched coupons	25	3 months
SS-10D3	Spring steel	3.1 ml MX-80 slurry+ scratched coupons	50	3 months
CS-11D3	Construction steel	3.1 ml MX-80 slurry+ unscratched coupons	25	3 months
CS-12D3	Construction steel	3.1 ml MX-80 slurry+ scratched coupons	25	3 months
CS-13D3	Construction steel	3.1 ml MX-80 slurry+ scratched coupons	50	3 months
T1-D3	Without coupon	3.1 ml MX-80 slurry	25	3 months
T2-D3	Without coupon	3.1 ml MX-80 slurry	50	3 months
CuNi-1D6	Cu-Ni alloy	3.1 ml MX-80 slurry	25	6 months
CuNi-2D6	Cu-Ni alloy	3.1 ml MX-80 slurry	50	6 months
CuNi-3D6	Cu-Ni alloy	3.1 MX-80 slurry with 1-2-3μM sulfide	25	6 months
CuNi-4D6	Cu-Ni alloy	3.1 MX-80 slurry with 1-2-3μM sulfide	50	6 months
SGI-5D6	Spheroidal Graphite Iron	3.1 ml MX-80 slurry	25	6 months
SGI-6D6	Spheroidal Graphite Iron	3.1 ml MX-80 slurry with (0.5 wt.%) α-Fe_2O_3	25	6 months
SGI-7D6	Spheroidal Graphite Iron	3.1 ml MX-80 slurry with (0.5 wt.%) α-Fe_2O_3	50	6 months
SS-8D6	Spring steel	3.1 ml MX-80 slurry+ unscratched coupons	25	6 months
SS-9D6	Spring steel	3.1 ml MX-80 slurry+ scratched coupons	25	6 months
SS-10D6	Spring steel	3.1 ml MX-80 slurry+ scratched coupons	50	6 months

CS-11D6	Construction steel	3.1 ml MX-80 slurry+ unscratched coupons	25	6months
CS-12D6	Construction steel	3.1 ml MX-80 slurry+ scratched coupons	25	6 months
CS-13D6	Construction steel	3.1 ml MX-80 slurry+ scratched coupons	50	6 months
T1-D6	Without coupon	3.1 ml MX-80 slurry	25	6 months
T2-D6	Without coupon	3.1 ml MX-80 slurry	50	6 months

Overview of buffer solutions used in this work

Table A 3 *Specifications of Buffer solutions used in this work. (910XXX - Catalog Number).*

Buffer	**Formulation**	**pH range (25 ℃)**	**Color**
Orion 910104	Water, Potassium Hydroxide, Potassium Hydrogen Phthalate	4.01 ± 0.01	Pink
Orion 910107	Water, Dibasic, Potassium Dihydrogen Phosphate, ,5-bromo-5-nitro-1,3-Dioxane, Sodium Phosphate	7.00 ± 0.01	Yellow
Orion 910110	Water, SodiumBicarbonate, Methylparaben, Sodium Carbonate	10.01 ± 0.01	Blue

Dissolved cations and anions evolution in pore water (supernatant) after 3, 6 and 9 months – static experiments (CuNi alloy system)

Table A 4 *Dissolved amounts of Na, Ca, K, Mg, F, Cl and SO4 ions in the pore water solutions in contact with Cu-Ni coupons after 3, 6 and 9 months static experiments. Numbers in parentheses correspond to the relative standard deviation in percentage.*

System/ Amounts in µg/L	Na	Ca	K	Mg	F	Cl	SO4
3months 25°C w/o sulfide	618500 (1.8)	11400 (1.0)	41957 (0.8)	2674 (1.7)	1100 (±5)	448400 (±5)	498400 (±5)
3months 50°C w/o sulfide	634600 (2.4)	12100 (0.8)	29220 (1.2)	2394 (1.9)	1100 (±5)	424100 (±5)	594900 (±5)
3months 25°C with 3µM sulfide	580600 (4.0)	8800 (0.3)	30239 (1.8)	2093 (1.6)	1100 (±5)	398500 (±5)	480900 (±5)
3months 50°C with 3µM sulfide	716500 (1.5)	24000 (1.1)	35858 (0.9)	10923 (1.4)	1000 (±5)	651900 (±5)	552600 (±5)
6months 25°C w/o sulfide	617100 (1.3)	12000 (0.9)	37770 (1.2)	2890 (1.8)	1200 (±5)	584200 (±5)	596800 (±5)
6months 50°C w/o sulfide	670900 (2.4)	13900 (0.7)	19080 (64.5)	2380 (0.2)	900 (±5)	568200 (±5)	659100 (±5)
6months 25°C with 3µM sulfide	583200 (1.2)	10000 (3.9)	15440 (2.7)	4290 (1.5)	1200 (±5)	401000 (±5)	479700 (±5)
6months 50°C with 3µM sulfide	753400 (2.7)	18400 (1.4)	30610 (2.4)	3930 (2.3)	1100 (±5)	617000 (±5)	614100 (±5)
9months 25°C w/o sulfide	652100 (3.5)	15400 (0.3)	52152 (1.9)	2515 (1.2)	1000 (±5)	640800 (±5)	640300 (±5)
9months 25°C with 3µM sulfide	632200 (0.1)	14900 (0.9)	55712 (2.0)	3473 (0.7)	1000 (±5)	495800 (±5)	619900 (±5)

Table A 5 *Dissolved amounts of Na, Ca, K, Mg, F, Cl and SO4 ions in the pore water solutions without coupon after 3, 6 and 9 months static experiments. Numbers in parentheses correspond to the relative standard deviation in percentage.*

System/ Amounts in µg/L	Na	Ca	K	Mg	F	Cl	SO4
3months 25°C w/o coupon	601300 (2.9)	9900 (0.6)	31098 (1.2)	1859 (1.9)	11600 (±5)	396900 (±5)	540900 (±5)
3months 50°C w/o coupon	638300 (1.9)	12200 (1.4)	32540 (2.2)	2680 (0.6)	5900 (±5)	418300 (±5)	518400 (±5)
6months 25°C w/o coupon	601300 (1.0)	12200 (0.6)	18290 (1.8)	3010 (0.9)	1200 (±5)	451500 (±5)	545000 (±5)
6months 50°C w/o coupon	704100 (1.3)	15300 (0.7)	21220 (77.4)	3460 (0.1)	1000 (±5)	622300 (±5)	766300 (±5)
9months 25°C w/o coupon	581200 (1.0)	9100 (1.8)	21809 (0.8)	2520 (1.9)	1100 (±5)	392900 (±5)	548800 (±5)

Dissolved cations and anions evolution in ground water (supernatant) after 3 and 6 months – dynamic experiments (CuNi alloy system)

Table A 6 *Dissolved amounts of Na, Ca, K, Mg, F, Cl and SO4 ions in the ground water solutions in contact with Cu-Ni coupons during 3 months dynamic experiments. Numbers in parentheses correspond to the relative standard deviation in percentage.*

25°C w/o sulfide(System)/ Amounts in µg/L	**Na**	**Ca**	**K**	**Mg**	**F**	**Cl**	**SO4**
A (4 weeks)	272700 (2.8)	3600 (3.4)	4157 (4.1)	643 (1.6)	900 (±5)	360600 (±5)	36500 (±5)
B (5 weeks)	273900 (2.4)	2900 (1.2)	3475 (5.8)	441 (1.1)	800 (±5)	339100 (±5)	17200 (±5)
C (6 weeks)	271700 (1.0)	2600 (0.9)	2283 (5.6)	436 (0.3)	800 (±5)	334500 (±5)	14200 (±5)
D (8 weeks)	250900 (2.8)	2800 (1.4)	1844 (1.7)	152 (5.7)	800 (±5)	357200 (±5)	8600 (±5)
E (10 weeks)	288100 (1.7)	3300 (3.0)	1813 (5.0)	168 (5.6)	800 (±5)	404200 (±5)	7400 (±5)
F (12 weeks)	282000 (2.4)	3100 (0.3)	1109 (4.5)	120 (5.4)	900 (±5)	367600 (±5)	6900 (±5)

50°C w/o sulfide(System)/ Amounts in µg/L	**Na**	**Ca**	**K**	**Mg**	**F**	**Cl**	**SO4**
A (4 weeks)	273600 (1.8)	3700 (2.9)	2291 (3.1)	572 (1.2)	800 (±5)	367600 (±5)	21600 (±5)
B (5 weeks)	285900 (3.6)	2900 (2.3)	4065 (2.8)	541 (1.8)	<100	444800 (±5)	27900 (±5)
C (6 weeks)	259600 (3.4)	2500 (1.3)	1637 (8.2)	423 (0.5)	600 (±5)	357000 (±5)	8900 (±5)
D (8 weeks)	267800 (1.1)	2500 (1.2)	1218 (6.4)	139 (3.9)	700 (±5)	328300 (±5)	8100 (±5)
E (10 weeks)	253600 (2.2)	2500 (0.1)	1185 (4.4)	104 (6.4)	700 (±5)	363200 (±5)	7400 (±5)
F (12 weeks)	271100 (2.5)	2500 (1.1)	996 (3.6)	80 (7.7)	<100	288700 (±5)	7100 (±5)
25°C with 1-2-3µM sulfide (System)/ Amounts in µg/L	**Na**	**Ca**	**K**	**Mg**	**F**	**Cl**	**SO4**
A (4 weeks)	301100 (2.7)	3300 (1.5)	6621 (3.6)	790 (1.0)	1000 (±5)	389000 (±5)	53300 (±5)
B (5 weeks)	268500 (5.9)	2200 (4.8)	3304 (3.3)	531 (0.4)	700 (±5)	326700 (±5)	11300 (±5)
C (6 weeks)	262000 (2.5)	2000 (3.1)	2993 (2.1)	494 (1.7)	700 (±5)	332000 (±5)	7700 (±5)
D (8 weeks)	258400 (3.9)	2600 (1.1)	2143 (0.9)	167 (5.2)	700 (±5)	644900 (±5)	6600 (±5)

E (10 weeks)	271200 (1.8)	3400 (1.9)	2285 (8.4)	154 (3.1)	700 (±5)	369500 (±5)	6300 (±5)
F (12 weeks)	280400 (1.6)	3000 (1.2)	1792 (4.1)	179 (0.6)	700 (±5)	473500 (±5)	6500 (±5)

50°C with 1-2-3µM sulfide (System)/ Amounts in µg/L	**Na**	**Ca**	**K**	**Mg**	**F**	**Cl**	**SO4**
A (4 weeks)	316000 (5.8)	3300 (1.8)	9653 (1.6)	859 (0.8)	1100 (±5)	389400 (±5)	61100 (±5)
B (5 weeks)	258300 (4.3)	2000 (1.3)	10066 (1.4)	710 (0.4)	700 (±5)	362000 (±5)	7100 (±5)
C (6 weeks)	282100 (3.3)	4800 (1.1)	26799 (4.9)	999 (0.8)	700 (±5)	398300 (±5)	6700 (±5)
D (8 weeks)	255400 (1.0)	6100 (1.1)	5464 (2.2)	247 (2.3)	700 (±5)	307900 (±5)	6600 (±5)
E (10 weeks)	255400 (0.9)	1600 (6.0)	3342 (1.3)	218 (1.2)	700 (±5)	363600 (±5)	6200 (±5)
F (12 weeks)	262700 (4.0)	1900 (2.9)	2006 (2.9)	186 (1.6)	700 (±5)	389700 (±5)	6500 (±5)

Table A 7 *Dissolved amounts of Na, Ca, K, Mg, F, Cl and SO4 ions in the ground water solutions in contact with Cu-Ni coupons during 6 months dynamic experiments. Numbers in parentheses correspond to the relative standard deviation in percentage.*

25°C w/o sulfide(System)/ Amounts in µg/L	**Na**	**Ca**	**K**	**Mg**	**F**	**Cl**	**SO4**
A (4 weeks)	225900 (2.9)	3300 (3.8)	108321 (2.8)	370 (2.4)	700 (±5)	597800 (±5)	13600 (±5)
B (5 weeks)	228700 (2.0)	3600 (6.5)	25788 (1.6)	260 (1.8)	<100	390200 (±5)	7300 (±5)
C (6 weeks)	242100 (1.2)	6500 (2.5)	46254 (1.0)	305 (0.3)	<100	403500 (±5)	5900 (±5)
D (8 weeks)	242300 (2.1)	3100 (2.5)	35921 (1.3)	349 (0.5)	600 (±5)	441700 (±5)	5600 (±5)
E (10 weeks)	257900 (1.2)	2500 (0.8)	32512 (1.2)	424 (5.8)	600 (±5)	361500 (±5)	5400 (±5)
F (12 weeks)	257200 (1.6)	2500 (2.1)	65203 (0.6)	345 (0.8)	<100	415400 (±5)	5700 (±5)

50°C w/o sulfide(System)/ Amounts in µg/L	Na	Ca	K	Mg	F	Cl	SO4
A (4 weeks)	235900 (3.6)	8400 (2.9)	32747 (4.7)	498 (1.3)	700 (±5)	381900 (±5)	8400 (±5)
B (5 weeks)	232000 (2.0)	5300 (1.9)	13198 (0.3)	478 (0.8)	700 (±5)	358500 (±5)	6000 (±5)
C (6 weeks)	238000 (2.5)	3800 (4.5)	12781 (0.3)	279 (2.8)	700 (±5)	367000 (±5)	5900 (±5)
D (8 weeks)	260000 (1.1)	2500 (2.3)	15384 (1.8)	343 (1.7)	600 (±5)	350200 (±5)	5700 (±5)
E (10 weeks)	253800 (1.3)	2400 (1.2)	18970 (1.0)	349 (1.9)	600 (±5)	366600 (±5)	5700 (±5)
F (12 weeks)	261200 (0.6)	2400 (2.2)	10489 (2.1)	323 (1.0)	600 (±5)	395400 (±5)	5700 (±5)

25°C with 1-2-3µM sulfide (System)/ Amounts in µg/L	Na	Ca	K	Mg	F	Cl	SO4
A (4 weeks)	230300 (4.0)	4000 (2.8)	88551 (4.4)	237 (2.0)	<100	435600 (±5)	16100 (±5)
B (5 weeks)	227300 (3.8)	3800 (1.7)	9198 (1.8)	276 (0.4)	900 (±5)	359600 (±5)	8200 (±5)
C (6 weeks)	248900 (1.4)	4100 (3.0)	9133 (1.3)	218 (1.8)	800 (±5)	383200 (±5)	6400 (±5)
D (8 weeks)	257800 (1.3)	3500 (1.7)	17053 (1.9)	323 (1.3)	900 (±5)	384100 (±5)	5900 (±5)
E (10 weeks)	257300 (1.4)	2900 (2.5)	8139 (1.4)	328 (1.0)	900 (±5)	466900 (±5)	6100 (±5)
F (12 weeks)	266600 (0.9)	300 (1.8)	13489 (0.9)	320 (1.3)	900 (±5)	371100 (±5)	6700 (±5)

50°C with 1-2-3µM sulfide (System)/ Amounts in µg/L	Na	Ca	K	Mg	F	Cl	SO4
A (4 weeks)	237600 (3.3)	3000 (0.4)	14014 (0.8)	350 (2.0)	1000 (±5)	358900 (±5)	19200 (±5)
B (5 weeks)	230900 (1.0)	3400 (1.0)	16686 (1.6)	286 (1.6)	900 (±5)	355800 (±5)	6300 (±5)
C (6 weeks)	254700 (0.6)	3800 (2.4)	15395 (0.9)	217 (2.2)	800 (±5)	393100 (±5)	6200 (±5)
D (8 weeks)	267600 (0.5)	2800 (1.9)	21340 (1.2)	289 (0.3)	900 (±5)	313200 (±5)	6200 (±5)
E (10 weeks)	265300 (0.6)	2900 (2.3)	7692 (4.4)	281 (0.7)	900 (±5)	375900 (±5)	6100 (±5)
F (12 weeks)	269900 (0.7)	2900 (1.2)	19610 (1.7)	286 (1.1)	900 (±5)	371500 (±5)	6200 (±5)

Table A 8 *Dissolved amounts of Na, Ca, K, Mg, F, Cl and SO4 ions in the ground water solutions without coupon during 3 and 6 months dynamic experiments. Numbers in parentheses correspond to the relative standard deviation in percentage.*

3months 25°C w/o coupon (System)/ Amounts in µg/L	**Na**	**Ca**	**K**	**Mg**	**F**	**Cl**	**SO4**
A (4 weeks)	269500 (0.9)	2600 (1.0)	3233 (2.2)	538 (1.0)	900 (±5)	505300 (±5)	16100 (±5)
B (5 weeks)	267800 (4.8)	2300 (3.8)	2122 (4.9)	456 (1.5)	800 (±5)	425300 (±5)	8900 (±5)
C (6 weeks)	250500 (2.4)	2300 (3.8)	1583 (5.4)	429 (1.0)	800 (±5)	252900 (±5)	6300 (±5)
D (8 weeks)	254500 (2.9)	2700 (1.6)	1619 (3.6)	204 (0.6)	800 (±5)	344100 (±5)	6100 (±5)
E (10 weeks)	268000 (1.6)	2900 (1.5)	1552 (4.4)	205 (4.3)	<100	379800 (±5)	6400 (±5)
F (12 weeks)	281700 (1.9)	3100 (3.0)	<100	125 (8.3)	900 (±5)	361200 (±5)	6800 (±5)

3months 50°C w/o coupon (System)/ Amounts in µg/L	**Na**	**Ca**	**K**	**Mg**	**F**	**Cl**	**SO4**
A (4 weeks)	386800 (1.3)	11100 (3.1)	59529 (1.2)	2026 (2.5)	1500 (±5)	515000 (±5)	139100 (±5)
B (5 weeks)	357000 (2.0)	4600 (0.6)	2240 (5.7)	628 (0.1)	1300 (±5)	479300 (±5)	19900 (±5)
C (6 weeks)	339000 (1.6)	3800 (0.9)	<100	415 (1.5)	<100	615300 (±5)	10200 (±5)
D (8 weeks)	316200 (4.5)	3700 (1.3)	643 (14.8)	136 (4.9)	800 (±5)	424100 (±5)	9300 (±5)
E (10 weeks)	308500 (1.8)	3700 (1.8)	<100	125 (8.1)	800 (±5)	465500 (±5)	9000 (±5)
F (12 weeks)	316400 (1.6)	4300 (1.3)	954 (18.5)	142 (3.9)	<100	838800 (±5)	9600 (±5)

6months 25°C w/o coupon (System)/ Amounts in µg/L	**Na**	**Ca**	**K**	**Mg**	**F**	**Cl**	**SO4**
A (6 weeks)	227800 (3.0)	3400 (2.4)	14275 (2.5)	380 (1.3)	700 (±5)	351900 (±5)	7600 (±5)
B (10 weeks)	238300 (1.6)	3400 (3.2)	40867 (2.1)	355 (0.4)	<100	380900 (±5)	6200 (±5)
C (14 weeks)	256400 (2.1)	3800 (4.8)	7026 (1.0)	268 (0.7)	700 (±5)	392600 (±5)	7700 (±5)
D (18 weeks)	257000 (1.1)	2500 (1.6)	4853 (2.1)	421 (0.4)	600 (±5)	351800 (±5)	5800 (±5)
E (22 weeks)	262500 (3.2)	2400 (0.7)	4973 (1.3)	388 (0.6)	700 (±5)	382700 (±5)	5700 (±5)
F (26 weeks)	251400 (2.5)	2300 (1.5)	24943 (1.2)	347 (0.7)	600 (±5)	394100 (±5)	5400 (±5)

6months 50°C w/o coupon (System)/ Amounts in µg/L	Na	Ca	K	Mg	F	Cl	SO4
A (6 weeks)	230300 (1.2)	5400 (2.5)	10993 (1.7)	374 (2.2)	700 (±5)	369900 (±5)	7200 (±5)
B (10 weeks)	237800 (3.7)	3200 (1.8)	24481 (2.6)	234 (2.8)	700 (±5)	380100 (±5)	6600 (±5)
C (14 weeks)	243400 (4.7)	2800 (3.0)	7598 (0.5)	260 (4.4)	700 (±5)	360600 (±5)	6200 (±5)
D (18 weeks)	262100 (1.7)	2500 (1.9)	18832 (1.9)	410 (2.9)	600 (±5)	358600 (±5)	5700 (±5)
E (22 weeks)	259100 (1.0)	2300 (1.2)	41723 (1.0)	319 (1.7)	600 (±5)	375300 (±5)	5600 (±5)
F (26 weeks)	244100 (1.4)	2600 (1.7)	19377 (2.4)	302 (1.0)	600 (±5)	357200 (±5)	5800 (±5)

Dissolved cations and anions evolution in pore water (supernatant) after 3, 6 and 9months – static experiments (Spheroidal graphite iron system)

Table A 9 *Dissolved amounts of Na, Ca, K, Mg, F, Cl and SO4 ions in the pore water solutions in contact with SGI coupons after 3, 6 and 9 months static experiments. Numbers in parentheses correspond to the relative standard deviation in percentage.*

System/ Amounts in µg/L	Na	Ca	K	Mg	F	Cl	SO4
3months 25°C w/o hematite	584800 (2.7)	11700 (1.4)	29096 (1.3)	2670 (1.9)	1200 (±5)	396600 (±5)	557700 (±5)
3months 50°C w/o hematite	640500 (0.7)	13000 (0.5)	29863 (1.7)	3458 (1.5)	1200 (±5)	472700 (±5)	631200 (±5)
3months 25°C with (0.5 wt.%) hematite	659500 (2.9)	12300 (1.6)	41959 (1.9)	3251 (2.4)	1200 (±5)	427100 (±5)	493100 (±5)
3months 50°C with (0.5 wt.%) hematite	630600 (1.2)	13300 (0.3)	29576 (0.4)	2987 (0.6)	1100 (±5)	397000 (±5)	544000 (±5)
6months 25°C w/o hematite	675600 (0.6)	15100 (1.1)	23620 (2.9)	4630 (0.9)	1100 (±5)	451700 (±5)	482900 (±5)
6months 50°C w/o hematite	737000 (2.7)	16800 (0.6)	19360 (0.4)	4050 (2.6)	1600 (±5)	533700 (±5)	704800 (±5)
6months 25°C with (0.5 wt.%) hematite	613800 (1.9)	12000 (1.3)	16280 (3.7)	3660 (0.3)	1200 (±5)	475200 (±5)	512700 (±5)
6months 50°C with	668800	14300	18570	3380	1600	596500	596500

(0.5 wt.%) hematite	(3.5)	(1.2)	(2.4)	(2.3)	(±5)	(±5)	(±5)
9months 25°C w/o hematite	755400 (0.4)	22600 (0.4)	99563 (0.8)	7318 (0.7)	1200 (±5)	827300 (±5)	656600 (±5)
9months 25°C with (0.5 wt.%) hematite	691400 (1.8)	15100 (0.4)	49679 (1.5)	2774 (0.3)	1000 (±5)	623900 (±5)	678700 (±5)

Dissolved cations and anions evolution in ground water (supernatant) after 3 and 6 months – dynamic experiments (Spheroidal graphite iron system)

Table A 10 *Dissolved amounts of Na, Ca, K, Mg, F, Cl and SO4 ions in the ground water solutions in contact with SGI coupons during 3 months dynamic experiments. Numbers in parentheses correspond to the relative standard deviation in percentage.*

25°C w/o hematite(System)/ Amounts in µg/L	**Na**	**Ca**	**K**	**Mg**	**F**	**Cl**	**SO4**
A (4 weeks)	262400 (4.3)	3400 (1.8)	20589 (4.8)	522 (1.2)	800 (±5)	350200 (±5)	21400 (±5)
B (5 weeks)	271600 (3.1)	2800 (4.3)	5535 (2.2)	538 (1.0)	900 (±5)	331700 (±5)	18300 (±5)
C (6 weeks)	258600 (2.9)	2500 (1.7)	1897 (6.9)	463 (1.1)	800 (±5)	355300 (±5)	7700 (±5)
D (8 weeks)	254000 (2.5)	2700 (1.3)	33023 (2.1)	225 (4.6)	800 (±5)	365800 (±5)	6600 (±5)
E (10 weeks)	262400 (3.7)	3000 (3.0)	5992 (1.4)	186 (2.3)	800 (±5)	359800 (±5)	6200 (±5)
F (12weeks)	291500 (0.2)	2900 (1.1)	1342 (8.2)	231 (3.1)	<100	387600 (±5)	6800 (±5)

25°C with (0.5 wt.%)hematite (System)/Amounts in µg/L	**Na**	**Ca**	**K**	**Mg**	**F**	**Cl**	**SO4**
A (4 weeks)	286100 (0.9)	3200 (0.3)	14896 (1.2)	738 (0.8)	1100 (±5)	382700 (±5)	54400 (±5)
B (5 weeks)	260900 (2.0)	2400 (2.7)	1571 (4.6)	542 (0.7)	800 (±5)	358100 (±5)	9300 (±5)
C (6 weeks)	265200 (1.6)	2600 (2.1)	<100	419 (1.0)	800 (±5)	386300 (±5)	7600 (±5)
D (8 weeks)	263800 (1.8)	3100 (1.1)	1828 (6.2)	168 (0.7)	800 (±5)	398800 (±5)	6900 (±5)
E (10 weeks)	286700 (2.1)	3400 (1.2)	22041 (1.8)	154 (3.0)	<100	489600 (±5)	7400 (±5)
F (12 weeks)	293500 (0.5)	3800 (1.2)	25496 (2.20)	132 (6.8)	<100	399300 (±5)	7300 (±5)

50°C with(0.5 wt.%) hematite (System)/Amounts in µg/L	Na	Ca	K	Mg	F	Cl	SO4
A (4 weeks)	310800 (1.2)	3900 (0.7)	2585 (6.0)	747 (1.1)	1000 (±5)	381100 (±5)	44400 (±5)
B (5 weeks)	278600 (3.5)	2000 (3.2)	<100	455 (0.2)	700 (±5)	435900 (±5)	7800 (±5)
C (6 weeks)	308900 (2.8)	2300 (0.9)	2367 (1.4)	386 (2.1)	<100	393400 (±5)	6400 (±5)
D (8 weeks)	284800 (0.6)	2600 (1.1)	2283 (7.4)	145 (5.3)	<100	371600 (±5)	6500 (±5)
E (10 weeks)	307300 (0.8)	3600 (2.2)	851 (14.0)	109 (5.4)	<100	405500 (±5)	8200 (±5)
F (12 weeks)	278500 (1.4)	4900 (1.3)	<100	120 (4.6)	<100	389500 (±5)	8000 (±5)

Table A 11 *Dissolved amounts of Na, Ca, K, Mg, F, Cl and SO4 ions in the ground water solutions in contact with SGI coupons during 6 months dynamic experiments. Numbers in parentheses correspond to the relative standard deviation in percentage.*

25°C w/o hematite(System)/ Amounts in µg/L	Na	Ca	K	Mg	F	Cl	SO4
A (4 weeks)	233500 (3.5)	3500 (0.3)	15372 (2.3)	323 (2.3)	700 (±5)	369500 (±5)	17600 (±5)
B (5 weeks)	237700 (2.3)	3400 (1.9)	7687 (0.8)	266 (0.4)	700 (±5)	419800 (±5)	6900 (±5)
C (6 weeks)	239100 (3.2)	3600 (3.7)	46570 (3.7)	264 (4.0)	700 (±5)	436400 (±5)	5900 (±5)
D (8 weeks)	256100 (0.3)	2100 (0.1)	7303 (6.9)	487 (1.3)	600 (±5)	360800 (±5)	6000 (±5)
E (10 weeks)	261300 (1.1)	2500 (3.5)	21526 (1.4)	402 (1.3)	600 (±5)	363200 (±5)	5700 (±5)
F (12weeks)	253300 (1.6)	2400 (2.3)	14196 (1.6)	353 (0.7)	600 (±5)	351200 (±5)	5700 (±5)

25°C with (0.5 wt.%)hematite (System)/Amounts in µg/L	Na	Ca	K	Mg	F	Cl	SO4
A (4 weeks)	230600 (3.5)	3300 (5.0)	10071 (1.0)	299 (1.0)	700 (±5)	356700 (±5)	12500 (±5)
B (5 weeks)	240500 (3.6)	3600 (3.2)	127838 (2.9)	233 (2.7)	<100	543900 (±5)	7000 (±5)
C (6 weeks)	292400 (3.5)	4100 (4.4)	54200 (3.8)	292 (1.5)	<100	429500 (±5)	6300 (±5)
D (8 weeks)	248200 (1.9)	2200 (0.5)	15618 (0.4)	397 (0.9)	600 (±5)	120900 (±5)	8400 (±5)

E (10 weeks)	258300 (0.6)	2500 (1.6)	17491 (1.1)	339 (0.8)	600 (±5)	348200 (±5)	6100 (±5)
F (12 weeks)	254100 (1.5)	2600 (1.2)	14821 (1.2)	317 (1.4)	600 (±5)	379500 (±5)	6000 (±5)

50°C with(0.5 wt.%) hematite (System)/Amounts in µg/L	**Na**	**Ca**	**K**	**Mg**	**F**	**Cl**	**SO4**
A (4 weeks)	236300 (2.6)	3400 (1.4)	13050 (0.6)	323 (1.2)	700 (±5)	372200 (±5)	14400 (±5)
B (5 weeks)	235900 (0.4)	3500 (2.9)	16806 (1.7)	414 (0.8)	700 (±5)	356200 (±5)	6400 (±5)
C (6 weeks)	249200 (1.2)	3300 (2.7)	9516 (1.4)	288 (3.4)	700 (±5)	377100 (±5)	6100 (±5)
D (8 weeks)	245200 (1.5)	2000 (1.9)	12098 (1.0)	373 (0.3)	700 (±5)	348400 (±5)	5900 (±5)
E (10 weeks)	252000 (2.4)	2100 (0.5)	6758 (0.5)	381 (1.0)	600 (±5)	303300 (±5)	5800 (±5)
F (12 weeks)	241100 (1.7)	2100 (0.7)	6420 (2.4)	396 (0.6)	600 (±5)	344300 (±5)	5800 (±5)

Dissolved cations and anions evolution in pore water (supernatant) after 3, 6 and 9months – static experiments (Spring steel system)

Table A 12 *Dissolved amounts of Na, Ca, K, Mg, F, Cl and SO4 ions in the pore water solutions in contact with SS coupons after 3, 6 and 9 months static experiments. Numbers in parentheses correspond to the relative standard deviation in percentage.*

System/ Amounts in µg/L	**Na**	**Ca**	**K**	**Mg**	**F**	**Cl**	**SO4**
3months 25°C w/o scratched	630900 (1.6)	13000 (0.8)	40045 (1.0)	3664 (0.6)	1100 (±5)	436900 (±5)	522400 (±5)
3months 50°C w/o scratched	640000 (0.3)	15000 (2.5)	49173 (0.4)	3675 (2.3)	1200 (±5)	585900 (±5)	599700 (±5)
3months 25°C with scratched	596800 (1.4)	96000 (0.7)	29408 (1.9)	2495 (0.5)	1300 (±5)	391600 (±5)	490500 (±5)
3months 50°C with scratched	719700 (1.8)	17400 (0.8)	58191 (3.0)	4327 (1.3)	1000 (±5)	600700 (±5)	594100 (±5)
6months 25°C w/o scratched	648700 (3.5)	12500 (0.5)	46430 (0.2)	3380 (0.2)	1300 (±5)	343800 (±5)	376100 (±5)
6months 50°C w/o scratched	639900 (1.6)	13900 (0.2)	23383 (0.6)	3618 (4.1)	1200 (±5)	558600 (±5)	680900 (±5)
6months 25°C with scratched	612400 (1.2)	11100 (1.5)	25260 (1.8)	3440 (0.9)	1300 (±5)	396500 (±5)	505900 (±5)
6months 50°C with scratched	679300 (3.8)	13800 (0.2)	17630 (1.7)	3210 (1.7)	1100 (±5)	514800 (±5)	628000 (±5)
9months 25°C w/o scratched	607400 (2.8)	10800 (2.6)	26038 (2.2)	3147 (1.0)	1100 (±5)	453700 (±5)	544400 (±5)
9months 25°C with scratched	660000 (2.0)	14300 (0.4)	51701 (0.6)	4468 (0.8)	1100 (±5)	301800 (±5)	345600 (±5)

Dissolved cations and anions evolution in ground water (supernatant) after 3 and 6 months – dynamic experiments (Spring steel system)

Table A 13 *Dissolved amounts of Na, Ca, K, Mg, F, Cl and SO4 ions in the ground water solutions in contact with SS coupons during 3 months dynamic experiments. Numbers in parentheses correspond to the relative standard deviation in percentage.*

25°C w/o scratched (System)/Amounts in µg/L	**Na**	**Ca**	**K**	**Mg**	**F**	**Cl**	**SO4**
A (4 weeks)	282300 (0.5)	3700 (1.6)	3199 (2.5)	912 (1.3)	800 (±5)	361900 (±5)	34600 (±5)
B (5 weeks)	274600 (2.9)	2500 (3.8)	1850 (2.3)	554 (1.5)	800 (±5)	375800 (±5)	14400 (±5)
C (6 weeks)	287300 (4.8)	3300 (2.7)	5514 (3.5)	492 (1.6)	<100	386500 (±5)	11300 (±5)
D (8 weeks)	269500 (1.4)	2800 (2.1)	1368 (9.0)	179 (3.7)	800 (±5)	367900 (±5)	9200 (±5)
E (10 weeks)	302300 (1.2)	3500 (0.6)	1135 (19.3)	186 (3.7)	900 (±5)	406900 (±5)	9300 (±5)
F (12weeks)	277100 (2.5)	3000 (2.1)	1615 (11.9)	123 (1.6)	<100	393900 (±5)	7900 (±5)

25°C with scratched (System)/Amounts in µg/L	**Na**	**Ca**	**K**	**Mg**	**F**	**Cl**	**SO4**
A (4 weeks)	291500 (2.6)	3100 (1.1)	4612 (0.9)	690 (1.1)	900 (±5)	302500 (±5)	42900 (±5)
B (5 weeks)	286300 (4.2)	3100 (1.9)	2223 (4.6)	485 (1.1)	800 (±5)	363300 (±5)	10000 (±5)
C (6 weeks)	263400 (2.4)	2700 (2.6)	1990 (3.9)	427 (1.0)	800 (±5)	229300 (±5)	6900 (±5)
D (8 weeks)	261100 (2.1)	3300 (0.9)	3766 (2.5)	188 (2.7)	<100	338000 (±5)	6300 (±5)
E (10 weeks)	282600 (1.9)	3500 (1.2)	3187 (3.5)	189 (4.2)	<100	380500 (±5)	6600 (±5)
F (12 weeks)	303600 (3.2)	3600 (2.4)	960 (3.6)	150 (6.7)	<100	386500 (±5)	7400 (±5)

50°C with scratched (System)/Amounts in µg/L	**Na**	**Ca**	**K**	**Mg**	**F**	**Cl**	**SO4**
A (4 weeks)	319800 (3.7)	5000 (1.6)	8835 (3.1)	1071 (1.5)	1200 (±5)	312900 (±5)	65000 (±5)
B (5 weeks)	282900 (2.9)	2200 (1.7)	1374 (2.6)	451 (0.5)	700 (±5)	395700 (±5)	7000 (±5)
C (6 weeks)	299500 (3.0)	2800 (7.6)	<100	396 (1.4)	700 (±5)	474200 (±5)	6700 (±5)

D (8 weeks)	280800 (5.6)	2700 (1.9)	855 (4.9)	104 (2.0)	700 (±5)	398400 (±5)	6800 (±5)
E (10 weeks)	283100 (1.5)	3100 (2.2)	624 (2.7)	97 (3.0)	700 (±5)	390500 (±5)	7300 (±5)
F (12 weeks)	284400 (0.6)	3200 (1.5)	<100	98(10.8)	700 (±5)	407800 (±5)	7100 (±5)

Table A 14 *Dissolved amounts of Na, Ca, K, Mg, F, Cl and SO4 ions in the ground water solutions in contact with SS coupons during 6 months dynamic experiments. Numbers in parentheses correspond to the relative standard deviation in percentage.*

25°C w/o scratched (System)/Amounts in µg/L	**Na**	**Ca**	**K**	**Mg**	**F**	**Cl**	**SO4**
A (6 weeks)	236600 (1.8)	4800 (1.1)	8615 (0.7)	439 (0.9)	700 (±5)	347400 (±5)	9100 (±5)
B (10 weeks)	249400 (4.4)	2900 (3.0)	9585 (0.7)	325 (1.6)	700 (±5)	354100 (±5)	6400 (±5)
C (14 weeks)	257800 (0.4)	3900 (1.3)	10090 (1.2)	279 (1.3)	700 (±5)	392900 (±5)	6400 (±5)
D (18 weeks)	253400 (1.4)	2500 (1.3)	7257 (3.4)	389 (1.5)	600 (±5)	359300 (±5)	5800 (±5)
E (22 weeks)	245500 (1.4)	2400 (1.4)	8956 (2.6)	380 (1.2)	600 (±5)	328200 (±5)	5400 (±5)
F (26 weeks)	257400 (2.6)	2400 (1.2)	51455 (2.7)	357 (0.8)	<100	384100 (±5)	5600 (±5)

25°C with scratched (System)/Amounts in µg/L	**Na**	**Ca**	**K**	**Mg**	**F**	**Cl**	**SO4**
A (6 weeks)	225600 (3.8)	3600 (1.6)	29244 (2.4)	262 (1.0)	800 (±5)	399700 (±5)	6400 (±5)
B (10 weeks)	220200 (7.2)	2900 (4.7)	5197 (1.8)	280 (0.9)	700 (±5)	356800 (±5)	6700 (±5)
C (14 weeks)	253200 (0.5)	3600 (2.5)	12199 (0.8)	248 (1.7)	<100	351000 (±5)	6500 (±5)
D (18 weeks)	259600 (0.9)	2400 (3.1)	4218 (4.2)	341 (0.7)	600 (±5)	332500 (±5)	6000 (±5)
E (22 weeks)	249900 (3.0)	2500 (2.3)	7481 (3.2)	318 (1.8)	600 (±5)	348300 (±5)	5700 (±5)
F (26 weeks)	260000 (3.3)	2600 (1.7)	7038 (1.0)	389 (0.3)	600 (±5)	352900 (±5)	5800 (±5)

50°C with scratched (System)/Amounts in µg/L	**Na**	**Ca**	**K**	**Mg**	**F**	**Cl**	**SO4**
A (6 weeks)	227500 (1.6)	3000 (2.7)	13536 (0.1)	356 (0.4)	700 (±5)	505900 (±5)	7800 (±5)

B (10 weeks)	236700 (4.7)	3400 (1.9)	11992 (1.0)	276 (2.6)	700 (±5)	367500 (±5)	6400 (±5)
C (14 weeks)	238300 (1.5)	3700 (2.1)	10211 (2.1)	266 (1.3)	800 (±5)	344100 (±5)	9300 (±5)
D (18 weeks)	268300 (0.4)	2300 (0.4)	8768 (1.9)	472 (1.2)	800 (±5)	358100 (±5)	15100 (±5)
E (22 weeks)	251800 (1.4)	2400 (1.3)	13553 (0.6)	340 (0.9)	700 (±5)	356800 (±5)	7200 (±5)
F (26 weeks)	259700 (2.0)	2500 (0.8)	5866 (5.5)	320 (0.6)	600 (±5)	358300 (±5)	6500 (±5)

Dissolved cations and anions evolution in pore water (supernatant) after 3, 6 and 9months – static experiments (Carbon steel system)

Table A 15 *Dissolved amounts of Na, Ca, K, Mg, F, Cl and SO4 ions in the pore water solutions in contact with CS coupons after 3, 6 and 9 months static experiments. Numbers in parentheses correspond to the relative standard deviation in percentage.*

System/ Amounts in µg/L	Na	Ca	K	Mg	F	Cl	SO4
3months 25°C w/o scratched	613300 (1.5)	9800 (1.0)	28013 (2.6)	2465 (1.1)	1200 (±5)	374100 (±5)	534000 (±5)
3months 50°C w/o scratched	637700 (2.4)	14300 (1.0)	31141 (1.7)	3308 (1.3)	1100 (±5)	441800 (±5)	565900 (±5)
3months 25°C with scratched	637400 (2.2)	10500 (0.1)	30523 (0.9)	2779 (0.8)	1200 (±5)	402900 (±5)	507100 (±5)
3months 50°C with scratched	652500 (1.8)	12800 (1.3)	29417 (4.0)	3106 (1.9)	1200 (±5)	344900 (±5)	476100 (±5)
6months 25°C w/o scratched	614200 (3.4)	11300 (2.1)	17170 (3.0)	3510 (2.1)	1300 (±5)	429200 (±5)	545000 (±5)
6months 50°C w/o scratched	673800 (3.1)	13700 (0.8)	14740 (2.2)	3510 (1.0)	1300 (±5)	468300 (±5)	630300 (±5)
6months 25°C with scratched	631900 (2.3)	12100 (0.7)	13620 (5.5)	3820 (1.3)	1300 (±5)	408900 (±5)	532900 (±5)
6months 50°C with scratched	701400 (2.3)	14400 (0.8)	13330 (1.3)	3810 (1.8)	1300 (±5)	557100 (±5)	703400 (±5)
9months 25°C w/o scratched	616000 (2.4)	11800 (1.1)	30120 (2.7)	3718 (0.3)	1100 (±5)	468000 (±5)	558500 (±5)
9months 25°C with scratched	883800 (1.2)	33900 (1.0)	185538 (2.1)	11092 (1.9)	1000 (±5)	106000 (±5)	581500 (±5)

Dissolved cations and anions evolution in ground water (supernatant) after 3 and 6 months – dynamic experiments (Carbon steel system)

Table A 16 *Dissolved amounts of Na, Ca, K, Mg, F, Cl and SO4 ions in the ground water solutions in contact with CS coupons during 3 months dynamic experiments. Numbers in parentheses correspond to the relative standard deviation in percentage.*

25°C w/o scratched (System)/Amounts in µg/L	**Na**	**Ca**	**K**	**Mg**	**F**	**Cl**	**SO4**
A (4 weeks)	314100 (4.3)	3500 (1.8)	4492 (3.6)	759 (0.6)	<100	406600 (±5)	55700 (±5)
B (5 weeks)	258400 (3.3)	2600 (1.6)	2474 (1.4)	518 (1.1)	800 (±5)	368400 (±5)	13900 (±5)
C (6 weeks)	258400 (3.5)	2800 (1.0)	1875 (7.8)	483 (1.0)	800 (±5)	337800 (±5)	6900 (±5)
D (8 weeks)	255700 (2.0)	2700 (2.5)	1561 (1.1)	233 (2.4)	800 (±5)	343800 (±5)	6200 (±5)
E (10 weeks)	251100 (1.2)	2700 (1.7)	1133 (15.2)	207 (6.6)	800 (±5)	380700 (±5)	6300 (±5)
F (12weeks)	281400 (2.6)	3000 (0.9)	2419 (9.1)	306 (0.2)	<100	407000 (±5)	6800 (±5)

25°C with scratched (System)/Amounts in µg/L	**Na**	**Ca**	**K**	**Mg**	**F**	**Cl**	**SO4**
A (4 weeks)	271800 (3.2)	2600 (2.9)	5398 (1.0)	509 (0.2)	1000 (±5)	354500 (±5)	24900 (±5)
B (5 weeks)	256800 (0.8)	2500 (2.9)	1582 (2.7)	413 (1.0)	800 (±5)	394600 (±5)	12800 (±5)
C (6 weeks)	283900 (3.3)	3300 (2.0)	2203 (3.2)	505 (0.6)	800 (±5)	369200 (±5)	10900 (±5)
D (8 weeks)	282400 (1.0)	3000 (2.6)	1213 (11.4)	147 (4.1)	900 (±5)	359800 (±5)	10400 (±5)
E (10 weeks)	246100 (1.9)	2600 (2.3)	1783 (11.0)	164 (3.6)	800 (±5)	374400 (±5)	8100 (±5)
F (12 weeks)	253700 (0.8)	3500 (2.1)	2625 (9.0)	187 (1.0)	800 (±5)	432300 (±5)	6300 (±5)

50°C with scratched (System)/Amounts in µg/L	**Na**	**Ca**	**K**	**Mg**	**F**	**Cl**	**SO4**
A (4 weeks)	289500 (0.9)	3800 (0.4)	3370 (3.0)	1775 (1.2)	1000 (±5)	367000 (±5)	39000 (±5)
B (5 weeks)	256800 (3.0)	2100 (1.8)	2105 (2.2)	478 (1.0)	700 (±5)	359900 (±5)	12900 (±5)
C (6 weeks)	266800 (1.6)	2000 (0.6)	1005 (7.6)	397 (1.0)	600 (±5)	366300 (±5)	6100 (±5)
D (8 weeks)	247600 (1.6)	2300 (1.6)	476 (15.5)	91 (3.7)	600 (±5)	396300 (±5)	5900 (±5)

E (10 weeks)	246400 (3.3)	2400 (1.5)	<100	72 (3.9)	600 (±5)	334400 (±5)	6100 (±5)
F (12 weeks)	255900 (2.7)	2500 (2.4)	<100	<100	700 (±5)	362300 (±5)	6300 (±5)

Table A 17 *Dissolved amounts of Na, Ca, K, Mg, F, Cl and SO4 ions in the ground water solutions in contact with CS coupons during 6 months dynamic experiments. Numbers in parentheses correspond to the relative standard deviation in percentage.*

25°C w/o scratched (System)/Amounts in µg/L	**Na**	**Ca**	**K**	**Mg**	**F**	**Cl**	**SO4**
A (6 weeks)	228800 (2.0)	3200 (0.9)	15041 (2.8)	344 (1.3)	700 (±5)	438500 (±5)	6900 (±5)
B (10 weeks)	240000 (4.2)	3200 (2.2)	26331 (4.3)	284 (1.2)	600 (±5)	392500 (±5)	6400 (±5)
C (14 weeks)	255200 (2.7)	4800 (2.9)	17498 (1.9)	339 (2.1)	<100	460400 (±5)	6300 (±5)
D (18 weeks)	246400 (0.5)	2300 (1.3)	4248 (2.5)	339 (2.1)	600 (±5)	410900 (±5)	5800 (±5)
E (22 weeks)	263500 (2.1)	2300 (1.3)	6655 (3.5)	325 (1.4)	600 (±5)	399200 (±5)	5700 (±5)
F (26 weeks)	257900 (0.8)	2400 (3.2)	9695 (1.1)	317 (1.2)	700 (±5)	343900 (±5)	5600 (±5)

25°Cwith scratched (System)/Amounts in µg/L	**Na**	**Ca**	**K**	**Mg**	**F**	**Cl**	**SO4**
A (6 weeks)	223700 (1.4)	3500 (4.3)	16439 (1.9)	341 (2.3)	700 (±5)	368200 (±5)	17800 (±5)
B (10 weeks)	234500 (4.1)	3600 (4.1)	93118 (3.6)	261 (1.2)	<100	455500 (±5)	8100 (±5)
C (14 weeks)	247400 (1.7)	3800 (2.2)	20030 (2.2)	240 (2.0)	700 (±5)	383200 (±5)	6600 (±5)
D (18 weeks)	265100 (1.2)	2700 (1.4)	6466 (5.4)	308 (2.5)	600 (±5)	373800 (±5)	6500 (±5)
E (22 weeks)	255900 (1.7)	2500 (0.7)	7176 (3.0)	349 (0.9)	600 (±5)	351800 (±5)	5600 (±5)
F (26 weeks)	262500 (2.1)	2600 (1.0)	7552 (1.2)	304 (2.8)	600 (±5)	345100 (±5)	5700 (±5)

50°C with scratched (System)/Amounts in µg/L	**Na**	**Ca**	**K**	**Mg**	**F**	**Cl**	**SO4**
A (6 weeks)	211700 (2.8)	2800 (3.4)	8927 (1.4)	350 (4.4)	700 (±5)	361700 (±5)	6700 (±5)
B (10 weeks)	242800 (1.1)	3100 (0.6)	20115 (1.4)	262 (1.7)	700 (±5)	382400 (±5)	6300 (±5)
C (14 weeks)	232500 (2.9)	3700 (0.8)	13529 (0.2)	260 (2.6)	700 (±5)	430700 (±5)	6300 (±5)

D (18 weeks)	258900 (2.2)	2200 (1.2)	8344 (1.4)	323 (0.4)	600 (±5)	431000 (±5)	5800 (±5)
E (22 weeks)	268100 (1.3)	2400 (1.9)	5026 (6.1)	289 (1.5)	600 (±5)	353200 (±5)	5900 (±5)
F (26 weeks)	251600 (1.2)	2400 (1.9)	5920 (3.3)	323 (0.2)	600 (±5)	468600 (±5)	5600 (±5)

Dissolved cations and anions evolution in pore water (supernatant) of GMZ bentonite after 3, 6, 9 and 12months – static experiments (Carbon steel - system)

Table A 18 *Dissolved amounts of Na, Ca, K, Mg, F, Cl and SO4 ions in the pore water solutions of GMZ bentonite in contact with CS coupons after 3, 6, 9 and 12 months static experiments. Numbers in parentheses correspond to the relative standard deviation in percentage.*

System/ Amounts in µg/L	Na	Ca	K	Mg	F	Cl	SO4
3months 25°C CS in GMZ bentonite	321000 (2.7)	2500 (3.5)	15177 (0.8)	772 (2.6)	2200 (±5)	452900 (±5)	17000 (±5)
3months 50°C CS in GMZ bentonite	407400 (2.7)	3600 (0.4)	18524 (0.4)	1319 (0.7)	2100 (±5)	618500 (±5)	22600 (±5)
6months 25°C CS in GMZ bentonite	307800 (1.5)	2000 (1.8)	4826 (3.8)	651 (1.0)	2300 (±5)	407700 (±5)	20900 (±5)
6months 50°C CS in GMZ bentonite	656300 (0.7)	14100 (0.2)	96306 (1.2)	5544 (1.4)	2000 (±5)	121900 (±5)	21200 (±5)
9months 25°C CS in GMZ bentonite	315300 (0.5)	2300 (3.0)	9431 (1.4)	723 (0.5)	2500 (±5)	410700 (±5)	16700 (±5)
12months 25°C CS in GMZ bentonite	368100 (1.2)	2500 (8.5)	6318 (3.0)	854 (2.6)	2700 (±5)	525700 (±5)	13800 (±5)

Table A 19 *Dissolved amounts of Na, Ca, K, Mg, F, Cl and SO4 ions in the pore water solutions of GMZ and MX-80 bentonite without coupon after 1 month of equilibrium period. Numbers in parentheses correspond to the relative standard deviation in percentage.*

System/ Amounts in µg/L	Na	Ca	K	Mg	F	Cl	SO4
GMZ bentonite	278900 (1.9)	1500 (1.0)	2500 (6.5)	462 (1.9)	1800 (±5)	354900 (±5)	13600 (±5)
MX-80bentonite	620100 (0.1)	24700 (0.7)	28400 (0.2)	3186 (1.6)	900 (±5)	594700 (±5)	695500 (±5)

All materials secondary phase characterization

(a) 6months 50°C: **(b) 6months 50°C:**

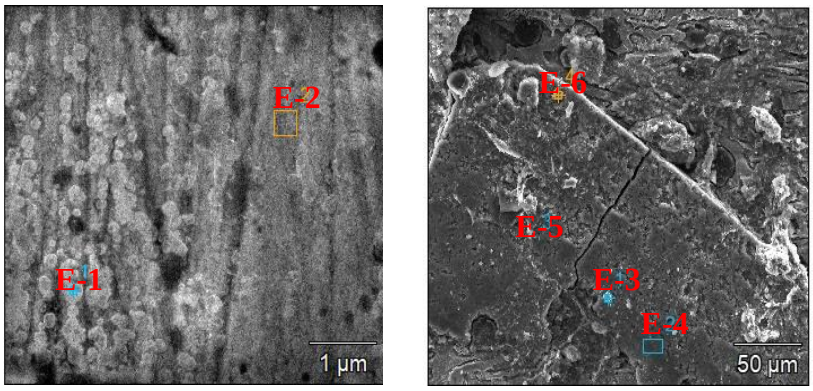

(c) 6months 50°C: **(d) 6months 50°C: CS**

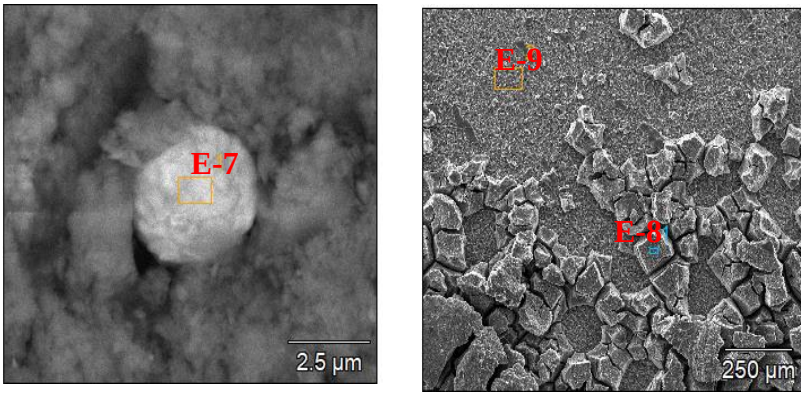

Figure A1 *Scanning electron micrographs (in SE mode) of (a)CuNi, (b)SGI, (c)SS and (d)CS coupons corroded for 6 months under static conditions at (50°C)elevated temperature (exact conditions are indicated above the micrographs).*

Table A 20 *Relative atomic concentrations by EDXS analyses at selected areas shown in above* ***Figure A1****. Relative errors are estimated to be within ± 10%.*

Area	C	O	S	Al	Si	Mn	Fe	Ni	Cu
E-1	5.4	4.5	4.5	0.4	0.8	0.7	/	22.6	61.0
E-2	4.2	2.0	2.1	/	0.3	1.0	0.9	33.3	56.2
	C	**O**	**S**	**Al**	**Si**	**Mn**	**Fe**	**Cl**	**Na**
E-3	8.1	/	57.4	0.6	2.2	/	31.0	/	0.5
E-4	5.1	52.6	0.3	0.7	18.6	/	19.3	1.1	1.6
E-5	4.4	55.3	0.3	0.7	18.4	/	17.5	1.0	1.6
E-6	7.1	5.5	/	0.9	2.9	0.6	82.6	/	0.2
E-7	5.9	/	55.0	0.7	1.9	0.7	26.8	/	/
E-8	4.2	56.5	0.1	1.9	17.7	/	17.5	/	1.7
E-9	7.6	35.9	0.2	0.2	3.7	1.0	50.2	0.1	/

Static conditions Cu-Ni systems (3, 6 and 9 months)

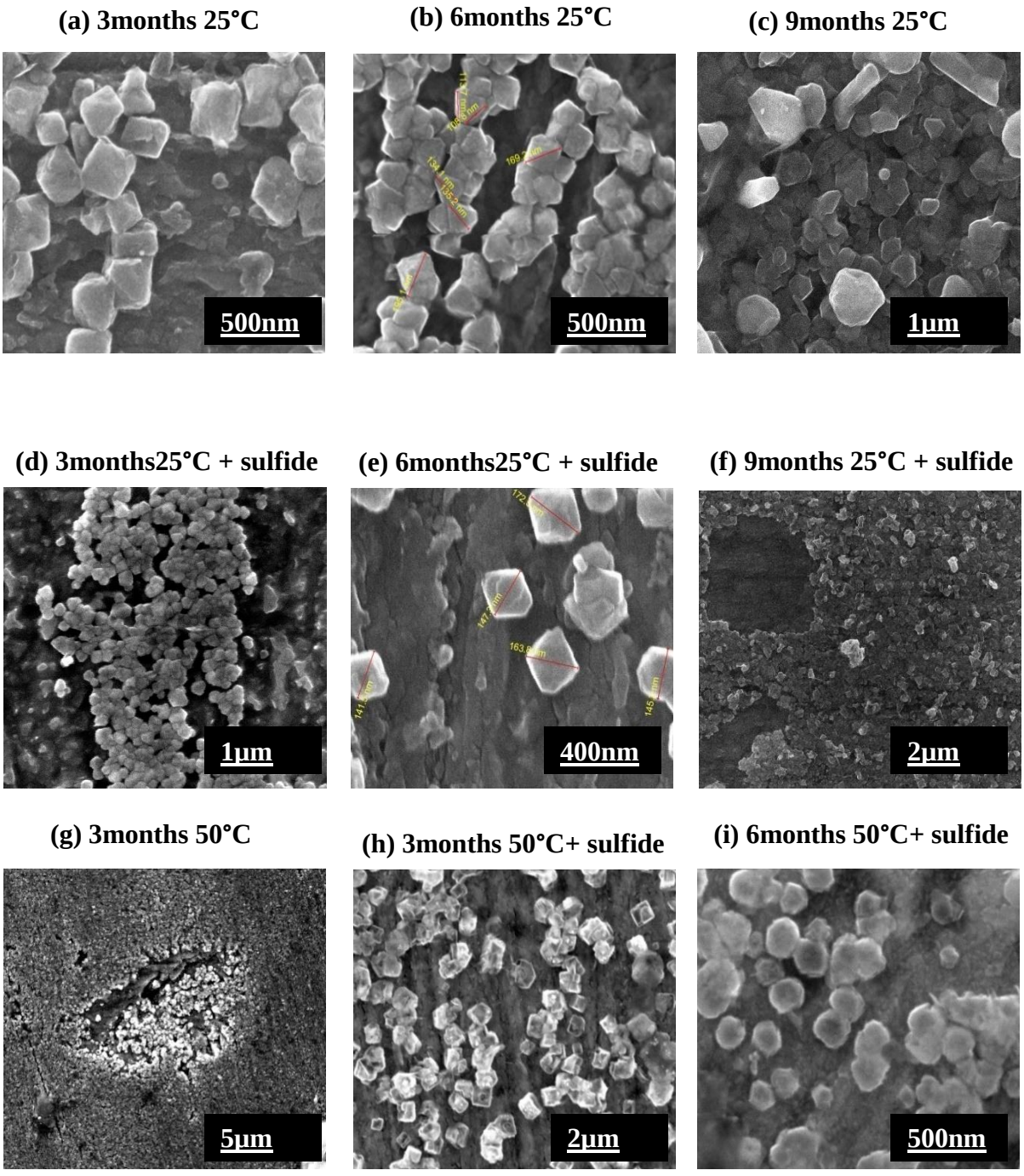

Figure A2 *Scanning electron micrographs (in SE mode) of all Cu-Ni coupons corroded for 3, 6 and 9 months under static conditions at different temperature (exact conditions are indicated above the micrographs).*

Dynamic conditions Cu-Ni systems (3 and 6 months)

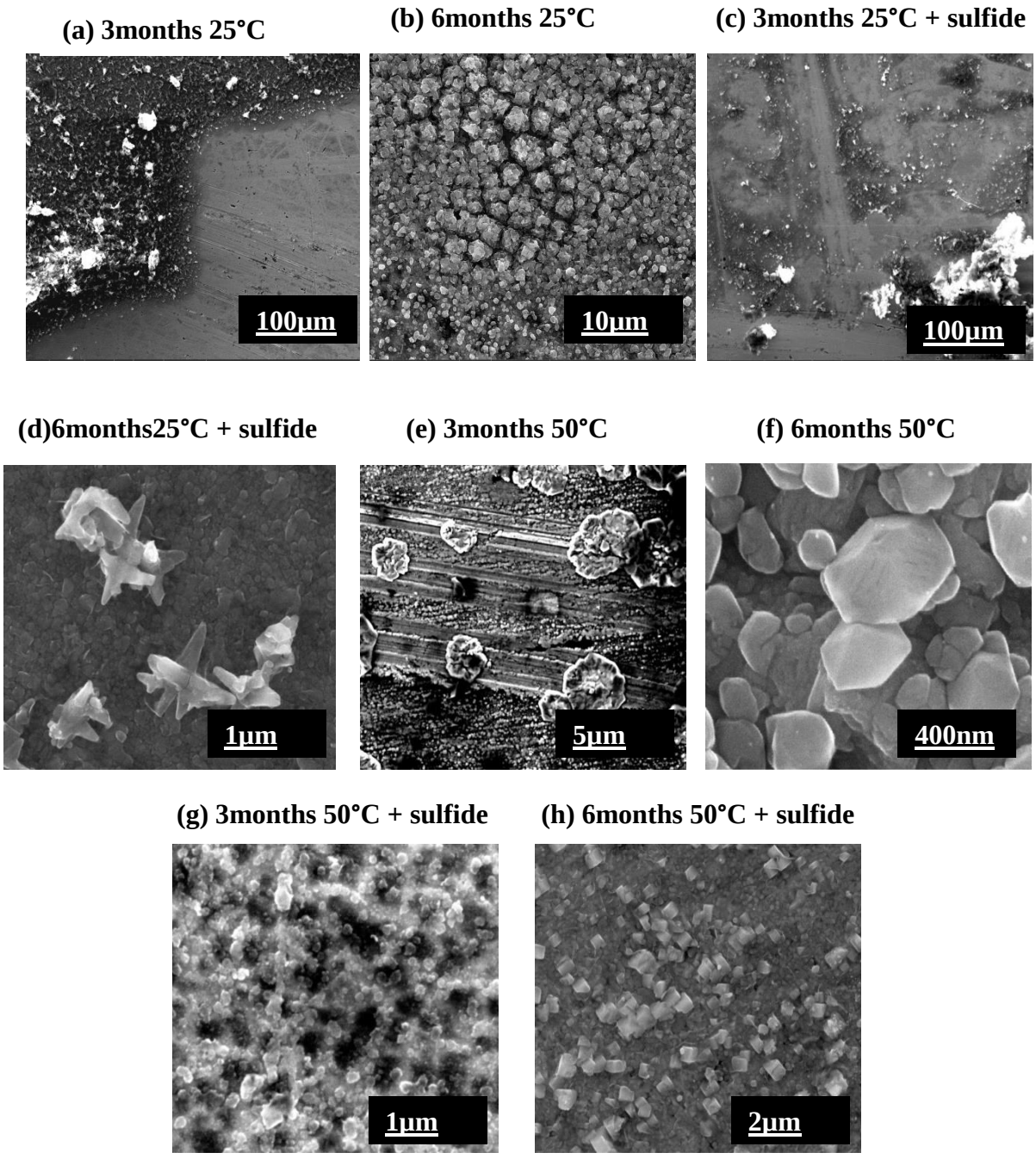

Figure A3 *Scanning electron micrographs (in SE mode) of all Cu-Ni coupons corroded for 3 and 6 months under dynamic conditions at different temperature (exact conditions are indicated above the micrographs).*

Static conditions SGI systems (3, 6 and 9 months)

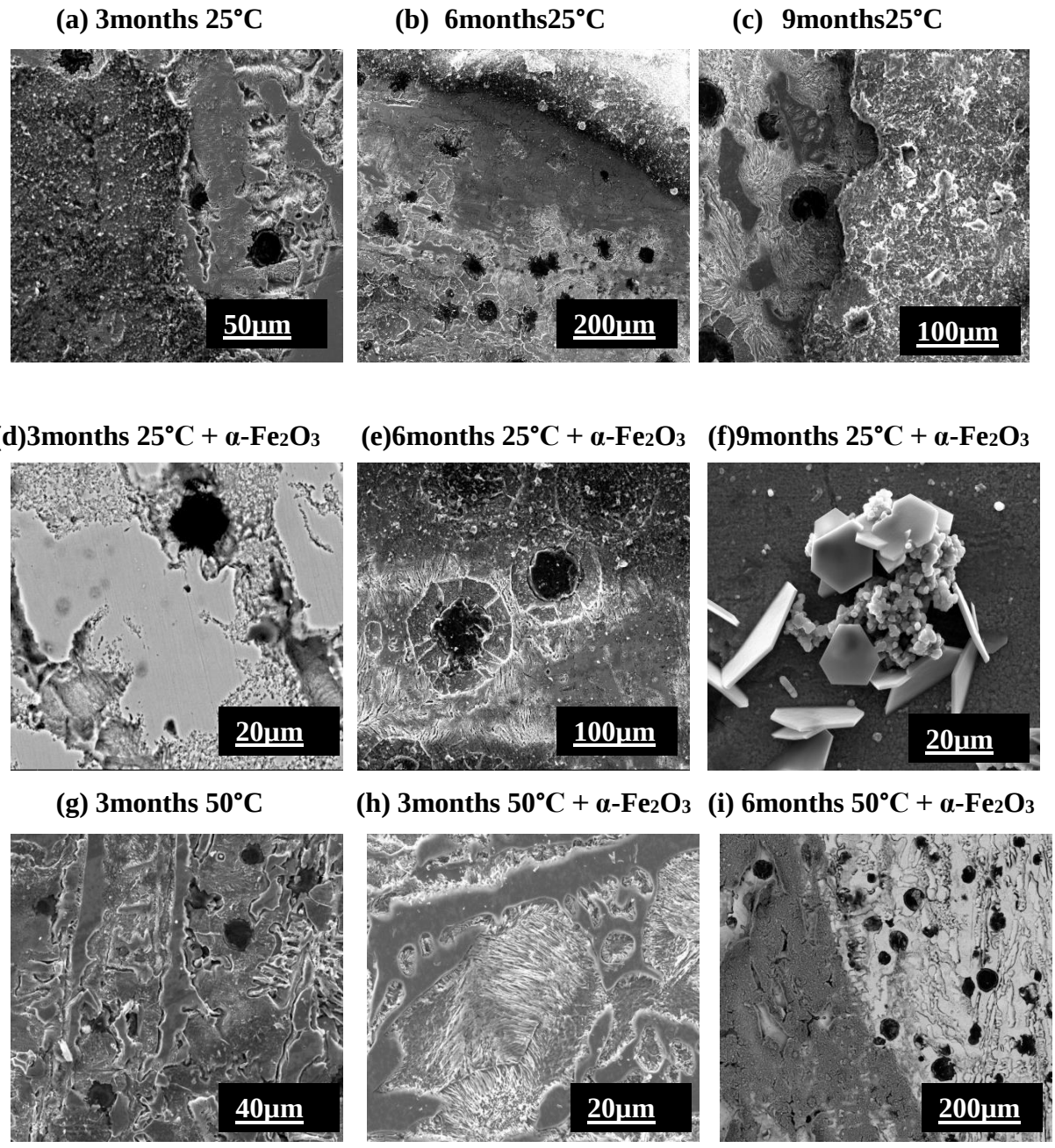

Figure A4 *Scanning electron micrographs (most of them in SE mode except (d, i)) of all SGI coupons corroded for 3, 6 and 9 months under static conditions at different temperatures (exact conditions are indicated above the micrographs).*

Dynamic conditions SGI systems (3 and 6 months)

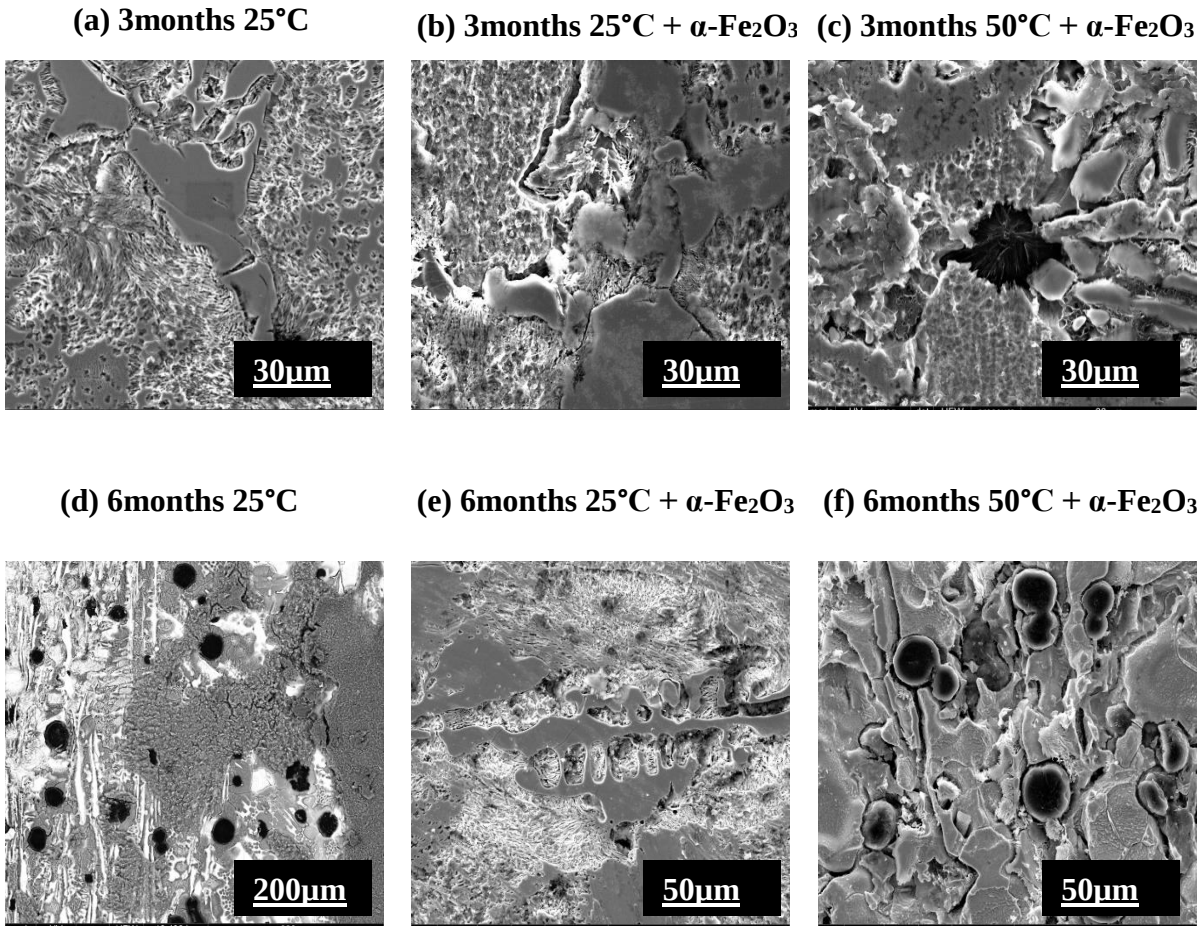

Figure A5 *Scanning electron micrographs (most of them in SE mode except (d)) of all SGI coupons corroded for 3 and 6 months under dynamic conditions at different temperatures (exact conditions are indicated above the micrographs).*

Static conditions SS systems (3, 6 and 9 months)

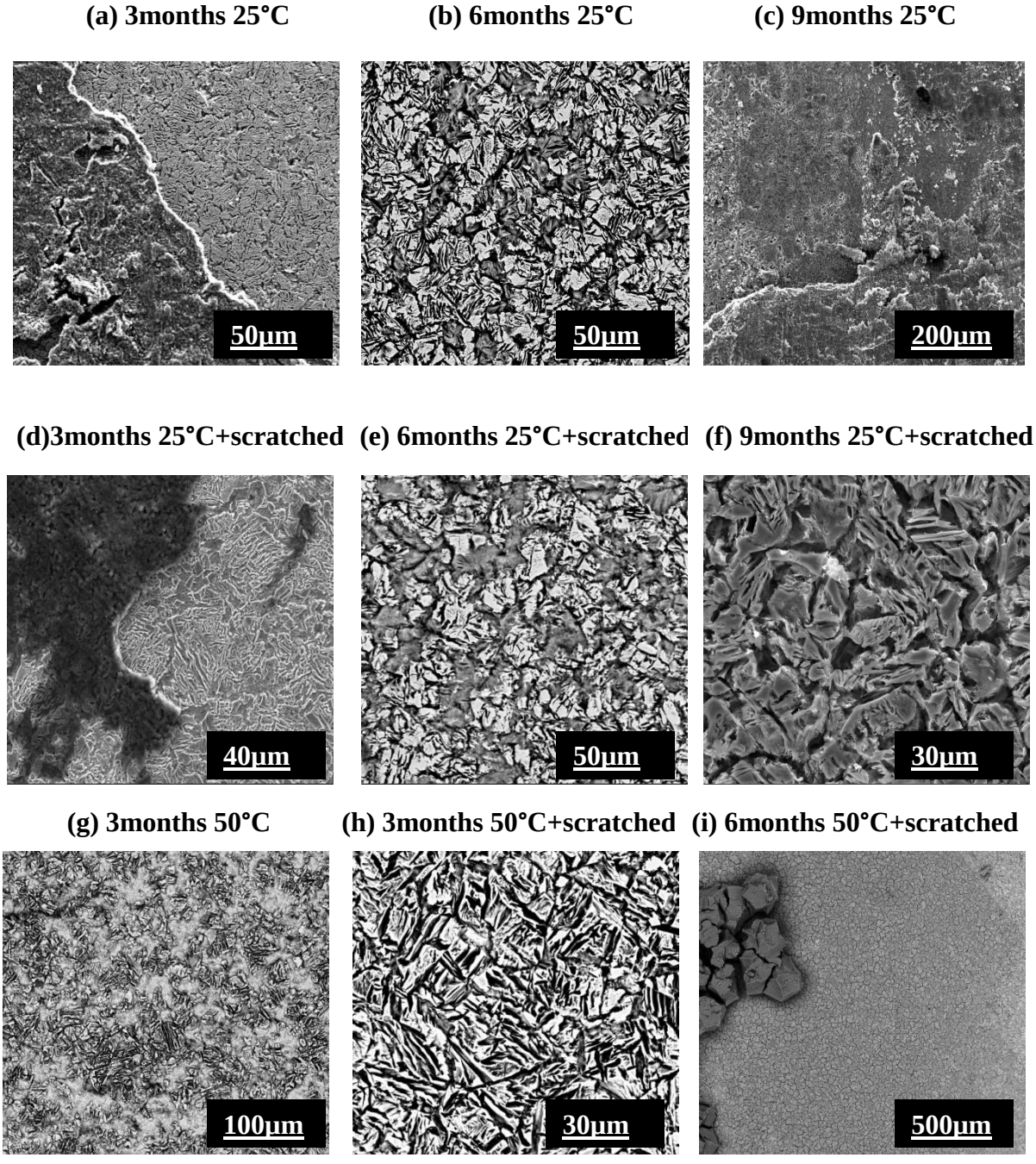

Figure A6 *Scanning electron micrographs (in SE mode) of all SS coupons corroded for 3, 6 and 9 months under static conditions at different temperatures (exact conditions are indicated above the micrographs).*

Dynamic conditions SS systems (3 and 6 months)

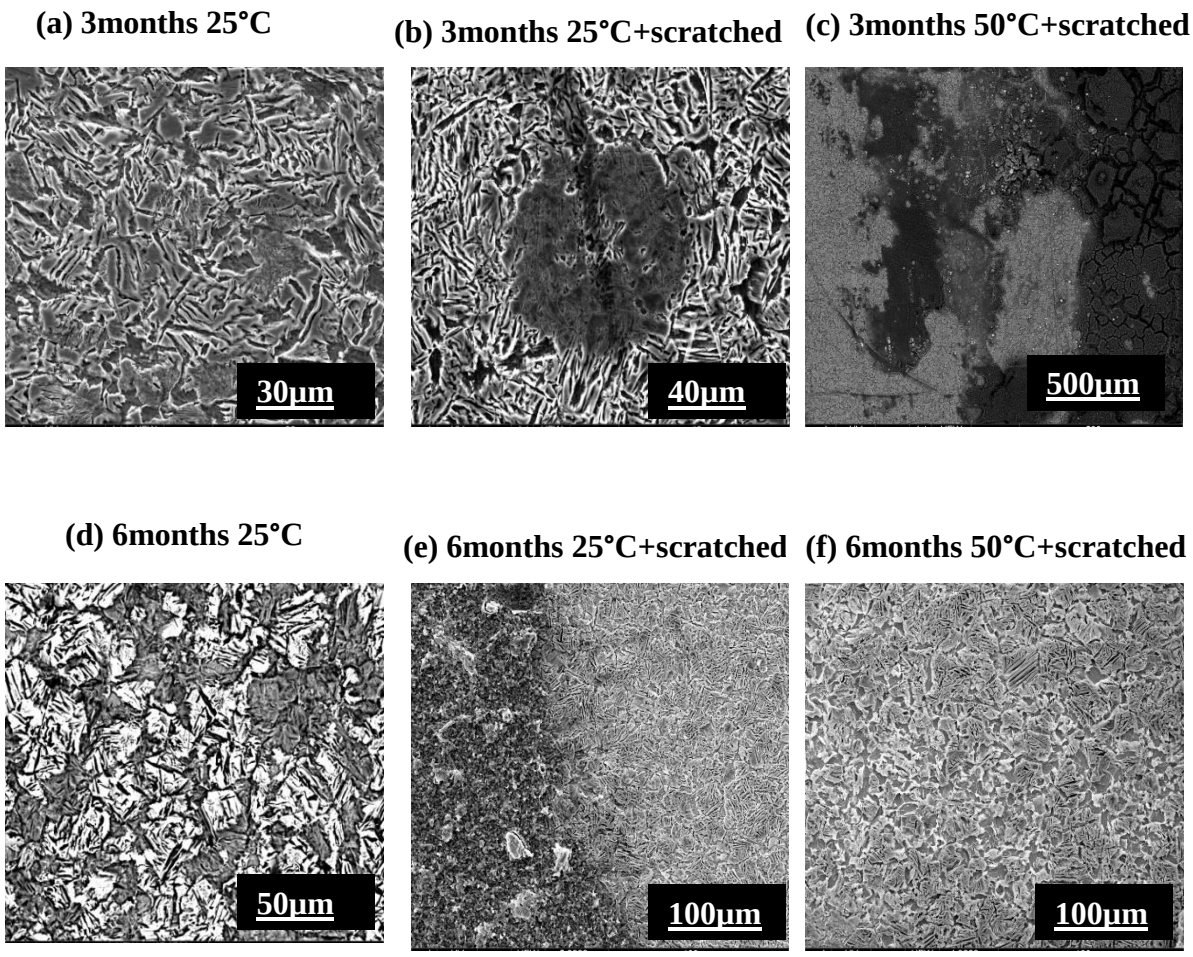

Figure A7 *Scanning electron micrographs (in SE mode) of all SS coupons corroded for 3 and 6 months under dynamic conditions at different temperatures (exact conditions are indicated above the micrographs).*

Static conditions CS systems (3, 6 and 9 months)

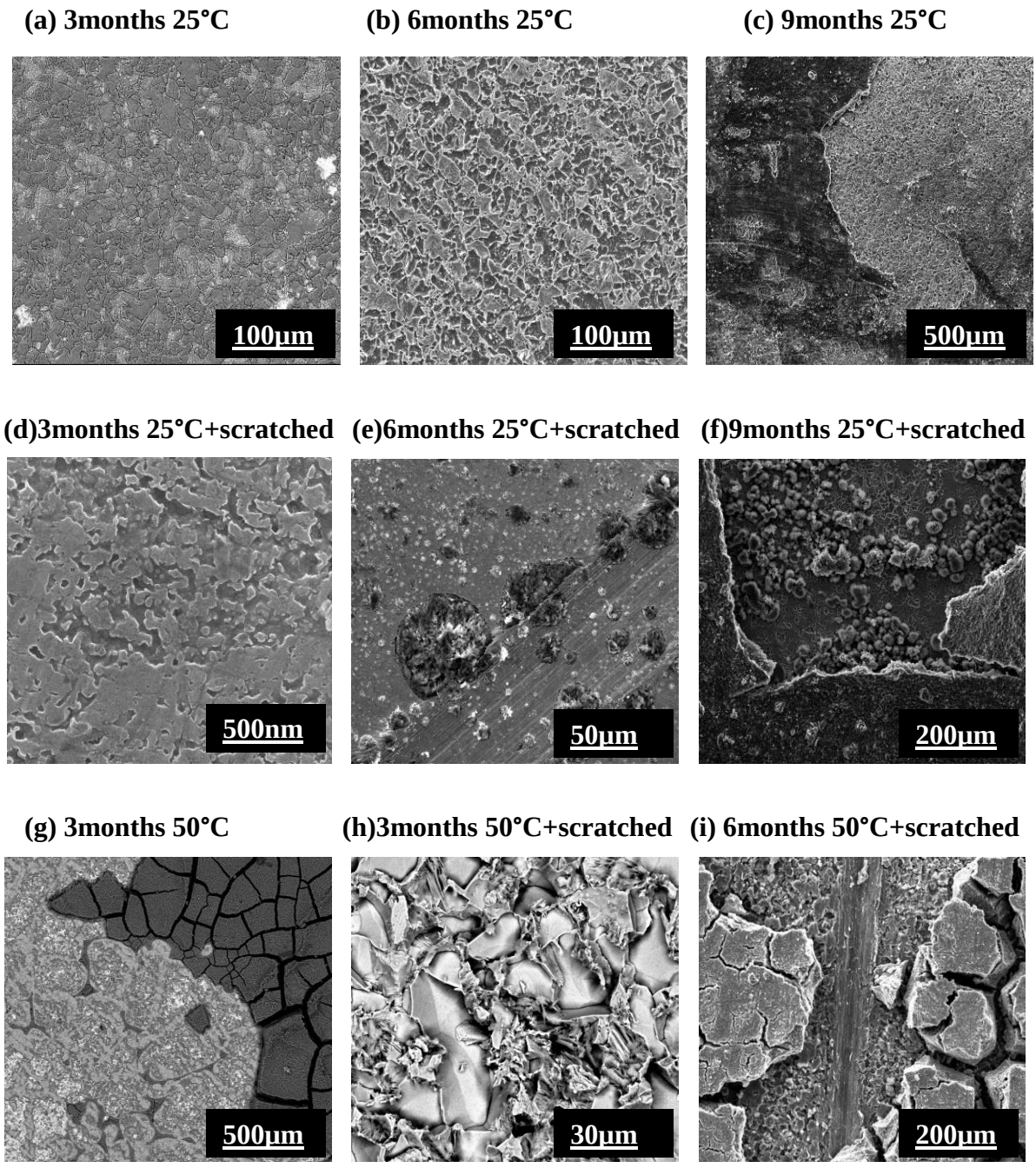

Figure A8 *Scanning electron micrographs (in SE mode) of all CS coupons corroded for 3, 6 and 9 months under static conditions at different temperature (exact conditions are indicated above the micrographs).*

Dynamic conditions CS systems (3 and 6 months)

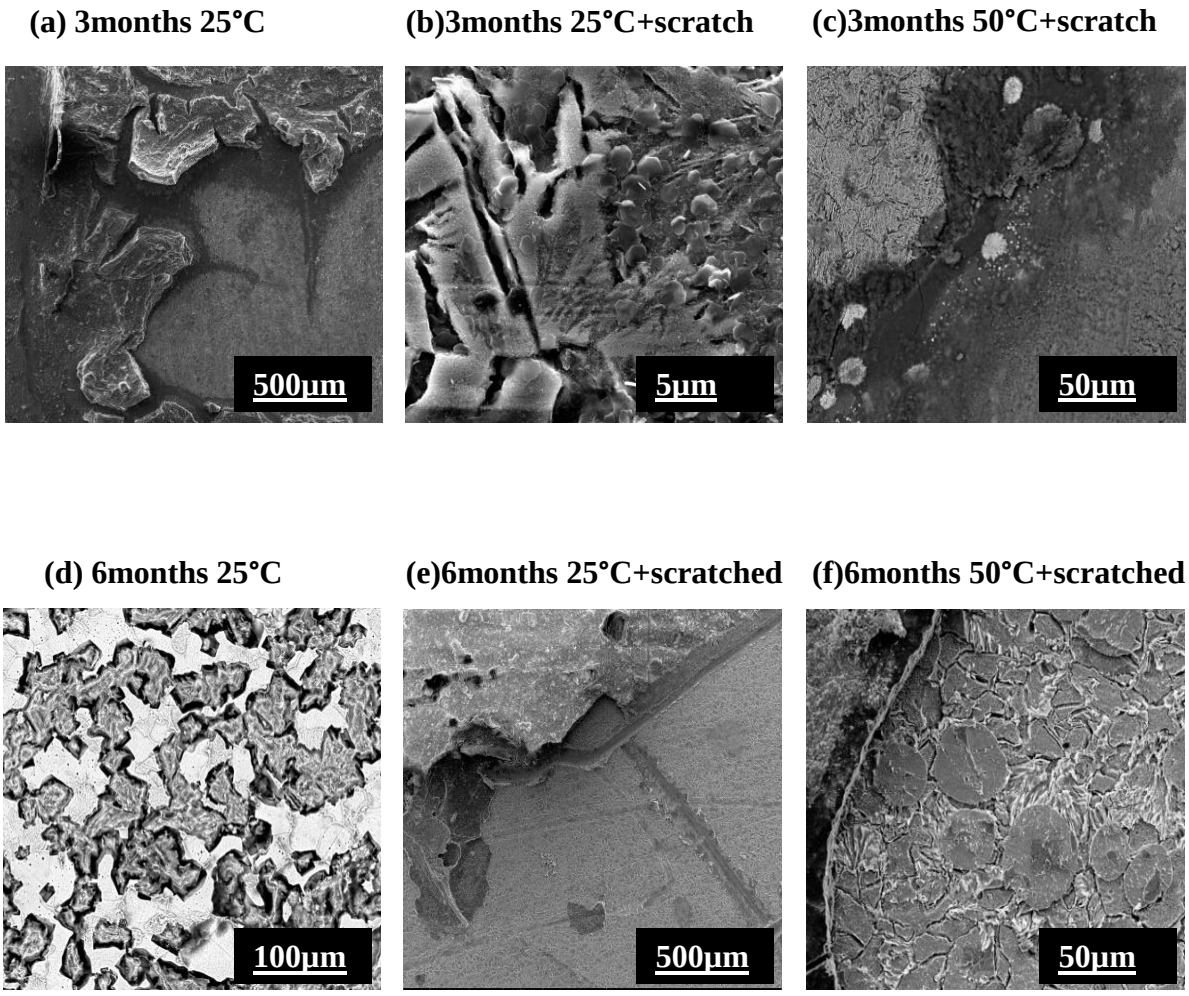

Figure A9 *Scanning electron micrographs (in SE mode) of all CS coupons corroded for 3 and 6 months under dynamic conditions at different temperature (exact conditions are indicated above the micrographs).*

Static conditions CS in GMZ bentonite systems (3, 6, 9 and 12 months)

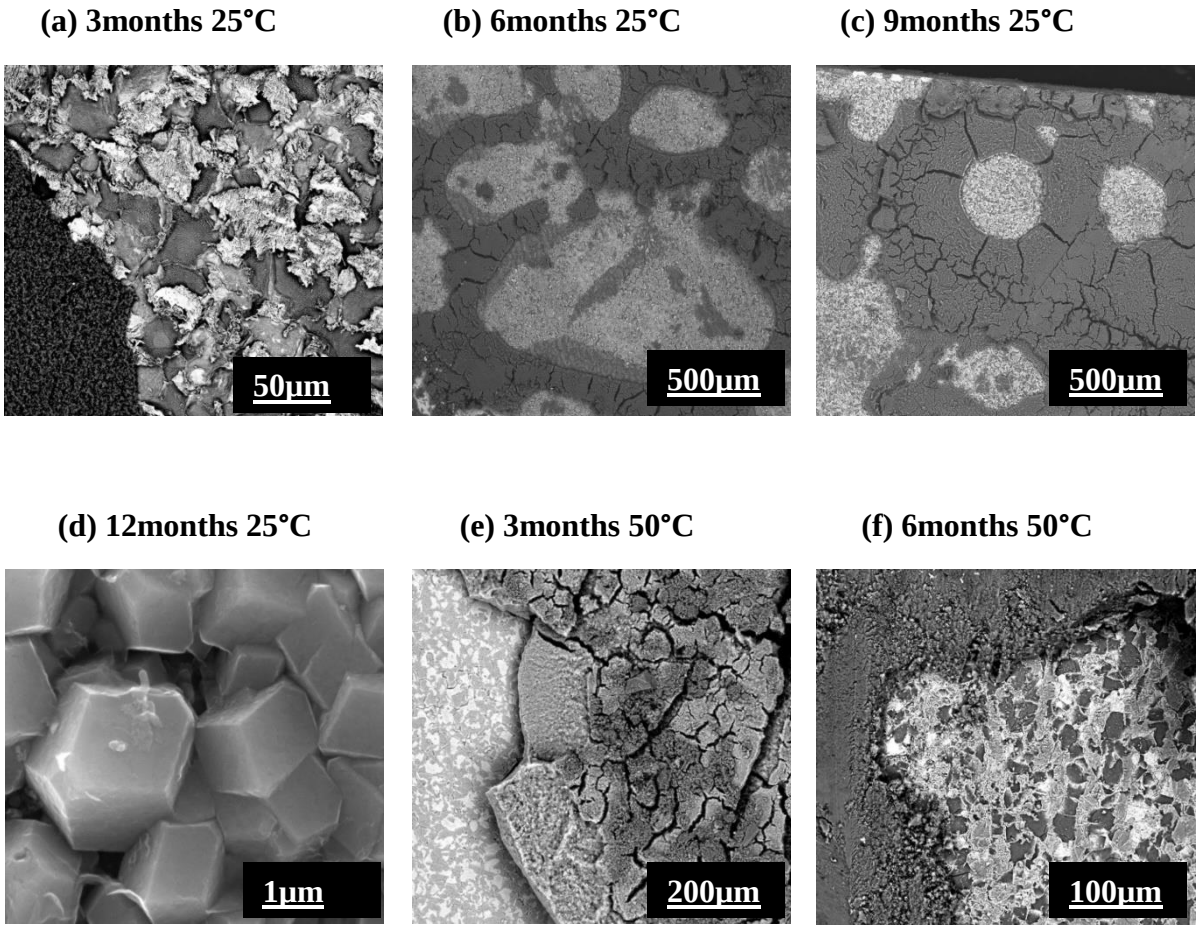

Figure A10 *Scanning electron micrographs (in SE mode) of all CS coupons in GMZ bentonite corroded for 3, 6, 9 and 12 months under static conditions at different temperature (exact conditions are indicated above the micrographs).*

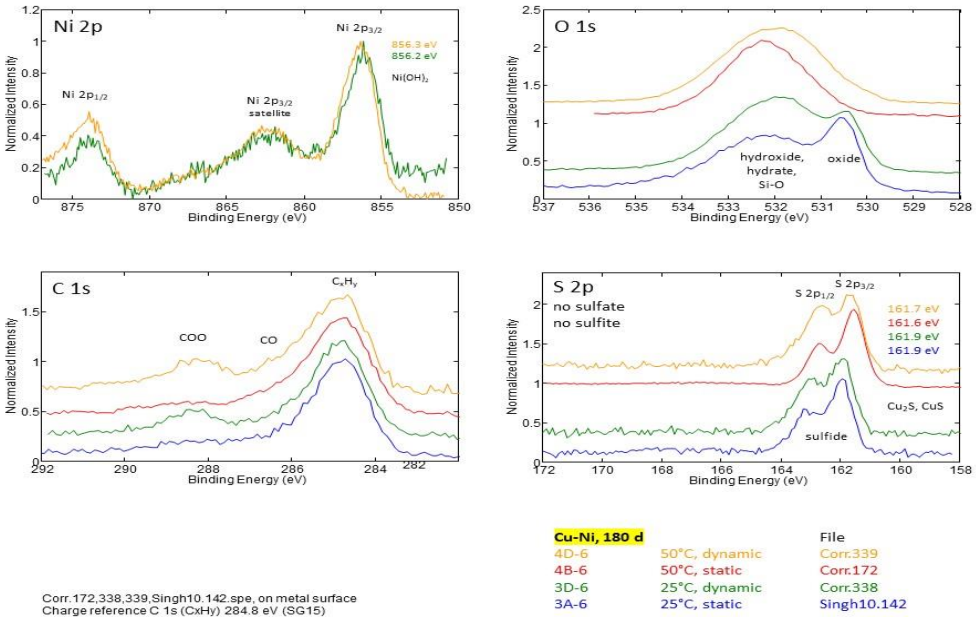

Figure A11 *X-ray photoelectron spectra recorded on CuNi alloy coupons corroded in MX-80 bentonite under static and dynamic conditions-I (exact conditions are indicated below the graphs).*

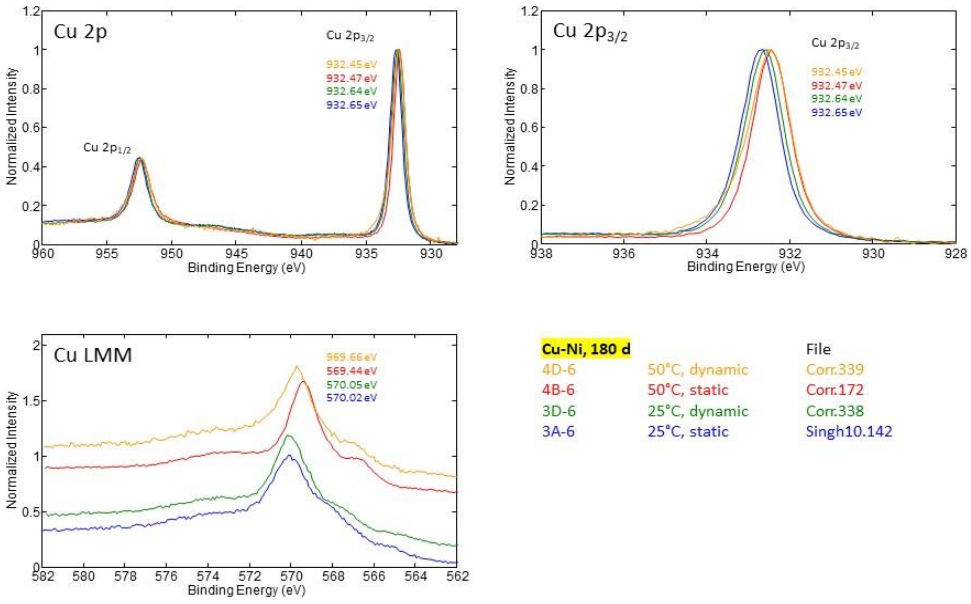

Figure A12 *X-ray photoelectron spectra recorded on CuNi alloy coupons corroded in MX-80 bentonite under static and dynamic conditions-II (exact conditions are indicated below the graphs).*

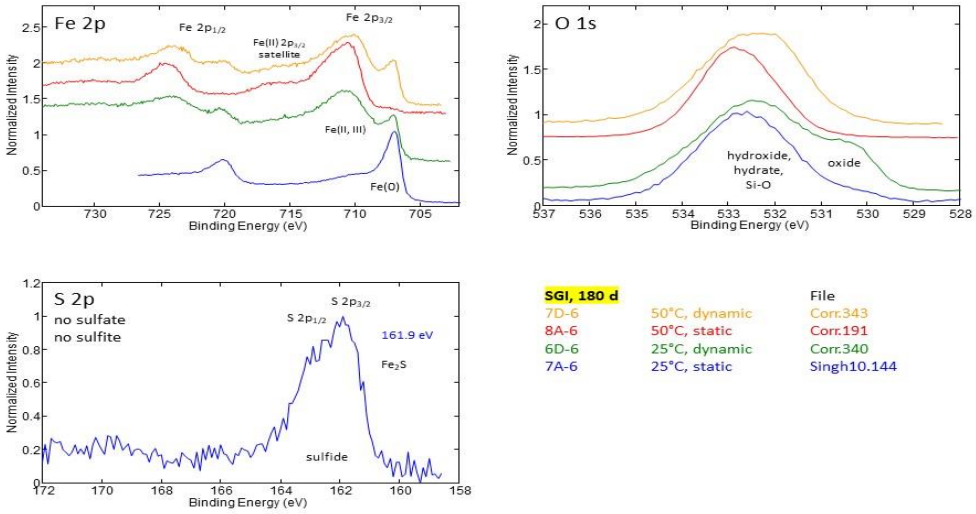

Figure A13 *X-ray photoelectron spectra recorded on SGI coupons corroded in MX-80 bentonite under static and dynamic conditions (exact conditions are indicated below the graphs).*

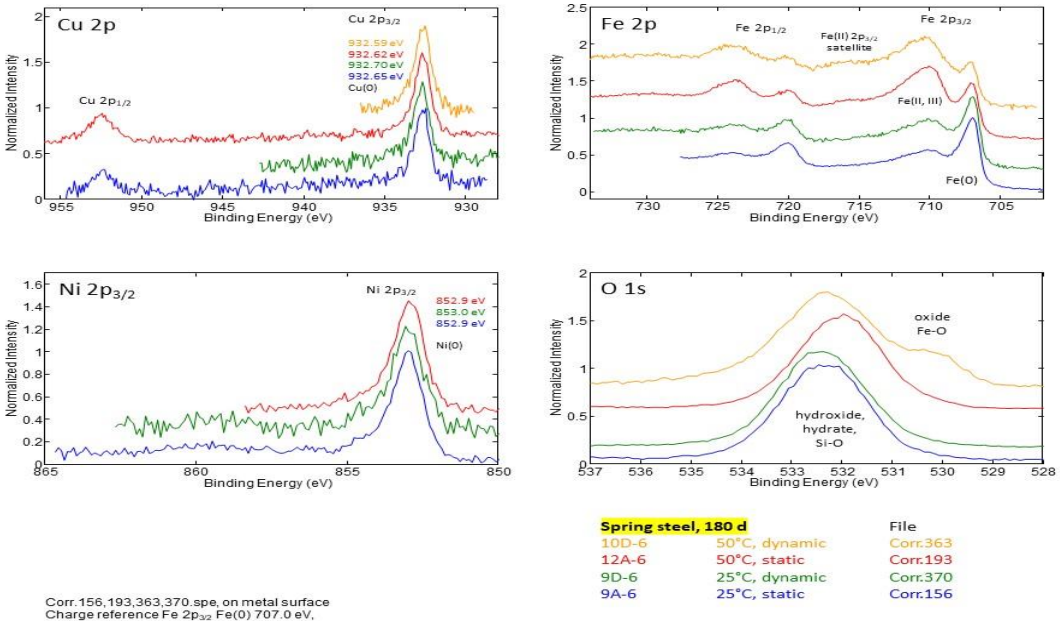

Figure A14 *X-ray photoelectron spectra recorded on SS coupons corroded in MX-80 bentonite under static and dynamic conditions-I (exact conditions are indicated below the graphs).*

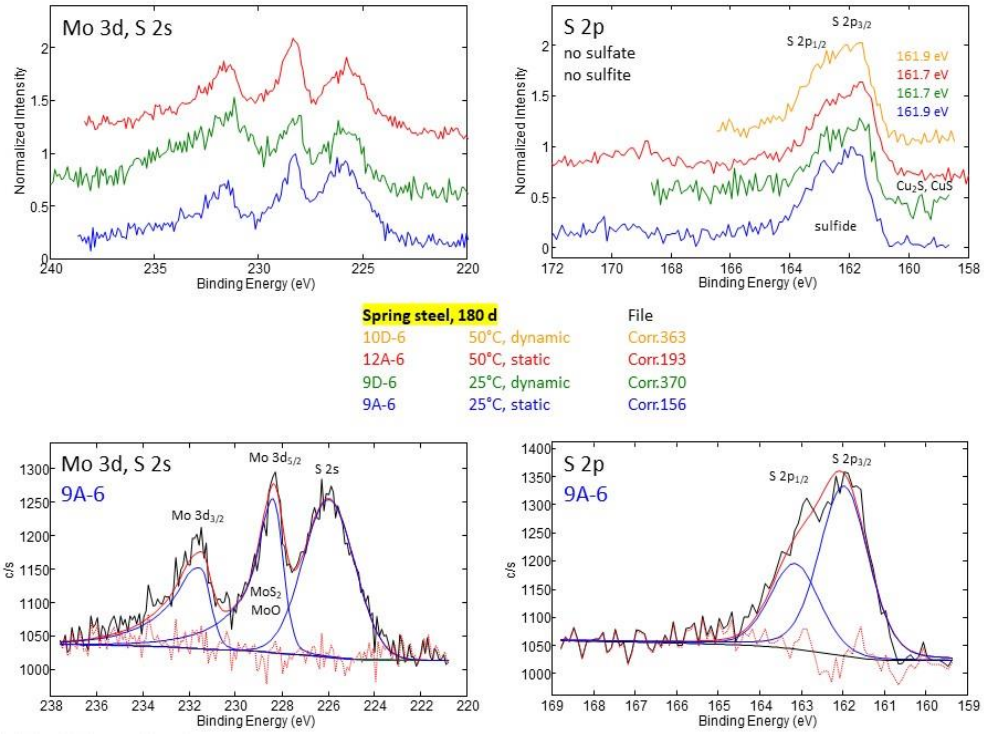

Figure A15 *X-ray photoelectron spectra recorded on SS coupons corroded in MX-80 bentonite under static and dynamic conditions-II (exact conditions are indicated middle of the graphs).*

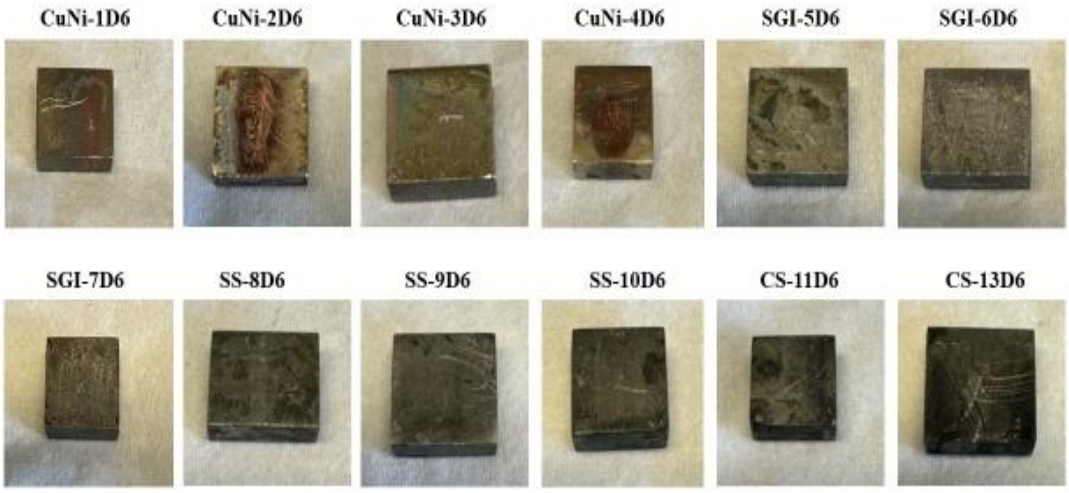

Figure A16 *Images of corroded metallic coupons of all four investigated materials (CuNi, SGI, SS and CS) in MX-80 bentonite under 6 months dynamic conditions at room and elevated temperature (exact conditions are indicated above image: details of conditions are indicated above image: details of condition can be found in* ***Table A 2*** *appendix).*

List of Tables and Figures